Západočeská univerzita v Plzni

Fakulta aplikovaných věd

Mikrostrukturálně orientovaný model transportu iontů v porézním prostředí

Ing. Jana Camprová Turjanicová

dizertační práce
k získání akademického titulu doktor
v oboru Aplikovaná mechanika

Školitel:	prof. Dr. Ing. Eduard Rohan, DSc.
Katedra:	Katedra mechaniky

Plzeň 2021

University of West Bohemia in Pilsen
Faculty of Applied Sciences

Microstructurally oriented model of ionic transport in porous medium

Ing. Jana Camprová Turjanicová

doctoral thesis
to obtain academic degree doctor
in Applied Mechanics

Tutor:	prof. Dr. Ing. Eduard Rohan, DSc.
Department:	Department of mechanics

Pilsen 2021

Prohlášení

Předkládám k posouzení a k obhajobě tuto disertační práci zpracovanou na závěr doktorského studia na Fakultě aplikovaných věd Západočeské univerzity v Plzni. Čestně prohlašuji, že jsem tuto disertační práci vypracovala samostatně a s použitím odborné literatury a pramenů uvedených v seznamu, který je součástí této práce. Zároveň čestně prohlašuji, že jsem při vypracování této práce zachovala postupy ve vědecké práci obvyklé.

V Plzni, 31.8. 2021 Ing. Jana Camprová Turjanicová

Declaration

I submit this Ph.D. thesis for the award of the degree of Doctor of Philosophy to the Department of Mechanics of the University of West Bohemia in Pilsen. I declare that I carried out the work reported in this thesis with the help of scientific literature that is properly cited and listed as a part of this text. I further declare that I did follow the scientific methods that are in agreement with the usual research ethics.

Pilsen, August 31, 2021 Ing. Jana Camprová Turjanicová

Poděkování

Vznik této práce byl podpořen projektem GACR 19-04956S Grantové agentury ČR, projektem Evropského fondu pro regionální rozvoj ”Aplikace moderních technologií v medicíně a průmyslu” (No. CZ.02.1.01/0.0/0.0/17 048/0007280), projektem LO1506 Ministerstva školství, mládeže a tělovýchovy ČR a v neposlední řadě studentským grantovým systémem SGS-2019-002.

Na tomto místě bych také ráda poděkovala svému školiteli prof. Dr. Ing. Eduardu Rohanovi, DSc. za vedení v průběhu celého mého studia na Fakultě aplikovaných věd a za cenné rady, bez nichž by tato práce nemohla vzniknout. Poděkování patří také Ing. Vladimíru Lukešovi, Ph.D. za rady spojené s tvorbou programů pro numerické simulace a vizualizace výsledků. Dále bych chtěla poděkovat Ing. Janu Heczkovi, Ph.D. za veškerou pomoc a podporu, které se mi od něj dostalo. Zvláštní poděkování bych ráda věnovala všem kolegům z Katedry mechaniky, přátelům a rodině za pochopení, trpělivost a podporu.

Acknowledgement

The research has been supported by the project GACR 19-04956S of the Scientific Foundation of the Czech Republic. The work was supported in a part also from European Regional Development Fund-Project “Application of Modern Technologies in Medicine and Industry” (No. CZ.02.1.01/0.0/0.0/17 048/0007280). The author is also grateful for the support to the project LO 1506 of the Czech Ministry of Education, Youth and Sports and to the project SGS-2019-002.

I want to thank my tutor, prof. Dr. Ing. Eduard Rohan, DSc., for all the help and guidance he provided me during my Ph.D. study. This work would not exist without him. I am very grateful to my colleague Ing. Vladimír Lukeš, Ph.D., for the help with the software tools for implementation and visualization of results. I would like to extend my thanks to Ing. Jan Heczko, Ph.D., for all the help and support he gave me. Last but not least, my huge thanks belong to all my colleagues, friends and family, for all the understanding, patience, and support.

Abstrakt

Tato disertační práce se zaměřuje na víceškálové modelování transportu iontů v porézním prostředí a jeho aplikaci na modelování tkáně kortikální kosti. Je uvažován dvoufázový materiál, kde tekutou složku tvoří nestlačitelný symetrický elektrolyt se dvěma typy rozpuštěných iontů. Pro pevnou fázi jsou uvažovány dva typy materiálu: v prvním případě se jedná o lineárně elastický materiál, ve druhém případě jde o slabě piezoelektrický materiál. V obou případech se na rozhraní fází nachází slabý záporný náboj. Přítomnost iontů v tekutině, její vazkost, blízkost náboje na rozhraní i deformace pevné fáze ovlivňují pohyb elektrolytu a tím také rozložení náboje. Výsledkem je komplexní matematický model, který je nutno linearizovat a převést do bezrozměrného tvaru. Tak jsou získány linearizované bezrozměrné matematické modely pro oba typy pevné fáze.

Část této práce se věnuje odvození víceškálového modelu transportu iontů v porézním prostředí pomocí metody unfoldingu. Metoda dvouškálové homogenizace, na které je metoda unfoldingu založena, vede na dva systémy rovnic. Řešením mikroskopického problému, který je definován na tzv. mikroskopické referenční buňce, je sada korektorových funkcí, které slouží k odvození homogenizovaných koeficientů. Tyto koeficienty jsou použity k odvození makroskopického problému, jenž popisuje celkové chování na makroskopické úrovni. Takto je odvozen statický dvouškálový model pro transport iontů v poroelastickém materiálu, který je dále rozšířen na model kvasi statický v poropiezoelektrickém materiálu.

Pro numerické simulace chování odvozených modelů byl vytvořen vlastní software pro řešení 3D úloh na obou škálách. Prostorová diskretizace na obou škálách je provedena pomocí metody konečných prvků. Chování obou modelů je ilustrováno pomocí několika testovacích úloh.

Tato práce také předkládá možnou metodu identifikace obtížně měřitelných materiálových parametrů suché kosti, která je modelovaná jako slabě piezoelektrický porézní materiál. Tato metoda je založena na optimalizaci pomocí citlivostní analýzy efektivních vztahů. K identifikaci daných materiálových parametrů je pak použit přístup tzv. fiktivního experimentu, který umožňuje generování experimentálních dat pro známé nastavení materiálových parametrů a dává nám tak nástroj na ověření správnosti odvozených vztahů. Přesnost odvozených citlivostních vztahů a také totálního diferenciálu účelové funkce je ověřena pomocí metody konečných diferencí. Za tímto účelem byl vytvořen software pro identifikaci materiálových parametrů, který částečně využívá dostupné softwarové knihovny zaměřené na optimalizaci.

V poslední části práce je model s uvažováním piezoelektrického jevu aplikován na modelování chování tkáně kortikální kosti. Za tímto účelem byla vytvořena výpočetní síť reprezentující mikrostrukturu tkáně a dále síť reprezentující makroskopický level, tedy jeden osteon. Pomocí numerických simulací bylo ilustrováno chování dvouškálového modelu kortikální kosti a to jak na makroskopické úrovni, tak pomocí rekonstrukcí řešení na úrovni mikroskopické.

Klíčová slova: transport iontů, homogenizace, kortikální kost, porézní materiál, piezoelektricita

Abstract

This thesis focuses on the multiscale modeling of ionic transport in porous medium and its application to modeling cortical bone tissue. It considers a two-phase material consisting of a fluid phase, which is modeled as an incompressible symmetric electrolyte solution with two types of the ionic specimen and a solid phase, for which two types of material models were considered. The first is the classic linear elastic material model, and the second is the model describing a material exhibiting weak piezoelectric properties. The solid-fluid interface is charged with a weak electrostatic charge. The presence of ions in the fluid phase, its viscosity, the proximity of a charged surface, and the deformation of the solid phase all influence the electrolyte movement and the charge distribution. This is described by a complex nonlinear multi-physical mathematical model, which is later non-dimensionalized and subsequently linearized. The two-scale model of ionic transport in the porous medium was derived by the unfolding method. At the microscopic level, it consists of local problems that are solved on the representative volume element. Their solutions serve to express effective coefficients that characterize the behavior of the homogenized material and are used in the derivation of the effective macroscopic problem. By this approach, the homogenized model of the steady-state flow of the electrolyte through the poroelastic medium is derived. It is then extended to describe the quasi-static state of the electrolyte flow through the weakly piezoelectric porous medium.

To simulate the behavior of the derived two-scale model, the software for numerical simulations of 3D problems on both scales was developed. It is based on the finite element method and it can be used for simulations of both types of considered porous media, elastic and piezoelectric, respectively.

One of the aims of this work is to provide a framework for the identification of difficultly measurable material parameters of cortical bone tissue. The identification problem is formed for the case of dry bone, which is modeled as weakly piezoelectric porous material. It uses the so-called fictitious experiment to generate experimental data for a known set of optimal parameters. The precision of the identification process is checked by the finite difference method. The identification process was implemented using a combination of in-house developed software and open-source optimization libraries.

The last part of this work concentrates on applying the presented effective model to the numerical modeling of cortical bone behavior. The computational meshes were generated to represent the lacunar-canalicular network and the single bone osteon, *i.e.* the micro- and macrostructure, respectively. The numerical simulations mimicking the experiment were performed to illustrate the behavior of the two-scale model. The influence of macroscopic phenomena on the microstructure is shown by the reconstruction of the solution on the microscopic scale.

Key words: ionic transport, homogenization, cortical bone, porous material, piezoelectricity

Contents

List of Figures

List of Tables

List of Symbols

Abbreviations

r.h.s.	Right Hand Side
BVP	Boundary Value Problem
FEM	Finite Element Method
LCN	Lacunar-Canalicular Network
LEPM	Linear Elastic Porous Medium
PEPM	Piezoelectric Porous Medium
RVE	Representative Volume Element
UFM	Unfolding homogenization Method

Physical constants

$\boldsymbol{A} = \{A_{ijkl}\}$	elasticity tensor
$\boldsymbol{d} = \{d_{ij}\}$	dielectric tensor
η_f	dynamic viscosity
$\boldsymbol{G} = \{G_{kij}\}$	piezoelectric coupling tensor
$\boldsymbol{g} = \{G_{kij}\}$	piezoelectric coupling tensor
κ	Debye-Hückel parameter
λ_D	Debye length parameter
$\mathcal{E}$	dielectric constant, $\mathcal{E} = \mathcal{E}_r\mathcal{E}_0$
μ_α^0	standard electrochemical potential expressed at infinite dilution
ν, ν_{ij}	Poisson's ratio
Pe_α	Peclet number for $\alpha-$th ionic species
ρ_f	fluid density
ρ_s	density of solid phase

Σ	surface charge at solid-fluid interface
c_c	characteristic concentration
D_α^0	diffusivity of the α-th ionic species
e	elementary charge
E, E_i	Young modulus
k_B	Boltzmann constant
l	characteristic dimension dimension of microscopic periodic structure
L_c	characteristic dimension of macroscopic domain
T	absolute temperature
z_α	valence of α-th ionic species

Variables

Φ_α	ionic potential, $\alpha = 1, 2$
Ψ	electrostatic potential related to EDL
Ψ_f	electrostatic potential of a fluid phase
Ψ_s	potential of solid phase
$\boldsymbol{u}$	displacement
$\boldsymbol{v}$	hydrodynamic velocity
$\boldsymbol{w}$	convective velocity
c_α	concentration of α-th ionic species
P	global pressure
p	fluid pressure

Effective coefficients

$\boldsymbol{\mathcal{A}} = \left\{\mathcal{A}_{ijkl}^\alpha\right\}$	elasticity/piezoelasticity tensor
$\boldsymbol{\mathcal{B}}$	Biot's tensor
$\boldsymbol{\mathcal{C}}^\alpha = \left\{\mathcal{C}_{ij}^\alpha\right\}$	tensor related to ionic potentials
$\boldsymbol{\mathcal{D}}^{\alpha\beta} = \left\{\mathcal{D}_{ij}^{\alpha\beta}\right\}$	diffusivity tensors
$\boldsymbol{\mathcal{J}}^\alpha = \left\{\mathcal{J}_{ij}^\alpha\right\}$	migration-diffusion tensors
$\boldsymbol{\mathcal{L}}^\alpha = \left\{\mathcal{L}_{ij}^\alpha\right\}$	coupling tensors

Other Symbols

$\boldsymbol{a} = \{a_k\}$	vector of identification parameters
$\boldsymbol{\sigma}_f$	stress tensor of the fluid phase
$\boldsymbol{\sigma}_s$	stress tensor of linear elastic solid phase
$\boldsymbol{\tau}_M$	Maxwell 2nd order tensor
$\boldsymbol{D}_s$	electric displacement
δ_{ij}	Kronecker's delta
$\boldsymbol{e}^k$	canonical base, $k = 1, \dots, d$
$\boldsymbol{f} = \{f_k\}$	external body force
γ	dimensionless parameter relating characteristic length of microstructure to Debye-Hückel parameter , $\gamma = \kappa^2 l^2$
$\boldsymbol{I}$	identity
$\boldsymbol{j}_\alpha$	migration-diffusion flux of the α-th ionic species
$\mathbf{E} = \{E_k\}$	electric field, $\mathbf{E} = -\nabla\Psi_f$
μ_α	electrochemical potential of α-th ionic species
$\boldsymbol{n}$	unit exterior normal
$\partial_a^{\text{tot}} F(\boldsymbol{a}, \boldsymbol{u})$	total derivative of objective function
∂_{a_i}	sensitivity on identification parameter a_i
$\boldsymbol{\sigma}_s^p$	stress tensor of piezoelectric solid phase
$\boldsymbol{e}(\boldsymbol{u})$	elastic strain tensor,$\boldsymbol{e}(\boldsymbol{u}) = \frac{1}{2}\left(\nabla\boldsymbol{u} + (\nabla\boldsymbol{u})^T\right)$
ε	scale parameter, $0 < \varepsilon << 1$
ζ	potential on solid-fluid interface known as $\zeta-$potential
c_α^b	concentration of α-th ionic species in bulk, $\alpha = 1, 2$
d	problem dimension
$F(\boldsymbol{a}, \boldsymbol{u})$	objective function dependent on design parameters and state variables
k^α	ionic energy parameter
N	number of ionic species in the electrolyte, usually N=2
N_σ	ratio between electrical and thermal energy, $N_\sigma = \frac{el\Sigma_c}{\mathcal{E} k_B T}$
q_s	electric volume charge

x	coordinate system on macroscopic scale (slow scale)
y	coordinate system on representative periodic cell (fast scale)
ϕ_f	porosity, volume fracture of fluid phase

Domains

Γ	solid-fluid interface on macroscopic scale
Γ_Y	solid-fluid interface on representative periodic element
Ω	bounded domain occupied by porous medium
Ω_f	fluid filled pore space
Ω_s	part of macroscopic domain occupied by solid matrix
$\partial\Omega$	boundary of the domain occupied by porous medium
$\partial_{\text{ext}}\Omega$	external part of the boundary of macroscopic domain
Y	representative periodic element
Y_f	part of representative periodic element occupied by fluid phase
Y_s	part of representative periodic element occupied by solid phase

Spaces

$H^1_{\#}(\Omega)$	space given as $\{\psi \in H^1(\Omega),\ L-\text{periodic in } x\}$
$L^2(\Omega)$	space of square-integrable functions
$\mathbf{H}^1_{\#0}(\Omega)$	space given as $\left\{\boldsymbol{\varphi} \in H^1(\Omega)^d, \boldsymbol{\varphi} = 0 \quad \text{on } \Gamma,\ L-\text{periodic in } x\right\}$
$\mathbf{H}^1_{\#}(\Omega)$	space given as $\left\{\boldsymbol{\varphi} \in H^1(\Omega)^d,\ L-\text{periodic in } x\right\}$
$H^1(\Omega)$	Sobolev space $W^{1,2}(\Omega)$

Superscripts

$\sqcup^0$	quantity is related to the slow macroscopic scale
$\sqcup^1$	quantity is related to the fast microscopic scale
$\sqcup^*$	dimensionless quantity, usually forcing term
$\sqcup^{\text{eff}}$	quantity is solution to dimensionalized macroscopic problem
$\sqcup^{\text{eq}}$	quantity in equilibrium
$\sqcup^{\text{ext}}$	external quantity
$\sqcup^{\text{mic}}$	fluctutions part of quantity reconstructed at microscale
$\sqcup^{\text{per}}$	pertubed quantity

$\sqcup^{\mathrm{per}}$	perturbation of quantity
$\sqcup^{\mathrm{rec}}$	quantity recovered at microscopic scale
$\sqcup^{\varepsilon}$	quantity/domain is related to the scale parameter ε (also quantity is dimensionless)

Subscripts

$\sqcup_{\mathrm{bulk}}$	quantity in bulk
$\sqcup_{\mathrm{EDL}}$	Quantity in EDL
$\sqcup_{c}$	characteristic quantity
$\sqcup_{f}$	quantity/domain is related to the fluid phase
$\sqcup_{s}$	quantity/domain is related to the solid phase
$\sqcup_{\alpha}$	quantity related to α-th ionic specimen
$\sqcup_{\beta}$	quantity related to β-th ionic specimen
$\sqcup_{\mathrm{exp}}$	data obtained from experiment

Chapter 1

Introduction

This chapter explains the importance of microstructure-oriented modeling of ionic transport in the porous media, especially biological tissues (such as cortical bone tissue). Next, it gives an overview of the present state of the research in this field and presents the aims of this thesis. Lastly, it provides an outline of the submitted work.

1.1 Motivation

The modeling of ionic transport is useful in a wide range of science fields, often in the context of homogenization. In geoscience, it is well known as a base for modeling swelling clays. It also serves well to model the charging units or batteries. And finally, in biomechanics, it can be used for modeling a variety of tissues. Our interest lies mainly in its use for modeling interactions between a cortical bone porous structure and the bone fluid in the pore space.

Cortical bone, as well as other biological tissues, is heterogeneous material constituted by multiple material phases at different scale levels. The macroscopically observed phenomena in biological tissues often originate from the processes associated with the microstructural level. For example, the remodeling and regrowth of bone tissue can be influenced by processes happening on such a small scale as a few hundreds of nanometers. On this scale, the cortical bone tissue consists of a solid bone matrix and a lacunar-canalicular network saturated by a bone fluid. Some of the studies, for example, (Lemaire et al. 2010b), (Lemaire et al. 2011), suggest that the osteocytes nested in the lacunae activate in reaction to the movement of charged ionic particles in the bone fluid.

From electrical measurements on the cortical bone, it is apparent that the solid matrix consisting of the apatite crystals and collagen fibers exhibits a quasi-permanent space charge. The collagen fibers also show piezoelectric behavior in response to the deformation of the solid matrix. The charge of the solid phase affects the distribution of ionic particles inside the bone fluid and thus influences the movement of the electrolyte in the lacunar-canalicular network. These effects, together with the microstructure of the cortical bone tissue, should be considered during the derivation of the model from its microscopic to its macroscopic scale. This thesis aims to provide an insight into the microstructure-oriented modeling of such multi-physics phenomena. We are especially interested in modeling a combination of electrochemical and mechanical phenomena, such as ionic transport through a poroelastic or porous piezoelectric medium.

The modeling of cortical bone tissue presents a unique challenge because of its highly hierarchical structure and complex interaction between phases. The composition of the material, as well as the difference in its microstructural geometrical arrangement, have a significant influence on the behavior of the macroscopically observed properties. These are also dependent on the spatial distribution and material properties of each constituent and their mutual interactions. To simulate such material by direct modeling of its whole microstructure in its complexity would be very taxing on the computational memory requirements and not practical for more extensive and more complex simulations. Instead, the heterogeneity of the material is usually dealt with through the means of microstructurally oriented modeling.

1.2 Methods and approaches for modeling heterogeneous materials

The transport of an electrolyte solution through a porous medium is a multiscale problem. It occurs due to the interactions between both phases, namely by the pressure or deformation-driven convective movement of the solvent, the movement of electrically charged particles in the proximity of the charged surface of the pore, and the electrochemical diffusion.

Different approaches can be applied in the mathematical modeling of heterogeneous material with multiple phases. One of the most intuitive and basic examples is mixture theory, which is sometimes used to identify homogenized material properties of composite materials. This method is based on averaging the material properties of all phases of heterogeneous material. It takes into consideration only volume fractions of each material phase and thus does not hold any information about the topology of material microstructure, (Siddique et al. 2017).

Some methods combine the averaging of the phase's properties with some degree of respect for the topology of microstructure. Some examples of this type of method are the Mori-Tanaka or Eshelby's method, which are used for the estimations of elastic properties of a material with elliptical inclusions,(Eshelby 1957; Benveniste 1987). These methods may serve as a computationally effective way to approximate the effective properties of materials with a certain shape of heterogeneities. However, these methods are not very suitable to model materials with more complex microstructures due to limitations imposed on the geometry of inclusions.

The more suitable methods are the ones based on an asymptotic analysis of the system. The main principle is that we let the scale parameter ε "vanish" from the partial differential equations (PDE) system that constitutes the problem, *i.e.* passing it to the limit $\varepsilon \to 0$. This results in a new limit PDE system describing a homogenized macroscopic model with homogenized coefficients, which express the influence of heterogeneities in microscale onto macroscopic behavior.

One of the efficient methods for asymptotic analysis is the so-called periodic unfolding homogenization method. The homogenization by unfolding is based on specific properties of the so-called unfolding operator. It was first first proposed in (Cioranescu et al. 2002) and then extended in (Cioranescu et al. 2008). It introduces recovery sequences of each variable consisting of its fast and slow (sometimes also ”fine” and ”coarse” or ”macroscopic” and ”microscopic”) components. One of the benefits of this method is that it deals with the weak form of the PDE system, which enables us to rely on the standard notion of weak convergence. This method also respects the microstructure of the porous medium and provides us with tools to recover the macroscopic solution on the microscopic scale. Thus, it is the method of our choice.

1.3 State of the art

During the last decade, a significant body of literature has been devoted to the modeling of the transport of an electrolyte solution through a porous medium. Here we comment only on those publications which, as we believe, are the most relevant and tightly related to the present work.

As stated above, a significant part of the related research on the matter concerns geosciences. One of the most recognized works in this field is the paper (Moyne and Murad 2002) which relies on the homogenization procedure to derive a macroscopic model of expansive clays composed of a charged solid phase saturated by an electrolyte solution. This microscopic model includes equations describing electro-hydrodynamics coupled with the equation governing the flow of the electrolyte solution, ion electrodiffusion, and electric potential distribution. Then the asymptotic homogenization is used to derive a two-scale model of electrokinetic phenomena, such as the electroosmotic flow driven by the streaming potential gradient, the electrophoretic motion of mobile charges, and the swelling induced by the osmosis. This model was later revisited in paper (Moyne and Murad 2006) with a more focus on the rigorous homogenization procedure and its analysis. A similar problem, *i.e.* the transport of an N-component electrolyte solution through a porous rigid body subjected to a static electric field, was also studied in (Looker and Carnie 2006), although no assumptions about the electric double layer were considered.

In biomechanical modeling, the authors of (Lemaire et al. 2006) and (Lemaire et al. 2010b) use a similar approach to study the bone fluid flows at two porosity levels in the cortical bone tissue. It is worth noting a possible application of that model in the studies of mechanosensing, (Lemaire et al. 2010a), and bone remodeling. These issues were treated in (Nguyen et al. 2009), where Biot’s poroelastic theory was applied to the three-dimensional anisotropic media to account for deformation-induced fluid flows in the osteonal matrix under the harmonic loading. Homogenization of the ionic exchange between the charged porous medium and the electrolyte solution was elaborated in (Lemaire et al. 2010a), being motivated by mechanosensing. A two-scale one-dimensional model for horizontal electroosmotic flows in several thin horizontal slits was proposed in (Amirat and Shelukhin 2008). Therein, the pressure gradient and a horizontal electrical field were recognized as the flow driving forces. Although this work is focused on one specific case and disregards any deformation of the solid part, it provides a helpful insight into the homogenization of the electroosmotic law for different types of multi-component electrolytes.

Most of the works devoted to the transport of an electrolyte solution through a porous medium assume that an electrolyte saturates a rigid porous medium, see (Allaire et al. 2013a; Allaire et al. 2013b), the deformation phenomenon or evolving porous structures were considered in some papers, see *e.g.* (Ray et al. 2012b; Allaire et al. 2015). Moreover, some other works, *e.g.* (Andreasen and Sigmund 2013; Rohan et al. 2016a; Sandström et al. 2016; Rohan and Lukeš 2015) treating the fluid-structure interaction without any electroosmotic or electromechanical coupling established useful platforms for extensions of those particular models to account for the phenomena featuring the transport of electrolytes. Such an extension was reported in (Allaire et al. 2015), which is motivated by the study of nuclear waste disposal. This work introduces the well-known system of equations governing ionic transport and extends it by the elasticity of the solid part. The coupling between fluid motion and deformation of the solid matrix was explored in the earlier work (Mikelić and Wheeler 2012). The authors show that by a suitable choice of time scale, the deformation of the porous medium becomes only weakly coupled to the electrokinetic system, which is advantageous for the model implementation and numerical simulations. For completeness, let us note that a non-stationary model of ionic transport consisting of the Stokes, Nernst-Planck, and Poisson systems of equations was reported in papers (Ray et al. 2012a; Schmuck and Bazant 2015) and (Frank et al. 2011), where the upscaling procedure was treated using the two-scale convergence.

The bone in its dry state exhibits piezoelectric behavior, which is one of the possible explanations behind mechanosensing and bone remodeling, as discussed in (Miara et al. 2005). The bone is modeled as a porous material consisting of a piezoelectric matrix and nested living cells. However, the authors consider piezoelectricity as a sole effect and do not include ionic transport.

The connection between piezoelectricity and electroosmotic effect in the bone was also discussed in (Lemaire et al. 2011). The authors perform a multiscale theoretical investigation of electric measurements in the bone and expand the known model of ionic transport by piezoelectricity equations. A general homogenization is also proposed for this model. A more rigorous homogenization of this model was proposed in an unpublished work (Rohan 2010).

We arrive to a conclusion based on our research of the available literature that although the ionic transport in porous structure is a well-known and studied problem, there are still several challenging issues. Namely, most of the papers cited above concern the theoretical issues of mathematical modeling without numerical simulations. As our interest lies in exploring this phenomenon, we are interested in the implementation of these models as well. Thus, in this work, we explore the available models of ionic transport through a deformable porous medium and provide some insight into the upscaling procedure, which leads to the derivation of homogenized models. We would also like to give some insight into the implementation of these models and explore the connection between microstructure and homogenized tensors. We believe that this will lead to a better understanding of the phenomena in the context of bone tissue modeling.

1.4 Aims

Motivated by state of the art and identified challenges, this thesis aims to apply the multiscale description of the cortical bone tissues to develop the microstructurally oriented model of the transport of an electrolyte solution through an electrically charged porous medium. This thesis explores the modeling of porous media with an elastic or piezoelectric solid matrix. The main focus of this work rests in the derivation of a suitable mathematical model for both these types of porous media and studying the changes of their macroscopic behavior in response to variations in the microstructure geometry. However, it also investigates the reconstruction of macroscopic processes at a microscopic scale via the downscaling process.

Such a model, with a slight adjustment to a specific problem, can find a range of practical applications. It can be used in geoscience to model swelling in clays or nuclear waste disposal. In other fields, such as in energetics, it can serve as a base for modeling fuel cells and liquid batteries. We are interested in the potential application of such a model to cortical bone tissue modeling. However, through the text of this work, the model of ionic transport is treated as generally as possible to be easily expandable to other applications.

For better clarity, the aims of this thesis can be summarized in the following points:

1. **To apply available methods to derive the homogenized model of ionic transport in deformable porous media and extend such model by considering piezoelectric behavior of the solid matrix and non-stationarity of the problem.** The suitable choice of homogenization method can also provide tools for the reconstruction of macroscopic variables on the microscopic scale and thus give us information about both scales.

2. **To implement the derived models and to investigate their behavior on both microscopic and macroscopic scales by using numerical simulations.** The software *SfePy* for solving coupled PDE’s can be used to implement derived problems on both scales. A simple geometry representation of both scales can serve to interpret the results of numerical simulations easily. A set of simple boundary value problems provides information on the macroscopic behavior of a porous medium. The reconstruction of the macroscopic solution on the microscale has to be also implemented to observe the effects at the microstructure level.

3. **To provide mathematical formulations, computational and numerical tools for the identification of indirectly measurable material parameters.** The optimization-based method can be used for the identification of such parameters. It comprises the derivation of sensitivity formulae for differentiation of specific objective function and their subsequent implementation.

4. **To apply the derived models in the modeling of cortical bone tissue.** This comprises the research of geometry and material parameters of both microstructure and macroscopic specimens. The complex geometry of

bone tissue structure needs to be suitably simplified for the numerical simulation. The behavior of the model (on both scales) is tested on illustrative numerical examples.

1.5 Scope and outline

This thesis is composed of six chapters, including this introduction. The research made on the subject by other researchers, in other words, state of the art, is summarized and cited in Section 1.3.

Chapter 2 aims to define the porous media and to give a deeper understanding of the problem of transport of a two-component electrolyte solution through a porous body. It introduces the set of equations describing various electrochemomechanical phenomena occurring on the microscopic scale of the two types of the charged porous medium.

Chapter 3 focuses on mathematical modeling of ionic transport through homogenization. It introduces the basic theory behind the chosen upscaling procedure. The two types of material that form the solid skeleton of the porous body are considered: the linear elastic material and piezoelectric material. The homogenized model of ionic transport in a deformable porous medium is derived in Sec. 3.2. The model of ionic transport is then extended to capture the piezoelectric behavior of the porous matrix. The derived homogenized model is presented in Sec. 3.3.

Chapter 4 provides an insight into the discretization and subsequent implementation of the homogenized models. The effective coefficients relevant to both mathematical models are quantified for varying characteristic parameters of the microstructure geometry. Furthermore, this section introduces the numerical solution of both presented homogenized models and investigates their behavior on simple numerical simulations.

At the beginning of Chapter 5, an overview of possible areas of application of the proposed poropiezoelectric model is given. The rest of this chapter focuses on their application to the modeling of the canalicular-lacunar network of the cortical bone tissue. It provides information about the properties of micro- and macrostructure and discusses the identification of material parameters. Sec. 5.2 proposes the process of identification of material parameters of dry cortical bone. This identification procedure is then validated by simulation of a fictitious experiment. The results of numerical simulation of the compression of single bone osteon are then reported on in Sec.5.3.

Finally, Chapter 6 summarizes the results of this thesis. The future research aims and topics are also discussed in this section

Chapter 2

Introduction to the ionic transport in porous media

In this chapter, we would like to introduce the necessary theoretical background needed to derive the ionic transport model in porous media. Firstly, we will introduce the domain decomposition of the porous media. Then, we will explain the theory behind charge distribution near the solid-fluid interface. And finally, we focus on the processes occurring in each phase of the porous medium and their mathematical description.

2.1 Definition of porous media

In general, a porous material is a heterogeneous material whose heterogeneity is caused by the existence of cavities, channels or pores embedded on various scales in a solid matrix. The main parameter, which characterizes the volume fraction of pores in the whole body, is called porosity and is usually defined by

$$\phi_f = \frac{V_{\text{pores}}}{V_{\text{body}}}. \tag{2.1.1}$$

The pore space is usually saturated by a fluid phase, in which numerous mechanical or electrochemical phenomena, such as fluid convection or diffusion, can take effect. This is the reason why we cannot see the porous material as homogeneous or even continuous material. Instead, to effectively work with the porous media, homogenization procedures are widely used.

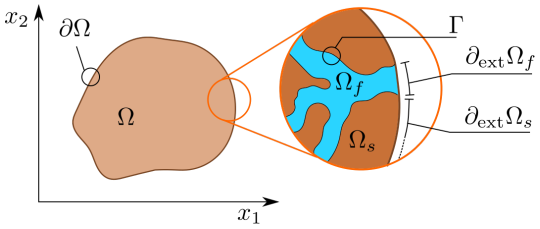

Figure 2.1: Decomposition of porous body Ω into solid and fluid phase, Ω_s and Ω_f, that have designated parts of the external boundary, $\partial_{\text{ext}}\Omega_s$ and $\partial_{\text{ext}}\Omega_f$, and interface Γ.

2.1.1 Domain decomposition

First, let us define the porous medium and its components. We consider porous medium occupying a bounded domain Ω with boundary $\partial\Omega$. The domain $\Omega \in \mathbb{R}^d$ is described by the coordinate system $0, x_1, x_2, \ldots, x_d$, where d is the dimension of the problem. It is composed of the fluid-filled pore space Ω_f and of the solid matrix $\Omega_s = \Omega \backslash \overline{\Omega}_f$. The solid-fluid interface is defined by relations $\Gamma = \partial\Omega_s \cap \partial\Omega_f$, see Fig. 2.1. In the notation of parts of the domain Ω, we used subscripts $\sqcup_s$ for the solid matrix and $\sqcup_f$ for the fluid. This notation will be used throughout the rest of the text also to denote the constants and variables belonging to their respective phase.

Further, we need to define the outer boundary, $\partial_{\text{ext}}\Omega_s \subset \partial\Omega$ and $\partial_{\text{ext}}\Omega_f \subset \partial\Omega$ such that

$$\begin{aligned} \partial_{\text{ext}}\Omega_s &= \partial\Omega_s \setminus \Gamma = \partial\Omega_s \cap \partial\Omega, \\ \partial_{\text{ext}}\Omega_f &= \partial\Omega_f \setminus \Gamma = \partial\Omega_f \cap \partial\Omega. \end{aligned}$$

By the symbol $\partial_{\text{ext}}\Omega_s$ we denote the outer boundary of the solid matrix and $\partial_{\text{ext}}\Omega_f$ the outer boundary of fluid-filled pores.

2.2 Electrical phenomena in the porous media

The following text aims to introduce the theory behind the different electrical phenomena in porous media. These occur naturally due to the adsorption of particles, the difference of potentials between phases, or the movement of the charged particles in the proximity of charged surface.

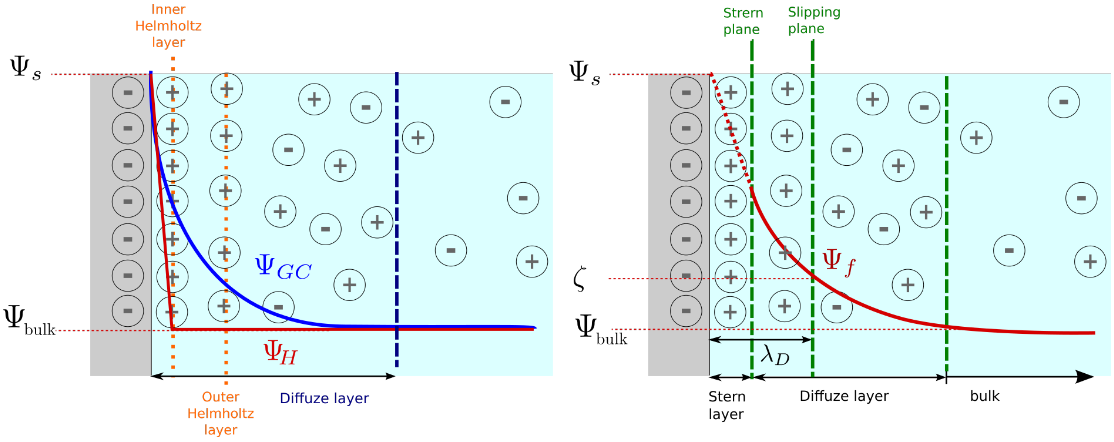

Figure 2.2: Models of the electrical double layer: Left - comparison of potential distribution according to Helmholtz model (Ψ_H) and Gouy-Chapman model (Ψ_{GC}); Right - Distribution of potential Ψ_f near solid-fluid interface according to Stern model.

2.2.1 Electrical double layer

This section describes the formation of the so-called electrical double layer (EDL), which represents the ionic charge distribution in an electrolyte in the proximity of charged pore surface. Several models describing the distribution of particles in the EDL were introduced throughout history.

The simplest approximation of EDL was given by Helmholtz, (Helmholtz 1879). In this model, the surface charge potential is linearly dissipated from the surface to the so-called inner Helmholtz layer, which lies in the distance of one molecular radius, see Fig. 2.2. However, this does not occur in nature.

The Gouy-Chapman model introduces the so-called diffuse double layer in which the change in concentration of the counterions near a charged surface follows the Boltzman distribution, (Gouy 1910; Chapman 1913). This model provides a better approximation of reality but still leaves something to be desired. For example, it assumes that there are no physical limits for the ions in their approach to the surface.

The most frequently used is the Stern model, (Stern 1924), sometimes called the Gouy-Chapman-Stern model that will be described below.

Stern model

To accurately describe the formation of EDL, the Stern model combines both Helmholtz and Gouy-Chapman theories, (Oldham 2008).

Let us consider the solid phase to be charged by a small negative charge which is constant in the whole phase. Thus, on the pore surface, attraction forces between negative charges on the solid-fluid interface and positive ions in the electrolyte solution cause the formation of an immobile layer of positively charged particles with a typical thickness of one molecular diameter, see Fig. 2.2.

The other component of EDL is the diffuse layer in which the attraction between particles is strong enough to influence fluid movement. With increasing distance from the pore surface, where the attraction forces decrease, the particles in the electrolyte are mobile once again. There is a conventionally introduced slipping plane that separates mobile and immobile fluid. It lies within the distance defined by the so-called Debye length λ_D. We will give the formulae expressing Debye length later. Farther away in bulk, the attraction forces cease to affect the ionic mobility and the solvent can be considered locally electrically neutral.

The effects of EDL on ionic transport depend on the pore size. We can distinguish three cases. In the case of too small pores, the attraction of ions can be stronger than the convection of the fluid. Thus, the attraction forces prevent fluid movement inside pores. On the other hand, in the case of too big pores, the attraction between ions has almost no effect compared to the scale of the problem, so that it can be neglected. Instead, its effect is often approximated by the ”slip-velocity” boundary condition. Therefore, in this work, we consider that the pore size is neither too big nor small, so that the effects of the EDL have to be considered.

Symbol	Quantity	Value	Units
e	Electron charge	1.6×10^{-19}	C
k_b	Boltzmann constant	1.38×10^{-23}	J/K
T	Absolute temperature	298	K
$\mathcal{E}$	Dielectric constant	6.93×10^{-10}	c/(mV)

Table 2.1: Description of used electrochemical constants.

2.2.2 The electrostatic potential of a phase

At the surface of any phase, separation of positive and negative charge components occurs to create a region of varying electrical potential Ψ. The electrical potential Ψ is defined as the work needed to move a unit charge from one point in an electric field to another. Considering a medium that consists of the solid and fluid phase, we can denote their electric potentials by Ψ_s and Ψ_f, respectively. We may assume that the electrostatic potential Ψ_s is constant in the whole solid phase for modeling purposes. The situation in the fluid phase is more complex due to the occurrence of EDL, see Fig. 2.2. In bulk, *i.e.* in a significant distance from the solid-fluid interface, we may consider the electrical potential Ψ_{bulk} to be constant. However, near the interface where the two phases come into contact, ions tend to arrange themselves to minimize their free energy. These effects result in a so-called Poisson-Boltzmann distribution of electrical potential in the double layer denoted by Ψ_{EDL}. To express the electrical potential in fluid Ψ_f, we recall the definition of electric potential. The work done in bringing an ion α up from bulk to a point in EDL is the electrical work done on or by the ion as it moves in response to the field, thus $\Psi_f = \Psi_{\mathrm{EDL}} - \Psi_{\mathrm{bulk}}$.

Potential at the solid-fluid interface

As we pointed out, we may assume the constant electrostatic potential Ψ_s in the whole solid phase. On the solid-fluid interface and in its close proximity, the electrostatic potential is assumed to be the same as on the surface of the solid phase. When measured by the standard electrokinetics method while considering no-slip hydrodynamic condition on the solid surface, the potential on the solid-fluid interface is usually known as ζ-potential. This parameter is widely used in the definition of EDL, as it is the potential at slipping plane, see also Fig. 2.2. However, the ζ-potential is more related to the electrochemical properties of the system and in many cases cannot be defined rigorously (Hunter 2001). More often, the surface charge density Σ, which is proportional to the normal derivative of Ψ_f, is used instead.

Streaming current and streaming potentials

The streaming potentials are generated by the flow of the electrolyte in the proximity of a charged surface. The fluid flow generated by nonelectrical forces, *i.e.* flow generated by mechanical deformation of the solid, also causes the movement of the ions in the same direction. This causes a potential difference between a point upstream and a point downstream which generates a steaming potential. That, in turn, causes the so-called streaming current in the reverse direction, which opposes the mechanical transfer of charge via the fluid flow, causing back-conduction by ion diffusion and electro-osmotic flow, see (Oatley-Radcliffe et al. 2017).

External electrical field

Apart from the potential of a phase, we may consider an external potential Ψ^{ext} taking effect. This potential is typically proportional to an externally imposed electrical field $\boldsymbol{E}^{\mathrm{ext}}$. The relation between external electrical field and exterior potential takes the form $\boldsymbol{E}^{\text{ext}} = -\nabla \Psi^{\text{ext}}$. Usually, the imposed electrical field $\boldsymbol{E}^{\text{ext}}$ is considered small compared to fields that occur in the EDL. This assumption enables us to linearize non-linear problems arising later in the text.

2.3 Processes in fluid phase

First, let us focus on the processes in the fluid phase. We consider the fluid to be an electrolyte solution of two ionic species with different valencies z_α , $\alpha = 1, 2$. The amount of each species in the electrolyte is characterized by its concentration c_α and has an electrochemical potential μ_α , (Hunter 2001)

$$\mu_\alpha = \mu_\alpha^0 + k_B T \ln c_\alpha + e z_\alpha \Psi_f \ , \tag{2.3.1}$$

where μ_α^0 is the standard electrochemical potential expressed at infinite dilution, k_B is the Boltzmann constant, T is the absolute temperature, e is the elementary charge and Ψ_f is the electrostatic potential in the fluid phase.

Usually, we distinguish three processes that influence ionic transport. The first is the solvent's convective movement, which is characterized by convective velocity $\boldsymbol{w}$. The convective velocity is equal to the hydrodynamic velocity in the rigid porous medium, but that is not the case in the deformable porous medium. The second process is the diffusion of the α-th ionic species in the solvent characterized by the diffusivity D_α^0. And finally, the third is the effect of an electrical field on the movement of electrically charged particles. In what follows, we introduce the system of equations describing these processes in the pore space Ω_f filled by the electrolyte solution. We give all the values of electrochemical constants used through this text in Tab. 2.1.

Remark 2.3.1 (Steady and quasi-steady processes) *This work considers two states of the electrolyte flow in porous media: steady state and quasi-steady state. By its definition, the process is in a steady state if the variables that define the behavior of the system or the process do not change in time, thus rendering all time derivatives zero.*

When the process is in a quasi-steady state, the system's variables may be time-dependent and their time derivatives do not vanish. However, we assume that all the processes are happening slowly enough, that all the inertial effects are negligible. We will always specify the considered state in the text. When using phrases as "time-dependent" or "non-steady state", we always refer to the quasi-steady state.

2.3.1 Eulerian mass conservation law

Let us introduce the Eulerian mass conservation law, for each species indexed by α,

$$\frac{\partial c_\alpha}{\partial t} + \nabla \cdot (\boldsymbol{j}_\alpha + \boldsymbol{w} c_\alpha) = 0 \qquad \text{in } \Omega_f, \alpha = 1, 2. \tag{2.3.2}$$

In (2.3.2) the effects of diffusion and migration caused by an external electrical field are unified into the so-called migration-diffusion flux $\boldsymbol{j}_\alpha$ given by

$$\boldsymbol{j}_\alpha = -\frac{c_\alpha D_\alpha^0}{k_B T}\nabla\mu_\alpha, \qquad \alpha = 1, 2. \tag{2.3.3}$$

The migration-diffusion fluxes $\boldsymbol{j}_\alpha$ hold a no-flux condition on the solid-fluid interface Γ

$$\boldsymbol{j}_\alpha \cdot \boldsymbol{n} = 0 \qquad \text{on } \Gamma, \alpha = 1, 2, \tag{2.3.4}$$

where $\boldsymbol{n}$ is the unit outer normal to Ω_f.

2.3.2 Electrokinetics

As was mentioned above, the electrokinetics of the fluid phase is characterized by the electrostatic potential Ψ_f, which is given as a solution to the Poisson problem

$$\mathcal{E}\Delta\Psi_f = -e\sum_{\beta=1}^{N=2} z_\beta c_\beta \quad \text{in } \Omega_f, \tag{2.3.5}$$

where $\mathcal{E} = \mathcal{E}_r\mathcal{E}_0$ is dielectric coefficient of the solvent that is assumed to be constant. The corresponding electrical field $\mathbf{E}$ is given by $\mathbf{E} = -\nabla\Psi_f$. We assume that the surface charge $-\Sigma_f$ is present at the solid-fluid interface Γ, thus the boundary condition reads

$$\mathcal{E}\nabla\Psi_f \cdot \boldsymbol{n} = -\Sigma_f \quad \text{on } \Gamma. \tag{2.3.6}$$

2.3.3 Modified Stokes problem

As mentioned above, in the case of the rigid porous medium, the convective velocity $\boldsymbol{w}$ equals to the hydrodynamic velocity $\boldsymbol{v}$ of the solvent. The velocity $\boldsymbol{v}$ is given by a modified Stokes problem where the driving forces are considered to be an external body force $\boldsymbol{f}$ and en electric force that acts on the fluid thanks to the presence of charged ionic species. The modified Stokes problem reads

$$\nabla p - \eta_f\Delta\boldsymbol{v} = \rho_f\boldsymbol{f} \underbrace{-e\sum_{\beta=1}^{N=2} z_\beta c_\beta \nabla\Psi_f}_{\text{electric force term}} \quad \text{in } \Omega_f, \tag{2.3.7}$$

where p is the fluid pressure, η_f is the dynamic viscosity of the electrolyte, and ρ_f is the fluid density. We consider the solvent to be incompressible; thus, we complete the Stokes problem by the condition of incompressibility, which reads

$$\nabla \cdot \boldsymbol{v} = 0 \quad \text{in } \Omega_f. \tag{2.3.8}$$

(2.3.7) is equivalent to the equilibrium equation for the fluid

$$-\nabla \cdot \boldsymbol{\sigma}_f = \rho_f\boldsymbol{f} \quad \text{in } \Omega_f, \tag{2.3.9}$$

where $\boldsymbol{\sigma}_f$ is the stress tensor of the fluid phase. It is a usual viscous stress tensor supplemented by a Maxwell 2nd order tensor $\boldsymbol{\tau}_M = \mathcal{E}\left(\boldsymbol{E}\otimes\boldsymbol{E} - \frac{1}{2}|\boldsymbol{E}|^2\boldsymbol{I}\right)$ and it reads

$$\boldsymbol{\sigma}_f = -p\boldsymbol{I} + 2\eta_f\boldsymbol{e}(\boldsymbol{v}) + \mathcal{E}\left(\boldsymbol{E}\otimes\boldsymbol{E} - \frac{1}{2}|\boldsymbol{E}|^2\boldsymbol{I}\right), \tag{2.3.10}$$

where $\boldsymbol{e}(\boldsymbol{v}) = \frac{1}{2}\left(\nabla \boldsymbol{v} + (\nabla \boldsymbol{v})^{\mathrm{T}}\right)$. Let us note that while considering the porous medium to be rigid, the influence of solid matrix on fluid phase can be expressed only by boundary conditions. Thus, the model of ionic transport in such a medium is given by (2.3.2)-(2.3.8). We expand this model to the case of a deformable porous medium in the following section.

2.4 Processes in solid matrix

In the following text, we propose two types of material models to describe the solid phase Ω_s. First, we introduce the standard linear elasticity model while assuming the solid phase to be deformable. The second model describes the piezoelectric solid phase, *i.e.* one that generates electrical potential under mechanical stress. We will later use both material models in an upscaling procedure, which will result in two two-scale models describing ionic transport in poroelastic and poropiezoelectric mediums, respectively.

2.4.1 Elastostatics

We consider the solid matrix to be deformable, while assuming only small deformation and rotation, which are usual assumptions of linear elasticity theory. The elastic properties of the matrix are characterized by an elasticity tensor $\boldsymbol{A} = \{A_{ijkl}\}$. The Cauchy stress tensor $\boldsymbol{\sigma}_s$ is given by the Hooke's law

$$\boldsymbol{\sigma}_s = \boldsymbol{A}\boldsymbol{e}(\boldsymbol{u}), \tag{2.4.1}$$

where $\boldsymbol{u}$ is the displacement field and $\boldsymbol{e}(\boldsymbol{u})$ is the strain tensor given by strain-displacement equation

$$\boldsymbol{e}(\boldsymbol{u}) = \frac{1}{2}\left(\nabla \boldsymbol{u} + (\nabla \boldsymbol{u})^T\right). \tag{2.4.2}$$

The fourth-order elasticity (or stiffness) tensor $\boldsymbol{A} = \{A_{ijkl}\}$ is symmetric positive definite tensor with symmetry $A_{ijkl} = A_{jikl} = A_{klij}$. The displacement $\boldsymbol{u}$ is then given by the linear elasticity equation

$$-\nabla \cdot \boldsymbol{\sigma}_s = -\nabla \cdot (\boldsymbol{A}\boldsymbol{e}(\boldsymbol{u})) = \rho_s \boldsymbol{f} \quad \text{in } \Omega_s, \tag{2.4.3}$$

where ρ_s is the density of solid.

In the case of the deformable medium, the convective velocity $\boldsymbol{w}$ is not simply equal to the hydrodynamic velocity $\boldsymbol{v}$. By extending the solid deformation velocity to the fluid part, we define convective velocity by

$$\boldsymbol{w} = \boldsymbol{v} - \frac{\partial \boldsymbol{u}}{\partial t}. \tag{2.4.4}$$

The last step is to define boundary conditions. On the solid-fluid interface Γ we should ensure continuity of the normal stresses and velocities

$$\partial_t \boldsymbol{u} = \boldsymbol{v} \quad \text{on } \Gamma, \tag{2.4.5}$$

$$\boldsymbol{\sigma}_f \cdot \boldsymbol{n} = \boldsymbol{\sigma}_s \cdot \boldsymbol{n} \quad \text{on } \Gamma. \tag{2.4.6}$$

The assumption of a deformable porous matrix will bring even more complexity to the model of ionic transport, but as will be shown later, introducing some simplifying assumptions will lead to only weakly coupled relations between the ion transport equations and elasticity.

2.4.2 Piezoelectricity

In this section, we would like to expand our model by assuming the solid matrix to be piezoelectric. Piezoelectric materials produce an electrical charge in response to applied mechanical stress and *vice versa*. Properties of such material are described by an elasticity tensor $\boldsymbol{A} = \{A_{ijkl}\}$, a dielectric tensor $\boldsymbol{d} = \{d_{ij}\}$ and a piezoelectric coupling tensor $\boldsymbol{g} = \{g_{kij}\}$.

One of the determining properties of the piezoelectric coupling tensor is its symmetry type. The third-order piezoelectric coupling tensor g_{kij} has the symmetry $g_{kji} = g_{kij}$. In the technical practice, the symmetric indices ij are usually replaced by a single index as

$$11 \to 1, \quad 22 \to 2, \quad 33 \to 3, \quad 23 \to 4, \quad 31 \to 5,, \quad 12 \to 6,$$

and the third-order piezoelectric tensor can be written in its symmetrical form

$$\boldsymbol{g} = \begin{bmatrix} G_{11} & G_{12} & G_{13} & G_{14} & G_{15} & G_{16} \\ G_{21} & G_{22} & G_{23} & G_{24} & G_{25} & G_{26} \\ G_{31} & G_{32} & G_{33} & G_{34} & G_{35} & G_{36} \end{bmatrix} \tag{2.4.7}$$

It has a maximum of 18 distinct components, but this number can be significantly reduced if certain symmetries exist in the material crystal structure, (Zou et al. 2013). The piezoelectric materials are classified into symmetry groups which are characterized by specific sparsity and symmetry patterns of the tensor $\boldsymbol{g}$, see (2.4.7).

The linear constitutive equations for piezoelectric material are

$$\begin{aligned} \boldsymbol{\sigma}_s^p &= \boldsymbol{A}\boldsymbol{e}(\boldsymbol{u}) - \boldsymbol{g}^T \nabla \Psi_s, \\ \boldsymbol{D}_s &= \boldsymbol{g}\boldsymbol{e}(\boldsymbol{u}) + \boldsymbol{d}\nabla \Psi_s, \end{aligned} \tag{2.4.8}$$

where $\boldsymbol{\sigma}_s^p$ is stress tensor and $\boldsymbol{D}_s$ is electric displacement. The solid matrix produces an electric potential Ψ_s in the solid in response to applied mechanical stress according to the following relations

$$\begin{aligned} -\nabla \cdot \sigma_s^p &= \boldsymbol{f} \quad \text{in } \Omega_s \\ -\nabla \cdot \boldsymbol{D}_s &= q_s \quad \text{in } \Omega_s, \end{aligned} \tag{2.4.9}$$

where q_s is electric volume charge. $(2.4.9)_1$ is referred to as piezoelectricity equation and $(2.4.9)_2$ as balance of charge equation.

Through (2.4.9), we introduced a new electrokinetic variable Ψ_s into the system, which is separated from the potential of fluid phase Ψ_f. This separation of variables is possible due to their different origin. To preserve their continuity, we have to take into consideration the conditions on the solid-fluid interface, (Lemaire et al. 2011). To prevent electrical jump Σ on the interface, we consider surface electrical charge $\Sigma_f = \Sigma_s = \Sigma$. Thus the interface conditions read

$$\begin{aligned} \Psi_f &= \Psi_s & &\text{on } \Gamma, \\ (\boldsymbol{g}\boldsymbol{e}(\boldsymbol{u}) + \boldsymbol{d}\nabla\Psi_s) \cdot \boldsymbol{n} &= -\Sigma & &\text{on } \Gamma, \\ \boldsymbol{\sigma}_s^p \cdot \boldsymbol{n} &= \boldsymbol{\sigma}_f \cdot \boldsymbol{n} & &\text{on } \Gamma. \end{aligned} \tag{2.4.10}$$

2.5 Conditions on outer boundary

Up to this point, we only provided the equations of the model and the conditions at the solid-fluid interface. The conditions on the exterior boundary are yet to be defined. To simplify the derivation of the two-scale model, we will assume that the problem is L-periodic where L is the characteristic size of the macroscopic domain Ω.

Remark 2.5.1 (L-periodicity) *Let us assume that domain Ω is defined as an N-dimensional block with the length of side $L > 0$, so that*

$$\Omega = \prod_{d=1}^{N} (0, L).$$

Any smooth variable ϕ is considered L-periodic if its value and partial derivatives are the same on the opposing sides of the block Ω.

Following this remark, we assume $\Psi_f, \Psi_f, c_\alpha, \boldsymbol{u}, \boldsymbol{v}$ and p to be L-periodic, unless stated otherwise.

The assumption of L-periodicity proves helpful during the upscaling process because it eliminates the need to deal with various conditions at the outer boundary. At the same time, it can be limiting for simulation of real processes with different than periodic conditions at the outer boundary. However, this limitation can be dealt with as will be shown later, see Remark 3.2.2 in Sec. 3.2.7.

Chapter 3

Mathematical modeling of porous medium

This chapter focuses on deriving a mathematical model of ionic transport in porous media through the homogenization process commonly used to deal with highly heterogeneous media. It provides insight into the chosen homogenization method and the upscaling process that leads to deriving effective properties and a homogenized model on the macroscopic scale. Two types of material models that describe the behavior of the solid phase will be considered in the following text. For the sake of clarity, we will refer to the linear elastic porous medium by the abbreviation LEPM and to the piezoelectric porous medium by PEPM.

3.1 Basics of homogenization

Homogenization is, in its basic form, the process of estimating the effective properties of heterogeneous media while using knowledge about the properties of their components. Different approaches can be used in mathematical modeling of heterogeneous material with multiple phases, such as the mixture theory or the self-consistent method. However, their specific requirements for microstructure geometry often limit their applicability. In this work, we apply the unfolding homogenization method to model the macroscopic behavior of the multiphase material while respecting its microstructure. Although the application of this method is limited to periodic structures, it has the advantage of providing a general framework that can be extended relatively easily. It also respects the geometrical arrangement and material constitution of the heterogeneous media.

3.1.1 Porous medium with periodic structure

First, let us define a parameter $\varepsilon, 0 < \varepsilon \ll 1$ as a ratio

$$\varepsilon = \frac{l}{L_c}, \tag{3.1.1}$$

where L_c is a characteristic dimension of the macroscopic domain and l is a characteristic dimension of the microscopic periodic structure. The parameter ε is called the scale parameter that characterize the size of the micropores.

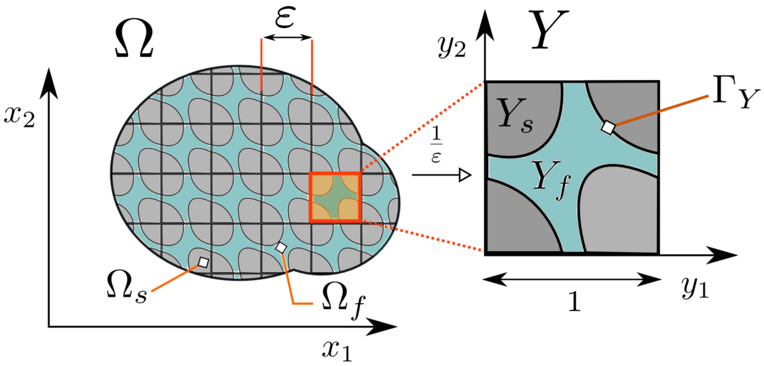

Figure 3.1: Domain Ω is generated by periodical repeating of copies of representative volume element (RVE) Y scale by ε. The RVE Y is decomposed into solid and fluid phase, Y_s and Y_f, with interface Γ_Y.

On the macroscopic scale, we consider the porous medium to occupy a domain $\Omega \in \mathbb{R}^d$ which was defined in Sec.2.1.1. The domain Ω is generated as a periodic lattice by repeating the representative volume element (RVE) occupying domain Y, with microscopic coordinate system $(y_1, y_2, ..., y_d)$. The RVE Y is has the shape of an d-dimensional block with the length of side $\hat{y}_i$

$$Y = \prod_{i=1}^{d}(0, \hat{y}_i) \subset \mathbb{R}^d. \tag{3.1.2}$$

.

Similarly to the domain Ω, the RVE Y can be divided into two subdomains Y_s and Y_f with interface Γ_Y, such that

$$Y = Y_s \cup Y_f \cup \Gamma_Y, \quad Y_f = Y \setminus \bar{Y}_s, \quad \Gamma_Y = \bar{Y}_s \cap \bar{Y}_f. \tag{3.1.3}$$

As was mentioned above, the RVE Y creates a characteristic sub-unit. By periodical repeating of scaled copies $Y^\varepsilon = \varepsilon Y$, we generate the whole domain Ω, see Fig. 3.1.

The shape and dimension of the RVE Y is naturally subjected to the microstructure of the porous medium. But for simplicity, we assume that the RVE Y has a unit side length, i.e. $\hat{y}_i = 1, i = 1, 2, 3$. This represents RVE Y as the unit square in $\mathbb{R}^2$ or the cubic cell in $\mathbb{R}^3$. Such representation of Y has a measure (in $\mathbb{R}^3$ volume of Y) $|Y| = 1$.

Remark 3.1.1 (Notation) *Through the rest of the text, we use the symbols* ∇_x *and* ∇_y *to denote gradient operators with respect to* x *and* y*, respectively. In order to simplify the notation, we will also use the following abbreviations: for any function* $v \in L^1(\Omega; \mathbb{R})$

$$\frac{1}{|Y_a|}\int_{Y_a} v \,\mathrm{dy} = \fint_{Y_a} v \,\mathrm{dy} \quad \text{and} \quad \int_{\Omega} \frac{1}{|Y_a|}\int_{Y_a} v \,\mathrm{dy} = \fint_{\Omega\times Y_a} v \,\mathrm{dy}, \tag{3.1.4}$$

where $Y_a \subset Y$*.*

3.1.2 Brief introduction to the unfolding method

One of the homogenization methods suitable for periodic porous media is the so-called unfolding method (further referred to by the abbreviation UFM), first proposed by (Cioranescu et al. 2002). The main idea behind UFM is to separate the characteristic scales by decomposing any oscillating function into average and fluctuating parts. The standard means of weak and strong convergence in $L(\Omega \times Y)$ can be applied to obtain the limit problem for $\varepsilon \to 0$ transformed by the so-called unfolding operator $\mathcal{T}_\varepsilon$. This results in the homogenized coefficients that characterize the influence of heterogeneities in microstructure onto macroscopic behavior. These coefficients are used to define a new limit PDE system that describes the homogenized macroscopic model.

The unfolding operator $\mathcal{T}_\varepsilon$, similar to the dilatation operator, is the main tool of UFM. Its definition is given below.

Definition 3.1.1 (Unfolding operator) *The domain Ω is generated as a lattice of scaled, non-overlapping copies of RVE $Y^\varepsilon = \varepsilon Y$ such that*

$$\Omega = \text{interior} \bigcup_{\xi \in \Xi^\varepsilon} \bar{\mathrm{Y}}^\varepsilon_\xi, \quad \bar{\mathrm{Y}}^\varepsilon_\xi = \varepsilon(\xi + \mathrm{Y}), \tag{3.1.5}$$

$$\textit{where } \Xi^\varepsilon = \left\{ \xi \in \mathbb{Z} | \varepsilon(\xi + Y) \subset \Omega \right\}. \tag{3.1.6}$$

For any $z \in \mathbb{R}^d$, let $[z]$ be the unique integer such that $z - [z] \in Y$. We may write $z = [z] + \{x\}$ for all $z \in \mathbb{R}^d$, so that for all $\varepsilon > 0$, we get unique decomposition

$$x = \varepsilon \left[\frac{x}{\varepsilon} \right]_y + \varepsilon \left\{ \frac{x}{\varepsilon} \right\}_y = \xi + \varepsilon y, \tag{3.1.7}$$

where

$$y = \left\{ \frac{x}{\varepsilon} \right\}_y \in Y, \quad \xi = \varepsilon \left[\frac{x}{\varepsilon} \right]_y. \tag{3.1.8}$$

Based on this decomposition the unfolding operator $\mathcal{T}_\varepsilon : L^2(\Omega;\mathbb{R}) \to L^2(\Omega \times Y;\mathbb{R})$ can be defined as follows: for any function $v \in L^1(\Omega;\mathbb{R})$

$$\mathcal{T}_\varepsilon(v)(x,y) = \begin{cases} v(\xi + \varepsilon y), & x \in \Omega, y \in Y, \\ 0, & \textit{otherwise.} \end{cases} \tag{3.1.9}$$

The unfolding operator $\mathcal{T}_\varepsilon(v)$ has the following three important properties: For all functions v and $u \in L^1(\Omega;\mathbb{R})$:

$$\begin{aligned} &(i)\ \mathcal{T}_\varepsilon(v(x)u(x)) = \mathcal{T}_\varepsilon(v(x))\mathcal{T}_\varepsilon(u(x)), \\ &(ii)\ \int_\Omega v(x)dx = \int_\Omega \frac{1}{|Y|} \int_Y \mathcal{T}_\varepsilon(v)(x,y)dxdy = \fint_{\Omega \times Y} \mathcal{T}_\varepsilon(v)(x,y), \\ &(iii)\ \mathcal{T}_\varepsilon(\nabla_x v(x)) = \frac{1}{\varepsilon}\nabla_y(\mathcal{T}_\varepsilon(v)(x,y)). \end{aligned} \tag{3.1.10}$$

The relation between ”slow” x and ”fast” y coordinates (sometimes also referred to as ”coarse” and ”fine”) is illustrated by Fig. 3.2.

As seen above, the unfolding operator transforms the integration domain Ω to $\Omega \times Y$ allowing us to use weak convergence in a functional Sobolev space

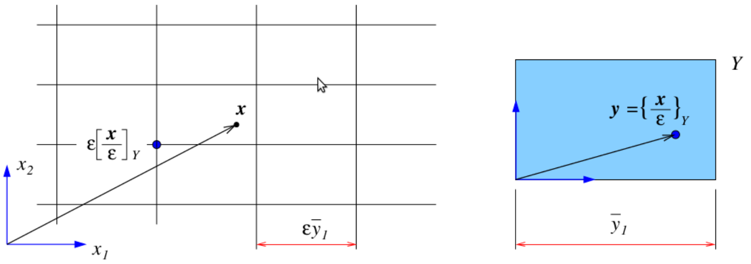

Figure 3.2: Relation between macroscopic x and microscopic y coordinates, (Rohan 2010).

$W(\Omega, Y)$ that possesses enough regularity for the functions defined in $\Omega \times Y$. The decomposition of any function v into the "macroscopic" part and the "microscopic" part is achieved trough introduction of a recovery sequence $v^{R,\varepsilon}$ associated with the problem solution.

Definition 3.1.2 (Recovery sequence) *The recovery sequence* $\left\{v^{R,\varepsilon}\right\}, \varepsilon \to 0$, *which is associated with the solution* v^ε *of a problem, is designed as follows:*

$$\begin{aligned} v^{R,\varepsilon} &= v^{0,\varepsilon}(x, x/\varepsilon) + \varepsilon v^{1,\varepsilon}(x, x/\varepsilon), \\ \mathcal{T}_\varepsilon\Big(v^{R,\varepsilon}(x)\Big) &= v^{0,\varepsilon}(\xi + \varepsilon y, y) + \varepsilon v^{1,\varepsilon}(\xi + \varepsilon y, y), \end{aligned} \tag{3.1.11}$$

where we consider decomposition of x *and* y *according to* (3.1.7) *and* (3.1.8) *and both* $v^{0,\varepsilon}(x,.)$ *and* $v^{1,\varepsilon}(x,.)$ *are* Y*-periodic. The following convergences are taken into account*

$$v^{0,\varepsilon} \rightharpoonup \bar{v}^0(x) \ \textit{weakly in } H^1(\Omega), \tag{3.1.12}$$

$$\mathcal{T}_\varepsilon\Big(v^{0,\varepsilon}\Big) \rightharpoonup v^0(x,y) \ \textit{weakly in } W(\Omega, Y), \tag{3.1.13}$$

$$\mathcal{T}_\varepsilon\Big(v^{1,\varepsilon}\Big) \rightharpoonup v^1(x,y) \ \textit{weakly in } W(\Omega, Y), \tag{3.1.14}$$

where $\bar{v}^0(x)$ *is the mea value of* $v^0(x,y)$ *given by* $|Y|^{-1} \int_Y v^0(x,y)\,\mathrm{d}y$.

This method also respects the microstructure of the porous medium and provides us with tools to reconstruct the macroscopic solution on the microscopic scale. However, the reconstruction procedure will be discussed later, see Sec. 3.3.8.

We provide only a brief introduction to the main principle of this homogenization method and refer to (Cioranescu et al. 2002; Cioranescu et al. 2008) for its more detailed description. However, to give a general idea of the process, we list the main steps of the unfolding method that we use to derive a homogenized model of a porous medium.

Basic outline of unfolding homogenization method:

1. Simplifying the microstructure of porous medium to periodically repeated representative volume element Y.
2. Decomposition of the problem variables into "macro-" and "microscopic" coordinates through the introduction of so-called recovery sequences.
3. Unfolding the problem describing porous medium into domain $\Omega \times Y$ by applying the unfolding operator.

4. Passing the problem to the limit for $\varepsilon \to 0$ by using properties of the unfolding operator $\mathcal{T}_\varepsilon$, which results in the two-scale limit problem.
5. Decomposition of limits as linear combinations of corrector base functions and thus obtaining the so-called splits.
6. Definition and subsequent solution of locals problems on the RVE Y, which determines the corrector base functions.
7. Determination of effective material coefficients from corrector base functions.
8. Definition of homogenized macroscopic problem in which the effective material coefficients occur.

The following text will employ these steps to derive the effective macroscopic model of ionic transport in porous media.

3.2 Model of ionic transport in deformable porous medium

The mathematical model of the deformable porous media (*i.e.* linear elastic porous media or LEPM) consists of (2.3.2)-(2.4.6), where the convective velocity $\boldsymbol{w}$ is defined by (2.4.4). This relation causes coupling between displacement $\boldsymbol{u}$ and electrokinetic variables.

It has been shown, (Allaire et al. 2015), that for a steady-state problem, where all the time derivatives vanish, the electrokinetic system can be considered decoupled and treated separately. Thus, as we show below, the homogenization of the problem splits into three separate parts: homogenization of electrokinetic system, homogenization of Poisson-Boltzmann equation, and homogenization of elasticity. Then, the displacement $\boldsymbol{u}$ will become weakly coupled with the potentials and velocity through the condition of stress continuity on the solid-fluid interface.

The following section summarizes the main steps leading to the derivation of an effective model of ionic transport through LEPM.

3.2.1 Dimensionless problem

In this part of the text, we will deal with the scaling of the mathematical model given above to obtain a dimensionless problem. There are some significant benefits to the scaling of mathematical models. The scale analysis of a mathematical model may be used to identify small parameters, such as the scale parameter ε described above. Another benefit of scaling is related to running numerical simulations, since scaling simplifies the choice of values for the input data greatly and makes the simulation results more widely applicable, see (Langtangen and Pedersen 2016).

Let L_c to be a characteristic size of domain Ω and l to be characteristic size of the microscopic level. We can define a small nondimensional parameter $\varepsilon = l/L_c \ll 1$ which represents the period of periodic porous domain Ω^ε. As a consequence, we can rescale the domain $\Omega^\varepsilon = \Omega/L_c$ and space variable $x' = x/L_c$. Introducing $L' = L/L_c$, the rescaled domain becomes $\Omega^\varepsilon = \prod^d(0, L')$.

Having in mind the scaling of the domain, the dimensionless operator ∇' can be defined by

$$\nabla' = L_c \nabla, \qquad \nabla = (\partial_x). \tag{3.2.1}$$

The dimensionless variables are expressed with help of the characteristic quantities denoted by the subscript $\sqcup_c$. As they are related to the scale parameter ε, we denote them all by the superscript $\sqcup^\varepsilon$.

$$p^\varepsilon = \frac{p}{p_c}\,, \quad \boldsymbol{v}^\varepsilon = \frac{\boldsymbol{v}}{v_c}\,, \quad \boldsymbol{w}^\varepsilon = \frac{\boldsymbol{w}}{v_c}\,, \quad \Psi_f^\varepsilon = \frac{\Psi_f}{\zeta}\,, \quad c_\alpha^\varepsilon = \frac{c_\alpha}{c_c}\,, \quad \boldsymbol{u}^\varepsilon = \frac{\boldsymbol{u}}{u_c}\,, \tag{3.2.2}$$

where p_c is characteristic pressure, $\boldsymbol{v}_c$ characteristic velocity, c_c characteristic concentration, u_c characteristic displacement and ζ stands for the $\zeta-$potential mentioned in Sec. 2.2.2.

Following (Karniadakis et al. 2005), we may introduce an ionic energy parameter $\kappa = \frac{e\zeta}{k_B T}$. Since the surface charge density Σ_f is given instead of the ζ potential, it is reasonable to choose $\kappa = 1$ and thus obtain ζ as a characteristic value of potential Ψ_f in form

$$\zeta = \frac{k_B T}{e}. \tag{3.2.3}$$

The potential ζ also occurs in the definition of the so-called Debye length λ_D. The Debye length for a symmetric electrolyte with $z_1 = -1, z_2 = +1$ reads

$$\lambda_D = \sqrt{\mathcal{E}\frac{\zeta}{ec_c}\left(\sum_{\beta=1}^{2} z_\beta^2\right)^{-1}} = \sqrt{\mathcal{E}k_B T\left(e^2 c_c \sum_{\beta=1}^{2} z_\beta^2\right)^{-1}}. \tag{3.2.4}$$

Let us remind that both ζ-potential and Debye length are involved in the definition of EDL thickness as was explained in Sec. 2.2.

Next, we introduce a dimensionless parameter γ that relates the ionic energy parameter $\kappa = 1$ and the characteristic length of microstructure l to the Debye length parameter λ_D as follows

$$\gamma = \frac{l^2}{\kappa \lambda_D^2} = \left(\frac{l}{\lambda_D}\right)^2. \tag{3.2.5}$$

Apart from this parameter, other two dimensionless parameters are employed in the dimensionless form of the system (2.3.2)-(2.3.8); these are the Peclet number $\mathrm{Pe}_\alpha, \alpha = 1, 2$, and the ratio between electrical and thermal energy N_σ, which are defined by

$$\mathrm{Pe}_\alpha = \frac{l^2 k_B T c_c}{\eta_f D_\alpha}, \quad N_\sigma = \frac{el\Sigma_c}{\mathcal{E}k_B T}. \tag{3.2.6}$$

The introduction of these nondimensional parameters, as well as the introduction of the scale parameter ε into the system, is shown in the Appendix. A.

What remains to do, is to define the dimensionless forcing terms which will be denoted by $\hat{\sqcup}$

$$\Psi'^{,\mathrm{ext}} = \frac{\Psi^{\mathrm{ext}}}{\zeta}\,, \quad \Sigma' = \frac{\Sigma}{\Sigma_c}\,, \quad \boldsymbol{f}' = \frac{\boldsymbol{f}L_c}{p_c}\,. \tag{3.2.7}$$

For future reference, we also introduce the dimensionless elasticity tensor $\boldsymbol{A}' = \boldsymbol{A}E_c^{-1}$, where E_c is the characteristic value of elastic moduli.

For the sake of brevity, we will skip the nondimensialization process and present only its result, *i.e.* the dimensionless form of the problem. Instead, we refer to Appendix A that describes the whole process of dimensional analysis of the quasi-steady state of the presented problem.

The introduction of dimensionless quantities does unnecessarily complicate the written form of the presented expressions. To simplify it, we will employ the following notation:

Remark 3.2.1 (Notation of dimensionless operator and quantities) *In rest of the text, we will drop the prime* $\sqcup'$ *when referring to dimensionless forcing terms given by* (3.2.7)*, rescaled length* L' *of domain* Ω^ε *and dimensionless elasticity tensor* $\boldsymbol{A}' = \boldsymbol{A}E_c^{-1}$*. From now on, symbols* $\boldsymbol{f}, \Sigma, \Psi^{\text{ext}}$*,* L *and* $\boldsymbol{A}$ *will refer to these dimensionless quantities, unless stated otherwise. In similar fashion, we will drop the prime denoting a dimensionless operator* ∇' *and refer to it by* ∇ *instead.*

Dimesionless problem Using the dimensionless form of the system (2.3.2)-(2.3.8) we can introduce the following steady-state problem. For given $\boldsymbol{f}$, Ψ^{ext} and Σ_f, find $\left(c_\alpha^\varepsilon, \Psi_f^\varepsilon, p^\varepsilon, \boldsymbol{w}^\varepsilon, \boldsymbol{u}^\varepsilon\right)$ which satisfy the following set of equations,

$$\begin{aligned}
\varepsilon^2 \Delta \boldsymbol{w}^\varepsilon - \nabla p^\varepsilon &= -\boldsymbol{f} + \sum_{\beta=1}^{2} z_\beta c_\beta^\varepsilon(x) \nabla \Psi_f^\varepsilon && \text{in } \Omega_f^\varepsilon, \\
\nabla \cdot \boldsymbol{w}^\varepsilon &= 0 && \text{in } \Omega_f^\varepsilon, \\
\varepsilon^2 \Delta \Psi_f^\varepsilon &= \gamma \sum_{\beta=1}^{2} z_\beta c_\beta^\varepsilon && \text{in } \Omega_f^\varepsilon, \\
\nabla \cdot (\mathrm{Pe}_\alpha \boldsymbol{w}^\varepsilon + \boldsymbol{j}_\alpha^\varepsilon) &= 0 && \text{in } \Omega_f^\varepsilon, \alpha = 1, 2, \\
-\nabla \cdot (\boldsymbol{A}\boldsymbol{e}(\boldsymbol{u}^\varepsilon)) &= \boldsymbol{f} && \text{in } \Omega_s^\varepsilon,
\end{aligned} \tag{3.2.8}$$

with interface conditions

$$\begin{aligned}
\boldsymbol{w}^\varepsilon &= 0 && \text{on } \Gamma^\varepsilon, \\
\boldsymbol{j}_\alpha^\varepsilon \cdot \boldsymbol{n} &= 0 && \text{on } \Gamma^\varepsilon, \alpha = 1, 2, \\
\varepsilon \nabla \Psi_f^\varepsilon \cdot \boldsymbol{n} &= -N_\sigma \Sigma && \text{on } \Gamma^\varepsilon, \\
\boldsymbol{A}\boldsymbol{e}(\boldsymbol{u}^\varepsilon) \cdot \boldsymbol{n} &= \boldsymbol{\sigma}_f^\varepsilon \cdot \boldsymbol{n} && \text{on } \Gamma^\varepsilon.
\end{aligned} \tag{3.2.9}$$

The ionic fluxes $\boldsymbol{j}_\alpha^\varepsilon, \alpha = 1, 2$, and fluid stress $\boldsymbol{\sigma}_f^\varepsilon$ are given by

$$\begin{aligned}
\boldsymbol{j}_\alpha^\varepsilon &= -\, c_\alpha^\varepsilon \nabla \left(\ln c_\alpha^\varepsilon \exp(z_\alpha \Psi_f^\varepsilon)\right), \alpha = 1, 2 \\
\boldsymbol{\sigma}_f^\varepsilon &= -\, p^\varepsilon \boldsymbol{I} + 2\varepsilon^2 \boldsymbol{e}(\boldsymbol{w}^\varepsilon) + \gamma^{-1}\varepsilon^2 \left(\nabla \Psi_f^\varepsilon \otimes \nabla \Psi_f^\varepsilon - \frac{1}{2} |\nabla \Psi_f^\varepsilon|^2 \boldsymbol{I}\right).
\end{aligned} \tag{3.2.10}$$

Concentrations c_β^ε, sum of potentials $(\Psi^\varepsilon + \Psi^{\text{ext}})$, convective velocity $\boldsymbol{w}^\varepsilon$ and pressure p^ε are L-periodic on Ω_f^ε. We also recall that the given surface charge density Σ is constant due to the assumed constant potential Ψ_s in the solid phase. Introduction of the parameter ε into (3.2.8), $(3.2.9)_3$ and $(3.2.10)_2$ is a natural consequence of the adimensional choices and dimensional analysis of the system. For a better understanding, how we introduced this parameter into the system, we refer to Appendix A.

3.2.2 Linearization

To apply the homogenization efficiently, the system (3.2.8)–(3.2.10) must be linearized. For this, we need to assum that applied fields Ψ^{ext} and $\boldsymbol{f}$ are sufficiently small. As a consequence, the state variables are only slightly perturbed from equilibrium, which justifies the linearization.

Following the linearization procedure in (Allaire et al. 2013b), any unknown a^ε can be decomposed into its equilibrium part $a^{\text{eq},\varepsilon}$ and its perturbation $a^{\text{per},\varepsilon}$. Thus, we consider following splits

$$\begin{aligned} c_\alpha^\varepsilon(x) &= c_\alpha^{\text{eq},\varepsilon}(x) + c_\alpha^{\text{per},\varepsilon}(x), & \Psi^\varepsilon{}_f(x) &= \Psi_f^{\text{eq},\varepsilon}(x) + \Psi_f^{\text{per},\varepsilon}(x), \\ \boldsymbol{w}^\varepsilon(x) &= \boldsymbol{w}^{\text{eq},\varepsilon}(x) + \boldsymbol{w}^{\text{per},\varepsilon}(x), & p^\varepsilon(x) &= p^\varepsilon(x) + p^{\text{per},\varepsilon}(x), \\ \boldsymbol{u}^\varepsilon(x) &= \boldsymbol{u}^{\text{eq},\varepsilon}(x) + \boldsymbol{u}^{\text{per},\varepsilon}(x), \end{aligned} \tag{3.2.11}$$

The equilibrium quantities labeled superscript $\sqcup^{\text{eq}}$, are solutions of the system (3.2.8)–(3.2.10) for $\boldsymbol{f} = 0$, $\Psi^{\text{ext}} = 0$, $\boldsymbol{w}^{\text{eq},\varepsilon} = 0$ and, by the consequence, zero diffusive fluxes $\boldsymbol{j}_\alpha^\varepsilon = 0$; the last statement follows from $(3.2.8)_4$, $(3.2.9)_2$, and $(3.2.10)_1$. Since the convective velocity vanishes at the equilibrium, we can state $\boldsymbol{w}^\varepsilon(x) = \boldsymbol{w}^{\text{per},\varepsilon}(x)$.

Equilibrium state quantities

The equilibrium solution defines the reference state of the electrolyte such that the linearized state problem governs the perturbations. The existence of equilibrium solution $(c_\alpha^{\text{eq},\varepsilon}, \Psi_f^{\text{eq},\varepsilon}, p^{\text{eq},\varepsilon}, \boldsymbol{u}^{\text{eq},\varepsilon})$ was shown in (Allaire et al. 2013a), whereby the three fields $c_\alpha^{\text{eq},\varepsilon}$, $\Psi_f^{\text{eq},\varepsilon}$ and $p^{\text{eq},\varepsilon}$ satisfy the following two relationships,

$$\begin{aligned} c_\alpha^{\text{eq},\varepsilon}(x) &= c_\alpha^b \exp(-z_\alpha \Psi_f^{\text{eq},\varepsilon}(x)), \\ p^{\text{eq},\varepsilon}(x) &= \sum_{\beta=1}^{2} c_\beta^{\text{eq},\varepsilon}(x), \end{aligned} \tag{3.2.12}$$

where c_α^b is the characteristic concentration in the bulk which represents the concentration of the α-th ionic species in a pore of infinite size. As a consequence of (3.2.12), the concentrations $c_\alpha^{\text{eq},\varepsilon}$ and subsequently the pressure $p^{\text{eq},\varepsilon}$ are determined by the potential $\Psi_f^{\text{eq},\varepsilon}$.

To compute $\Psi_f^{\text{eq},\varepsilon}$, the asymptotic analysis of the dimensionless Poisson-Boltzmann equation given by $(3.2.8)_3$ and $(3.2.9)_3$ has been treated in (Allaire et al. 2013a). Therefore, for the sake of completeness, we only provide the resulting expressions here. Substituting equilibrium concentration $(3.2.12)_1$ into the Poisson-Boltzmann $(3.2.8)_3$ and $(3.2.9)_3$, one gets

$$\begin{aligned} \varepsilon^2 \nabla^2 \Psi_f^{\text{eq},\varepsilon} =& \gamma \sum_{\beta=1}^{2} z_\beta c_\beta^b \exp(-z_\beta \Psi_f^{\text{eq},\varepsilon}) \qquad \text{in } \Omega_f^\varepsilon, \\ \varepsilon \nabla \Psi_f^{\text{eq},\varepsilon} \cdot \boldsymbol{n} =& -N_\sigma \Sigma_f \qquad \text{on } \Gamma^\varepsilon, \end{aligned} \tag{3.2.13}$$

where the L-periodicity of $\Psi_f^{\text{eq},\varepsilon}$ is prescribed on the external boundary $\partial_{\text{ext}}\Omega_f^\varepsilon$. The solvability of (3.2.13) for homogeneous Neumann condition, *i.e.* the in case that $\Sigma = 0$, requires that the r.h.s. of $(3.2.13)_1$ integrated in Ω_f^ε must vanish. This is satisfied provided the so-called electroneutrality condition in bulk holds,

$$\sum_{\beta}^{2} z_\beta c_\beta^b = 0. \tag{3.2.14}$$

We adhere to this condition, hence the existence of a unique solution $\Psi_f^{\text{eq},\varepsilon} \in H^1_\#(\Omega_f^\varepsilon)$ is guaranteed, see (Allaire et al. 2010). From the physical point of view, it ensures that $\Psi_f^{\text{eq},\varepsilon}$ vanishes for the zero surface charge.

Although we assume Σ to be a constant defined on the interface Γ^ε, even for a periodic distribution of charges $\mathcal{T}_\varepsilon(\Sigma) = \tilde{\Sigma}(y)$, $y \in \Gamma_Y$, the problem (3.2.13) yields εY-periodic solutions $\Psi^{\text{eq},\varepsilon}$ in Ω_f^ε, recalling the "macroscopic" L-periodicity on $\partial_{\text{ext}}\Omega_f^\varepsilon$. This property allows us to consider only the local problem in the zoomed RVE represented by cell Y_f.

Then,

$$\Psi_f^{\text{eq},\varepsilon}(x) = \Psi_f^{\text{eq}}(y), \quad c_\alpha^{\text{eq},\varepsilon}(x) = c_\alpha^{\text{eq}}(y), \tag{3.2.15}$$

where concentrations $c_\alpha^{\text{eq}}(y), \alpha = 1, 2$ obey the form of the Boltzmann distribution

$$c_\alpha^{\text{eq}}(y) = c_\alpha^b \exp(-z_\alpha \Psi_f^{\text{eq}}(y)). \tag{3.2.16}$$

The potential $\Psi_f^{\text{eq}}(y) \in H^1_\#(Y_f)$ is a solution to the Poisson-Boltzmann equation (3.2.13) imposed in Y_f, in particular

$$\begin{aligned} \nabla_y^2 \Psi_f^{\text{eq}} &= \gamma \sum_{\beta=1}^{2} z_\beta c_\beta^b \exp(-z_\beta \Psi_f^{\text{eq}}) \quad \text{in } Y_f, \\ \nabla_y \Psi_f^{\text{eq}} \cdot \boldsymbol{n} &= -N_\sigma \Sigma \quad \text{on } \Gamma_Y. \end{aligned} \tag{3.2.17}$$

The notes on solution of problem given by (3.2.17) are summed up in Appendix B.

To conclude, by virtue of (3.2.12), the unfolded equilibrium concentrations $\mathcal{T}_\varepsilon(c_\alpha^{\text{eq},\varepsilon})$ and the unfolded pressure field $\mathcal{T}_\varepsilon(p^{\text{eq},\varepsilon})$ are Y-periodic functions. Moreover, the unfolded displacements are also Y-periodic functions, whereby the macroscopic strains vanish. Therefore, we neglect any influence of the equilibrium displacements field on the reference configuration associated with the linearization procedure considered in what follows. Note that the equilibrium pore geometry might be perturbed due to the local strains in Y_s.

Perturbed state quantities

As the further step in the linearization, the total electrostatic potential Ψ_f^ε is decomposed according to phenomena that participate in the total electric field. Thus, it can be given as a superposition $\Psi_f^\varepsilon = \Psi^\varepsilon + \Phi_\alpha^\varepsilon + \Psi^{\text{ext}}$ of local particular electric fields associated with the following potentials:

- imposed potential Ψ^{ext}, which yields the external electrical field $\mathbf{E} = -\nabla\Psi^{\text{ext}}$ and is independent of ε;
- potential Ψ^ε reflects only the effects of the EDL on the ion distribution; in equilibrium, Ψ^ε is a solution of (3.2.13);

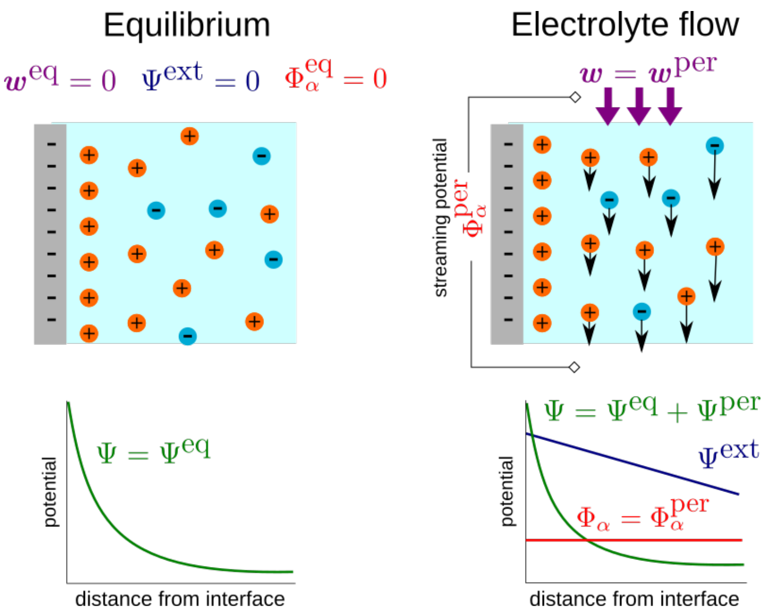

Figure 3.3: Potential decomposition near the solid-fluid interface in the equilibrium and under the electrolyte flow. Left: Equilibrium state, at which the potential of fluid phase consists only of the electrokinetic potential of EDL, so that $\Psi_f^{eq} = \Psi^{eq}$; Right: Occurrence of streaming potentials $\Phi_\alpha = \Phi_\alpha^{per}$ and the potential decomposition under the electrolyte flow and the effect of external potential Ψ^{ext}.

- ionic potential Φ_α^ε (often referred to as the streaming potential) represents the electric field produced by the motion of $\alpha-$th ionic species. In equilibrium, Φ_α^ε vanishes since both the convection $\boldsymbol{w}^\varepsilon$ and the ionic flux $\boldsymbol{j}_\alpha^\varepsilon$ vanish. Thus, the ionic potential is identified by its perturbation only, $\Phi_\alpha^\varepsilon(x) = \Phi_\alpha^{per,\varepsilon}$.

Since in equilibrium the ionic potential Φ_α^{eq} vanishes and there is no imposed potential Ψ^{ext}, the total electrostatic potential in equilibrium Ψ_f^{eq} is given only by the electrokinetic potential of EDL, so that $\Psi_f^{eq} = \Psi^{eq}$ and (3.2.17) transforms into the problem of Ψ^{eq} only. The decomposition of the potential in equilibrium and under the flow is illustrated in Fig. 3.3.

Ionic concentrations can be expressed in the context of Boltzmann distribution, so that

$$c_\alpha^\varepsilon(x) = c_\alpha^b \exp\left[-z_\alpha \left(\Psi^\varepsilon(x) + \Phi_\alpha^\varepsilon(x) + \Psi^{ext}(x)\right)\right]. \tag{3.2.18}$$

The introduction of ionic potentials $\Phi_\alpha^\varepsilon, \alpha = 1, 2$, proves to be useful in the decoupling of the electrokinetic system, as they effectively substitute the ionic concentrations $c_\alpha^{per,\varepsilon}$ as the unknowns. Also, it will help to eliminate the boundary condition $(3.2.9)_3$ from the system because their choice does not influence the mobility of particles, see (O'Brien and White 1978). The boundary condition $(3.2.13)_2$ is used only to define the distribution of potential in equilibrium $\Psi^{eq,\varepsilon}$.

The linearization of (3.2.18) by the first-order Taylor expansion yields

$$c_\alpha^{per,\varepsilon}(x) = -c_\alpha^{eq,\varepsilon}(x) z_\alpha \left(\Psi^{per,\varepsilon}(x) + \Phi_\alpha^{per,\varepsilon}(x) + \Psi^{ext}(x)\right). \tag{3.2.19}$$

Further, following the work (Moyne and Murad 2006), it is convenient to introduce the so-called global pressure P^ε,

$$P^\varepsilon = p^{\mathrm{per},\varepsilon} + \sum_{\beta=1}^{2} c_\beta^{\mathrm{eq},\varepsilon} z_\beta \left(\Psi^{\mathrm{per},\varepsilon} + \Phi_\beta^{\mathrm{per},\varepsilon} + \Psi^{\mathrm{ext}}\right) , \tag{3.2.20}$$

which consists of the hydrodynamic pressure perturbation $p^{\mathrm{per},\varepsilon}$ and the osmotic pressure, see (Lemaire et al. 2010b).

Finally, the decomposition of unknown fields (3.2.11) is substituted into the dimensionless problem (3.2.8)-(3.2.10) and (3.2.19) is employed to express $c_\alpha^{\mathrm{per},\varepsilon}(x)$. Note that products of the small quantities, *e.g.* $(c_\alpha^{\mathrm{per},\varepsilon})^2$, are neglected. Due to the linearization and the introduction of the global pressure (3.2.20), the nondimensionalized problem splits into three subproblems that can be solved subsequently.

Linearized electrokinetic system Given the body forces $\boldsymbol{f}$ and potential Ψ^{ext}, find L-periodic functions $(\boldsymbol{w}^{\mathrm{per},\varepsilon}, P^\varepsilon, \Phi_\alpha^{\mathrm{per},\varepsilon}, \Psi^{\mathrm{per},\varepsilon})$ and $\boldsymbol{u}^{\mathrm{per},\varepsilon}$ which solve the following three subproblems:

1. Electrokinetic problem: Find $(\boldsymbol{w}^{\mathrm{per},\varepsilon}, P^\varepsilon, \Phi_\alpha^{\mathrm{per},\varepsilon})$ which satisfy

$$\begin{aligned}
\varepsilon^2 \nabla^2 \boldsymbol{w}^{\mathrm{per},\varepsilon} - \nabla P^\varepsilon = - \sum_{\beta=1}^{2} z_\beta c_\beta^{\mathrm{eq},\varepsilon} (\nabla \Phi_\beta^{\mathrm{per},\varepsilon} + \nabla \Psi^{\mathrm{ext}}) - \boldsymbol{f} \quad & \text{in } \Omega_f^\varepsilon, \\
\nabla \cdot \boldsymbol{w}^{\mathrm{per},\varepsilon} = 0 \quad & \text{in } \Omega_f^\varepsilon, \\
\nabla \cdot \left(c_\alpha^{\mathrm{eq},\varepsilon} \left(\nabla \Phi_\alpha^{\mathrm{per},\varepsilon} + \nabla \Psi^{\mathrm{ext}} + \frac{\mathrm{Pe}_\alpha}{z_\alpha} \boldsymbol{w}^{\mathrm{per},\varepsilon} \right) \right) = 0 \quad & \text{in } \Omega_f^\varepsilon, \\
\boldsymbol{w}^{\mathrm{per},\varepsilon} = 0 \quad & \text{on } \Gamma^\varepsilon, \\
(\nabla \Phi_\alpha^{\mathrm{per},\varepsilon} + \nabla \Psi^{\mathrm{ext}}) \cdot \boldsymbol{n} = 0 \quad & \text{on } \Gamma^\varepsilon.
\end{aligned} \tag{3.2.21}$$

2. Electrostatic EDL problem: Find $\Psi^{\mathrm{per},\varepsilon}$ which satisfies

$$\begin{aligned}
-\varepsilon^2 \nabla^2 \Psi^{\mathrm{per},\varepsilon} + \gamma \left(\sum_{\beta=1}^{2} z_\beta^2 c_\beta^{\mathrm{eq},\varepsilon} \right) \Psi^{\mathrm{per},\varepsilon} = -\gamma \sum_{\beta=1}^{2} z_\beta^2 c_\beta^{\mathrm{eq},\varepsilon} (\Phi_\beta^{\mathrm{per},\varepsilon} + \Psi^{\mathrm{ext}}) \quad & \text{in } \Omega_f^\varepsilon, \\
\nabla \Psi^{\mathrm{per},\varepsilon} \cdot \boldsymbol{n} = 0 \quad \text{on } \Gamma^\varepsilon. &
\end{aligned} \tag{3.2.22}$$

3. Deformation problem: Find $\boldsymbol{u}^{\mathrm{per},\varepsilon}$ which satisfies

$$\begin{aligned}
-\nabla \cdot (\boldsymbol{A}\boldsymbol{e}(\boldsymbol{u}^{\mathrm{per},\varepsilon})) = \boldsymbol{f} \quad & \text{in } \Omega_s^\varepsilon, \\
(\boldsymbol{A}\boldsymbol{e}(\boldsymbol{u}^{\mathrm{per},\varepsilon})) \cdot \boldsymbol{n} = \boldsymbol{\sigma}_f^\varepsilon \cdot \boldsymbol{n} \quad & \text{on } \Gamma^\varepsilon,
\end{aligned} \tag{3.2.23}$$

   with the linearized fluid stress given by

$$\begin{aligned}
\boldsymbol{\sigma}_f^\varepsilon = & -P^\varepsilon \boldsymbol{I} + 2\varepsilon^2 \boldsymbol{e}(\boldsymbol{w}^{\mathrm{per},\varepsilon}) + \sum_{\beta=1}^{N=2} z_\beta c_\beta^{\mathrm{eq},\varepsilon} (\Psi^{\mathrm{per},\varepsilon} + \Phi_j^\varepsilon + \Psi^{\mathrm{ext}}) \boldsymbol{I} + \\
& + \frac{\varepsilon^2}{\gamma} \left(\nabla \Psi^{\mathrm{eq},\varepsilon} \otimes \nabla \Psi^{\mathrm{per},\varepsilon} + \nabla \Psi^{\mathrm{per},\varepsilon} \otimes \nabla \Psi^{\mathrm{eq},\varepsilon} - \nabla \Psi^{\mathrm{eq},\varepsilon} \cdot \nabla \Psi^{\mathrm{per},\varepsilon} \boldsymbol{I} \right).
\end{aligned} \tag{3.2.24}$$

It is worth to note that, due to the linearization and decoupling into three subproblems, $(3.2.21)_4$,$(3.2.21)_5$, $(3.2.22)_2$ and $(3.2.23)_2$ present standard boundary conditions on the interface Γ^ε, rather than transmission conditions, as it was in problem (3.2.8)–(3.2.10).

3.2.3 Two-scale problem of electrokinetic system

In the following part, we use homogenization by UFM to derive a limit two-scale problem from the system (3.2.21). First, we recall the geometrical structure of the porous medium, which was described in more detail in Sec. 3.1. We consider domain Ω^ε to be ε-periodic, generated as a lattice of RVE Y composed of fluid and solid part Y_f and Y_s and their interface Γ_Y.

Let us also recall sthe olution of Poisson-Boltzmann equation in equilibrium Ψ^{eq} (see Appendix B) and express the concentration $c_\alpha^{\mathrm{eq}}(y)$ on the RVE Y as

$$c_\alpha^{\mathrm{eq}}(y) = c_\alpha^b \exp(-z_\alpha \Psi^{\mathrm{eq}}(y)), \tag{3.2.25}$$

where c_α^b is the concentration in bulk. By this approach, the concentration can be computed separately from the rest of the system and thus is eliminated as a variable.

In order to apply UFM to the system (3.2.21), we have to express it in its weak form first. First, we deploy functional spaces for the velocity and potentials.

Definition 3.2.1 (Functional spaces) *Let $\mathcal{O} \subset \mathbb{R}^d$ be an open bounded domain containing homologous surfaces $\Sigma_\natural \subset \partial\mathcal{O}$ and $\Sigma_\flat \subset \partial\mathcal{O}$, such that $\Sigma_\flat = \partial\mathcal{O} \setminus \Sigma_\natural$, which make possible to introduce the notion of $\mathcal{O}$-periodic functions. Further, let $\mathcal{O}_p \subset \mathcal{O}$, $p = s, f$ and $\Gamma_{fs} = \overline{\mathcal{O}_s} \cap \overline{\mathcal{O}_f}$ be the interface between the two subdomains. The following functional spaces associated with the subdomains $\mathcal{O}_p$ will be employed,*

$$\begin{aligned}
\mathbf{H}^1_\#(\mathcal{O}_p) &= \left\{\boldsymbol{\varphi} \in H^1(\mathcal{O}_p)^d,\ \mathcal{O} - \textit{periodic in } x\right\},\\
\mathbf{H}^1_{\#0}(\mathcal{O}_p) &= \left\{\boldsymbol{\varphi} \in H^1(\mathcal{O}_p)^d, \boldsymbol{\varphi} = 0 \textit{ on } \Gamma_{fs},\ \mathcal{O} - \textit{periodic in } x\right\},\\
H^1_\#(\mathcal{O}_p) &= \left\{\psi \in H^1(\mathcal{O}_p),\ \mathcal{O} - \textit{periodic in } x\right\},
\end{aligned}$$

where $H^1(\mathcal{O}_p)$ is the Sobolev space $W^{1,2}(\mathcal{O}_p)$, subscript $p = s, f$. In our setting, domain $\mathcal{O}_p$ can be identified with Ω_p^ε or with representative unit cell Y_p.

Weak formulation

The weak form of decoupled system (3.2.21) is obtained by using standard per-partes integration and reads: Find $(\boldsymbol{w}^{\mathrm{per},\varepsilon}, P^\varepsilon, \Phi_\alpha^{\mathrm{per},\varepsilon}) \in \mathbf{H}^1_{\#0}(\Omega_f^\varepsilon) \times [H^1_\#(\Omega_f^\varepsilon)]^d$, such that

$$\begin{aligned}
\varepsilon^2 \int_{\Omega_f^\varepsilon} \nabla \boldsymbol{w}^{\mathrm{per},\varepsilon} : \nabla \tilde{\boldsymbol{\vartheta}}\,\mathrm{d}x + \int_{\Omega_f^\varepsilon} \tilde{\boldsymbol{\vartheta}}\,(\nabla P^\varepsilon - \boldsymbol{f})\,\mathrm{d}x &= \sum_{\beta=1}^{2} z_\beta \int_{\Omega_f^\varepsilon} c_\beta^{\mathrm{eq},\varepsilon} \tilde{\boldsymbol{\vartheta}} \cdot (\nabla \Phi_\beta^{\mathrm{per},\varepsilon} - \nabla \Psi^{\mathrm{ext}})\,\mathrm{d}x\\
\int_{\Omega_f^\varepsilon} c_\alpha^{\mathrm{eq},\varepsilon} \frac{\mathrm{Pe}_\alpha}{z_\alpha} \boldsymbol{w}^{\mathrm{per},\varepsilon} \nabla \tilde{\varphi}_\alpha\,\mathrm{d}x &= -\int_{\Omega_f^\varepsilon} c_\alpha^{\mathrm{eq},\varepsilon} \left(\nabla \Phi_\alpha^{\mathrm{per},\varepsilon} - \nabla \Psi^{\mathrm{ext}}\right) \nabla \tilde{\varphi}_\alpha\,\mathrm{d}x,\\
\int_{\Omega_f^\varepsilon} \tilde{q} \nabla \cdot \boldsymbol{w}^{\mathrm{per},\varepsilon}\,\mathrm{d}x &= 0,
\end{aligned} \tag{3.2.26}$$

for all $\tilde{\boldsymbol{\vartheta}} \in \mathbf{H}^1_{\#0}(\Omega_f^\varepsilon)$, $\tilde{q} \in H^1_\#(\Omega_f^\varepsilon)$ and $\tilde{\varphi}_\alpha \in H^1_\#(\Omega_f^\varepsilon), \alpha = 1, 2$.

To upscale this problem, we need to perform an asymptotic analysis. In the following part, we provide the convergences necessary for passing (3.2.26) to the limit $\varepsilon \to 0$.

Convergences

The *a priori* estimates and the standard results for the homogenization theory, see (Cioranescu et al. 2008), enable us to assume, that the solution of (3.2.21) is given by the so-called recovery sequences which are defined in Definition 3.1.2. Applying the unfolding operator $\mathcal{T}_\varepsilon$ to the recovery sequences of variables $\boldsymbol{w}^{\mathrm{per},\varepsilon}, P^\varepsilon$, and $\Phi_\alpha^{\mathrm{per},\varepsilon}, \alpha = 1,2$ yields

$$\begin{aligned}
\mathcal{T}_\varepsilon\Big(\boldsymbol{w}^{R,\varepsilon}(x)\Big) &\approx \boldsymbol{w}^0(x,y) + \varepsilon \boldsymbol{w}^1(x,y) + \mathcal{O}(\varepsilon^2), \\
\mathcal{T}_\varepsilon\Big(P^{R,\varepsilon}(x)\Big) &\approx P^0(x,y) + \varepsilon P^1(x,y) + \mathcal{O}(\varepsilon^2), \\
\mathcal{T}_\varepsilon\Big(\Phi_\alpha^{R,\varepsilon}(x)\Big) &\approx \Phi_\alpha^0(x,y) + \varepsilon \Phi_\alpha^1(x,y) + \mathcal{O}(\varepsilon^2), \quad \alpha = 1,2.
\end{aligned} \tag{3.2.27}$$

Next, we must choose the test functions with respect to the parameter ε in a suitable form. This can be most simply accomplished by considering test functions with the same decomposition as the recovery sequences associated with the corresponding variables. Application of the unfolding operator on the recovery sequences of test functions $\tilde{\boldsymbol{\vartheta}}, \tilde{q}$ and $\tilde{\varphi}_\alpha, \alpha = 1,2$ yields expressions analogical to (3.2.27), so that

$$\begin{aligned}
\mathcal{T}_\varepsilon\Big(\tilde{\boldsymbol{\vartheta}}^{R,\varepsilon}(x)\Big) &\approx \tilde{\boldsymbol{\vartheta}}^0(x,y) + \varepsilon \tilde{\boldsymbol{\vartheta}}^1(x,y) + \mathcal{O}(\varepsilon^2), \\
\mathcal{T}_\varepsilon\Big(\tilde{q}^{R,\varepsilon}(x)\Big) &\approx \tilde{q}^0(x,y) + \varepsilon \tilde{q}^1(x,y) + \mathcal{O}(\varepsilon^2), \\
\mathcal{T}_\varepsilon\Big(\tilde{\varphi}_\alpha^{R,\varepsilon}(x)\Big) &\approx \tilde{\varphi}_\alpha^0(x,y) + \varepsilon \tilde{\varphi}_\alpha^1(x,y) + \mathcal{O}(\varepsilon^2), \alpha = 1,2.
\end{aligned} \tag{3.2.28}$$

Moreover, the unfolding operator allows us to use weak convergences. According to (Allaire et al. 2015), there exist limits $(\boldsymbol{w}^0, P^0) \in L^2(\Omega; H^1_\#(Y_f)^d) \times L^2(\Omega)$ and $\{\Phi_\alpha^0, \Phi_\alpha^1\}_{\alpha=1,2} \in (H^1(\Omega) \times L^2(\Omega; H^1_\#(Y_f)))^2$ such that following convergences for $\varepsilon \to 0$ hold

$$\begin{aligned}
\mathcal{T}_\varepsilon(\boldsymbol{w}^\varepsilon) &\rightharpoonup \boldsymbol{w}^0 && \text{w. in } L^2(\Omega \times Y_f), \\
\varepsilon\mathcal{T}_\varepsilon(\nabla \boldsymbol{w}^\varepsilon) &\rightharpoonup \nabla_y \boldsymbol{w}^0 && \text{w. in } L^2(\Omega \times Y_f), \\
\mathcal{T}_\varepsilon(P^\varepsilon) &\to P^0 && \text{s. in } L^2(\Omega), \\
\mathcal{T}_\varepsilon(\nabla P^\varepsilon) &\rightharpoonup \nabla_x P^0 + \nabla_y P^1 && \text{w. in } L^2(\Omega \times Y_f), \\
\mathcal{T}_\varepsilon(\{\Phi_\alpha^\varepsilon\}) &\to \left\{\Phi_\alpha^0\right\} && \text{s. in } L^2(\Omega), \\
\mathcal{T}_\varepsilon(\{\nabla\Phi_\alpha^\varepsilon\}) &\rightharpoonup \left\{\nabla_x \Phi_\alpha^0 + \nabla_y \Phi_\alpha^1\right\} && \text{w. in } L^2(\Omega \times Y_f),
\end{aligned} \tag{3.2.29}$$

for $\alpha = 1,2$.

Furthermore, $(\boldsymbol{w}^0, P^0, \{\Phi_\alpha^0, \Phi_\alpha^1\})$ is the unique solution of the corresponding two-scale limit problem, which will be defined below.

Two-scale problem

To obtain two-scale problem, we start by adding the recovery sequences of the variables $\boldsymbol{w}^{\mathrm{per},\varepsilon}, P^\varepsilon, \Phi_\alpha^{\mathrm{per},\varepsilon}$ and of the associated test functions $\tilde{\boldsymbol{\vartheta}}, \tilde{q}, \tilde{\varphi}_\alpha, \alpha = 1,2$ into (3.2.26). We proceed to apply the unfolding operator $\mathcal{T}_\varepsilon$, see Remark 3.1.1, which enables us to translate the problem into two-scales as shown by (3.2.27) and (3.2.28). The resulting expression is passed to the limit by using convergences (3.2.29) for $\varepsilon \to 0$. Let us demonstrate this process on the first term of $(3.2.26)_1$:

$$\varepsilon^2 \int\limits_{\Omega_f^\varepsilon} \nabla \boldsymbol{w}^{R,\varepsilon}(x) : \nabla \tilde{\boldsymbol{\vartheta}}^{R,\varepsilon}(x)dx = \varepsilon^2 \fint\limits_{\Omega\times Y_f} \mathcal{T}_\varepsilon\Big(\nabla \boldsymbol{w}^{R,\varepsilon}(x)\Big) : \mathcal{T}_\varepsilon\Big(\nabla \tilde{\boldsymbol{\vartheta}}^{R,\varepsilon}(x)\Big) \xrightarrow{\varepsilon\to 0}$$

$$\xrightarrow{\varepsilon\to 0} \fint\limits_{\Omega\times Y_f} \nabla_y \boldsymbol{w}^0 : \nabla_y \tilde{\boldsymbol{\vartheta}}^0.$$

We can apply the same procedure to the rest of the terms that occur in the weak form (3.2.26) of the decoupled electrokinetic system thus obtaining a two-scale limit problem: Find $(\boldsymbol{w}^0, P^0, \{\Phi_\alpha^0, \Phi_\alpha^1\}), \alpha = 1, 2$, such that

$$\begin{aligned}
&\fint\limits_{\Omega\times Y_f} \nabla_y \boldsymbol{w}^0 : \nabla_y \tilde{\boldsymbol{\vartheta}}^0 + \fint\limits_{\Omega\times Y_f} \tilde{\boldsymbol{\vartheta}}^0 \left(\nabla_x P^0 + \nabla_y P^1 - \boldsymbol{f}\right) = \\
&\qquad\qquad = \sum_{\beta=1}^{N=2} z_\beta \fint\limits_{\Omega\times Y_f} c_\beta^{\mathrm{eq},\varepsilon} \tilde{\boldsymbol{\vartheta}}^0 \cdot \left(\nabla_x \Phi_\beta^0 + \nabla_y \Phi_\beta^1 + \mathbf{E}\right), \\
&\fint\limits_{\Omega\times Y_f} \tilde{q}^0 \nabla_y \cdot \boldsymbol{w}^0 = 0, \qquad\qquad\qquad\qquad\qquad\qquad\qquad\qquad (3.2.30)\\
&\fint\limits_{\Omega\times Y_f} c_\alpha^{\mathrm{eq},\varepsilon} \frac{\mathrm{Pe}_\alpha}{z_\alpha} \boldsymbol{w}^0 \cdot \left(\nabla_x \tilde{\varphi}_\alpha^0 + \nabla_y \tilde{\varphi}_\alpha^1\right) = \\
&\qquad\qquad = - \fint\limits_{\Omega\times Y_f} c_\alpha^{\mathrm{eq},\varepsilon} \left(\nabla_x \Phi_\alpha^0 + \nabla_y \Phi_\alpha^1 + \mathbf{E}\right) \cdot \left(\nabla_x \tilde{\varphi}_\alpha^0 + \nabla_y \tilde{\varphi}_\alpha^1\right),
\end{aligned}$$

for any test functions $\tilde{\boldsymbol{\vartheta}}^0 \in \mathbf{H}^1_{\#0}(\Omega_f^\varepsilon)$, $\tilde{q}^0 \in H^1_{\#}(\Omega_f^\varepsilon)$ and $\tilde{\varphi}_\alpha^0 \in H^1_{\#}(\Omega_f^\varepsilon), \alpha = 1, 2$.

The local problems, relevant to the microscopic scale, can be derived from the limit problem above, usually by letting vanish all the components of the test functions, which are not relevant to the microscopic scale (i.e. $\boldsymbol{\varphi}^0 = 0, \psi^0 = 0$). We recognized two different macroscopic fluxes in the limit two-scale problem, namely $(\nabla_x \Phi_\beta^0 + \mathbf{E})$ and $(\nabla_x P^0 - \boldsymbol{f})$. Therefore, we introduce the scale decomposition formulae of the limits $\boldsymbol{w}^0, \Phi_\alpha^1, P^1$ that read

$$\begin{aligned}
\boldsymbol{w}^0(x, y) &= \sum_{\beta=1}^{2} \boldsymbol{\omega}^{\beta,k}(y) \left(\frac{\partial \Phi_\beta^0}{\partial x_k} + \mathrm{E}_k\right)(x) + \boldsymbol{\omega}^{P,k}(y) \left(f_k - \frac{\partial P^0}{\partial x_k}\right)(x), \\
\Phi_\alpha^1(x, y) &= \sum_{\beta=1}^{2} \theta_\alpha^{\beta,k}(y) \left(\frac{\partial \Phi_\beta^0}{\partial x_k} + \mathrm{E}_k\right)(x) + \theta_\alpha^{P,k}(y) \left(f_k - \frac{\partial P^0}{\partial x_k}\right)(x), \qquad (3.2.31)\\
P^1(x, y) &= \sum_{\beta=1}^{2} \pi^{\beta,k}(y) \left(\frac{\partial \Phi_\beta^0}{\partial x_k} + \mathrm{E}_k\right)(x) + \pi^{P,k}(y) \left(f_k - \frac{\partial P^0}{\partial x_k}\right)(x),
\end{aligned}$$

where we introduced the two families of corrector base functions $(\boldsymbol{\omega}^{P,k}, \pi^{P,k}, \theta_\alpha^{P,k})$ and $(\boldsymbol{\omega}^{\beta,k}, \pi^{\beta,k}, \theta_\alpha^{\beta,k}), \beta = 1, 2$, that are indexed by $k \in \{1, \ldots, d\}$. Recall that d is the spatial dimension of the problem. Note, that the standard Einstein summation convention holds.

3.2.4 Two-scale problem of potential perturbation

We now turn to the (3.2.22) for the potential perturbation $\Psi^{\mathrm{per},\varepsilon}$. The process of the asymptotic analysis remains the same, therefore we report on the most important steps of the upscaling process.

Weak formulation

We assume that the functional spaces are given by (**??**). By using standard integration by parts, we transform problem (3.2.22) into its weak form, which reads: Find $\Psi^{\mathrm{per},\varepsilon} \in H^1_{\#}(\Omega^\varepsilon_f)$, such that

$$\varepsilon^2 \int\limits_{\Omega^\varepsilon_f} \nabla \Psi^{\mathrm{per},\varepsilon} \cdot \tilde{\psi}_f \,\mathrm{d}x + \beta \int\limits_{\Omega^\varepsilon_f} \left(\sum_{\beta=1}^{N=2} z_\beta c_\beta^{\mathrm{eq},\varepsilon} \right) \Psi^{\mathrm{per},\varepsilon} \tilde{\psi}_f \,\mathrm{d}x =$$

$$= -\gamma \sum_{\beta=1}^{N=2} z_\beta \int\limits_{\Omega^\varepsilon_f} c_\beta^{\mathrm{eq},\varepsilon} \left(\Phi^\varepsilon_\beta + \Psi^{\mathrm{ext}} \right) \tilde{\psi}_f \,\mathrm{d}x, \qquad \forall \tilde{\psi}_f \in H^1_{\#}(\Omega^\varepsilon_f). \quad (3.2.32)$$

Note that the functions $c_\beta^{\mathrm{eq},\varepsilon}$ are already determined by the equilibrium solution (3.2.12).

Convergences

The approximation recovery sequence for the potential perturbation, after application of the unfolding operator $\mathcal{T}_\varepsilon$, reads

$$\mathcal{T}_\varepsilon \Big(\Psi^{R,\varepsilon}(x) \Big) \approx \Psi^0(x,y) + \varepsilon \Psi^1(x,y) + \mathcal{O}(\varepsilon^2). \quad (3.2.33)$$

Note that we choose test functions $\tilde{\psi}_f$ to have analogical decomposition. There exist a limit $\Psi^0 \in L^2(\Omega; H^1_{\#}(Y_f))$ such that the following convergences for $\varepsilon \to 0$ hold

$$\begin{aligned} \mathcal{T}_\varepsilon(\Psi^\varepsilon) &\rightharpoonup \Psi^0 \qquad \text{w. in } L^2(\Omega \times Y_f), \\ \mathcal{T}_\varepsilon(\varepsilon \nabla \Psi^\varepsilon) &\rightharpoonup \nabla_y \Psi^0 \qquad \text{w. in } L^2(\Omega \times Y_f). \end{aligned} \quad (3.2.34)$$

Furthermore, $\Psi^0(x,y)$ is the unique solution of the corresponding two-scale limit problem given below.

Two-scale problem

We follow the same steps as in the derivation of the two-scale problem of electrokinetics. By adding the recovery sequences of variable $\Psi^{\mathrm{per},\varepsilon}$ (3.2.33) and the associated test function $\tilde{\psi}_f$ and by subsequent application of the unfolding operator $\mathcal{T}_\varepsilon$, we translate (3.2.32) into its microscopic and macroscopic parts. Then, using convergences (3.2.34), a limit expression is found. The limit two-scale problem reads: Find $\Psi^0 \in H^1_{\#}(\Omega^\varepsilon_f)$ such that

$$\fint\limits_{\Omega \times Y_f} \nabla_y \Psi^0 \nabla_y \tilde{\psi}_f^{\,0} + \beta \fint\limits_{\Omega \times Y_f} \left(\sum_{\beta=1}^{N=2} z_\beta c_\beta^{\mathrm{eq},\varepsilon} \right) \Psi^0 \tilde{\psi}_f^{\,0} = -\beta \sum_{\beta=1}^{N=2} z_\beta \fint\limits_{\Omega \times Y_f} c_\beta^{\mathrm{eq},\varepsilon} (\Phi^0_\beta + \Psi^{\mathrm{ext}}) \tilde{\psi}_f^{\,0}, \quad (3.2.35)$$

for all $\tilde{\psi_f}^0 \in H^1_\#(\Omega^\varepsilon_f)$. Introducing the corrector base functions $\varpi^\alpha, \alpha = 1, 2$, we may separate the fast and slow scale using a separation formula

$$\Psi^0(x, y) = \sum_{\beta=1}^{2} \varpi^\beta(y) \left(\Phi^0_\beta(x) + \Psi^{\text{ext}}(x)\right). \tag{3.2.36}$$

3.2.5 Two-scale problem of displacement perturbation

Lastly, we homogenize the linearized equation for displacement perturbation $\boldsymbol{u}^{\text{per},\varepsilon}$ governed by (3.2.23), which are only weakly coupled to the electrokinetic system discussed above. We do not provide rigorous homogenization (that can be found in (Allaire et al. 2015)), only the main steps needed to obtain the homogenization results.

Weak formulation

Once again, we employ functional spaces given by (**??**). The weak form of (3.2.23) is obtained by integration per-partes and reads: find $\boldsymbol{u}^{\text{per},\varepsilon} \in H^1_\#(\Omega^\varepsilon_s)^d$, such that

$$\int_{\Omega^\varepsilon_s} \boldsymbol{A}\boldsymbol{e}\left(\boldsymbol{u}^{\text{per},\varepsilon}\right) : \boldsymbol{e}\left(\tilde{\boldsymbol{v}}\right) \mathrm{d}x = \int_{\Gamma^\varepsilon} \boldsymbol{\sigma}^\varepsilon_f \boldsymbol{n} \cdot \tilde{\boldsymbol{v}} \,\mathrm{d}S + \int_{\Omega^\varepsilon_s} \boldsymbol{f} \cdot \tilde{\boldsymbol{v}} \,\mathrm{d}x, \tag{3.2.37}$$

for all $\tilde{\boldsymbol{v}} \in H^1_\#(\Omega^\varepsilon_s)^d$. After application of the Stokes divergence theorem, it becomes

$$\int_{\Omega^\varepsilon_s} \boldsymbol{A}\boldsymbol{e}\left(\boldsymbol{u}^{\text{per},\varepsilon}\right) : \boldsymbol{e}\left(\tilde{\boldsymbol{v}}\right) \mathrm{d}x = -\int_{\Omega^\varepsilon_s} \boldsymbol{\sigma}^\varepsilon_f : \nabla \tilde{\boldsymbol{v}} \,\mathrm{d}x + \int_{\Omega^\varepsilon_s} \boldsymbol{f} \cdot \tilde{\boldsymbol{v}} \,\mathrm{d}x, \tag{3.2.38}$$

for all $\tilde{\boldsymbol{v}} \in H^1_\#(\Omega^\varepsilon_s)^d$.

Convergences

We introduce the recovery sequence for displacement perturbation and apply the unfolding operator $\mathcal{T}_\varepsilon$, so that the following approximation holds

$$\mathcal{T}_\varepsilon\left(\boldsymbol{u}^{R,\varepsilon}(x)\right) \approx \boldsymbol{u}^0(x, y) + \varepsilon \boldsymbol{u}^1(x, y) + \mathcal{O}(\varepsilon^2). \tag{3.2.39}$$

We assume that the test function $\tilde{\boldsymbol{v}}$ has the same decomposition. The necessary *a priori* estimates can be found in (Allaire et al. 2015). With their help it can be shown that there exist limits $\boldsymbol{u}^0 \in H^1_\#(\Omega^\varepsilon_s)^d$ and $\boldsymbol{u}^1 \in L^2(\Omega; H^1_\#(\Omega^\varepsilon_s)^d)$ such that the following convergences for $\varepsilon \to 0$ hold

$$\begin{aligned} \mathcal{T}_\varepsilon(\boldsymbol{u}^{\text{per},\varepsilon}) &\rightharpoonup \boldsymbol{u}^0 \qquad \text{w. in } L^2(\Omega \times Y_s), \\ \mathcal{T}_\varepsilon(\nabla \boldsymbol{u}^{\text{per},\varepsilon}) &\rightharpoonup \nabla_x \boldsymbol{u}^0 + \nabla_y \boldsymbol{u}^1 \qquad \text{w. in } L^2(\Omega \times Y_s), \\ \mathcal{T}_\varepsilon\left(\boldsymbol{\sigma}^\varepsilon_f\right) &\rightharpoonup \boldsymbol{\sigma}^1_f \qquad \text{w. in } L^2(\Omega \times Y_f), \end{aligned} \tag{3.2.40}$$

where

$$\begin{aligned} \boldsymbol{\sigma}^1_f = &- P^0(x)\boldsymbol{I} + \sum_{\beta=1}^{N=2} z_\beta c^{\text{eq},\varepsilon}_\beta(y)(\Psi^0(x, y) + \Phi^0(x) + \Psi^{\text{ext}}(x))\boldsymbol{I} \\ &+\gamma^{-1}\left(\nabla_y \Psi^{\text{eq}}(y) \otimes \nabla_y \Psi^0(x, y) + \nabla_y \Psi^0(y) \otimes \nabla_y \Psi^{\text{eq}}(y) - \nabla_y \Psi^{\text{eq}}(y) \cdot \nabla_y \delta\Psi^0(y)\boldsymbol{I}\right). \end{aligned} \tag{3.2.41}$$

By applying the unfolding operator to (3.2.38) and by using convergences (3.2.40), we get the two-scale limit problem for displacement perturbation.

Two-scale limit problem

The two-scale limit problem reads: Find $\boldsymbol{u}^0 \in H^1_{\#}(\Omega^\varepsilon_s)^d$ and $\boldsymbol{u}^1 \in L^2(\Omega; H^1_{\#}(\Omega^\varepsilon_s)^d)$ such that

$$\fint_{\Omega\times Y_s} \boldsymbol{A}\left(e_x\left(\boldsymbol{u}^0\right) + e_y\left(\boldsymbol{u}^1\right)\right) : \left(e_x\left(\tilde{\boldsymbol{v}}^0\right) + e_y\left(\tilde{\boldsymbol{v}}^1\right)\right) = \\ -\fint_{\Omega\times Y_s} \boldsymbol{\sigma}^1_f : \left(\nabla_x \tilde{\boldsymbol{v}}^0 + \nabla_y \tilde{\boldsymbol{v}}^1\right) + \fint_{\Omega\times Y_s} \boldsymbol{f}\cdot\tilde{\boldsymbol{v}}^0, \quad (3.2.42)$$

for all $\tilde{\boldsymbol{v}}^0 \in H^1_{\#}(\Omega^\varepsilon_s)^d$ and $\tilde{\boldsymbol{v}}^1 \in L^2(\Omega; H^1_{\#}(\Omega^\varepsilon_s)^d)$.

Once again, it is important to separate the fast and slow scale by employing the scale separation formula that reads

$$\boldsymbol{u}^1(x,y) = \sum_{i,j=1}^{d} \boldsymbol{w}^{ij}(y) e_{ij}\left(\boldsymbol{u}^0(x)\right) - P^0(x)\boldsymbol{w}^P(y) + \sum_{\alpha=1}^{N} \boldsymbol{w}^\alpha(y) z_\alpha \left(\Phi^0_\alpha(x) + \Psi^{\mathrm{ext}}(x)\right), \quad (3.2.43)$$

where $\boldsymbol{w}^{ij}$, $\boldsymbol{w}^P$ and $\boldsymbol{w}^\alpha$ are the corrector base functions that are obtained as the solution of the three local cell problems given below.

3.2.6 Local problems

The corrector basis functions introduced in (3.2.31), (3.2.36) and (3.2.43) are solutions to the local autonomous problems (also cell problems) defined in subdomains of the representative periodic cell Y. By virtue of linearization, which decomposes the problem (3.2.21) into three subproblems, the local problems are decoupled and split into the following three groups:

- Group 1: two local problems related to the electrokinetic system with responses $(\boldsymbol{\omega}^{P,k}, \pi^{P,k}, \theta^{P,k}_\beta)$ and $(\boldsymbol{\omega}^{\alpha,k}, \pi^{\alpha,k}, \theta^{\alpha,k}_\beta)$, $\alpha, \beta = 1, 2$, $k = 1, \dots, d$.
- Group 2: one local problem related to the electrostatic potential in the EDL with solution ϖ^α, $\alpha = 1, 2$.
- Group 3: three local problems related to poroelasticity with solutions $\boldsymbol{w}^{ij}$, $\boldsymbol{w}^P$ and $\boldsymbol{w}^\alpha$

All the six local problems are introduced below.

Cell problems: Group 1

The first autonomous cell problem of this group is related to the macroscopic pressure gradient: Find $(\boldsymbol{\omega}^{P,k}, \pi^{P,k}, \theta_\beta^{P,k}) \in \mathbf{H}^1_{\#0}(Y_f)$, $k = 1, 2, 3,\ \beta = 1, 2$:

$$
\begin{gathered}
\fint_{Y_f} \nabla_y \boldsymbol{\omega}^{P,k}(y) : \nabla_y \tilde{\boldsymbol{\vartheta}}\, \mathrm{d}V + \fint_{Y_f} \pi^{P,k}(y) \nabla_y \cdot \tilde{\boldsymbol{\vartheta}}\, \mathrm{d}V = \fint_{Y_f} \vartheta_k + \sum_{\beta=1}^{2} \fint_{Y_f} z_\beta c_\beta^{\mathrm{eq}}(y) \tilde{\boldsymbol{\vartheta}} \cdot \nabla_y \theta_\beta^{P,k}\, \mathrm{d}V, \\
\fint_{Y_f} \tilde{q} \nabla_y \cdot \boldsymbol{\omega}^{P,k}(y)\, \mathrm{d}V = 0, \\
\fint_{Y_f} c_\beta^{\mathrm{eq}}(y) \nabla_y \tilde{\varphi} \nabla_y \theta_\beta^{P,k}\, \mathrm{d}V + \fint_{Y_f} c_\beta^{\mathrm{eq}}(y) \mathrm{Pe}_\beta z_\beta^{-1} \tilde{\varphi} \nabla_y \cdot \boldsymbol{\omega}^{P,k}(y)\, \mathrm{d}V = 0,
\end{gathered}
\tag{3.2.44}
$$

for all test functions $\tilde{\boldsymbol{\vartheta}} \in \mathbf{H}^1_{\#0}(Y_f)$, $\tilde{q} \in L^2(Y_f)$, $\tilde{\varphi} \in H^1_{\#}(Y_f)^N$.

The second autonomous cell problem that corresponds to the macroscopic diffusive flux, reads for each species $\alpha = 1, 2$: Find $(\boldsymbol{\omega}^{\alpha,k}, \pi^{\alpha,k}, \theta_\beta^{\alpha,k}) \in \mathbf{H}^1_{\#0}(Y_f)$, $k = 1, \ldots, d$:

$$
\begin{gathered}
\fint_{Y_f} \nabla_y \boldsymbol{\omega}^{\alpha,k}(y) : \nabla_y \tilde{\boldsymbol{\vartheta}}\, \mathrm{d}V + \fint_{Y_f} \pi^{\alpha,k}(y) \nabla_y \cdot \tilde{\boldsymbol{\vartheta}}\, \mathrm{d}V = \sum_{\beta=1}^{2} \fint_{Y_f} z_\beta c_\beta^{\mathrm{eq}}(y) (\delta_{\alpha\beta} \mathbf{e}^k + \nabla_y \theta_\beta^{\alpha,k}) \cdot \tilde{\boldsymbol{\vartheta}}\, \mathrm{d}V, \\
\fint_{Y_f} \tilde{q} \nabla_y \cdot \boldsymbol{\omega}^{\alpha,k}(y)\, \mathrm{d}V = 0, \\
\fint_{Y_f} c_\beta^{\mathrm{eq}}(y) \mathrm{Pe}_\beta z_\beta^{-1} \tilde{\varphi} \nabla_y \cdot \boldsymbol{\omega}^{\alpha,k}(y)\, \mathrm{d}V = - \fint_{Y_f} c_\beta^{\mathrm{eq}}(y) (\delta_{\alpha\beta} \mathbf{e}^k + \nabla_y \theta_\beta^{\alpha,k}) \nabla_y \tilde{\varphi}\, \mathrm{d}V,
\end{gathered}
\tag{3.2.45}
$$

for all test functions $\tilde{\boldsymbol{\vartheta}} \in \mathbf{H}^1_{\#0}(Y_f), \tilde{q} \in L^2(Y_f), \tilde{\varphi} \in H^1_{\#}(Y_f)^N$. The symbol $\mathbf{e}^k$ denotes the canonical basis of $\mathbb{R}^d$, $k = 1, ..., d$ and $\delta_{\alpha\beta}, \alpha = 1, 2, \beta = 1, 2$ the Kronecker symbol.

Cell problems: Group 2

The cell problem associated with the macroscopic ionic potential reads for each species $\alpha = 1, 2$: Find the corrector base functions $\varpi^\alpha \in H^1_{\#}(Y_f), \alpha = 1, 2$, such that

$$
\fint_{Y_f} \nabla_y \varpi^\alpha \cdot \nabla_y \tilde{\varphi}\, \mathrm{d}V + \gamma \fint_{Y_f} \sum_{\beta=1}^{2} \left(z_\beta^2 c_\beta^{\mathrm{eq}}(y) \right) \varpi^\alpha \tilde{\varphi}\, \mathrm{d}V = - \fint_{Y_f} \gamma z_\alpha^2 c_\alpha^{\mathrm{eq}}(y) \tilde{\varphi}\, \mathrm{d}V, \tag{3.2.46}
$$

for all test functions $\tilde{\varphi} \in H^1_{\#}(Y_f)$.

Cell problems: Group 3

The following three cell problems are relevant to the homogenization of displacement perturbation. One can realize that the first two cell problems are identical to the ones that occur in the derivation of Biot's poroelasticity equation, *e.g.* (Rohan et al. 2016b).

The first cell problem reads: find $\boldsymbol{w}^{ij} \in \boldsymbol{V}^1(Y_s)^d, \fint_{Y_s} \boldsymbol{w}^{ij}\,\mathrm{d}V = 0$ such that

$$a_{Y_s}\left(\boldsymbol{w}^{ij} + \boldsymbol{\Pi}^{ij},\, \tilde{\boldsymbol{v}}\right) = 0, \tag{3.2.47}$$

for any test function $\tilde{\boldsymbol{v}} \in \mathbf{H}^1_{\#}(Y_s)^d$. The symbol $\boldsymbol{\Pi}^{ij}$ denotes the so-called transformation vectors $\boldsymbol{\Pi}^{ij} = (\Pi^{ij}_k), i, j, k = 1, \ldots, d$ with $\Pi^{ij}_k = y_j \delta_{ik}$ that enable us to establish local displacements defined in Y generated by an affine transformation of macroscopic strains $e_x(\boldsymbol{u}^0)$; it holds that $e_y\left(\boldsymbol{\Pi}^{ij} e^x_{ij}(\boldsymbol{u}^0)\right) = e_x(\boldsymbol{u}^0)$.

The second cell problem reads: find $\boldsymbol{w}^P \in \mathbf{H}^1_{\#}(Y_s)^d, \fint_{Y_s} \boldsymbol{w}^P\,\mathrm{d}V = 0$ such that

$$a_{Y_s}\left(\boldsymbol{w}^P,\, \tilde{\boldsymbol{v}}\right) = -\fint_{\Gamma_Y} \tilde{\boldsymbol{v}} \cdot \boldsymbol{n}\,\mathrm{dS}_y, \tag{3.2.48}$$

for any test function $\tilde{\boldsymbol{v}} \in \mathbf{H}^1_{\#}(Y_s)^d$.

Finally, the third cell problem that connects displacement perturbation and ionic potentials reads: Find $\boldsymbol{w}^\alpha \in \mathbf{H}^1_{\#}(Y_s)^d, \fint_{Y_s} \boldsymbol{w}^\alpha\,\mathrm{d}V = 0$ such that

$$\begin{aligned} a_{Y_s}(\boldsymbol{w}^\alpha,\, \tilde{\boldsymbol{v}}) = & -\fint_{\Gamma_Y} \tilde{\boldsymbol{v}} \cdot c^{\mathrm{eq}}_\alpha \boldsymbol{I} \cdot \boldsymbol{n}\,\mathrm{dS}_y - \\ & - \gamma^{-1} \fint_{\Gamma_Y} \tilde{\boldsymbol{v}} \cdot \left(\nabla_y \Psi^{\mathrm{eq}} \otimes \nabla_y \varpi^\alpha + \nabla_y \varpi^\alpha \otimes \nabla_y \Psi^{\mathrm{eq}} - \nabla_y \Psi^{\mathrm{eq}} \cdot \nabla_y \varpi^\alpha \boldsymbol{I}\right) \cdot \boldsymbol{n}\,\mathrm{dS}_y, \end{aligned} \tag{3.2.49}$$

for any test function $\tilde{\boldsymbol{v}} \in \mathbf{H}^1_{\#}(Y_s)^d$.

3.2.7 Macroscopic model

By virtue of the homogenization method, the limit two-scale equations (3.2.30), (3.2.35) and (3.2.42) involve cell integrals of the two-scale functions which can be expressed in terms of the corrector basis functions. Below we list the expressions of homogenized coefficients which constitute the effective material parameters of the upscaled porous medium, (Allaire et al. 2013a).

The first group of corrector functions defines the following homogenized coefficients

$$\begin{aligned} \mathcal{J}^\alpha_{lk} &= \fint_{Y_f} \boldsymbol{\omega}^{\alpha,k}(y) \cdot \mathbf{e}^l\,\mathrm{d}V, \\ \mathcal{K}_{lk} &= \fint_{Y_f} \boldsymbol{\omega}^{P,k}(y) \cdot \mathbf{e}^l\,\mathrm{d}V, \\ \mathcal{D}^{\alpha\beta}_{lk} &= \fint_{Y_f} c^{\mathrm{eq}}_\alpha(y) \left(\boldsymbol{\omega}^{\alpha,k}(y) + \frac{z_\beta}{\mathrm{Pe}_\beta}\left(\mathbf{e}^k \delta_{\alpha\beta} + \nabla_y \theta^{\alpha,k}_\beta(y)\right)\right) \cdot \mathbf{e}^l\,\mathrm{d}V, \\ \mathcal{L}^\alpha_{lk} &= \fint_{Y_f} c^{\mathrm{eq}}_\alpha(y) \left(\boldsymbol{\omega}^{P,k}(y) + \frac{z_\alpha}{\mathrm{Pe}_\alpha} \nabla_y \theta^{P,k}_\alpha(y)\right) \cdot \mathbf{e}^l\,\mathrm{d}V, \end{aligned} \tag{3.2.50}$$

where $\boldsymbol{\mathcal{K}} = (\mathcal{K}_{lk})$ is the permeability tensor, $\boldsymbol{\mathcal{D}}^{\alpha\beta} = (\mathcal{D}^{\alpha\beta}_{lk})$ are diffusivity tensors; in particular $\boldsymbol{\mathcal{D}}^{\alpha\beta}$ describes diffusion of species α due to the streaming potential gradient of the species β. Tensors $\boldsymbol{\mathcal{J}}^{\alpha} = (\mathcal{J}^{\alpha}_{lk})$ are related to the flow driven by ionic potentials, and $\boldsymbol{\mathcal{L}}^{\alpha} = (\mathcal{L}^{\alpha}_{lk})$, also known as the coupling tensor, expresses the diffusivity of α-th species due to the global pressure gradient.

The second and the third group of the corrector functions constitute the poroelastic coefficients modified by the presence of the streaming potentials and the external electric field,

$$\begin{aligned}
\mathcal{A}_{ijkl} =& a_{Y_s}\left(\boldsymbol{w}^{ij} + \boldsymbol{\Pi}^{ij},\, \boldsymbol{w}^{kl} + \boldsymbol{\Pi}^{kl}\right),\\
\mathcal{B}_{ij} =& \delta_{ij}\phi_f + a_{Y_s}\left(\boldsymbol{w}^{P},\, \boldsymbol{\Pi}^{ij}\right),\\
\mathcal{C}^{\alpha}_{ij} =& a_{Y_s}\left(\boldsymbol{w}^{\alpha},\, \boldsymbol{\Pi}^{ij}\right) + \sum_{\beta=1}^{2} z_\beta \boldsymbol{I} \fint_{Y_f} c^{\text{eq}}_{\beta}(y)\left(\varpi^{\alpha}(y) + \delta_{\alpha\beta}\right)\,\mathrm{d}V + \\
&+ \fint_{Y_f} \gamma^{-1}\left(\nabla_y \Psi^{\text{eq}} \otimes \nabla_y \varpi^{\alpha} + \nabla_y \varpi^{\alpha}_{\otimes} \nabla_y \Psi^{\text{eq}} - \nabla_y \Psi^{\text{eq}} \cdot \nabla_y \varpi^{\alpha} \boldsymbol{I}\right)\,\mathrm{d}V.
\end{aligned} \tag{3.2.51}$$

The tensor $\boldsymbol{\mathcal{A}} = (\mathcal{A}_{ijkl})$ is the fourth-order positive definite effective elasticity tensor of a drained skeleton, $\boldsymbol{\mathcal{B}} = (\mathcal{B}_{ij})$ is the Biot's coupling tensor related to the pressure. These effective coefficients are sometimes referred to as the Biot poroelasticity coefficients.

The coefficient $\boldsymbol{\mathcal{C}}^{\alpha} = (\mathcal{C}^{\alpha}_{ij})$ is the tensor responsible for weak coupling between electrokinetics and poroelasticity.

The macroscopic problem can be derived from the two-scale equations (3.2.30), (3.2.35) and (3.2.42), usually by letting all the components of the test functions, which are not relevant to the macroscopic scale, vanish. The resulting system of equations can be rewritten in terms of the effective coefficients, see (3.2.50) and (3.2.51), and thus, the dimensionless macroscopic problem reads: Find $(P^0, \Phi^0_\alpha, \boldsymbol{u}^0) \in (L^2(\Omega) \times L^2(\Omega) \times \mathbf{H}^1(\Omega)), \alpha = 1, 2$, such that

$$\begin{aligned}
&-\sum_{\beta=1}^{2} \int_{\Omega} \boldsymbol{\mathcal{J}}^{\beta}(\nabla_x \Phi^0_\beta + \boldsymbol{E}) \nabla_x q \,\mathrm{d}V + \int_{\Omega} \boldsymbol{\mathcal{K}}(\nabla_x P^0 - \boldsymbol{f}) \nabla_x q \,\mathrm{d}V = 0,\\
&-\sum_{\beta=1}^{2} \int_{\Omega} \boldsymbol{\mathcal{D}}^{\alpha\beta}(\nabla_x \Phi^0_\beta + \boldsymbol{E}) \nabla_x \tilde{\psi}_f \,\mathrm{d}V + \int_{\Omega} \boldsymbol{\mathcal{L}}^{\alpha}(\nabla_x P^0 - \boldsymbol{f}) \nabla_x \tilde{\psi}_f \,\mathrm{d}V = 0,\\
&\int_{\Omega} \boldsymbol{\mathcal{A}} e_x\left(\boldsymbol{u}^0\right) : e_x\left(\tilde{\boldsymbol{v}}\right) \mathrm{d}V - \int_{\Omega} \boldsymbol{\mathcal{B}} P^0 : e_x\left(\tilde{\boldsymbol{v}}\right) \mathrm{d}V - \\
&\qquad - \sum_{\beta=1}^{2} \int_{\Omega} \boldsymbol{\mathcal{C}}^{\beta}(\Phi^0_\beta + \Psi^{\text{ext}}) : e_x\left(\tilde{\boldsymbol{v}}\right) \mathrm{d}V = \int_{\Omega} \boldsymbol{f} \cdot \tilde{\boldsymbol{v}} \,\mathrm{d}V,
\end{aligned} \tag{3.2.52}$$

for all test functions $q \in L^2(\Omega), \varphi \in L^2(\Omega)$ and $\boldsymbol{v} \in \mathbf{H}^1(\Omega)$. The equation $(3.2.52)_3$ is the so-called extended Biot equation and it is weakly coupled to the electrokinetic system $(3.2.52)_1$ and $(3.2.52)_2$ through coefficients $\boldsymbol{\mathcal{C}}^{\alpha}$.

One may recall that for the derivation of the homogenized macroscopic model (3.2.52), we did assume L-periodic boundary conditions on the outer boundary $\partial\Omega$, see also Remark 2.5.1. This assumption simplified the homogenization process, as it eliminated the necessity to deal with upscaling of various boundary conditions on $\partial\Omega$. As we already discussed in Sec.2.5, this limits the applicability of the derived model (3.2.52) to periodic problems only, however. To extend the model (3.2.52), so that it can be used for other than periodic problems, we propose its treatment in the following Remark.

Remark 3.2.2 (Dealing with L-periodicity) *By virtue of per-partes derivation, we may obtain the differential (sometimes also strong or classical) form of the problem* (3.2.52)*. Then it is possible to forgo the assumption of L-periodicity and split the boundary $\partial\Omega$ into parts, such that for any variable φ we may impose the classical Dirichlet type condition on the part of the boundary $\partial_\varphi\Omega$ and the Neumann type condition on the part of the boundary $\partial^N_\varphi\Omega = \partial\Omega \setminus \partial_\varphi\Omega$.*

Following Remark 3.2.2, we introduce the macroscopic homogenized equations in their differential form (for $\alpha = 1, 2$)

$$
\begin{aligned}
-\nabla_x \cdot \left(\boldsymbol{\mathcal{A}} e_x(\boldsymbol{u}^0)\right) + \nabla_x \cdot \left(\boldsymbol{\mathcal{B}} P^0 + \sum_{\beta=1}^{2} \boldsymbol{\mathcal{C}}^\beta (\Phi^0_\beta + \Psi^{\text{ext}})\right) &= \boldsymbol{f} \quad \text{in } \Omega,\\
\nabla_x \cdot \left(\sum_{\beta=1}^{2} \boldsymbol{\mathcal{J}}^\beta (\nabla_x \Phi^0_\beta + \mathbf{E}) - \boldsymbol{\mathcal{K}}(\nabla_x P^0 - \boldsymbol{f})\right) &= 0 \quad \text{in } \Omega,\\
\nabla_x \cdot \left(\sum_{\beta=1}^{2} \boldsymbol{\mathcal{D}}^{\alpha\beta} \left(\nabla_x \Phi^0_\beta + \mathbf{E}\right) - \boldsymbol{\mathcal{L}}^\alpha (\nabla_x P^0 - \boldsymbol{f})\right) &= 0 \quad \text{in } \Omega,
\end{aligned}
\tag{3.2.53}
$$

where we distinguish the fluid seepage velocity $\boldsymbol{w}^0$, the porous body stress $\boldsymbol{\sigma}^0$ and the ionic diffusion fluxes $\boldsymbol{j}^0_\alpha, \alpha = 1, 2$,

$$
\begin{aligned}
\boldsymbol{w}^0 &= \sum_{\beta=1}^{2} \boldsymbol{\mathcal{J}}^\beta (\nabla_x \Phi^0_\beta + \mathbf{E}) - \boldsymbol{\mathcal{K}}(\nabla_x P^0 - \boldsymbol{f}) \quad \text{in } \Omega,\\
\boldsymbol{\sigma}^0 &= \boldsymbol{\mathcal{A}} e_x(\boldsymbol{u}^0) - P^0 \boldsymbol{\mathcal{B}} - \sum_{\beta}^{2} \boldsymbol{\mathcal{C}}^\beta (\Phi^0_\beta + \Psi^{\text{ext}}), \quad \text{in } \Omega\\
\boldsymbol{j}^0_\alpha &= \sum_{\beta=1}^{2} \boldsymbol{\mathcal{D}}^{\alpha\beta} \left(\nabla_x \Phi^0_\beta + \mathbf{E}\right) - \boldsymbol{\mathcal{L}}^\alpha (\nabla_x P^0 - \boldsymbol{f}) \quad \text{in } \Omega, \quad \alpha = 1, 2.
\end{aligned}
\tag{3.2.54}
$$

The total velocity $\boldsymbol{w}^0$ can be split into the pressure driven velocity $\boldsymbol{w}_p$ and the potential driven velocity $\boldsymbol{w}_{\Phi_\alpha}, \alpha = 1, 2$

$$
\begin{aligned}
\boldsymbol{w}_p &= -\boldsymbol{\mathcal{K}}(\nabla_x P^0 - \boldsymbol{f}) \quad \text{in } \Omega,\\
\boldsymbol{w}_{\Phi_\alpha} &= \boldsymbol{\mathcal{J}}^\alpha (\nabla_x \Phi^0_\alpha + \mathbf{E}) \quad \text{in } \Omega, \quad \alpha = 1, 2.
\end{aligned}
\tag{3.2.55}
$$

The formulation of the macroscopic homogenized problem is based on the system (3.2.53) that must be completed by a suitable set of boundary conditions. Following Remark 3.2.2, we impose the Neumann type conditions on the respective parts of boundary, so that

$$
\begin{aligned}
\boldsymbol{n} \cdot \boldsymbol{\sigma}^0 &= \bar{\boldsymbol{\sigma}}, \text{ on } \partial^N_u \Omega,\\
\boldsymbol{n} \cdot \boldsymbol{j}^0_\alpha &= \bar{j}_\alpha, \text{ on } \partial^N_{\Phi_\alpha} \Omega, \quad \alpha = 1, 2,\\
\boldsymbol{n} \cdot \boldsymbol{w}^0 &= \bar{w}, \text{ on } \partial^N_P \Omega.
\end{aligned}
\tag{3.2.56}
$$

whereby the complementary Dirichlet type conditions must be imposed as follows

$$\begin{aligned} \boldsymbol{u}^0 &= \bar{\boldsymbol{u}}, \text{ on } \partial_u\Omega, \\ P^0 &= \bar{P}, \text{ on } \partial_P\Omega, \\ \Phi^0_\alpha &= \bar{\Phi}_\alpha, \text{ on } \partial_{\Phi_\alpha}\Omega, \quad \alpha = 1,2. \end{aligned} \tag{3.2.57}$$

Above, all quantities marked by the bar, $\bar{\square}$ are given.

By this process, we introduce different than periodic conditions to the system. However, the weak formulation is fundamental to the application of the finite element method (FEM) and is necessary for numerical modeling (see Chapter 4). We obtain the weak formulation by employing per-partes integration to the (3.2.53)–(3.2.57). This weak form of the macroscopic problem has no limitation of L-periodicity imposed on the boundary conditions.

In this section, we did derive the homogenized macroscopic model describing the steady state of the flux of a symmetric electrolyte in the solid skeleton made of an elastic electric conductor. In the following part of this work, we will deal with the non-steady flux of the same electrolyte but with the solid skeleton that exhibits weak piezoelectric properties. This will essentially serve as an extension of the problem (3.2.53)–(3.2.57).

3.3 Model of ionic transport in piezoelectric porous medium

In this section, we would like to expand the presented model by assuming the piezoelectric solid matrix. As we stated above, we will refer to this type of porous medium by PEPM. The material of the solid skeleton is characterized by an elasticity tensor $\boldsymbol{A} = \{A_{ijkl}\}$, a dielectric tensor $\boldsymbol{d} = \{d_{ij}\}$ and a piezoelectric coupling tensor $\boldsymbol{g} = \{g_{kij}\}$. The homogenization of such material will lead us to the coupled model, which cannot be simplified easily.

To describe the behavior of the PEPM solid matrix, we simply substitute the piezoelectric constitutive equations (2.4.8) into the balance equations (2.4.9). We get the system of equations that describes the processes in the solid phase and complete it by the interface conditions (2.4.10) so that it reads

$$\begin{aligned} -\nabla\cdot\left(\boldsymbol{A}\boldsymbol{e}\left(\boldsymbol{u}\right) - \boldsymbol{g}^T\nabla\Psi_s\right) &= \boldsymbol{f} \quad \text{in } \Omega_s \\ -\nabla\cdot\left(\boldsymbol{g}\boldsymbol{e}\left(\boldsymbol{u}\right) + \boldsymbol{d}\nabla\Psi_s\right) &= q_s \quad \text{in } \Omega_s, \\ \Psi_f &= \Psi_s, \quad \text{on } \Gamma \\ \left(\boldsymbol{g}\boldsymbol{e}\left(\boldsymbol{u}\right) + \boldsymbol{d}\nabla\Psi_s\right)\cdot\boldsymbol{n} &= -\Sigma, \quad \text{on } \Gamma \\ \boldsymbol{\sigma}^p_s\cdot\boldsymbol{n} &= \boldsymbol{\sigma}_f\cdot\boldsymbol{n} \quad \text{on } \Gamma. \end{aligned} \tag{3.3.1}$$

To form the mathematical model of transport of an electrolyte solution through a PEPM, we have to complete the (3.3.1) by the system (2.3.2)–(2.3.8) that describes processes in the fluid phase.

We will consider the quasi-steady state of the problem as described in Remark 2.3.1. This will enable us to extend our model even further. Assuming that there exists a semi-permeable membrane on the interface Γ, the ionic exchange between phases can occur. This is characterized by the change of interface condition on migration-diffusion fluxes (2.3.4), which becomes

$$\boldsymbol{j}_\alpha \cdot \boldsymbol{n} = k^\alpha \frac{\partial c_\alpha}{\partial t} \qquad \text{on } \Gamma, \alpha = 1, 2, \tag{3.3.2}$$

where k_α are coefficients quantifying ionic surface exchanges, see for example (Lemaire et al. 2010a).

As some of the equations remain the same for both types of solid phase, we will only report on the new and changed ones.

3.3.1 Dimensionless problem

We apply the same approach as the one presented in Sec. 3.2.1 to obtain the linearized dimensionless equations describing the behavior of PEPM. The dimensional analysis of (2.3.2)–(2.3.8) remains the same, thus, we provide a procedure to obtain dimensionless and linearized form only of (3.3.1) in the following text.

To obtain a dimensionless form of (3.3.1), we use the same dimensionless choices as in Sec. 3.2.1. In addition, we introduce dimensionless piezoelectric coupling $\boldsymbol{g}'$ and volume electric charge q_s' in the following manner,

$$\boldsymbol{g}' = \boldsymbol{g}/g_c, \qquad {q_s}' = q_s \Sigma_c E_c/(p_c g_c),$$

where a g_c is the characteristic value of piezoelectric coupling. Then, we employ the following dimensionless parameters

$$M_g = \frac{k_B T g_c}{l p_c e},\ M_\Psi = \frac{\epsilon_s k_B T E_c}{g_c l p_c e},\ C_p = \frac{\Sigma_c E_c}{p_c g_c}. \tag{3.3.3}$$

The introduction of these parameters into (3.3.1) leads to derivation of its dimensionless form. To simplify the notation, the superscripts $\sqcup'$ were dropped, for reference see Remark 3.2.1.

Nondimensionalized problem

The equations of dimensionless problem consist of system (3.2.21)-(3.2.22) that is completed by the dimensionless form of (3.3.1) which reads

$$\begin{aligned}
&-\nabla \cdot \left(\boldsymbol{A}\boldsymbol{e}\left(\boldsymbol{u}\right) - \varepsilon M_g \bar{\boldsymbol{g}}^T \nabla \Psi_s^\varepsilon\right) = 0 && \text{in } \Omega_s\\
&-\nabla \cdot \left(\varepsilon \bar{\boldsymbol{g}} \boldsymbol{e}\left(\boldsymbol{u}^\varepsilon\right) + \varepsilon^2 M_\Psi \bar{\boldsymbol{d}} \nabla {\Psi^\varepsilon}_s\right) = C_p \boldsymbol{q} && \text{in } \Omega_s,\\
&\left(\boldsymbol{A}\boldsymbol{e}\left(\boldsymbol{u}\right) - \varepsilon M_g \bar{\boldsymbol{g}}^T \nabla {\Psi^\varepsilon}_s\right) \cdot \boldsymbol{n} = \\
&\quad = \left(-p^\varepsilon \boldsymbol{I} + 2\varepsilon^2 \boldsymbol{e}\left(\boldsymbol{w}\right) + \frac{\varepsilon^2}{\beta}\left(\boldsymbol{E}^\varepsilon \otimes \boldsymbol{E}^\varepsilon - \frac{1}{2}|\boldsymbol{E}^\varepsilon|^2 \boldsymbol{I}\right)\right) \cdot \boldsymbol{n} && \text{on } \Gamma,\\
&\Psi_f^\epsilon = \Psi_s^\epsilon && \text{on } \Gamma,\\
&\left(\bar{\boldsymbol{g}} \boldsymbol{e}\left(\boldsymbol{u}^\varepsilon\right) - \varepsilon M_\Psi \bar{\boldsymbol{d}} \nabla \Psi_s^\varepsilon\right) \cdot \boldsymbol{n} = -C_p \Sigma && \text{on } \Gamma.
\end{aligned} \tag{3.3.4}$$

It is evident from dimensional analysis that the dielectric tensor $\boldsymbol{d} = \{d_{ij}\}$ and the piezoelectric coupling tensor $\boldsymbol{g} = \{g_{kij}\}$ have the following scaling:

$$\left.\begin{aligned} \boldsymbol{g} &= \varepsilon \bar{\boldsymbol{g}},\\ \boldsymbol{d} &= \varepsilon^2 \bar{\boldsymbol{d}}, \end{aligned}\right\} \quad \text{in } \Omega_s. \tag{3.3.5}$$

This scaling is typical for weakly piezoelectric materials and is in agreement with the analysis performed in the paper (Lemaire et al. 2011) and also (Rohan and Lukeš 2018). Let us remind that the introduction of the scaling parameter ε into the system via dimensional analysis is described in Appendix A.

It should be noted that different scaling of these coefficients will naturally result in the different effects of the piezoelectric coupling on the macroscopic behavior. More insight into the homogenization of piezoelectric material with different order of scaling can provide the works (Miara et al. 2005) and (Rohan 2010).

Since we consider a quasi-steady state of the problem, we can treat the model describing ionic transport through PEPM as coupled through the conditions on the solid-fluid interface only. Let us note that the fully time-dependent problem would be more complex. Its treatment would prove difficult because the system of equations would become strongly coupled and the solid-fluid interaction would have to be treated more carefully, see *e.g.* (Mikelić and Wheeler 2012).

3.3.2 Linearization

Using the same approach as in Sec. 3.2.2, we want to linearize the equations describing PEPM in the proximity of equilibrium. Thus, we need to prove the existence of an equilibrium solution for the piezoelectric part of the problem (3.3.4) first.

Solution in equilibrium

From the definition of equilibrium we get the following: There are no imposed external forces $\boldsymbol{f} = 0$, $\boldsymbol{q} = 0$, $\Psi^{\mathrm{ext}} = 0$ and all fluxes are zero $\boldsymbol{j}_\alpha^{\mathrm{eq},\varepsilon} = \boldsymbol{0}, \boldsymbol{j}_\alpha^{\mathrm{eq},\varepsilon} \cdot \boldsymbol{n} = 0$ and $\nabla \log(c_\alpha^{\mathrm{eq},\varepsilon} \exp(z_\alpha \Psi_f^{\mathrm{eq},\varepsilon})) = 0$. Consequently $\boldsymbol{w}^{\mathrm{eq},\varepsilon} = \boldsymbol{0}$ and $\boldsymbol{u}^{\mathrm{eq},\varepsilon} = \boldsymbol{u}^{\mathrm{eq},\varepsilon}(x)$. The process to obtain the equilibrium solution is similar to the one stated in Appendix B.

Basically, we search for a solution of the following problem: find $\boldsymbol{u}^{\mathrm{eq}}$ and Ψ_s^{eq} such that

$$\begin{aligned} -\nabla \cdot \left(\boldsymbol{A}\boldsymbol{e}\left(\boldsymbol{u}^{\mathrm{eq}}\right) - \varepsilon M_g \bar{\boldsymbol{g}}^T \nabla \Psi_s^{\mathrm{eq}}\right) = 0, &\quad \text{in } \Omega_s \\ -\nabla \cdot \left(\varepsilon \bar{\boldsymbol{g}} \boldsymbol{e}\left(\boldsymbol{u}^{\mathrm{eq}}\right) + \varepsilon^2 M_\Psi \bar{\boldsymbol{d}} \nabla \Psi_s^{\mathrm{eq}}\right) = 0 &\quad \text{in } \Omega_s, \\ \left(\boldsymbol{A}\boldsymbol{e}\left(\boldsymbol{u}\right) - \varepsilon M_g \bar{\boldsymbol{g}} \nabla {\Psi^\varepsilon}_s\right) \cdot \boldsymbol{n} = C_p \Sigma &\quad \text{on } \Gamma. \end{aligned} \tag{3.3.6}$$

Following the approach by (Moyne and Murad 2003) we find out that displacement and potential of the solid are of type

$$\boldsymbol{u}^{\mathrm{eq},\varepsilon} = \varepsilon \boldsymbol{u}_\pi^1 \left(\frac{x}{\varepsilon}\right), \quad \Psi_s^{\mathrm{eq},\varepsilon} = \Psi_s^{\mathrm{eq}} \left(\frac{x}{\varepsilon}\right) \quad x \in \Omega_s^\varepsilon, \tag{3.3.7}$$

where both $\boldsymbol{u}_{\pi}^{1}$ and Ψ_s^{eq} are Y-periodic functions defined as a solution to

$$\begin{aligned}
&\nabla_y \cdot (\boldsymbol{A} e_y \left(\boldsymbol{u}_{\pi}^{1}\right) - M_g \bar{\boldsymbol{g}}^T \nabla_y \Psi_s^0) = 0, \quad \text{in } Y_s,\\
&\nabla_y \cdot (\bar{\boldsymbol{g}} e_y \left(\boldsymbol{u}_{\pi}^{1}\right) - M_\Psi \bar{\boldsymbol{d}}^T \nabla_y \Psi_s^0) = 0, \quad \text{in } Y_s\\
&(\bar{\boldsymbol{g}} e_y \left(\boldsymbol{u}_{\pi}^{1}\right) - M_\Psi \bar{\boldsymbol{d}}^T \nabla_y \Psi_s^0) \cdot \boldsymbol{n} = 0, \quad \text{on } \Gamma_Y\\
&(\boldsymbol{A} e_y \left(\boldsymbol{u}_{\pi}^{1}\right) - M_g \bar{\boldsymbol{g}}^T \nabla_y \Psi_s^0) \cdot \boldsymbol{n} =\\
&= \left(-\sum_{\beta=1}^{2} c_\beta^{\mathrm{eq}} \exp - z_\beta \Psi_f^{\mathrm{eq}} \boldsymbol{I} + \gamma^{-1} \left(\nabla_y \Psi_f^{\mathrm{eq}} \otimes \nabla_y \Psi_f^{\mathrm{eq}} - \frac{1}{2} |\nabla_y \Psi_f^{\mathrm{eq}}|^2 \boldsymbol{I}\right)\right) \cdot \boldsymbol{n}, \quad \text{on } \Gamma_Y.
\end{aligned} \tag{3.3.8}$$

Similarly to the equilibrium solution of the Poisson-Boltzmann problem, see Appendix B, the Neumann boundary condition (3.3.6) appears only in the equilibrium solution and we can eliminate it from the problem of perturbations during linearization.

The process of linearization is performed as in section Sec. 3.2.2 by splitting all unknowns into their equilibrium and perturbation parts. In the case of PEPM, we will extend the splits (3.2.11) by

$$\Psi_s^{\varepsilon}(x) = \Psi_s^{\mathrm{eq},\varepsilon}(x) + \Psi_s^{\mathrm{per},\varepsilon}(x),$$

and knowing the equilibrium solutions of (3.2.12), (3.2.17) and (3.3.8), the problem is transformed into a problem of perturbed quantities only. From now on, we will state all the equations of the model for better clarity and readability of the text.

Linearized piezoelectric system The dimensionless linearized problem of perturbed quantities reads: Find $(\boldsymbol{w}^{\mathrm{per},\varepsilon}, P^{\mathrm{per},\varepsilon}, \Phi_\alpha^{\mathrm{per},\varepsilon}, \Psi^{\mathrm{per},\varepsilon}, \Psi_s^{\mathrm{per},\varepsilon}, \boldsymbol{u}^{\mathrm{per},\varepsilon})$, such that following equations hold

$$\begin{aligned}
\varepsilon^2 \Delta \Psi^{\mathrm{per},\varepsilon} + \gamma \sum_{\beta=1}^{2} z_\beta^2 c^{\mathrm{eq},\varepsilon} \Psi^{\mathrm{per},\varepsilon} + \gamma \sum_{\beta=1}^{N} z_\beta^2 c^{\mathrm{eq},\varepsilon} (\Phi_\beta^{\mathrm{per},\varepsilon} + \Psi^{\mathrm{ext}}) &= 0 && \text{in } \Omega_f^{\varepsilon},\\
c_\alpha^{\mathrm{eq},\varepsilon} \partial_t (\Phi_\beta^{\mathrm{per},\varepsilon} + \Psi^{\mathrm{per},\varepsilon}) + \nabla \cdot (\boldsymbol{j}_\alpha^{\mathrm{per},\varepsilon}) + \frac{{P^{\varepsilon}}_{\alpha}}{z_\alpha} \nabla \cdot (\boldsymbol{w}^{\mathrm{per},\varepsilon} c_\alpha^{eq,\varepsilon}) &= 0 && \text{in } \Omega_f^{\varepsilon},\\
\nabla P^{\varepsilon} - \varepsilon^2 \Delta (\boldsymbol{w}^{\mathrm{per},\varepsilon} + U_L \partial_t \boldsymbol{u}^{\mathrm{per},\varepsilon}) - \sum_{\beta=1}^{2} z_\beta c^{\mathrm{eq},\varepsilon} (\nabla \Phi_\beta^{\mathrm{per},\varepsilon} + \nabla \Psi^{\mathrm{ext}}) &= \boldsymbol{f} && \text{in } \Omega_f^{\varepsilon},\\
\nabla \cdot (\boldsymbol{w}^{\mathrm{per},\varepsilon} + U_L \partial_t \boldsymbol{u}^{\mathrm{per},\varepsilon}) &= 0 && \text{in } \Omega_f^{\varepsilon},\\
-\nabla \cdot (\boldsymbol{A} \boldsymbol{e} (\boldsymbol{u}^{\mathrm{per},\varepsilon}) - \varepsilon M_g \bar{\boldsymbol{g}}^T \nabla \Psi_s^{\mathrm{per},\varepsilon}) &= \boldsymbol{f} && \text{in } \Omega_s^{\varepsilon},\\
-\nabla \cdot (\varepsilon \bar{\boldsymbol{g}} \boldsymbol{e} (\boldsymbol{u}^{\mathrm{per},\varepsilon}) + \varepsilon^2 M_\Psi \bar{\boldsymbol{d}} \nabla \Psi_s^{\mathrm{per},\varepsilon}) &= C_p \boldsymbol{q} && \text{in } \Omega_s^{\varepsilon},
\end{aligned} \tag{3.3.9}$$

with the interface conditions being

$$\begin{aligned}
&\varepsilon \nabla (\Psi^{\mathrm{per},\varepsilon}) \cdot \boldsymbol{n} = 0, && \text{on } \Gamma^{\varepsilon},\\
&\boldsymbol{j}_\alpha^{\mathrm{per},\varepsilon} \cdot \boldsymbol{n} = -\varepsilon k_\alpha z_\alpha c_\alpha^{\mathrm{eq},\varepsilon} \partial_t (\Phi_\alpha^{\mathrm{per},\varepsilon} + \Psi^{\mathrm{per},\varepsilon}), && \text{on } \Gamma^{\varepsilon},\\
&(\boldsymbol{A} \boldsymbol{e} (\boldsymbol{u}^{\mathrm{per},\varepsilon}) - \varepsilon M_g \bar{\boldsymbol{g}}^T \nabla \delta \Psi_s^{\mathrm{per},\varepsilon}) \cdot \boldsymbol{n} = \boldsymbol{\sigma}_f^{\varepsilon} \cdot \boldsymbol{n}, && \text{on } \Gamma^{\varepsilon},\\
&(\bar{\boldsymbol{g}} \boldsymbol{e} (\boldsymbol{u}^{\mathrm{per},\varepsilon}) + \varepsilon M_\Psi \bar{\boldsymbol{d}} \nabla \Psi_s^{\mathrm{per},\varepsilon}) \cdot \boldsymbol{n} = 0, && \text{on } \Gamma^{\varepsilon},
\end{aligned} \tag{3.3.10}$$

and $\boldsymbol{u}^{\mathrm{per},\varepsilon}$, $\Psi^{\mathrm{per},\varepsilon}$, $\Phi_\beta^{\mathrm{per},\varepsilon}$ and $\boldsymbol{w}^{\mathrm{per},\varepsilon}$ being Y-periodic. While using global pressure P^ε given by (3.2.20), the linearized stress in fluid $\boldsymbol{\sigma}_f^\varepsilon$ becomes

$$\boldsymbol{\sigma}_f^\varepsilon = -P^\varepsilon \boldsymbol{I} + 2\varepsilon^2 \boldsymbol{e}\left(\boldsymbol{w}^\varepsilon\right) + 2U_L\varepsilon^2 \boldsymbol{e}\left(\partial_t \boldsymbol{u}^{\mathrm{per},\varepsilon}\right) + \sum_{\beta=1}^{2} z_\beta c^{\mathrm{eq},\varepsilon}(\Phi_\beta^{\mathrm{per},\varepsilon} + \Psi^{\mathrm{per},\varepsilon} + \Psi^{\mathrm{ext}})\boldsymbol{I} +$$

$$+ \frac{\varepsilon^2}{\gamma}\left(\nabla\Psi^{\mathrm{eq},\varepsilon} \otimes \nabla\Psi^{\mathrm{per},\varepsilon} + \nabla\Psi^{\mathrm{per},\varepsilon} \otimes \nabla\Psi^{\mathrm{eq},\varepsilon} - \nabla\Psi^{\mathrm{eq},\varepsilon}\cdot\nabla\Psi^{\mathrm{per},\varepsilon}\boldsymbol{I}\right), \quad (3.3.11)$$

and the linearized migration-diffusion fluxes $\boldsymbol{j}_\alpha^{\mathrm{per},\varepsilon}$ read

$$\boldsymbol{j}_\alpha^{\mathrm{per},\varepsilon} = c_\alpha^{\mathrm{eq},\varepsilon}(\nabla\Phi_\alpha^{\mathrm{per},\varepsilon} + \nabla\Psi^{\mathrm{ext}}). \quad (3.3.12)$$

Further, we subject the presented linearized system to the UFM. The following section presents the main steps of this procedure and their results.

3.3.3 Homogenization of piezoelectric porous medium

One of the prerequisites of the UFM is to work with weak forms of equations (3.3.9)–(3.3.12). Remember that the spaces of admissible variables were given in Definition 3.2.1.

We assume that $\boldsymbol{f} \in \mathbf{L}^2(\Omega_f^\varepsilon)$, $\boldsymbol{q} \in \mathbf{L}^2(\Omega_s^\varepsilon)$ and $\boldsymbol{E} \in \mathbb{R}^3$ are given, whereby $\Psi^{\mathrm{ext}} = x \cdot \boldsymbol{E}$. Using standard per-partes integration, (3.3.9)-(3.3.12) are transformed into their weak form given bellow.

Weak formulation Find $(\boldsymbol{w}^{\mathrm{per},\varepsilon}, P^\varepsilon, \Phi_\alpha^{\mathrm{per},\varepsilon}, \Psi^{\mathrm{per},\varepsilon}) \in \mathbf{H}^1_{\#0}(\Omega_f^\varepsilon) \times [H^1_\#(\Omega_f^\varepsilon)]^3$ $\alpha = 1, 2$, and $(\Psi_s^{\mathrm{per},\varepsilon}, \boldsymbol{u}^{\mathrm{per},\varepsilon}) \in \mathbf{H}^1_{\#0}(\Omega_s^\varepsilon) \times [H^1_\#(\Omega_s^\varepsilon)]^3$ such that the following equations hold

$$\begin{aligned}
&\int_{\Omega_s} \left[\boldsymbol{A}\boldsymbol{e}\left(\boldsymbol{u}^{\mathrm{per},\varepsilon}\right) - \varepsilon M_g \bar{\boldsymbol{g}}^T \nabla\Psi_s^{\mathrm{per},\varepsilon}\right] : \boldsymbol{e}\left(\tilde{\boldsymbol{v}}\right) \mathrm{d}V - \int_\Gamma \boldsymbol{\sigma}_s^\varepsilon \cdot \boldsymbol{n}\tilde{\boldsymbol{v}}\,\mathrm{d}S = \int_{\Omega_s} \boldsymbol{f}\cdot\tilde{\boldsymbol{v}}\,\mathrm{d}V,\\
&\int_{\Omega_s} \left[\varepsilon\bar{\boldsymbol{g}}\boldsymbol{e}\left(\boldsymbol{u}^{\mathrm{per},\varepsilon}\right) + \varepsilon^2 M_\Psi \bar{\boldsymbol{d}}\nabla\Psi_s^{\mathrm{per},\varepsilon}\right] \cdot \nabla\tilde{\psi}_s\,\mathrm{d}V = \int_{\Omega_s} C_p \bar{\boldsymbol{q}}\tilde{\psi}_s\,\mathrm{d}V,
\end{aligned} \quad (3.3.13)$$

for all $\tilde{\psi}_s \in H^1_\#(\Omega_s^\varepsilon)$ and $\tilde{\boldsymbol{v}} \in \mathbf{H}^1_\#(\Omega_s^\varepsilon)$,

$$\begin{aligned}
&\int_{\Omega_f^\varepsilon} \tilde{q}\nabla\cdot(\boldsymbol{w}^{\mathrm{per},\varepsilon} + U_L\partial_t\boldsymbol{u}^{\mathrm{per},\varepsilon}) = 0,\\
&\varepsilon^2\int_{\Omega_f^\varepsilon} \nabla(\boldsymbol{w}^{\mathrm{per},\varepsilon} + U_L\partial_t\boldsymbol{u}^{\mathrm{per},\varepsilon}) : \nabla\tilde{\boldsymbol{\vartheta}}\,\mathrm{d}x + \int_{\Omega_f^\varepsilon} P^\varepsilon\nabla\tilde{\boldsymbol{\vartheta}}\,\mathrm{d}x =\\
&\qquad = \int_{\Omega_f^\varepsilon} \tilde{\boldsymbol{\vartheta}}\cdot\boldsymbol{f}\,\mathrm{d}x + \sum_{\beta=1}^{2} z_\beta \int_{\Omega_f^\varepsilon} c_\beta^{\mathrm{eq},\varepsilon}\tilde{\boldsymbol{\vartheta}}\cdot(\nabla\Phi_\beta^{\mathrm{per},\varepsilon} + \boldsymbol{E})\,\mathrm{d}x,
\end{aligned} \quad (3.3.14)$$

for all $\tilde{\boldsymbol{\vartheta}} \in \mathbf{H}^1_{\#0}(\Omega^\varepsilon_f), \tilde{q} \in L^2(\Omega^\varepsilon_f)$,

$$\int\limits_{\Omega^\varepsilon_f} c^{\mathrm{eq},\varepsilon}_\alpha (\partial_t \Psi^{\mathrm{per},\varepsilon} + \partial_t \Phi^{\mathrm{per},\varepsilon}_\alpha) \tilde{\varphi}_\alpha \, \mathrm{d}x - \int\limits_{\Omega^\varepsilon_f} c^{\mathrm{eq},\varepsilon}_\alpha \frac{\mathrm{Pe}_\alpha}{z_\alpha} (\boldsymbol{w}^{\mathrm{per},\varepsilon}) \cdot \nabla \tilde{\varphi}_\alpha \, \mathrm{d}x =$$
$$= \int\limits_{\Omega^\varepsilon_f} c^{\mathrm{eq},\varepsilon}_\alpha (\nabla \Psi^{\mathrm{per},\varepsilon} + \boldsymbol{E}) \nabla \tilde{\varphi}_\alpha \, \mathrm{d}x - \int\limits_{\Gamma^\varepsilon} \varepsilon \tilde{\varphi}_\alpha \boldsymbol{n} \cdot k^\alpha z_\alpha c^{\mathrm{eq},\varepsilon}_\alpha (\partial_t \Psi^{\mathrm{per},\varepsilon} + \partial_t \Phi^{\mathrm{per},\varepsilon}_\alpha), \tag{3.3.15}$$

for $\alpha = 1, 2$ and for all $\tilde{\varphi}_\alpha \in H^1_\#(\Omega^\varepsilon_f)^2$,

$$\varepsilon^2 \int\limits_{\Omega^\varepsilon_f} \nabla \Psi^{\mathrm{per},\varepsilon} \cdot \nabla \tilde{\psi}_f \, \mathrm{d}x + \gamma \int\limits_{\Omega^\varepsilon_f} \left(\sum_{\beta=1}^{2} z^2_\beta c^{\mathrm{eq},\varepsilon}_\beta \right) \Psi^{\mathrm{per},\varepsilon} \tilde{\psi}_f \, \mathrm{d}x =$$
$$= -\gamma \sum_{\beta=1}^{2} z^2_\beta \int\limits_{\Omega^\varepsilon_f} c^{\mathrm{eq},\varepsilon}_\beta \left(\Phi^{\mathrm{per},\varepsilon}_\beta + \Psi^{\mathrm{ext}} \right) \tilde{\psi}_f \, \mathrm{d}x, \tag{3.3.16}$$

for all $\tilde{\psi}_f \in H^1_\#(\Omega^\varepsilon_f)$.

The second term in $(3.3.13)_1$ can be rewritten by using the continuity of stresses and Stokes divergence theorem, becoming

$$\int\limits_{\Gamma} \boldsymbol{\sigma}^\varepsilon_s \cdot \boldsymbol{n} \tilde{\boldsymbol{v}} \, \mathrm{d}S = \int\limits_{\Gamma} \boldsymbol{\sigma}^\varepsilon_f \cdot \boldsymbol{n} \tilde{\boldsymbol{v}} \, \mathrm{d}S = - \int\limits_{\Omega_f} \nabla \cdot (\boldsymbol{\sigma}^\varepsilon_f \tilde{\boldsymbol{v}}) \, \mathrm{d}S = \int\limits_{\Omega_f} \boldsymbol{f} \cdot \tilde{\boldsymbol{v}} \, \mathrm{d}V - \int\limits_{\Omega_f} \boldsymbol{\sigma}^\varepsilon_f : \nabla \tilde{\boldsymbol{v}} \, \mathrm{d}V, \tag{3.3.17}$$

where we substitute $\nabla \cdot (\boldsymbol{\sigma}^\varepsilon_f \tilde{\boldsymbol{v}})$ by (3.2.21) and where the fluid stress $\boldsymbol{\sigma}^\varepsilon_f$ is given by (3.3.11). Next, we deal with the r.h.s. forcing terms that appear in both (3.3.17) and $(3.3.13)_1$ with regards to the fluid and the solid part. Since we consider the boundary conditions to be periodic and continuous stresses at the solid-fluid interface, according to (Allaire et al. 2015), the volume force $\boldsymbol{f}$ must satisfy the compatibility condition

$$\int\limits_{\Omega} \boldsymbol{f} \, \mathrm{d}V = 0.$$

Considering this force compatibility condition and the (3.3.17), the piezoelasticity equation $(3.3.13)_1$ becomes

$$\int\limits_{\Omega_s} [\boldsymbol{A} \boldsymbol{e}(\boldsymbol{u}^{\mathrm{per},\varepsilon}) - \varepsilon M_g \bar{\boldsymbol{g}} \nabla \Psi^{\mathrm{per},\varepsilon}_s] : \boldsymbol{e}(\tilde{\boldsymbol{v}}) \, \mathrm{d}V + \int\limits_{\Omega_f} \boldsymbol{\sigma}^\varepsilon_f : \nabla \tilde{\boldsymbol{v}} \, \mathrm{d}V = \int\limits_{\Omega} \boldsymbol{f} \cdot \tilde{\boldsymbol{v}} \, \mathrm{d}V, \tag{3.3.18}$$

for all test functions $\tilde{\boldsymbol{v}} \in \mathbf{H}^1_\#(\Omega^\varepsilon_s)$

3.3.4 Two-scale problem for piezoelectric medium

The two-scale limit problem can be obtained due to the weak convergences in the unfolded domain $\Omega \times Y$. In our case, we apply the the unfolding operator $\mathcal{T}_\varepsilon$, which is described in Sec. 3.1.2, to obtain the unfolded equations of the problem's weak form. For a more rigorous definition of the unfolding method, we refer to (Cioranescu et al. 2008).

Convergences

The unfolded equations of the weak form given by (3.3.13)–(3.3.16) are obtained using the unfolding operator $\mathcal{T}_\varepsilon$ defined in A, see (Cioranescu et al. 2008). Due to the a priori estimates on the solutions of (3.3.13)–(3.3.16), according to (Allaire et al. 2015), the following convergence result for $\varepsilon \to 0$ and any fixed time $t > 0$ can be proved: There exist limit fields $(\boldsymbol{w}^0, P^0) \in L^2(\Omega; H^1_\#(Y_f)^d) \times L^2(\Omega)$, $\{\Phi^0_\alpha, \Phi^1_\alpha\}_{\alpha=1,2} \in (H^1(\Omega) \times L^2(\Omega; H^1_\#(Y_f)))^2$, $\Psi^0 \in L^2(\Omega; H^1_\#(Y_f))$, $\boldsymbol{u}^0 \in H^1_\#(\Omega^\varepsilon_s)^d$ and $\boldsymbol{u}^1 \in L^2(\Omega; H^1_\#(\Omega^\varepsilon_s)^d)$ such that the following convergences hold

$$
\begin{aligned}
\mathcal{T}_\varepsilon(\boldsymbol{w}^{\mathrm{per},\varepsilon}) &\rightharpoonup \boldsymbol{w}^0 && \text{w. in } L^2(\Omega \times Y_f),\\
\varepsilon\mathcal{T}_\varepsilon(\nabla \boldsymbol{w}^{\mathrm{per},\varepsilon}) &\rightharpoonup \nabla_y \boldsymbol{w}^0 && \text{w. in } L^2(\Omega \times Y_f),\\
\mathcal{T}_\varepsilon(P^\varepsilon) &\to P^0 && \text{s. in } L^2(\Omega),\\
\mathcal{T}_\varepsilon(\nabla P^\varepsilon) &\rightharpoonup \nabla_x P^0 + \nabla_y P^1 && \text{w. in } L^2(\Omega \times Y_f),\\
\mathcal{T}_\varepsilon\Big(\Big\{\Phi^{\mathrm{per},\varepsilon}_\beta\Big\}\Big) &\to \Big\{\Phi^0_\beta\Big\} && \text{s. in } L^2(\Omega),\\
\mathcal{T}_\varepsilon\Big(\Big\{\nabla\Phi^{\mathrm{per},\varepsilon}_\beta\Big\}\Big) &\rightharpoonup \Big\{\nabla_x \Phi^0_\beta + \nabla_y \Phi^1_\beta\Big\} && \text{w. in } L^2(\Omega \times Y_f),\\
\mathcal{T}_\varepsilon(\Psi^{\mathrm{per},\varepsilon}_s) &\rightharpoonup \Psi^0 && \text{w. in } L^2(\Omega \times Y_f),\\
\mathcal{T}_\varepsilon(\varepsilon\nabla\Psi^{\mathrm{per},\varepsilon}) &\rightharpoonup \nabla_y \Psi^0 && \text{w. in } L^2(\Omega \times Y_f),\\
\mathcal{T}_\varepsilon(\boldsymbol{u}^{\mathrm{per},\varepsilon}) &\rightharpoonup \boldsymbol{u}^0 && \text{w. in } L^2(\Omega \times Y_s),\\
\mathcal{T}_\varepsilon(\nabla \boldsymbol{u}^{\mathrm{per},\varepsilon}) &\rightharpoonup \nabla_x \boldsymbol{u}^0 + \nabla_y \boldsymbol{u}^1 && \text{w. in } L^2(\Omega \times Y_s),\\
\mathcal{T}_\varepsilon\Big(\boldsymbol{\sigma}^\varepsilon_f\Big) &\rightharpoonup \boldsymbol{\sigma}^1_f && \text{w. in } L^2(\Omega \times Y_f),
\end{aligned}
\tag{3.3.19}
$$

where $\boldsymbol{\sigma}^1_f$ is given by (3.2.41). As a consequence of the above convergences, shortened asymptotic expansions of the unfolded unknown fields can be introduced, which satisfy the same convergence result. These form the recovery sequences in subdomains Ω^ε_f and Ω^ε_s (see Remark 3.1.2)

$$
\begin{aligned}
\mathcal{T}_\varepsilon\Big(\chi^\varepsilon_f \boldsymbol{w}^{\mathrm{per},\varepsilon}\Big) &\approx \boldsymbol{w}^0(t,x,y), & \mathcal{T}_\varepsilon\Big(\chi^\varepsilon_f P^\varepsilon\Big) &\approx P^0(t,x) + \varepsilon P^1(t,x,y),\\
\mathcal{T}_\varepsilon\Big(\chi^\varepsilon_f \Psi^{\mathrm{per},\varepsilon}_f\Big) &\approx \Psi^0_f(t,x,y), & \mathcal{T}_\varepsilon(\chi^\varepsilon_s \boldsymbol{u}^{\mathrm{per},\varepsilon}) &\approx \boldsymbol{u}^0(t,x) + \varepsilon \boldsymbol{u}^1(t,x,y),\\
\mathcal{T}_\varepsilon(\chi^\varepsilon_s \Psi^{\mathrm{per},\varepsilon}_s) &\approx \Psi^0_s(t,x,y), & \mathcal{T}_\varepsilon\Big(\chi^\varepsilon_f \Phi^{\mathrm{per},\varepsilon}_\alpha\Big) &\approx \Phi^0_\alpha(t,x) + \varepsilon \Phi^1_\alpha(t,x,y), \quad \alpha = 1,2,
\end{aligned}
\tag{3.3.20}
$$

where χ^ε_s and χ^ε_f are characteristic functions of subdomains Ω^ε_f and Ω^ε_s, respectively. Furthermore, $(\boldsymbol{w}^0, P^0, \{\Phi^0_\alpha, \Phi^1_\alpha\})\alpha = 1, 2$, Ψ^0_f, Ψ^0_s and $(\boldsymbol{u}^0, \boldsymbol{u}^1)$ are the unique solutions to the corresponding two-scale limit problems. All these functions depend on time t, however, we only treat the quasi-static problem where the time dependence is not involved significantly, following the approach of (Rohan et al. 2019). Analogous approximations of recovery sequences are considered for the test functions $(\tilde{\boldsymbol{\vartheta}}, \tilde{q}, \tilde{\varphi}_\alpha, \tilde{\psi}_f, \tilde{\psi}_s, \tilde{\boldsymbol{v}})$, which are associated with the unknowns $(\boldsymbol{w}^\varepsilon, P^\varepsilon, \Phi^\varepsilon_\alpha, \Psi^\varepsilon, , \Psi^\varepsilon_s, \boldsymbol{u}^\varepsilon)$.

Equations of the two-scale problem

The equations of the two-scale limit problem are obtained by substituting the recovery sequences (3.3.20) into the weak form of the problem (3.3.13)–(3.3.16), as follows:

Mechanics of solid:

$$\begin{aligned}\fint_{\Omega\times Y_s} \left[\boldsymbol{A}\left(e_x\left(\boldsymbol{u}^0\right)+e_y\left(\boldsymbol{u}^1\right)\right)-M_g\bar{\boldsymbol{g}}\nabla_y\Psi^0_s\right] : \left(e_x\left(\tilde{\boldsymbol{v}}^0\right)+e_y\left(\boldsymbol{v}^1\right)\right) = \\ = -\fint_{\Omega\times Y_f} \boldsymbol{\sigma}^1_f : \left(\nabla_x\tilde{\boldsymbol{v}}^0+\nabla_y\tilde{\boldsymbol{v}}^1\right)+\fint_{\Omega\times Y_s} \boldsymbol{f}\cdot\tilde{\boldsymbol{v}}^0,\end{aligned} \tag{3.3.21}$$

for all $\tilde{\boldsymbol{v}}^0 \in \mathbf{H}^1_{\#}(\Omega^\varepsilon_s)$.

Electricity of the solid:

$$\fint_{\Omega\times Y_s} \bar{\boldsymbol{g}} : \left[e_x\left(\boldsymbol{u}^0\right)+e_y\left(\boldsymbol{u}^1\right)\right]\cdot\nabla_y\tilde{\psi_s}^0+\fint_{\Omega\times Y_s} M_\Psi\nabla_y\Psi^0_s\cdot\nabla_y\tilde{\psi_s}^0=\fint_{\Omega\times Y_s} C_p\boldsymbol{q}\tilde{\psi_s}^0, \tag{3.3.22}$$

for all $\tilde{\psi_s}^0 \in H^1_{\#}(\Omega^\varepsilon_s)$.

Stokes: Find $(\delta\boldsymbol{w}^0, P^0, \{\Phi^0_\beta, \Phi^1_\beta\})$:

$$\begin{aligned}\fint_{\Omega\times Y_f} \nabla_y(\boldsymbol{w}^0) : \nabla_y\tilde{\boldsymbol{\vartheta}}^0+\fint_{\Omega\times Y_f} P^1\nabla_y\tilde{\boldsymbol{\vartheta}}^0 = \\ =\fint_{\Omega\times Y_f} \tilde{\boldsymbol{\vartheta}}^0\cdot(\boldsymbol{f}+\nabla_x P^0)+\sum_{\beta=1}^{N=2} z_\beta\fint_{\Omega\times Y_f} c^{\mathrm{eq}}_\beta\left[\tilde{\boldsymbol{\vartheta}}^0\left(\nabla_x\Phi^0_\beta+\nabla_y\Phi^1_\beta+\boldsymbol{E}\right)\right],\end{aligned} \tag{3.3.23}$$

$$\fint_{\Omega\times Y_f} \tilde{q}^0\nabla_y\cdot(\boldsymbol{w}^0+U_L\partial_t\boldsymbol{u}^0)=0, \tag{3.3.24}$$

for all $\tilde{\boldsymbol{\vartheta}}^0 \in \mathbf{H}^1_{\#0}(\Omega^\varepsilon_f)$ and $\tilde{q}^0 \in L^2(\Omega^\varepsilon_f)$.

Ionic transport:

$$\begin{aligned}\fint_{\Omega\times Y_f} c^{\mathrm{eq}}_\alpha(\partial_t\Psi^0+\partial_t\Phi^0)\tilde{\varphi}^0_\alpha-\fint_{\Omega\times Y_f} c^{\mathrm{eq}}_\alpha(\nabla_x\Phi^0_\alpha+\nabla_y\Phi^1_\alpha+\boldsymbol{E})\cdot(\nabla_x\tilde{\varphi}^0_\alpha+\nabla_x\tilde{\varphi}^1_\alpha)+ \\ +\fint_{\Omega\times Y_f} c^{\mathrm{eq}}_\alpha\frac{\mathrm{Pe}_\alpha}{z_\alpha}\left[(\nabla_x\tilde{\varphi}^0_\alpha+\nabla_y\tilde{\varphi}^1_\alpha)\cdot\boldsymbol{w}^0\right]=0.\end{aligned} \tag{3.3.25}$$

for all $\tilde{\varphi}^0_\alpha \in H^1_{\#}(\Omega^\varepsilon_f)$.

Poisson-Boltzmann: Find $\delta\Psi^0(x,y)$:

$$\fint_{\Omega\times Y_f} \nabla_y\Psi^0\nabla_y\tilde{\psi_f}^0+\gamma\fint_{\Omega\times Y_f}\left(\sum_{\beta=1}^{N=2} z^2_\beta c^{\mathrm{eq}}_\beta\right)\Psi^0\tilde{\psi_f}^0=-\gamma\sum_{\beta=1}^{N=2} z^2_\beta\fint_{\Omega\times Y_f} c^{\mathrm{eq}}_\beta(\Phi^0_\beta+\Psi^{\mathrm{ext}})\tilde{\psi_f}^0, \tag{3.3.26}$$

for all $\tilde{\psi_f}^0 \in H^1_{\#}(\Omega^\varepsilon_f)$.

To separate the fast and the slow variables, we introduce the so-called scale-separation formulae, which allow us to establish local problems for characteristic responses. Therefore, scale decomposition formulae of the limits $\boldsymbol{w}^0, P^1, \Phi^1_\alpha, \alpha =$

$1,2$, are introduced as

$$\begin{aligned} \boldsymbol{w}^0(x,y,t) &= \sum_{\beta=1}^{2} \boldsymbol{\omega}^{\beta,k}(y)\left(\frac{\partial \Phi^0_\beta}{\partial x_k} + E_k\right)(x) + \boldsymbol{\omega}^{P,k}(y)\left(f_k - \frac{\partial P^0}{\partial x_k}\right)(x), \\ \Phi^1_\alpha(x,y,t) &= \sum_{\beta=1}^{2} \theta^{\beta,k}(y)\left(\frac{\partial \Phi^0_\beta}{\partial x_k} + E_k\right)(x) + \theta^{P,k}(y)\left(f_k - \frac{\partial P^0}{\partial x_k}\right)(x), \\ P^1(x,y,t) &= \sum_{\beta=1}^{2} \pi^{\beta,k}(y)\left(\frac{\partial \Phi^0_\beta}{\partial x_k} + E_k\right)(x) + \pi^{P,k}(y)\left(f_k - \frac{\partial P^0}{\partial x_k}\right)(x), \end{aligned} \tag{3.3.27}$$

where two families of corrector base functions $(\boldsymbol{\omega}^{P,k}, \pi^{P,k}, \theta^{P,k}_\beta)$, $(\boldsymbol{\omega}^{\alpha,k}, \pi^{\alpha,k}, \theta^{\alpha,k}_\beta)$, $\alpha = 1,2$, were introduced, indexed by $k \in \{1,\ldots,d\}$, where d is spatial dimension of the problem. The standard Einstein summation convention holds.

Similarly, the scale decomposition formulae of the limits Ψ^0_f, Ψ^0_s and $\boldsymbol{u}^1$ read

$$\begin{aligned} \Psi^0_f(t,x,y) &= \sum_{\beta=1}^{2} \varpi^\beta(y)\left(\Phi^0_\beta(x) + \Psi^{\text{ext}}(x)\right), \\ \Psi^0_s(t,x,y) &= \eta^{ij}(y)e_{ij}\left(\boldsymbol{u}^0(x)\right) - P^0(x)\eta^P(y) + \sum_{\beta=1}^{2} \eta^\beta(y) z_\beta \left(\Phi^0_\beta(x) + \Psi^{\text{ext}}(x)\right), \\ \boldsymbol{u}^1(t,x,y) &= \boldsymbol{w}^{ij}(y)e_{ij}\left(\boldsymbol{u}^0(x)\right) - P^0(x)\boldsymbol{w}^P(y) + \sum_{\beta=1}^{2} \boldsymbol{w}^\beta(y) z_\beta \left(\Phi^0_\beta(x) + \Psi^{\text{ext}}(x)\right), \end{aligned} \tag{3.3.28}$$

where $\varpi^\beta, \boldsymbol{w}^{ij}, \boldsymbol{w}^P, \boldsymbol{w}^\alpha, \eta^{ij}, \eta^P, \eta^\alpha, \alpha = 1,2$, are corrector base functions that are obtained as the solutions of the local cell problems introduced below.

3.3.5 Local problems

The local problems, which are relevant to the microscopic scale, can be derived from the limit problems (3.3.21)-(3.3.26) given above, usually by letting to vanish all the components of the test functions that are not relevant to the microscopic scale. This results in three groups of local problems that are listed below. The first two groups correspond to their counterparts that we gave in the previous section, *i.e.* the local problems (3.2.44)–(3.2.45). Still, we will list them below for the sake of completeness.

The first group of local problems consists of the two autonomous problems solved on the cell Y. The local problem that gives the response to the macroscopic pressure gradient reads: Find $(\boldsymbol{\omega}^{P,k}, \pi^{P,k}, \theta^{P,k}_\alpha) \in \mathbf{H}^1_{\#0}(Y_f)$, $k = 1,2,3,\ \alpha = 1,2$:

$$\begin{aligned} \fint_{Y_f} \nabla_y \boldsymbol{\omega}^{P,k}(y) : \nabla_y \tilde{\boldsymbol{\vartheta}}\, \mathrm{d}V + \fint_{Y_f} \pi^{P,k}(y) \nabla_y \cdot \tilde{\boldsymbol{\vartheta}}\, \mathrm{d}V &= \fint_{Y_f} \tilde{\vartheta}^k + \sum_{\beta=1}^{2} \fint_{Y_f} z_\beta c^{\text{eq}}_\beta(y) \tilde{\boldsymbol{\vartheta}} \nabla_y \theta^{P,k}_\beta\, \mathrm{d}V, \\ \fint_{Y_f} \tilde{q} \nabla_y \cdot \boldsymbol{\omega}^{P,k}(y)\, \mathrm{d}V &= 0, \end{aligned} \tag{3.3.29}$$

$$\fint_{Y_f} c^{\text{eq}}_\alpha(y) \nabla \theta^{P,k}_\alpha \nabla_y \tilde{\varphi}_\alpha\, \mathrm{d}V + \fint_{Y_f} c^{\text{eq}}_\alpha(y) \mathrm{Pe}_\alpha z_\alpha^{-1} \tilde{\varphi}_\alpha \nabla \cdot \boldsymbol{\omega}^{P,k}(y)\, \mathrm{d}V = 0,$$

for any test functions $\tilde{\boldsymbol{\vartheta}} \in \mathbf{H}^1_{\#0}(Y_f)$, $\tilde{q} \in L^2(Y_f)$, $\tilde{\varphi}_\alpha \in H^1_{\#}(Y_f)^2$.

The weak form of the second autonomous cell problem that returns the response to the macroscopic diffusive flux reads: Find $(\boldsymbol{\omega}^{\alpha,k}, \pi^{\alpha,k}, \theta^{\alpha,k}_\beta) \in \mathbf{H}^1_{\#0}(Y_f)$, $k = 1,2,3,\ \alpha = 1,2,\ \beta = 1,2$:

$$\fint_{Y_f} \nabla_y \boldsymbol{\omega}^{\alpha,k}(y) : \nabla_y \tilde{\boldsymbol{\vartheta}}\,\mathrm{d}V + \fint_{Y_f} \pi^{\alpha,k}(y) \nabla_y \cdot \tilde{\boldsymbol{\vartheta}}\,\mathrm{d}V = \sum_{\beta=1}^{2} \fint_{Y_f} z_\beta c^{\mathrm{eq}}_\beta(y) \tilde{\boldsymbol{\vartheta}} (\delta_{\alpha\beta} \boldsymbol{e}^k + \nabla_y \theta^{\alpha,k}_\beta)\,\mathrm{d}V,$$

$$\fint_{Y_f} \tilde{q} \nabla_y \cdot \boldsymbol{\omega}^{\alpha,k}(y)\,\mathrm{d}V = 0, \tag{3.3.30}$$

$$\fint_{Y_f} c^{\mathrm{eq}}_\beta(y)(\delta_{\alpha\beta}\boldsymbol{e}^k + \nabla\theta^{\alpha,k}_\beta)\nabla_y \tilde{\varphi}_\beta\,\mathrm{d}V + \fint_{Y_f} c^{\mathrm{eq}}_\beta(y)\mathrm{Pe}_\beta z_\beta^{-1} \tilde{\varphi}_\beta \nabla \cdot \boldsymbol{\omega}^{\alpha,k}(y)\,\mathrm{d}V = 0,$$

for any test functions $\tilde{\boldsymbol{\vartheta}} \in \mathbf{H}^1_{\#0}(Y_f)$, $\tilde{q} \in L^2(Y_f)$, $\tilde{\varphi}_\beta \in H^1_{\#}(Y_f)^2$.

The second group consists of two auxiliary cell problems for $\alpha = 1,2$ that relate to perturbation of potential. They read: Find the corrector base functions $\varpi^\alpha \in H^1_{\#}(Y_f), \alpha = 1,2$, such that

$$\fint_{Y_f} \nabla\varpi^\alpha \cdot \nabla\tilde{\psi}_f\,\mathrm{d}V + \gamma \fint_{Y_f} \sum_{\beta=1}^{2} \left(z^2_\beta c^{\mathrm{eq}}_\beta(y)\right) \varpi^\alpha \tilde{\psi}_f\,\mathrm{d}V = -\fint_{Y_f} \gamma z^2_\alpha c^{\mathrm{eq}}_\alpha(y) \tilde{\psi}_f\,\mathrm{d}V, \tag{3.3.31}$$

for any test functions $\tilde{\psi}_f \in H^1_{\#}(Y_f)$.

The third group of local problems differs from its counterpart from Sec. 3.2.6, which describes the local responses in LEPM. That is to be expected as in the case of PEPM, this group is related to the response to the deformation and the change in charge of the solid phase. For the sake of brevity, we employ the following bilinear forms

$$\begin{aligned}
a_{Y_s}(\boldsymbol{\omega},\, \boldsymbol{\varphi}) &= \fint_{Y_s} \boldsymbol{A} e_y(\boldsymbol{\omega}) : e_y(\boldsymbol{\varphi})\,\mathrm{d}V,\\
g_{Y_s}(\boldsymbol{\omega},\, \varphi) &= \fint_{Y_s} [\boldsymbol{g} : e_y(\boldsymbol{\omega})] \cdot \nabla_y \phi\,\mathrm{d}V,\\
g^*_{Y_s}(\boldsymbol{\omega},\, \varphi) &= \fint_{Y_s} M_g \boldsymbol{g}^T \nabla_y \varphi : e_y(\boldsymbol{\omega})\,\mathrm{d}V,\\
d_{Y_s}(\psi,\, \varphi) &= \fint_{Y_s} M_\Psi \nabla_y \psi \cdot \nabla_y \varphi\,\mathrm{d}V,
\end{aligned} \tag{3.3.32}$$

Finally, we introduce the three local problems that constitute the third group. They read as follows:

- Find $\boldsymbol{w}^{ij} \in \mathbf{H}^1_{\#}(Y_s), \fint_{Y_s} \boldsymbol{w}^{ij}\,\mathrm{d}V = 0, \eta^{ij} \in H^1_{\#}(\Omega^\varepsilon_s)$ such that

  $$\begin{aligned}
  a_{Y_s}\left(\boldsymbol{w}^{ij} + \boldsymbol{\Pi}^{ij},\, \tilde{\boldsymbol{v}}\right) - g^*_{Y_s}\left(\tilde{\boldsymbol{v}},\, \eta^{ij}\right) &= 0\\
  g_{Y_s}\left(\boldsymbol{w}^{ij} + \boldsymbol{\Pi}^{ij},\, \tilde{\psi}_s\right) + d_{Y_s}\left(\eta^{ij},\, \tilde{\psi}_s\right) &= 0,
  \end{aligned} \tag{3.3.33}$$

  for any test functions $\tilde{\boldsymbol{v}} \in \mathbf{H}^1_{\#}(Y_s)$ and $\tilde{\psi}_s \in H^1_{\#}(\Omega^\varepsilon_s)$. Recall that the symbol $\boldsymbol{\Pi}^{ij}$ denotes the so-called transformation vectors $\boldsymbol{\Pi}^{ij} = (\Pi^{ij}_k), i,j,k = 1,\ldots,d$, which can transform the macroscopic deformation $\boldsymbol{u}_0(x)$ from Ω into the coordinate system of RVE Y, so that $\Pi^{ij}_k = y_j\delta_{ik}$.

- Find $\boldsymbol{w}^P \in \mathbf{H}^1_\#(Y_s), \fint_{Y_s} \boldsymbol{w}^P \,\mathrm{d}V = 0, \eta^P \in H^1_\#(\Omega^\varepsilon_s)$ such that

$$
\begin{aligned}
a_{Y_s}\left(\boldsymbol{w}^P,\, \tilde{\boldsymbol{v}}\right) - g^*_{Y_s}\left(\tilde{\boldsymbol{v}},\, \eta^P\right) &= -\fint_{\Gamma_Y} \tilde{\boldsymbol{v}} \cdot \boldsymbol{n} \,\mathrm{dS}_y, \\
g_{Y_s}\left(\boldsymbol{w}^P,\, \tilde{\psi}_s\right) + d_{Y_s}\left(\eta^P,\, \tilde{\psi}_s\right) &= 0,
\end{aligned}
\tag{3.3.34}
$$

for any test functions $\tilde{\boldsymbol{v}} \in \mathbf{H}^1_\#(Y_s)$ and $\tilde{\psi}_s \in H^1_\#(\Omega^\varepsilon_s)$.

- Find $\boldsymbol{w}^\alpha \in \mathbf{H}^1_\#(Y_s), \fint_{Y_s} \boldsymbol{w}^\alpha \,\mathrm{d}V = 0, \eta^\alpha \in H^1_\#(\Omega^\varepsilon_s)$ such that

$$
\begin{aligned}
& a_{Y_s}\left(\boldsymbol{w}^\alpha,\, \tilde{\boldsymbol{v}}\right) - g^*_{Y_s}\left(\tilde{\boldsymbol{v}},\, \eta^\alpha\right) = -\sum_{\beta=1}^{2} \fint_{\Gamma_Y} \tilde{\boldsymbol{v}} \cdot \left(z_\beta c^{\mathrm{eq}}_\beta \left(\delta_{\alpha\beta} + \varpi^\alpha\right) \boldsymbol{I}\right) \cdot \boldsymbol{n} \,\mathrm{dS}_y - \\
& - \fint_{\Gamma_Y} \tilde{\boldsymbol{v}} \cdot \left(\frac{1}{\gamma}\left(\nabla_y \Psi^{\mathrm{eq}} \otimes \nabla_y \varpi^\alpha + \nabla_y \varpi^\alpha \otimes \nabla_y \Psi^{\mathrm{eq}} - \nabla_y \Psi^{\mathrm{eq}} \cdot \nabla_y \varpi^\alpha \boldsymbol{I}\right)\right) \cdot \boldsymbol{n} \,\mathrm{dS}_y, \\
& g_{Y_s}\left(\boldsymbol{w}^\alpha,\, \tilde{\psi}_s\right) + d_{Y_s}\left(\eta^\alpha,\, \tilde{\psi}_s\right) = 0,
\end{aligned}
\tag{3.3.35}
$$

for any test functions $\tilde{\boldsymbol{v}} \in \mathbf{H}^1_\#(Y_s)$ and $\tilde{\psi}_s \in H^1_\#(\Omega^\varepsilon_s)$.

It is apparent that the cell problems corresponding to the electrokinetic system can be treated separately, while the cell problems related to poroelasticity are coupled through the r.h.s. of (3.3.35) with the solutions $\varpi^\alpha, \alpha = 1, 2$, of the auxiliary cell problems (3.3.31).

3.3.6 Homogenized coefficients

Below, we list expressions of homogenized coefficients which arise from the upscaling of (3.3.13)–(3.3.16). These coefficients constitute the effective material parameters of the upscaled porous medium and are expressed in terms of the corrector basis functions. We may distinguish two groups of coefficients according to which corrector functions they are related to.

The first group of the corrector functions defines the following homogenized coefficients

$$
\begin{aligned}
\mathcal{J}^\alpha_{lk} &= \fint_{Y_f} \boldsymbol{\omega}^{\alpha,k}(y) \cdot \mathbf{e}^l \,\mathrm{d}V, \\
\mathcal{K}_{lk} &= \fint_{Y_f} \boldsymbol{\omega}^{P,k}(y) \cdot \mathbf{e}^l \,\mathrm{d}V, \\
\mathcal{D}^{\alpha\beta}_{lk} &= \fint_{Y_f} c^{\mathrm{eq}}_\beta(y) \left(\frac{\mathrm{Pe}_\beta}{z_\beta} \boldsymbol{\omega}^{\alpha,k}(y) + \left(\mathbf{e}^k \delta_{\alpha\beta} + \nabla_y \theta^{\alpha,k}_\beta(y)\right)\right) \cdot \mathbf{e}^l \,\mathrm{d}V, \\
\mathcal{L}^\alpha_{lk} &= \fint_{Y_f} c^{\mathrm{eq}}_\alpha(y) \left(\frac{\mathrm{Pe}_\alpha}{z_\alpha} \boldsymbol{\omega}^{P,k}(y) + \nabla_y \theta^{P,k}_\alpha(y)\right) \cdot \mathbf{e}^l \,\mathrm{d}V,
\end{aligned}
\tag{3.3.36}
$$

which are idential to the ones describing the model of ionic transport through LEPM, see (3.2.50). There are the permeability tensor $\boldsymbol{\mathcal{K}} = (\mathcal{K}_{lk})$, the diffusivity tensors $\boldsymbol{\mathcal{D}}^{\alpha\beta} = (\mathcal{D}^{\alpha\beta}_{lk})$, the tensors $\boldsymbol{\mathcal{J}}^{\alpha} = (\mathcal{J}^{\alpha}_{lk})$ related to the flow driven by electric fields and coupling tensors $\boldsymbol{\mathcal{L}}^{\alpha} = (\mathcal{L}^{\alpha}_{lk})$.

In comparison with the coefficients of the steady-state model of ionic transport through LEPM, see (3.2.50), four new effective coefficients arise,

$$\begin{aligned}
\boldsymbol{\mathcal{Q}}^{\alpha\beta} &= \fint_{Y_f} c^{\text{eq}}_{\alpha}(y)(\varpi^{\beta}(y) + \delta_{\alpha\beta})\,\mathrm{d}V \\
\hat{\boldsymbol{\mathcal{Q}}}^{\alpha\beta} &= \fint_{Y_f} c^{\text{eq}}_{\alpha}(y)\varpi^{\beta}(y)\,\mathrm{d}V \\
\boldsymbol{\mathcal{S}}^{\alpha\beta} &= \fint_{Y_\Gamma} -z_\alpha c^{\text{eq}}_{\alpha}(y)\hat{k}_\alpha(\varpi^{\beta}(y) + \delta_{\alpha\beta}) \cdot \boldsymbol{n}\,\mathrm{dS}_y \\
\hat{\boldsymbol{\mathcal{S}}}^{\alpha\beta} &= \fint_{Y_\Gamma} -z_\alpha c^{\text{eq}}_{\alpha}(y)\hat{k}_\alpha\varpi^{\beta}(y) \cdot \boldsymbol{n}\,\mathrm{dS}_y,
\end{aligned} \tag{3.3.37}$$

which are connected to the terms including time derivatives ∂_t and serve to couple the electrokinetics, ionic transport and mechanics. The coefficients $\boldsymbol{\mathcal{S}}^{\alpha\beta}$ bring ionic exchanges up to the macroscopic scale. It can be shown that these coefficients meet Onsager's reciprocity conditions, (Allaire et al. 2010).

The second group is relevant to the piezoelectric behavior of the macroscopic body and consists of the following coefficients,

$$\begin{aligned}
\mathcal{A}_{ijkl} &= a_{Y_s}\left(\boldsymbol{w}^{ij} + \boldsymbol{\Pi}^{ij},\, \boldsymbol{w}^{kl} + \boldsymbol{\Pi}^{kl}\right) + d_{Y_s}\left(\eta^{ij},\, \eta^{kl}\right) = \\
&= a_{Y_s}\left(\boldsymbol{w}^{kl} + \boldsymbol{\Pi}^{kl},\, \boldsymbol{\Pi}^{ij}\right) - g^{*}_{Y_s}\left(\boldsymbol{\Pi}^{ij},\, \eta^{kl}\right), \\
\mathcal{B}_{ij} &= \phi_f\delta_{ij} + a_{Y_s}\left(\boldsymbol{w}^{P},\, \boldsymbol{\Pi}^{ij}\right) - g^{*}_{Y_s}\left(\boldsymbol{\Pi}^{ij},\, \eta^{P}\right), \\
\mathcal{C}^{\alpha}_{ij} &= a_{Y_s}\left(\boldsymbol{w}^{\alpha},\, \boldsymbol{\Pi}^{ij}\right) - g^{*}_{Y_s}\left(\boldsymbol{\Pi}^{ij},\, \eta^{\alpha}\right) + \sum_{\beta=1}^{2} z_\beta \boldsymbol{I} \fint_{Y_f} c^{0}_{\beta}(y)\left(\varpi^{\alpha}(y) + \delta_{\alpha\beta}\right)\mathrm{d}V + \\
&\quad + \fint_{Y_f} \gamma^{-1}\left(\nabla_y\Psi^{\text{eq}} \otimes \nabla_y\varpi^{\alpha} + \nabla_y\varpi^{\alpha} \otimes \nabla_y\Psi^{\text{eq}} - \nabla_y\Psi^{\text{eq}} \cdot \nabla_y\varpi^{\alpha}\boldsymbol{I}\right)\mathrm{d}V, \\
\mathcal{M} &= \fint_{Y_\Gamma} \boldsymbol{w}^{P}(y) \cdot \boldsymbol{n}\,\mathrm{dS}_y = a_{Y_s}\left(\boldsymbol{w}^{P},\, \boldsymbol{w}^{P}\right) + d_{Y_s}\left(\eta^{P},\, \eta^{P}\right), \\
\mathcal{N}^{\alpha} &= \fint_{Y_\Gamma} \boldsymbol{w}^{\alpha}(y) \cdot \boldsymbol{n}\,\mathrm{dS}_y,
\end{aligned} \tag{3.3.38}$$

where $\boldsymbol{\mathcal{A}} = (\mathcal{A}_{ijkl})$ the fourth-order symmetric positive definite effective tensor of a piezoelectric drained skeleton, $\boldsymbol{\mathcal{B}} = (\mathcal{B}_{ij})$ is the coupling tensor related to the pressure. These effective coefficients are similar to the Biot poroelasticity coefficients, however, they are extended by the piezoelectric term.

The coefficient $\boldsymbol{\mathcal{C}}^{\alpha} = (\mathcal{C}^{\alpha}_{ij})$ is the tensor responsible for the coupling between the electrokinetic and poropiezoelectric system.

The two sets of effective coefficients that are defined by (3.3.36)–(3.3.38) characterize macroscopic behavior of the PEPM saturated by an electrolyte solution and occur in the definition of the macroscopic homogenized problem.

3.3.7 Macroscopic model

The homogenized model describing macroscopic behavior is derived from the two-scale limit problems (3.3.21)-(3.3.26) by letting to vanish all the components of the test functions that are not relevant to the macroscopic scale. We present the macroscopic model in its nondimensional form: Find $P^0 \in L^2(\Omega), \boldsymbol{u}^0 \in \mathbf{H}^1_{\#0}(\Omega)$ and $\Phi^0_\alpha \in H^1_\#(\Omega), \alpha = 1, 2$, such that

$$\begin{aligned}
&\int_\Omega \boldsymbol{\mathcal{K}}(\boldsymbol{f} - \nabla_x P^0)\nabla_x q \,\mathrm{d}V + \int_\Omega \mathcal{M}\partial_t P^0 q \,\mathrm{d}V - \int_\Omega q\boldsymbol{\mathcal{B}} : e_x\left(\partial_t \boldsymbol{u}^0\right) + \\
&\quad + \sum_{\beta=1}^{2} \left[\int_\Omega \boldsymbol{\mathcal{J}}^\beta(\nabla_x \Phi^{\mathrm{eff}}_\beta + \boldsymbol{E})\nabla_x q \,\mathrm{d}V - \int_\Omega \mathcal{N}^\beta(\partial_t \Phi^0_\beta - \partial_t \Psi^{\mathrm{ext},*}) q \,\mathrm{d}V\right] = 0 \\
&\sum_{\beta=1}^{2} \left[\int_\Omega (\boldsymbol{\mathcal{Q}}^{\alpha\beta} + \boldsymbol{\mathcal{S}}^{\alpha\beta})\partial_t \Phi^0_\beta \varphi \,\mathrm{d}V + \int_\Omega (\hat{\boldsymbol{\mathcal{Q}}}^{\alpha\beta} + \hat{\boldsymbol{\mathcal{S}}}^{\alpha\beta})\partial_t \Psi^{\mathrm{ext},*} \varphi \,\mathrm{d}V\right] + \\
&\quad + \int_\Omega \boldsymbol{\mathcal{L}}^\alpha(\boldsymbol{f} - \nabla_x P^0)\nabla_x \varphi \,\mathrm{d}V + \sum_{\beta=1}^{2} \int_\Omega \boldsymbol{\mathcal{D}}^{\alpha\beta}(\nabla_x \Phi^0_\beta + \boldsymbol{E})\nabla_x \varphi = 0, \\
&\int_\Omega \left[\boldsymbol{\mathcal{A}} e_x\left(\boldsymbol{u}^0\right) - \boldsymbol{\mathcal{B}} P^0\right] : e_x\left(\boldsymbol{v}\right) \mathrm{d}V + \sum_{\beta=1}^{2} \int_\Omega \boldsymbol{\mathcal{C}}^\alpha(\Phi^0_\beta + \Psi^{\mathrm{ext},*}) : e_x\left(\boldsymbol{v}\right) \mathrm{d}V = \\
&\quad = \int_\Omega \boldsymbol{f} \cdot \boldsymbol{v} \,\mathrm{d}V,
\end{aligned} \tag{3.3.39}$$

for all $\varphi \in H^1_\#(\Omega), q \in L^2(\Omega), \boldsymbol{v} \in \mathbf{H}^1_{\#0}(\Omega)$ with L-periodic boundary conditions.

Once again, we don't want to limit ourself to L-periodic problems only. Following the approach proposed in the Remark 3.2.2, we introduce the macroscopic homogenized model in its differential form, which reads: Find $P^0, \boldsymbol{u}^0$ and $\Phi^0_\alpha, \alpha = 1, 2$, such that

$$\begin{aligned}
&\nabla_x \cdot \left[\boldsymbol{\mathcal{K}}(\boldsymbol{f} - \nabla_x P^0) + \sum_{\beta=1}^{2} \boldsymbol{\mathcal{J}}^\beta(\nabla_x \Phi^0_\beta + \boldsymbol{E})\right] + \\
&\qquad + \mathcal{M}\partial_t P^0 - \boldsymbol{\mathcal{B}} : e_x\left(\partial_t \boldsymbol{u}^0\right) - \mathcal{N}^\beta(\partial_t \Phi^0_\beta - \partial_t \Psi^{\mathrm{ext}}) = 0 \\
&\sum_{\beta=1}^{2} \left[(\boldsymbol{\mathcal{Q}}^{\alpha\beta} + \boldsymbol{\mathcal{S}}^{\alpha\beta})\partial_t \Phi^0_\beta + (\hat{\boldsymbol{\mathcal{Q}}}^{\alpha\beta} + \hat{\boldsymbol{\mathcal{S}}}^{\alpha\beta})\partial_t \Psi^{\mathrm{ext}}\right] + \\
&\quad + \nabla_x \cdot \left[\boldsymbol{\mathcal{L}}^\alpha(\boldsymbol{f} - \nabla_x P^0) + \sum_{\beta=1}^{2} \boldsymbol{\mathcal{D}}^{\alpha\beta}(\nabla_x \Phi^0_\beta + \boldsymbol{E})\right] = 0, \\
&\quad - \nabla_x \cdot \boldsymbol{\mathcal{A}} e_x\left(\boldsymbol{u}^0\right) + \nabla_x \cdot \left[\boldsymbol{\mathcal{B}} P^0 - \sum_{\beta=1}^{2} \boldsymbol{\mathcal{C}}^\alpha(\Phi^0_\beta + \Psi^{\mathrm{ext},*})\right] = \boldsymbol{f},
\end{aligned} \tag{3.3.40}$$

for $\alpha = 1, 2$ and completed by boundary conditions given below. We can distinguish the fluid seepage velocity $\boldsymbol{w}^0$, the ionic diffusion fluxes $\boldsymbol{j}^0_\alpha, \alpha = 1, 2$, and the porous body stress $\boldsymbol{\sigma}^0$,

$$\begin{aligned}
\boldsymbol{w}^0 &= \sum_{\beta=1}^{2} \boldsymbol{\mathcal{J}}_\beta(\nabla_x \Phi_\beta^0 + \mathbf{E}) - \boldsymbol{\mathcal{K}}(\nabla_x P^0 - \boldsymbol{f}) \quad \text{in } \Omega, \\
\boldsymbol{\sigma}^0 &= \boldsymbol{\mathcal{A}} e_x(\boldsymbol{u}^0) - P^0 \hat{\boldsymbol{\mathcal{B}}} + \sum_{\beta}^{2} \boldsymbol{\mathcal{C}}^\beta(\Phi_\beta^0 + \Psi^{\text{ext}}) \quad \text{in } \Omega, \\
\boldsymbol{j}_\alpha^0 &= \sum_{\beta=1}^{2} \boldsymbol{\mathcal{D}}_{\alpha\beta}\left(\nabla_x \Phi_\beta^0 + \mathbf{E}\right) - \boldsymbol{\mathcal{L}}_\alpha(\nabla_x P^0 - \boldsymbol{f}) \quad \text{in } \Omega \quad \alpha = 1, 2.
\end{aligned} \tag{3.3.41}$$

The total velocity $\boldsymbol{w}^0$ can be split into three components; pressure driven velocity $\boldsymbol{w}_p$ and potential driven velocity $\boldsymbol{w}_{\Phi_\alpha}, \alpha = 1, 2$, such that

$$\begin{aligned}
\boldsymbol{w}_p &= \mathcal{K}(\nabla_x P^{\text{eff}} - \boldsymbol{f}) \quad \text{in } \Omega, \\
\boldsymbol{w}_{\Phi_\alpha} &= \boldsymbol{\mathcal{J}}^\alpha(\nabla_x \Phi_\alpha^0 + \mathbf{E}), \alpha = 1, 2 \quad \text{in } \Omega.
\end{aligned} \tag{3.3.42}$$

The system (3.3.40) needs to be completed by a suitable set of boundary conditions. For any variable a we may impose the Dirichlet type condition on boundary $\partial_a \Omega$ and the Neumann type condition on boundary $\partial_a^N \Omega = \partial\Omega \backslash \partial_a \Omega$. the Neumann type condition on boundary $\partial_a^N \Omega$ read

$$\begin{aligned}
\boldsymbol{n} \cdot \boldsymbol{\sigma}^0 &= \bar{\boldsymbol{g}}, \text{ on } \partial_u^N \Omega, \\
\boldsymbol{n} \cdot \boldsymbol{j}_\alpha^0 &= \bar{j}_\alpha, \text{ on } \partial_{\Phi_\alpha}^N \Omega, \quad \alpha = 1, 2, \\
\boldsymbol{n} \cdot \boldsymbol{w}^0 &= \bar{w}, \text{ on } \partial_P^N \Omega.
\end{aligned} \tag{3.3.43}$$

whereby the complementary Dirichlet type conditions must be imposed as follows

$$\begin{aligned}
&\boldsymbol{u}^0 = \bar{\boldsymbol{u}}, \text{ on } \partial_u \Omega, \\
&P^0 = \bar{P}, \text{ on } \partial_P \Omega, \\
&\Phi_\alpha^0 = \bar{\Phi}_\alpha, \text{ on } \partial_{\Phi_\alpha} \Omega, \quad \alpha = 1, 2.
\end{aligned} \tag{3.3.44}$$

The weak form of the problem (3.3.40)–(3.3.44), which is necessary for the finite element method, is easily obtained again by integration by parts.

Remark 3.3.1 (Dimensionalized quantities) *There are benefits to presenting the homogenized model in its nondimensional form, especially in the context of numerical simulations. In order to interpret the results of such simulation, it may be more beneficial to return computed quantities to their physical dimensions. That may be achieved easily by recalling the adimensional choices made in Sec.3.2.1 and Sec.3.3.1. That gives us the following macroscopic dimensionalized quantities*

$$P^{\text{eff}} = p_c P^0, \quad \Phi_\alpha^{\text{eff}} = \zeta \Phi_\alpha^0, \quad \boldsymbol{u}^{\text{eff}} = u_c \boldsymbol{u}^0, \quad \boldsymbol{w}^{\text{eff}} = v_c \boldsymbol{w}^0$$

where

$$p_c = c_c k_B T, \quad \zeta = \frac{k_B T}{e}, \quad u_c = \frac{p_c L_c}{E_c}, \quad v_c = \varepsilon^2 \frac{p_c L_c}{\eta_f},$$

for more informations about the dimensional analysis see Appendix A. It is also possible to obtain the dimensionalized hydrostatic pressure $p^{\text{eff}} = p_c p^0$ *where* p^0 *is computed from the global pressure* P^0 *and the potentials* Φ_α^0 *by the following formula*

$$p^0 = P^0 + \sum_{\beta=1}^{2} \fint_{Y_f} c_\beta^{\text{eq}} - \sum_{\alpha,\beta=1}^{2} z_\alpha \boldsymbol{\mathcal{Q}}^{\alpha\beta}\left(\Phi^0 + \Psi^{ext}\right),$$

for the proof see (Allaire et al. 2015).

3.3.8 Reconstruction of macroscopic solution at the microscale

One of the most remarkable advantages of the chosen homogenization method is the possibility to reconstruct macroscopic fields on the microscopic scale. After computing the solution to the macroscopic problem (3.3.39), in other words the global (dimensionless) response $\left\{\boldsymbol{u}^0, P^0, \Phi^0_\beta\right\}$, it is possible to reconstruct the associated microscopic quantities. This process is also called down-scaling in contrast to the up-scaling process that leads to the macroscopic model and we will describe it in the following text.

We consider a given finite scale $\varepsilon_0 > 0$ corresponding to real size of the microstructure, which will enable us to form the following remark.

Definition 3.3.1 (Partition of cell Y) *For a given $\varepsilon_0 > 0$, we introduce the rescaled cell $Y^{\varepsilon_0} = \varepsilon_0 Y$. Further, we introduce its local copies Y^{K,ε_0} labeled by index K. We consider the domain Ω generated as a lattice of non-overlapping copies Y^{K,ε_0} with $\{x^K\}_K$ being the set of their centers (in macroscopic coordinates). Thus, the partitioning $Y_{\varepsilon 0(\Omega)}$ of Ω is defined as*

$$Y_{\varepsilon_0}(\Omega) = \bigcup_K \bar{Y}^{K,\varepsilon_0}, \qquad Y^{K,\varepsilon_0} = Y^{\varepsilon_0} + x^K,$$

For any global position $x \in Y^{K,\varepsilon_0}$, the local "microscopic" coordinates

$$y = (x - x^K)/\varepsilon_0, \tag{3.3.45}$$

are introduced, such that $y \in Y$, (Rohan et al. 2021).

For a defined partitioning $Y_{\varepsilon_0}(\Omega)$ of the domain Ω, we will recover the macroscopic fields in Ω using a nonlocal reconstruction procedure, which is based on the so-called folding approach.

The folding method of reconstruction lies in using the so-called folding operator, which can be considered the inverse operation to the periodic unfolding. This approach enables us to "fold" the macroscopic responses $(\boldsymbol{u}^0(x), P^0(x), \Phi^0_\beta(x))$ using the scale separation splits related to the periodic lattice.

The folding operator $\mathcal{F}^{\varepsilon_0}$ folds any macroscopic field $f^0(x)$ onto the partitioning $Y_{\varepsilon_0}(\Omega)$, so that the local microscopic fields are given by the so-called folding mapping (Rohan et al. 2016b), such that

$$\mathcal{F}^{\varepsilon_0}(\hat{x}) : (\boldsymbol{u}^0, P^0, \Phi^0_\beta) \rightarrow (\boldsymbol{u}^{\mathrm{rec}}, P^{\mathrm{rec}}, \boldsymbol{w}^{\mathrm{rec}}, \Phi^{\mathrm{rec}}_\beta)(y), \qquad y \in Y_{\varepsilon_0}(\Omega). \tag{3.3.46}$$

The folding operator $\mathcal{F}^{\varepsilon_0}$ combines the corrector base functions defined in Y with the interpolated macroscopic responses transformed to the local zoomed RVE $Y_{\varepsilon_0}(x)$ by the interpolation operator $\mathcal{Q}^{\varepsilon_0}$. The $\mathcal{Q}^{\varepsilon_0}$ is defined by an Q_1 interpolation scheme in the sense of the FEM approximation over partitioning $Y_{\varepsilon_0}(\Omega)$ of Ω.

It should be noted that the folding approach requires smoothness of gradients $\nabla_x f^0(x)$. This can be achieved by introducing a projection $\Pi_\varepsilon\left[g\right]$ of a given function $g(x)$ into the space of piecewise polynomials defined over the partition $Y_{\varepsilon_0}(\Omega)$.

To apply the folding approach, we first introduce the smoothed gradients $\Pi_{\varepsilon_0}\left[\partial^x_k P^0\right]$, $\Pi_{\varepsilon_0}\left[e^x_{ij}\boldsymbol{u}^0\right]$ and $\Pi_{\varepsilon_0}\left[\partial^x_k \Phi^0_\alpha\right]$ for $\alpha = 1, 2$. By introducing them into the split forms (3.3.27)–(3.3.28), for any $x \in \Omega$ and $y \in Y$ assigned to x by virtue of (3.3.45), the microscopic fields can be reconstructed using the following formulae:

$$\begin{aligned} \Phi_\alpha^{\mathrm{mic}}(x,y,t) &= \theta^{0,k}(y)\left(f_k - \Pi_{\varepsilon_0}\left[\partial_k^x P^0\right]\right)(x)+ \\ &\quad + \sum_{\beta=1}^{2} \theta^{\beta,k}(y)\left(\Pi_{\varepsilon_0}\left[\partial_k^x \Phi_\beta^0\right] + E_k\right)(x), \end{aligned} \tag{3.3.47}$$

$$\begin{aligned} P^{\mathrm{mic}}(x,y,t) &= \pi^{0,k}(y)\left(f_k - \Pi_{\varepsilon_0}\left[\partial_k^x P^0\right]\right)(x)+ \\ &\quad + \sum_{\beta=1}^{2} \pi^{\beta,k}(y)\left(\Pi_{\varepsilon_0}\left[\partial_k^x \Phi_\beta^0\right] + E_k\right)(x), \end{aligned} \tag{3.3.48}$$

$$\begin{aligned} \boldsymbol{u}^{\mathrm{mic}}(x,y,t) &= \tilde{\boldsymbol{w}}^{ij}(y)\Pi_{\varepsilon_0}\left[e_{ij}^x \boldsymbol{u}^0\right] - P^0(x)\boldsymbol{w}^P(y)+ \\ &\quad + \sum_{\beta=1}^{2} \boldsymbol{w}^\beta(y) z_\beta \left(\Phi_\beta^0(x) + \Psi^{\mathrm{ext}}(x)\right), \end{aligned} \tag{3.3.49}$$

where by $\tilde{\square}$ we denote the extensions of quantities from Y_s to entire Y. Now the fields that are relevant to the microscopic heterogeneity are evaluated using

$$\begin{aligned} P^{\mathrm{rec}}(x,t) &= P^0(x,t) + \varepsilon_0 P^{\mathrm{mic}}(x,y,t) \\ \boldsymbol{u}^{\mathrm{rec}}(x,t) &= \boldsymbol{u}^0(x,t) + \varepsilon_0 \boldsymbol{u}^{\mathrm{mic}}(x,y,t) \\ \Phi_\alpha^{\mathrm{rec}}(x,t) &= \Phi_\alpha^0(x,t) + \varepsilon_0 \Phi_\alpha^{\mathrm{mic}}(x,y,t), \alpha = 1,2. \end{aligned} \tag{3.3.50}$$

In addition, by the virtue of the $(3.3.27)_1$,$(3.3.27)_1$ and $(3.3.27)_2$, we obtain a reconstruction of velocity and potential fields

$$\begin{aligned} \boldsymbol{w}^{\mathrm{rec}}(x,y,t) &= \sum_{\beta=1}^{2} \boldsymbol{\omega}^{\beta,k}(y)\left(\Pi_{\varepsilon_0}\left[\partial_k^x \Phi_\beta^0\right] + E_k\right)(x)+ \\ &\quad + \boldsymbol{\omega}^{0,k}(y)\left(f_k - \Pi_{\varepsilon_0}\left[\partial_k^x P^0\right]\right)(x), \end{aligned} \tag{3.3.51}$$

$$\Psi_f^{\mathrm{rec}}(x,y,t) = \sum_{\beta=1}^{2} \varpi^\beta(y)\left(\Phi_\beta^0(x) + \Psi^{\mathrm{ext}}(x)\right), \tag{3.3.52}$$

$$\begin{aligned} \Psi_s^{\mathrm{rec}}(x,y,t) &= \eta^{ij}(y)\Pi_{\varepsilon_0}\left[e_{ij}^x \boldsymbol{u}^0\right] - P^0(x)\eta^P(y)+ \\ &\quad + \sum_{\beta=1}^{2} \eta^\beta(y) z_\beta \left(\Phi_\beta^0(x) + \Psi^{\mathrm{ext}}(x)\right), \end{aligned} \tag{3.3.53}$$

The reconstruction of the solution is useful for determining the actual influence of macroscopic processes on the microscopic scale.

Chapter 4

Implementation and illustrative examples

This section aims to explore and illustrate the properties of the homogenized two-scale models described in the preceding sections. For this purpose, we present numerical simulations of both types of porous medium, LEPM and PEPM.

The first part of this chapter, *i.e.* Sec. 4.1, focuses on the implementation of the homogenized model derived for LEPM that was presented in Sec. 3.2. We present the NUMERICAL algorithm of numerical implementation and provide some insight into spatial discretization. Then, we perform a parametric study to illustrate the impact of change in microstructure on the homogenized material properties. We test the behavior of the homogenized macroscopic model on a steady-state problem. A part of the presented results was published in our work (Turjanicová et al. 2019).

In Sec. 4.2, we provide numerical results of the simulations performed on the model of the quasi-static ionic transport through PEPM that was derived in Sec. 3.3. To illustrate the behavior of the homogenized model, we present a simple test problem mimicking an experiment.

We use software *SfePy* to implement all presented mathematical models. *SfePy* is in-house developed software for solving problems with coupled partial differential equations (PDEs) in weak forms by means of the FEM for 2D and 3D problems, (Cimrman 2014). It is based on the *Python* programming language and it provides programming tools for the implementation of problems on multiple scales. Implementation of the presented mathematical models also required the development of separate code written in the *Python* language and which uses some of the Python-based open-source packages, namely *NumPy* and *SciPy*, (Virtanen et al. 2020).

4.1 Numerical modeling of poroelastic medium

This section focuses on the numerical simulations that illustrate the properties of the homogenized two-scale model describing the steady state of ionic transport in the LEPM. For this purpose, we present a numerical simulation of the steady state of flow of the electrolyte solution through the LEPM occupying a simple-shaped macroscopic domain Ω, with a simple periodic microstructure.

Symbol	Quantity	Value	Unit
η_f	Dynamic viscosity	1×10^{-3}	kg/(ms)
D_1^0	Diffusivity of 1st ionic species (Cl^-)	20.32×10^{-10}	m^2/s
D_2^0	Diffusivity of 2nd ionic species (Na^+)	13.33×10^{-10}	m^2/s
l	Characteristic pore size	1.0×10^{-7}	m
c_c	Characteristic concentration	6.02×10^{24}	$\mathrm{particles}/\mathrm{m}^3$
Σ	Surface charge density	-0.129	C/m^2
E_c	Young modulus	7.3×10^{9}	Pa
ν	Poisson's ration	0.39	-

Table 4.1: Mechanical and piezoelectric constants used in BVP I and BVP II, source (Allaire et al. 2015)

Instead of describing the content of this section, we will provide a comprehensive list of steps taken to implement the two-scale mathematical model of ionic transport in the LEPM. Each step provides references to the particular problems that are being solved. The structure of this section will reflect this list.

4.1.1 Steps of numerical implementation

The presented examples do not consider any volume forces and also disregard the effects of an external electric field, thus we put $\boldsymbol{f} = \mathbf{0}$ and $\boldsymbol{E} = \mathbf{0}$. The used electrochemical and mechanical quantities and parameters are in Tabs. 2.1 and 4.1. All the computations are performed for the given pore size l and, as a consequence, given scale parameter ε.

The numerical simulation of the problem can be divided into several steps:

1. Solve potential distribution in equilibrium Ψ^{eq} on RPC Y as a solution of (3.2.17).
2. Compute concentration c_β^{eq} from (3.2.25).
3. Compute the corrector functions $(\boldsymbol{\omega}^{P,k}, \pi^{P,k}, \theta_j^{P,k})$ and $(\boldsymbol{\omega}^{\alpha,k}, \pi^{\alpha,k}, \theta_\beta^{\alpha,k}), \alpha = 1, 2$ related to the electrokinetic system as a solution of local problems (3.2.44) and (3.2.45).
4. Compute effective coefficients relevant to the decoupled electrokinetic system, see (3.2.50).
5. Compute corrector functions $\varpi^\alpha, \alpha = 1, 2$ related to potential perturbation as a solution of local problems (3.2.46).
6. Compute corrector functions $(\boldsymbol{w}^{ij}, \boldsymbol{w}^P, \boldsymbol{w}^\alpha), \alpha = 1, 2$ related to displacement perturbation as a solution to the local problems (3.2.47)-(3.2.49).
7. Compute effective coefficients relevant to extended Biot poroelasticity, see (3.2.51).
8. Compute solution to macroscopic homogenized system of equations (3.2.52).

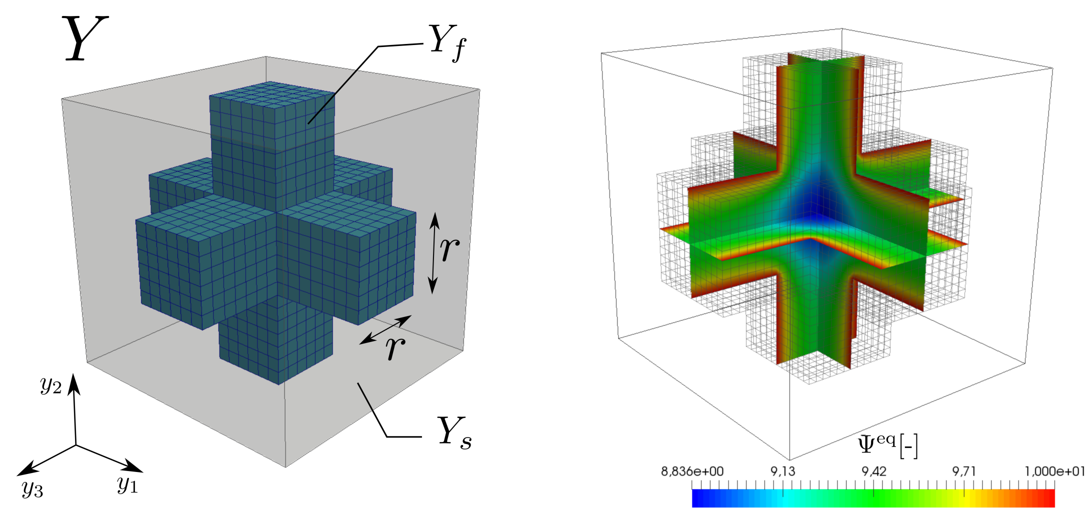

(a) (b)

Figure 4.1: Left: Geometry representation of microstructure for parametric study and parametrization of RPC Y; Right: Potential Ψ^{eq}[-] distribution on microscale, solution of Poisson-Boltzmann problem in equilibrium.

Note that we presented a significant part of the mathematical equations in their dimensionless form. The dimensionless form is beneficial for implementation purposes, as it minimizes possible numerical errors that would arise due to significant differences in the magnitude of some parameters or variables. For example, the electrokinetic quantities are much smaller than the elastic modulus, thus choosing a suitable numerical method and its precision can be problematic. Therefore, we performed all the numerical simulations for the dimensionless form of equations. And thus, a part of the presented results is given in their dimensionless form as well. This regards the solution of computations on the microscopic scale and especially the values of effective coefficients.

In contrast, the results of the macroscopic problem will be stated in their dimensionalized form as we feel it is more important to their interpretation. We recall their dimensionalized form by using the dimensional choices explained previously; see Remark 3.3.1.

4.1.2 Numerical simulations at the microscopic level

To begin implementing the upscaled two-scale problem, we have to start from the computations on the lower scale. First, we introduce the simplified geometry representation of microstructure using RVE Y and its discretization into the computational mesh. Both the topology and the dimensions of pores have a significant influence on the homogenized material properties. To show this, we will perform a parametric study of the varying size of pore cross-section and its effect on the homogenized coefficients.

Following the steps proposed above, we have to solve the Poisson-Boltzmann problem in equilibrium (3.2.17) on RVE Y before proceeding further. The result is used in the computations of local problems and the subsequent calculation of effective coefficients.

Geometrical representation of microstructure

We aim to study the dependency of the effective coefficients on a change of the microstructure geometry. For this purpose, we choose only a simple geometry representation in the form of three interconnected canals aligned with y_1-, y_2- and y_3-directions through a continuous matrix, see Fig. 4.1a. The cross-section of the canals is a square with edge length r. Changing the parameter r leads to a change in porosity $\phi_f = \frac{|Y_f|}{|Y|}$.

We generated the mesh representing the cell Y by a mesh generation script, which forms a part of the *SfePy* software. For meshing, we used the linear hexahedron elements.

Potential distribution in equilibrium

The first step in obtaining effective coefficients is to compute the distribution of potential in equilibrium Ψ_f^{eq} on the microscopic scale, see Appendix B. All used electrokinetic quantities can be found in Tab.4.1. For this part, we consider the elasticity tensor of the solid to be isotropic and defined by the Young modulus $E_c = 7.3 \times 10^9$[Pa] and Poisson's ratio $\nu = 0.39$. Isotropy of the material on the microscopic scale will prove useful for the parametric study.

The distribution of potential in equilibrium Ψ_f^{eq} that is obtained as a solution to the Poisson-Boltzmann problem (3.2.17) is shown in Fig. 4.1b. The potential in equilibrium Ψ_f^{eq} has its maximum on the solid-fluid interface, where the surface charge Σ is prescribed. The potential Ψ_f^{eq} gradually decreases with increasing distance from the interface. This meets our general expectation about Poisson-Boltzmann's potential distribution near the solid-fluid interface, see Sec.2.2.2. The resulting potential distribution Ψ_f^{eq} is needed for computation of concentration c_β^{eq} from (3.2.25) that is necessary for subsequent calculations.

Influence of varying microstructure on effective tensors

Effective coefficients are computed with the help of correctors functions, i.e. solutions of the three groups of local cell problems (3.2.44)–(3.2.45),(3.2.46) and (3.2.47)–(3.2.49). We have two sets of effective coefficients; the first one is the set of coefficients that are related to the decoupled electrokinetic system and given by (3.2.50) and the second one is the set related to weakly coupled Biot poroelasticity equation and given by (3.2.51). For future reference, the index $\alpha = 1$ refers to the anions with valency $z_1 = -1$ and index $\alpha = 2$ to the cations with valency $z_2 = +1$.

We study the dependency of effective coefficients on the change in porosity $\hat{\phi}_f$, caused by variation in y_1-direction canal size parameter r. In accordance with the choice of the symmetric microstructure, we expect the components of effective coefficients related to y_2- and y_3-direction to be equal.

The dependencies of the diagonal components of electrokinetic and poroelasticity coefficients (dimensionless) are shown in Figs. 4.2 and 4.3. As expected, the components of effective coefficients related to y_2- and y_3-direction follow the same dependency curve. The components related to the y_1-direction follow the same trend but are not equal to the rest. As we consider isotropic elastic properties

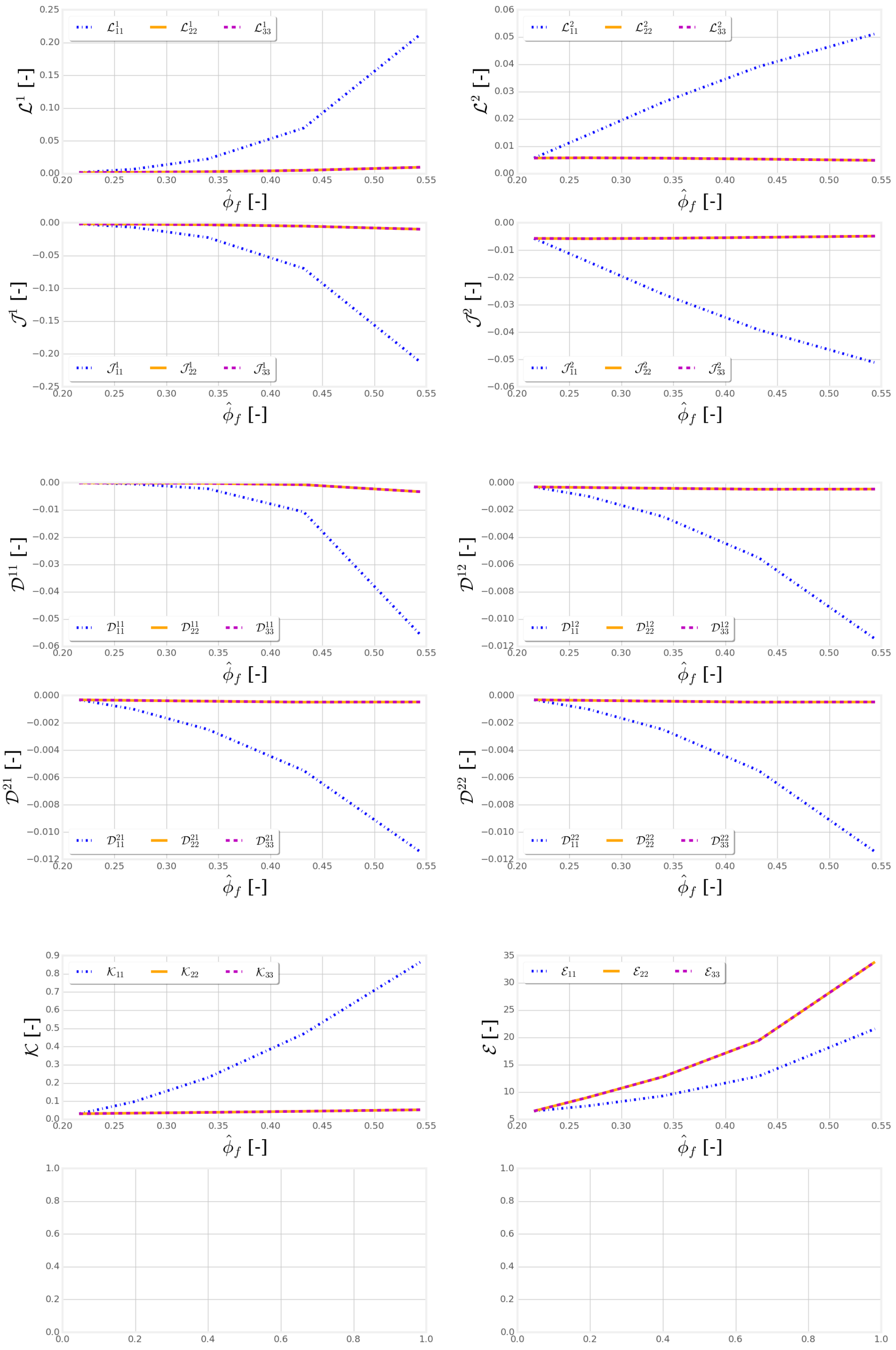

Figure 4.2: Dependency of dimensionless effective tensors $\boldsymbol{\mathcal{J}}^1, \boldsymbol{\mathcal{J}}^2$ relevant to migration-diffusion, coupling tensors $\boldsymbol{\mathcal{L}}^1, \boldsymbol{\mathcal{L}}^2$, diffusivity tensors $\boldsymbol{\mathcal{D}}^{11}, \boldsymbol{\mathcal{D}}^{22}$ and permeability tensor $\boldsymbol{\mathcal{K}}$ on porosity $\hat{\phi}_f$

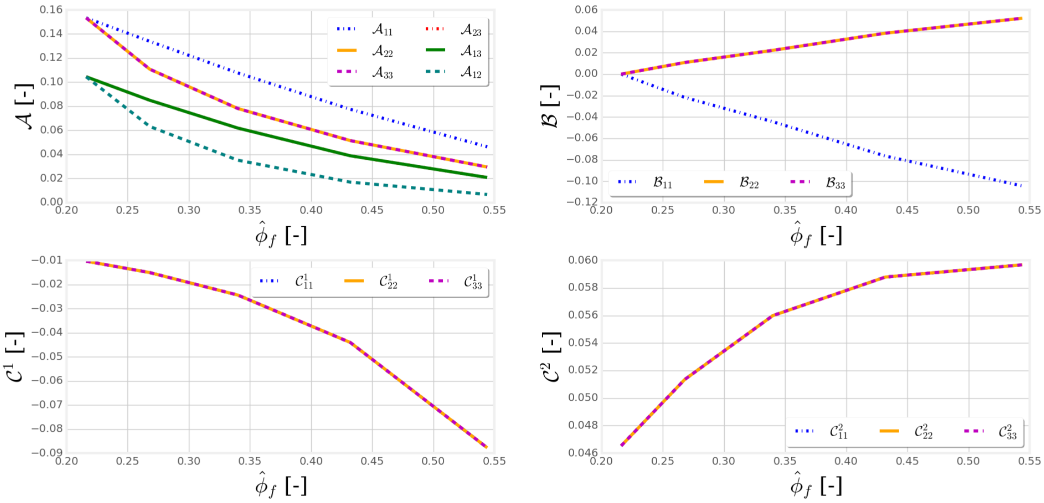

Figure 4.3: Dependency of components of dimensionless effective elasticity tensor $\boldsymbol{\mathcal{A}}$, ionic potential tensors $\boldsymbol{\mathcal{C}}^1, \boldsymbol{\mathcal{C}}^2$ and Biot's tensor $\boldsymbol{\mathcal{B}}$ on porosity $\hat{\phi}_f$

of the solid phase on the microscopic level, this anisotropy is caused purely by microstructure geometry.

Fig. 4.3 shows the dependency of the effective coefficient related to poroelasticity on the porosity of the microstructure. The components of dimensionless poroelasticity tensor $\boldsymbol{\mathcal{A}}$ decrease with the increasing porosity. This is to be expected as the fraction of stiffer solid matrix decreases as well. On the other hand, the components of the Biot coefficient $\boldsymbol{\mathcal{B}}$ increase with the rising porosity. Finally, the lower half of the figure shows ionic potential tensors $\boldsymbol{\mathcal{C}}^1$ and $\boldsymbol{\mathcal{C}}^2$. The components of $\boldsymbol{\mathcal{C}}^1$ related to all three directions are equal. This applies to the components of $\boldsymbol{\mathcal{C}}^2$ as well. However, the components of tensor $\boldsymbol{\mathcal{C}}^1$ decrease with the increasing porosity while the components of tensor $\boldsymbol{\mathcal{C}}^2$ increase. This is caused by the different valency of both considered ionic species, which influence the corrector base function $\boldsymbol{w}^\alpha$, see (3.2.49), and consequentially $\boldsymbol{\mathcal{C}}^\alpha$, see $(3.2.51)_3$.

Similar nonlinear behavior is obtained for the other electrokinetic tensors, as seen in Fig. 4.2. We observe the decrease in the components of the migration-diffusion tensors $\boldsymbol{\mathcal{J}}^1$ and $\boldsymbol{\mathcal{J}}^2$ related to anions and cations, respectively. The components of coupling tensors $\boldsymbol{\mathcal{L}}^1$ and $\boldsymbol{\mathcal{L}}^2$ decrease with the increasing porosity.

In the lower part of Fig. 4.2 we observe increase in permeability $\boldsymbol{\mathcal{K}}$, as expected. The last part of this figure depicts the decreasing components of diffusivity tensors $\boldsymbol{\mathcal{D}}^{11}$ and $\boldsymbol{\mathcal{D}}^{22}$. The diagonal components of $\boldsymbol{\mathcal{D}}^{12}$ and $\boldsymbol{\mathcal{D}}^{21}$ are equal to those of $\boldsymbol{\mathcal{D}}^{22}$. In comparison, the components of $\boldsymbol{\mathcal{D}}^{11}$ are of slightly higher value; This corresponds to the choice of the diffusivity $D_1 > D_2$, see Tab. 4.1.

4.1.3 Numerical simulations at the macroscopic level

In this section, we proceed to perform the numerical simulations at the macroscopic level. To describe the macroscopic behavior, we use effective coefficients computed for the microstructure with three interconnected canals of the same canal diameter, *i.e.* the isotropic effective coefficients.

Semi-discretized steady state macroscopic problem

We introduce the semi-discretized form of macroscopic problem used for finite element (FE) modeling. The column vectors $\mathbf{P}^0, \mathbf{\Phi}_\alpha^0, \alpha = 1,2$, and $\mathbf{u}^0$ represent all degrees of freedom of FE mesh nodes associated with partitioning of the macroscopic domain Ω. We introduce FE approximations of terms involved in the macroscopic problem (3.2.52) describing the steady-state flow of the electrolyte through the LEPM as follows

$$
\begin{array}{lcllcl}
\boldsymbol{q}^T\mathbb{K}\mathbf{P}^0 & \approx & \int_\Omega \boldsymbol{\mathcal{K}}\nabla_x\mathbf{P}^0\nabla_x q dV, & \boldsymbol{q}^T\mathbb{J}^\alpha\mathbf{\Phi}_\alpha^0 & \approx & \int_\Omega \boldsymbol{\mathcal{J}}^\alpha\nabla_x\Phi_\alpha^0\nabla_x q\,\mathrm{d}V, \\
\boldsymbol{q}^T\mathbf{f}_J^\alpha & \approx & \int_\Omega \boldsymbol{\mathcal{J}}^\alpha q\nabla_x\cdot\mathbf{E}\,\mathrm{d}V, & \boldsymbol{q}^T\mathbf{f}_K & \approx & \int_\Omega \boldsymbol{\mathcal{K}}q\nabla_x\cdot\boldsymbol{f}\,\mathrm{d}V, \\
\boldsymbol{\varphi}^T\mathbb{L}^\alpha\mathbf{P}^0 & \approx & \int_\Omega \frac{D_\alpha\mathbb{L}^\alpha}{k_BT}\nabla_x\mathbf{P}^0\nabla_x s\,\mathrm{d}V, & \boldsymbol{\varphi}^T\mathbb{D}^{\alpha\beta}\mathbf{\Phi}_\beta^0 & \approx & \int_\Omega \boldsymbol{\mathcal{D}}^{\alpha\beta}\nabla_x\mathbf{\Phi}_\beta^0\nabla_x s\,\mathrm{d}V, \\
\boldsymbol{\varphi}^T\mathbf{f}_D^{\alpha\beta} & \approx & \int_\Omega \boldsymbol{\mathcal{D}}^{\alpha\beta}s\nabla_x\cdot\mathbf{E}\,\mathrm{d}V, & \mathbf{v}^T\mathbb{B}\mathbf{P}^0 & \approx & \int_\Omega \boldsymbol{\mathcal{B}}\mathbf{P}^0 : e_x(\boldsymbol{v})\,\mathrm{d}V, \\
\mathbf{v}^T\mathbb{C}^\alpha\mathbf{\Phi}_\alpha^0 & \approx & \int_\Omega \boldsymbol{\mathcal{C}}^\alpha\Phi_\alpha^0 : e_x(\boldsymbol{v})\,\mathrm{d}V, & \mathbf{v}^T\mathbb{A}\mathbf{u}^0 & \approx & \int_\Omega \boldsymbol{\mathcal{A}}e_x(\boldsymbol{u}^0) : e_x(\boldsymbol{v})\,\mathrm{d}V, \\
\mathbf{v}^T\mathbf{f}_C^\alpha & \approx & \int_\Omega \boldsymbol{\mathcal{C}}^\alpha\nabla_x\Psi^{\mathrm{ext}}\cdot\boldsymbol{v}\,\mathrm{d}V, & \mathbf{v}^T\mathbf{f} & \approx & \int_\Omega \boldsymbol{f}\cdot\boldsymbol{v}\,\mathrm{d}V.
\end{array}
$$

Using the notations just introduced, we can write the steady state linear macroscopic problem in the matrix form

$$
\begin{bmatrix} \mathbb{K} & -\mathbb{J}^1 & -\mathbb{J}^2 & \mathbf{0} \\ \mathbb{L}^1 & -\mathbb{D}^{11} & -\mathbb{D}^{12} & \mathbf{0} \\ \mathbb{L}^2 & -\mathbb{D}^{21} & -\mathbb{D}^{22} & \mathbf{0} \\ \mathbb{B} & -\mathbb{C}^1 & -\mathbb{C}^2 & \mathbb{A} \end{bmatrix} \begin{bmatrix} \mathbf{P}^0 \\ \mathbf{\Phi}_1^0 \\ \mathbf{\Phi}_2^0 \\ \mathbf{u}^0 \end{bmatrix} = \begin{bmatrix} \mathbf{f}_J^1 + \mathbf{f}_J^2 + \mathbf{f}_K \\ \mathbf{f}_D^{11} + \mathbf{f}_D^{12} \\ \mathbf{f}_D^{21} + \mathbf{f}_D^{22} \\ \mathbf{f}_C^1 + \mathbf{f}_C^2 + \mathbf{f} \end{bmatrix}. \tag{4.1.1}
$$

It is immediately evident, that the electrokinetic system can be solved separately from the problem of poroelasticity and return the solution $(\mathbf{P}^0, \mathbf{\Phi}_\alpha^0), \alpha = 1,2$. The macroscopic displacement is than given by

$$
\mathbf{u}^0 = \mathbb{A}^{-1}\left(-\mathbb{B}\mathbf{P}^0 + \mathbb{C}^1\mathbf{\Phi}_1^0 + \mathbb{C}^2\mathbf{\Phi}_2^0 + \mathbf{f}_C^1 + \mathbf{f}_C^2 + \mathbf{f}\right).
$$

Solution of macroscopic problem

For the purpose of numerical simulations, we propose a simple experiment, see Fig. 4.4, where a small cuboid specimen with the dimensions $L \times a \times a$, where $L = 0.001$m and $a = 0.0003$m, is placed between two ionic reservoirs and separated by semipermeable membranes. These membranes enable ionic exchange but prevent fluid flow. The specimen is occupied by a LEPM with microstructure size given by $\varepsilon := \varepsilon_0 = 0.05$

To describe the boundary conditions, we refer to the faces of the porous specimen by the intuitive notation, such that Γ_E stands for the "east side" with the normal vector aligned with x_1-axis, whereas the "north side" Γ_N has its normal aligned with x_2-axis. Then Γ_T and Γ_B refer to the top and bottom sides, respectively, see Fig. 4.4. On Γ_T and Γ_B part of the boundary, the porous specimen is clamped.

This experiment is focused on the observation of the displacement and pressure distribution under the ionic potentials change. To this aim, we propose four macroscopic problems with varying boundary conditions related to ionic potentials. The homogenized macroscopic problem is given by the system of equations (3.2.52) completed by its respective boundary conditions. In what follows, we

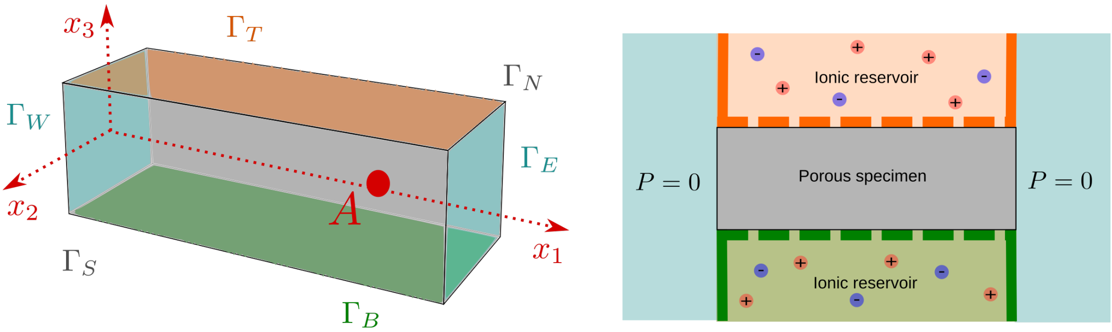

Figure 4.4: Left: Block test geometry for computation of homogenized macroscopic problem, with parts of the boundary and the position of the point A marked; Right: Illustration of boundary conditions setup that mimics simple experiment.

define the two sets of boundary conditions, thus obtaining two boundary problems. The following part of the text describes the two boundary value problems (BVP).

The problem is computed in its dimensionless form to prevent numerical errors. Then, using the dimensionless choices from Section 3.2.1, we recover the dimensional form of respective macroscopic quantities.

Boundary value problems

The boundary value problem is defined by (3.2.52) and by boundary conditions of the Neumann type (3.2.56) and the Dirichlet type (3.2.57) which are prescribed on the six faces of the macroscopic specimen (a 3D block), see Fig. 4.4, as follows

- on Γ_W and Γ_E: $\boldsymbol{n} \cdot \boldsymbol{\sigma}^{\text{eff}} = -\boldsymbol{n} P^{\text{eff}} = \boldsymbol{0}, \qquad P^{\text{eff}} = 0, \quad \boldsymbol{n} \cdot \boldsymbol{j}_\alpha^{\text{eff}} = 0,$
- on Γ_T: $u_n = 0$ and $\sigma_t = 0, \quad \boldsymbol{n} \cdot \boldsymbol{w}^{\text{eff}} = 0, \quad \Phi_1^{\text{eff}} = \bar{\Phi}_1, \quad \boldsymbol{\mathcal{J}}^2 \nabla \Phi_2^{\text{eff}} \cdot \boldsymbol{n} = \bar{g},$
- on Γ_B: $u_n = 0$ and $\sigma_t = 0, \quad \boldsymbol{n} \cdot \boldsymbol{w}^{\text{eff}} = 0, \quad \Phi_1^{\text{eff}} = \bar{\Phi}_1, \quad \boldsymbol{\mathcal{J}}^2 \nabla \Phi_2^{\text{eff}} \cdot \boldsymbol{n} = b\bar{g},$

where $\sigma_t = \boldsymbol{t} \otimes \boldsymbol{n} : \boldsymbol{\sigma}^{\text{eff}}$ for any tangent vector $\boldsymbol{t}$, whereas $u_n = \boldsymbol{n} \cdot \boldsymbol{u}$. The following values are used, $\bar{\Phi}_1 = 0.1$ and $\bar{g} = 0.001$. By the choice of parameter b we distinguish two BVPs.

The first one, referred to as BVP I, is defined by choice $b = 1$, so that the boundary conditions are symmetric on boundaries Γ_T and Γ_B. Therefore, the symmetric distribution of macroscopic quantities is obtained correspondingly, as seen in Fig. 4.5. The deformed shape is visualized by the wire-frame, whereby the displacement field is enlarged by factor $2 \cdot 10^5$. The swelling of the macroscopic body occurs mainly in the region, where Φ_2^{eff} attains the lowest values.

By taking $b = 5$, we get the second boundary value problem, referred to as BVP II. In this case, we increased the influx of Φ_2^{eff} on the boundary Γ_B. This leads to the contraction of the porous specimen near this surface, as seen in Fig. 4.6. Naturally, the non-symmetrical boundary conditions result in a non-symmetric distribution of the macroscopic quantities. This effect is most visible on the swelling of the macroscopic body, which tends to react to the distribution of Φ_2^{eff}, swelling slightly more in places where Φ_2^{eff} is somewhat lower. In this case, the deformed shape is visualized by the wire-frame enlarged by a factor of $2 \cdot 10^4$.

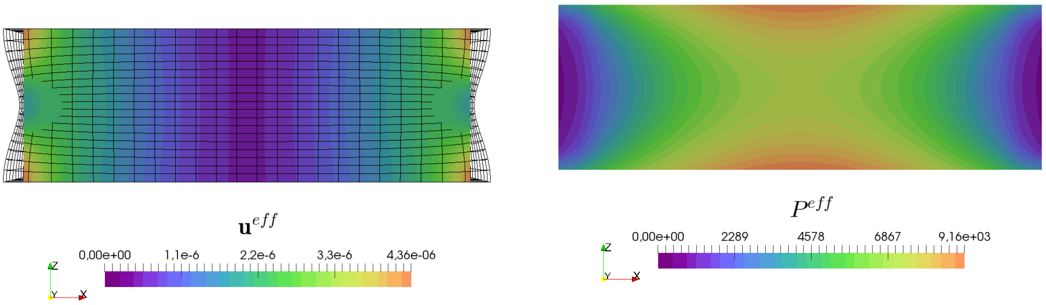

(a) Distribution of displacement $\boldsymbol{u}^{\text{eff}}$[m].

(b) Distribution of global pressure P^{eff}[Pa].

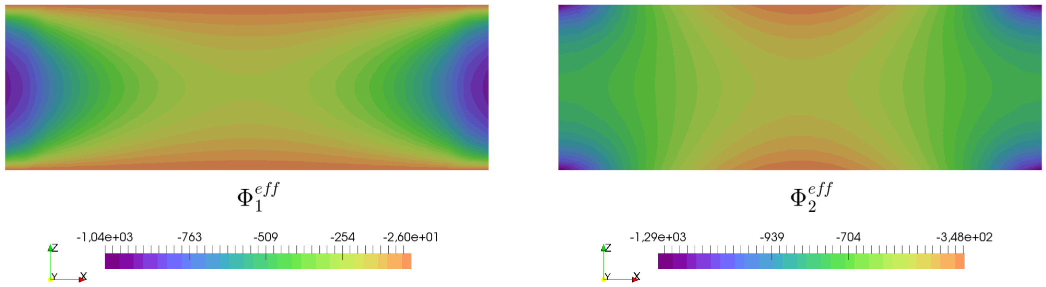

(c) Distribution of potential Φ_1^{eff}[J/C].

(d) Distribution of potential Φ_2^{eff}[J/C].

Figure 4.5: The dimensionalized macroscopic fields obtained as a solution of the BVP I.

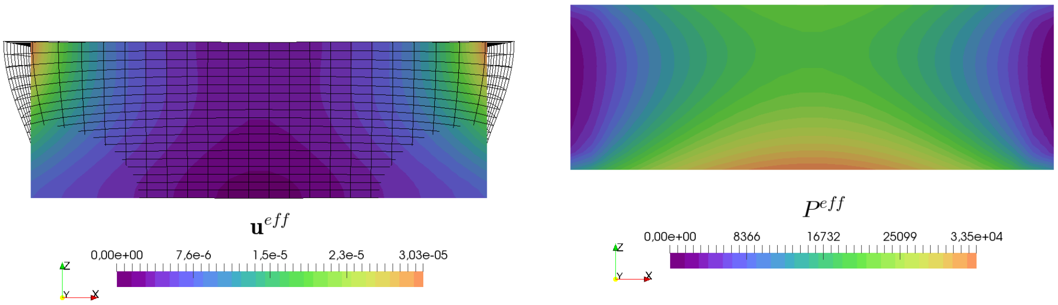

(a) Distribution of displacement $\boldsymbol{u}^{\text{eff}}$[m].

(b) Distribution of global pressure P^{eff}[Pa].

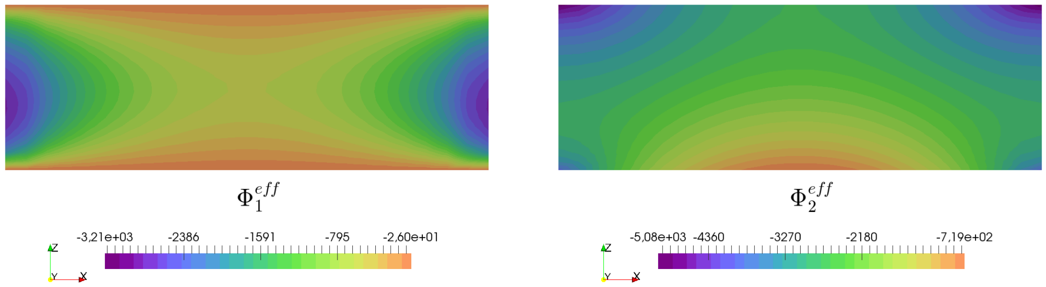

(c) Distribution of potential Φ_1^{eff}[J/C].

(d) Distribution of potential Φ_2^{eff}[J/C].

Figure 4.6: The dimensionalized macroscopic fields obtained as a solution of the BVP I.

4.2 Numerical modeling of piezoelectric porous medium

In this section, we deal with numerical modeling of quasi-steady flow of electrolyte solution through PEPM that was presented in Sec. 3.3. The implementation of the mathematical model follows similar steps as those stated in Sec. 4.1.1. Although we do not provide a comprehensive list of steps, we recapitulate them for the sake of clarity.

First, the Poisson-Boltzmann equation in equilibrium (3.2.17) is solved, which yields the equilibrium potential Ψ_f^{eq}. Than, the corrector basis functions are computed from local problems (3.3.29)-(3.3.31) and (3.3.33)-(3.3.35). The homogenized coefficients relevant to the macroscopic problem are enumerated from expressions (3.3.36)–(3.3.38). And finally, the solution of homogenized macroscopic problem is computed from (3.3.39).

4.2.1 Description of microscopic level

The microstructure geometry remains the same as for poroelastic medium, *i.e.* it is represented by the same RPC Y depicted in Fig. 4.1a. The microstructure size is given by $\varepsilon := \varepsilon_0 = 0.05$ which determines the influence of the piezoelectric coupling $\boldsymbol{g}$ and dielectric tensor $\boldsymbol{d}$. The values of electrochemical constants are taken from Tab. 4.1. However, the piezoelectric material usually exhibits some degree of anisotropy. Therefore, we forgo previously used mechanical parameters and choose a new one instead. We use barium–titanite $BaTiO_3$ to constitute the material of the piezoelectric matrix in our numerical tests, see (Miara et al. 2005). The material properties of solid matrix are characterized by elasticity tensor A_{ijkl}, piezoelectric coupling G_{ijk} and dielectric tensor d_{ij},

$$\boldsymbol{A} = \begin{bmatrix} 1.504 & 0.656 & 0.659 & 0 & 0 & 0 \\ 0.656 & 1.504 & 0.659 & 0 & 0 & 0 \\ 0.659 & 0.659 & 1.455 & 0 & 0 & 0 \\ 0 & 0 & 0 & 0.424 & 0 & 0 \\ 0 & 0 & 0 & 0 & 0.439 & 0 \\ 0 & 0 & 0 & 0 & 0 & 0.439 \end{bmatrix} \times 10^{11} [\mathrm{Pa}]$$

$$\boldsymbol{g} = \begin{bmatrix} 0 & 0 & 0 & 0 & 11.404 & 0 \\ 0 & 0 & 0 & 0 & 0 & 11.404 \\ -4.322 & -4.322 & 17.360 & 0 & 0 & 0 \end{bmatrix} [\mathrm{C/m^2}],$$

$$\boldsymbol{d} = \begin{bmatrix} 1.284 & 0 & 0 \\ 0 & 1.284 & 0 \\ 0 & 0 & 1.505 \end{bmatrix} \times 10^{-8} [\mathrm{C/Vm}].$$

The chosen elastic properties are anisotropic. That is in contrast with computations made in previous Sec. 4.1 and we expect it to lead to a different result on the macroscopic specimen.

4.2.2 Semi discretized model of piezoelectric time-dependent macroscopic problem

We introduce the semi-discretized form of macroscopic problem for finite element (FE) modeling.

The computational time T is discretized into the n equidistant time levels with the fixed time step Δt. The column vectors $\mathbf{P}^n, \mathbf{\Phi}^n_\alpha, \alpha = 1, 2$, and $\mathbf{u}^n$ contain all degrees of freedom at n-th time level. We present the following approximations of the terms involved in the macroscopic problem (3.3.39):

$$\begin{array}{lcllcl}
\mathbf{q}^T \mathbb{K} \mathbf{P}^n & \approx & \int_\Omega \boldsymbol{\mathcal{K}} \nabla_x P^n \nabla_x q dV, & \mathbf{q}^T \mathbb{J}^\alpha \mathbf{\Phi}^n_\alpha & \approx & \int_\Omega \boldsymbol{\mathcal{J}}^\alpha \nabla_x \Phi^n_\alpha \nabla_x q \, \mathrm{d}V, \\
\boldsymbol{\varphi}^T \mathbb{L}^\alpha \mathbf{P}^n & \approx & \int_\Omega \boldsymbol{\mathcal{L}}^\alpha \nabla_x P^n \nabla_x \tilde{\varphi} \, \mathrm{d}V, & \boldsymbol{\varphi}^T \mathbb{D}^{\alpha\beta} \mathbf{\Phi}^n_\beta & \approx & \int_\Omega \boldsymbol{\mathcal{D}}^{\alpha\beta} \nabla_x \Phi^n_\beta \nabla_x \tilde{\varphi} \, \mathrm{d}V, \\
\mathbf{q}^T \mathbb{M}^\alpha \mathbf{P}^n & \approx & \int_\Omega \boldsymbol{\mathcal{M}}^\alpha P^n \nabla_x \tilde{q} \, \mathrm{d}V, & \mathbf{v}^T \mathbb{B} \mathbf{P}^n & \approx & \int_\Omega \boldsymbol{\mathcal{B}} P^n : e_x(\boldsymbol{v}) \, \mathrm{d}V, \\
\mathbf{v}^T \mathbb{C}^\alpha \mathbf{\Phi}^n_\alpha & \approx & \int_\Omega \boldsymbol{\mathcal{C}}^\alpha \Phi^n_\alpha : e_x(\boldsymbol{v}) \, \mathrm{d}V, & \mathbf{v}^T \mathbb{A} \mathbf{u}^n & \approx & \int_\Omega \boldsymbol{\mathcal{A}} e_x(\boldsymbol{u}^n) : e_x(\boldsymbol{v}) \, \mathrm{d}V, \\
\boldsymbol{\varphi}^T \mathbb{Q}^{\alpha\beta} \mathbf{\Phi}^n_\beta & \approx & \int_\Omega (\boldsymbol{\mathcal{Q}}^{\alpha\beta} + \boldsymbol{\mathcal{S}}^{\alpha\beta}) \Phi^n_\beta \tilde{\varphi}, & \mathbf{q}^T \mathbb{N}^\alpha \mathbf{\Phi}^n_\alpha & \approx & \int_\Omega \boldsymbol{\mathcal{N}}^\alpha \Phi^n_\alpha \nabla_x q,
\end{array}$$

with time derivatives approximated by forward finite differences. Then, the discretized problem for $\boldsymbol{f} = \mathbf{0}, \boldsymbol{E} = \mathbf{0}$ reads

$$\begin{bmatrix} \Delta t \mathbb{K} + \mathbb{M} & -\Delta t \mathbb{J}^1 + \mathbb{N} & -\Delta t \mathbb{J}^2 + \mathbb{N} & -\mathbb{B} \\ \Delta t \mathbb{L}^1 & \mathbb{Q}^{11} - \Delta t \mathbb{D}^{11} & \mathbb{Q}^{12} - \Delta t \mathbb{D}^{12} & \mathbf{0} \\ \Delta t \mathbb{L}^2 & \mathbb{Q}^{21} - \Delta t \mathbb{D}^{21} & \mathbb{Q}^{22} - \Delta t \mathbb{D}^{22} & \mathbf{0} \\ \mathbb{B} & -\mathbb{C}^1 & -\mathbb{C}^2 & \mathbb{A} \end{bmatrix} \begin{bmatrix} \mathbf{P}^n \\ \mathbf{\Phi}^n_1 \\ \mathbf{\Phi}^n_2 \\ \mathbf{u}^n \end{bmatrix} = \begin{bmatrix} \mathbb{M} \\ \sum\limits_{\beta=1}^{2} \mathbb{Q}^{1\beta} + \mathbb{N}^1 \\ \sum\limits_{\beta=1}^{2} \mathbb{Q}^{2\beta} + \mathbb{N}^2 \\ \mathbb{B} \end{bmatrix} \begin{bmatrix} \mathbf{P}^{n-1} \\ \mathbf{\Phi}^{n-1}_1 \\ \mathbf{\Phi}^{n-1}_2 \\ \mathbf{u}^{n-1} \end{bmatrix}. \tag{4.2.1}$$

The initial values of $\mathbf{P}^0, \mathbf{\Phi}^0_\alpha, \alpha = 1, 2$, and $\mathbf{u}^0$ are taken from a solution of steady state problem. It can be shown that the discretized matrix form of the steady state problem (3.3.39) is formally the same as the one given by (4.1.1).

4.2.3 Solution of steady-state problem

The first step to solve discretized problem (4.2.1) is to obtain the initial values of macroscopic variables. They can be taken as a solution to the steady-state boundary value problem given by (3.3.39) and a set of boundary conditions.

Boundary value problem III

The BVP III is defined by steady-state form of (3.3.39) and by the following boundary conditions:

- on Γ_W: $P^{\text{eff}} = 2.0$, $\boldsymbol{n} \cdot \boldsymbol{j}^0_\alpha = 0$, $\boldsymbol{n} \cdot \boldsymbol{\sigma}_s = 0$,
- on Γ_E $P^{\text{eff}} = 1.0$, $\boldsymbol{n} \cdot \boldsymbol{j}^0_\alpha = 0$, $\boldsymbol{n} \cdot \boldsymbol{\sigma}_s = 0$,
- on Γ_T: $\Phi^{\text{eff}}_1 = \bar{\Phi}_1$, $\quad \boldsymbol{n} \cdot \boldsymbol{\mathcal{J}}^2 \nabla \Phi^{\text{eff}}_2 = \bar{g}$, $\quad \boldsymbol{u}^{\text{eff}} = \mathbf{0}$, $\boldsymbol{n} \cdot \boldsymbol{w} = 0$,
- on Γ_B: $\Phi^{\text{eff}}_1 = \bar{\Phi}_1$, $\quad \boldsymbol{n} \cdot \boldsymbol{\mathcal{J}}^2 \nabla \Phi^{\text{eff}}_2 = \bar{g}$, $\quad \boldsymbol{u}^{\text{eff}} = \mathbf{0}$,$\boldsymbol{n} \cdot \boldsymbol{w} = 0$,

where $\Gamma_A, A \in \{W, E, T, B\}$ refer to the boundaries of porous specimen, see Fig. 4.4. The following values are used, $\bar{\Phi}_1 = 0.1$ and $\bar{g} = 0.001$. This choice of boundary conditions enables us to see the influence of pressure P^0 on the other macroscopic variables.

The steady-state solution of BVP III (*i.e.* solution at $t = 0$) is visualized on the left side of Fig. 4.9. Note that we provide dimensionalized forms of all presented macroscopic fields; see Remark 3.3.1. We observe the deformation of the macroscopic specimen that is caused by the distribution of pressure P^{eff}. We also observe the almost symmetrical distribution of potential Φ_1^{eff} and Φ_2^{eff}.

Using (3.3.42), we may compute the dimensionalized total velocity $\boldsymbol{w}^0$ and its parts $\boldsymbol{w}_p$ and $\boldsymbol{w}_{\Phi_\alpha}, \alpha = 1, 2$ and visualize them in Fig.4.10 on the left. It is evident that the part of the velocity caused by a pressure gradient, *i.e.* $\boldsymbol{w}_p$, contributes to the overall velocity $\boldsymbol{w}$ the most. The visualization of velocity components $\boldsymbol{w}_{\Phi_\alpha}, \alpha = 1, 2$, *i.e.* the flux driven by gradient of potentials, shows that $\boldsymbol{w}_{\Phi_1} > \boldsymbol{w}_{\Phi_2}$. We theorize that it can be explained by attraction forces between ionic specimen with $z_2 = +1$ and negatively charged wall of the microchannels. This could hinder the movement of the positively charged ions and, through the viscous drag, the fluid itself.

Poroelastic vs poropiezoelectric model

The presented simple numerical example BVP III can serve to compare the differences between solutions of poroelastic and piezoelectric models. Note that the semi-discretized matrix form of both macroscopic problems (3.2.52) and (3.3.39) is formally given by (4.1.1) and thus the only difference between them should be caused by different expressions of effective coefficients, *i.e.* expressions (3.2.51) and (3.3.38). In our comparison, we use the microstructure and its material properties given in Sec. 4.2.1 for both models. We follow the same procedure as the one we have used in the previous example and find the macroscopic solution of BVP III for the model describing LEPM and PEPM. Then we visualize the distribution of displacement along the x_1-axis of macroscopic specimen for both cases, see Fig. 4.7.

4.2.4 Solution of time-dependent problem

Finally, we may proceed to solve the time-dependent problem (4.2.1). To demonstrate the macroscopic behavior of our effective model of poropiezoelectric medium, we modify the presented BVP III slightly; we will linearly increase pressure on Γ_E, so that $P^n(t) = 1.0 + \bar{P}t$ on Γ_E. The initial values of effective quantities $(P^n, \Phi_\alpha^0, \boldsymbol{u}^0), \alpha = 1, 2$, are taken from the steady-state solution of BVP III for $\boldsymbol{f} = \boldsymbol{0}, \boldsymbol{E} = \boldsymbol{0}$. The computational time was taken $t \in [0, T]$, where $T = 1s$ and time step $\Delta t \approx 0.05$s.

Vizualization of time-dependency of solution in the given point A of macroscopic specimen (for reference see Fig. 4.4) shows the linear behavior of our model, see Fig. 4.8. The distribution of macroscopic fields at slice through x_1x_2-plane at time $t \in \{0, T\} = \{0, 1\}s$ is depicted in Figs. 4.9 and 4.10.

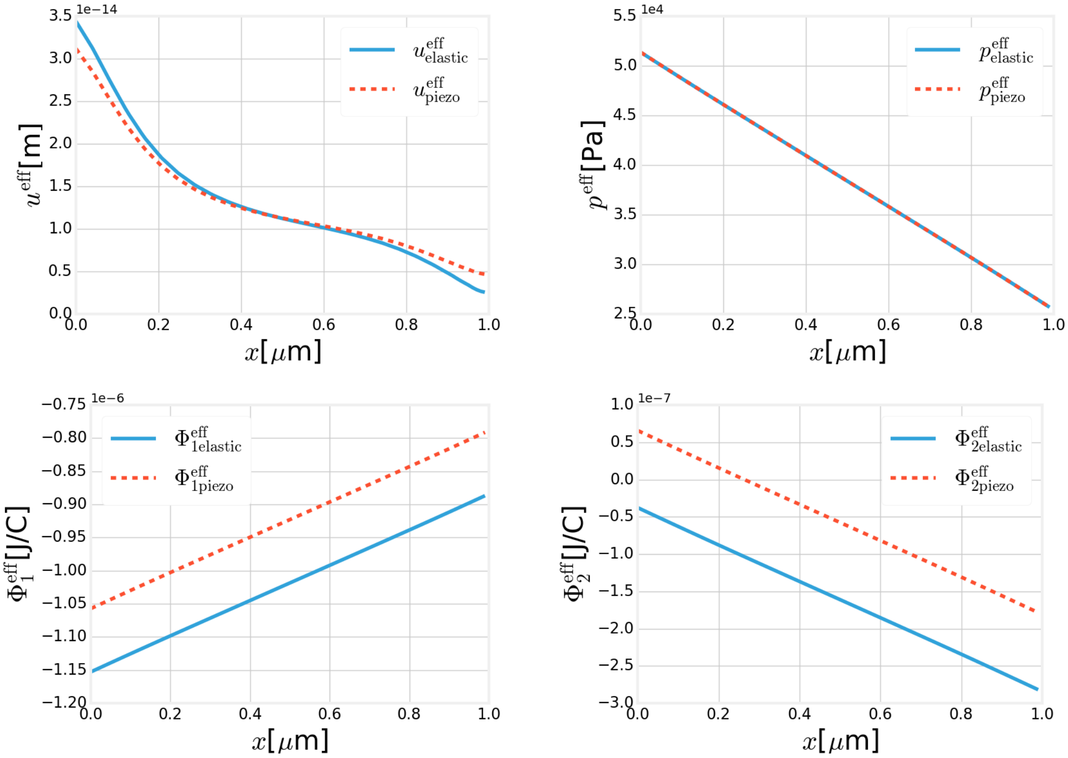

Figure 4.7: Comparison of poroelastic and poropiezoelectric model: distribution of macroscopic fields $\boldsymbol{u}^{\text{eff}}$, P^{eff}, $\Phi^{\text{eff}}_\alpha, \alpha = 1, 2$, obtained as solution of BVP III, along x_1-axis.

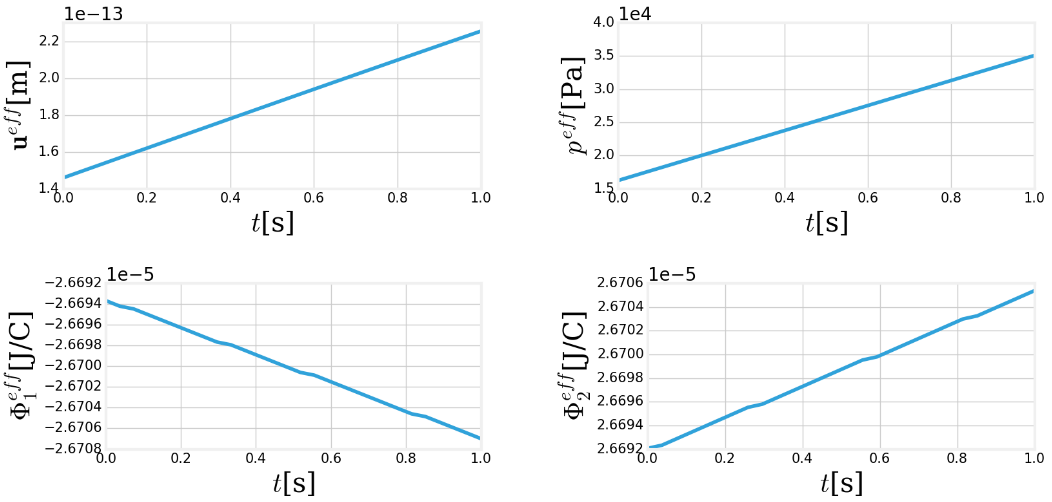

Figure 4.8: Evolution of macroscopic fields $\boldsymbol{u}^{\text{eff}}$, P^{eff}, $\Phi^{\text{eff}}_\alpha, \alpha = 1, 2$ obtained as a solution to homogenized piezoelectric problem at point A of macroscopic specimen, BVP III

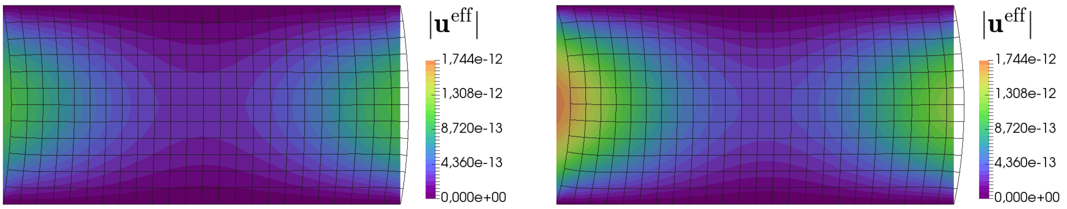

(a) Distribution of displacement $\boldsymbol{u}^0$[m] at $t = 0$

(b) Distribution of displacement $\boldsymbol{u}^0$[m] at $t = T$

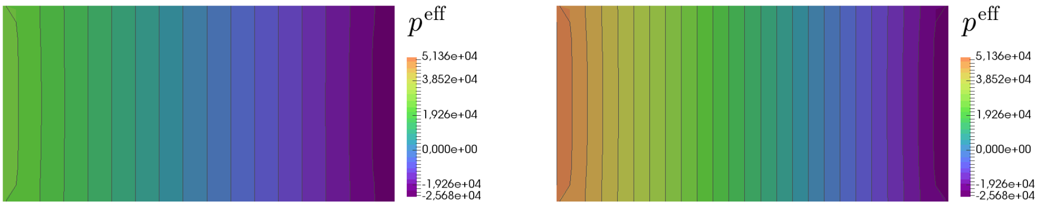

(c) Distribution of global pressure P^0[Pa] at $t = 0$

(d) Distribution of global pressure P^0[Pa] at $t = T$

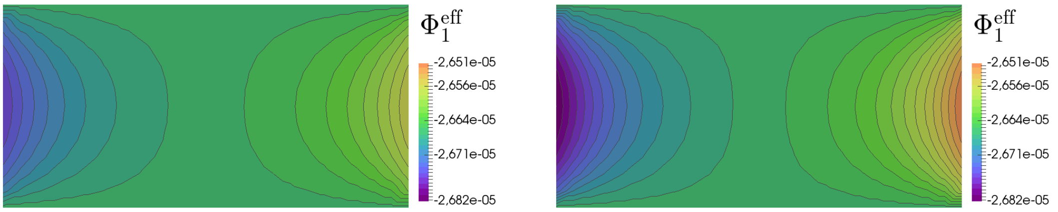

(e) Distribution of potential Φ_1^0[J/C] at $t = 0$

(f) Distribution of potential Φ_1^0[J/C] at $t = T$

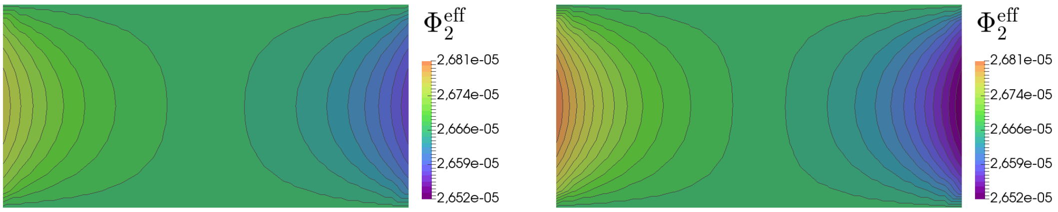

(g) Distribution of potential Φ_2^0[J/C] at $t = 0$

(h) Distribution of potential Φ_2^0[J/C] at $t = T$

Figure 4.9: Solution of time-dependent homogenized piezoelectric problem at computational times $t = 0$ and $t = T$, BVP III

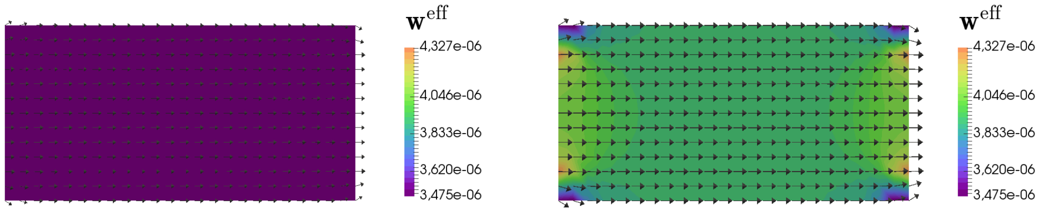

(a) Distribution of velocity $\boldsymbol{w}^{\text{eff}}0$[m/s] at $t = 0$

(b) Distribution of velocity $\boldsymbol{w}^{\text{eff}}$[m/s] at $t = T$

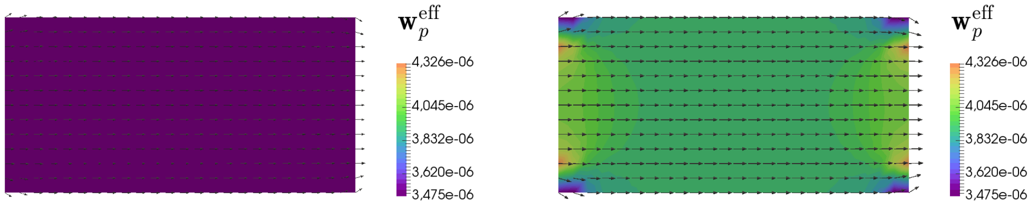

(c) Distribution of velocity $\boldsymbol{w}_p^{\text{eff}}$[m/s] at $t = 0$

(d) Distribution of velocity $\boldsymbol{w}_p^{\text{eff}}$[m/s] at $t = T$

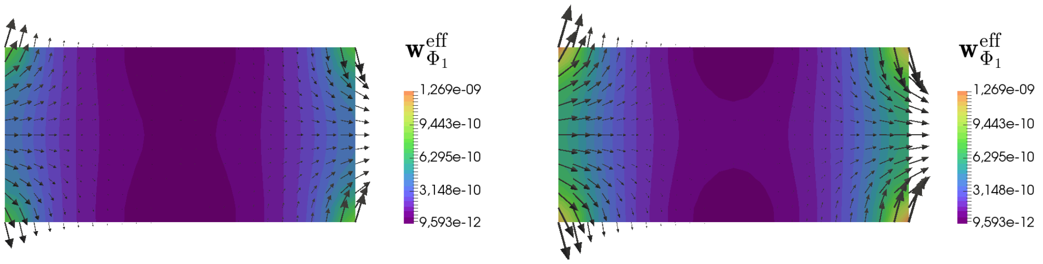

(e) Distribution of velocity $\boldsymbol{w}_{\Phi_1}^{\text{eff}}$[m/s] at $t = 0$

(f) Distribution of velocity $\boldsymbol{w}_{\Phi_1}^{\text{eff}}$[m/s] at $t = T$

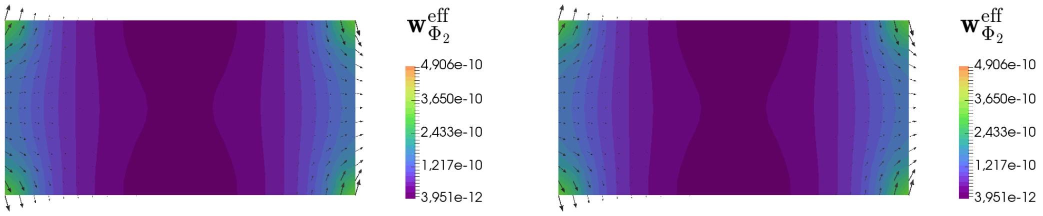

(g) Distribution of velocity $\boldsymbol{w}_{\Phi_2}^{\text{eff}}$[m/s] at $t = 0$

(h) Distribution of velocity $\boldsymbol{w}_{\Phi_2}^{\text{eff}}$[m/s] at $t = 0$

Figure 4.10: Solution of time-dependent homogenized piezoelectric problem at computational times $t = 0$ and $t = T$, BVP III

Chapter 5

Applications

This chapter will provide insight into the possible applications of the presented mathematical models in multiple scientific fields, the most significant being geoscience, energetics, and biomechanics.

Applications in geoscience

The need for effective modeling of the transport of an electrolyte through an electrically charged porous medium in geoscience lies mainly in the problem of swelling of clays. One of the first iterations of such a model was introduced by (Moyne and Murad 2002) and it was later developed by (Allaire et al. 2015).

The swelling of clays is of great importance in geoscience. The self-sealing capacity of clays makes them suitable barriers against environmental pollution by preventing the spread of a pollutant or leakage of contaminated water. Swelling is also a major concern in civil engineering. It can cause volume changes and shifting of the ground resulting in disruption of the stability of man-made structures. On the other hand, the electrokinetic coupling between hydraulic-driven flow and charge transport occurring in the clays play a significant role in electrokinetic remediation of metal-contaminated soils, see (Murad and Moyne 2008).

The majority of clays usually don't exhibit piezoelectric behavior. Therefore, the model presented in Sec. 3.2 is used for the modeling of swelling clays. In some cases that depend on clay particles' deformability, this model can be simplified even further. Suppose the solid particles can be considered rigid. In that case, the solid-fluid interaction will be represented only by the surface charge on their interface and the model will be reduced to the PDEs that describe the fluid phase only, see (Allaire et al. 2013b).

Applications in energetics

The mathematical modeling of ionic transport in piezoelectric porous medium contributes to advances in research, development, and innovation in energetics, especially in the modeling of electrochemical energy storage systems. Between the possible applications of the model presented in Sec. 3.3, which describes the electrolyte flow through PEPM, belong energy conversion in fuel cells, energy storage in batteries, and electrochemical supercapacitors, see (Schmuck and Bazant 2015) and (Emereuwa 2020).

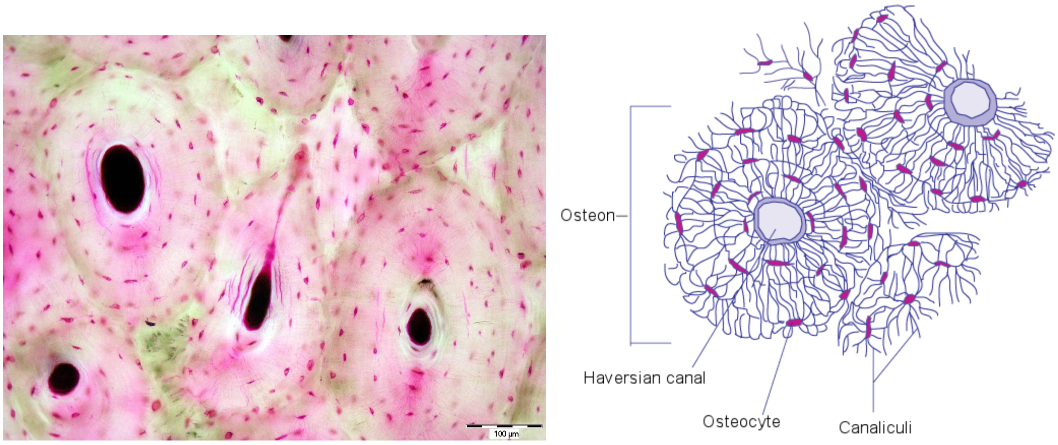

Figure 5.1: Cortical bone structure.

Applications in biomechanics

In biomechanics, electrochemical interactions between ions and negatively charged surfaces of the porous material occur in a few types of biological tissues. For example, in recent years, a significant amount of research has been made into the expansive nature of cartilaginous soft, hydrated tissues. This research helps with the development and design of new biomaterials, such as filling porous materials used in implants and the creation of scaffolds for cell seeding.

However, our interest lies in the modeling of the cortical bone porous structure, where the transport of the ions in the proximity of charged collagen-apatite matrix has shown to play a role in bone regrowth and remodeling. Upon stress, bone tissue generates an electrical potential that directly influences the activity of bone cells. With this in mind, the model of ionic transport in PEPM that was described in Sec. 3.3 seems suitable to the modeling of the cortical bone tissue.

5.1 Modeling of cortical bone porous tissue

The following part of the text focuses solely on the computational modeling of cortical bone as a two-scale material. It reports on the inner structure of the cortical bone and proposes the simplified geometry representations of both structural levels. A significant part of this text deals with the properties of both of the material phases present on the microscopic scale. It proposes an identification procedure for obtaining the parameters that are not directly measurable. Then, we use the findings of this section to perform a numerical simulation of a single bone osteon.

5.1.1 Cortical bone structure

The cortical bone is a strictly hierarchical system with a complicated porous structure on different scale levels. From the macroscopic point of view, the cortical bone tissue consists of a system of approximately cylindrical sub-units called osteons, see Fig. 5.1. Each osteon has a radius of approximately 100-150 μm, (Yoon and Cowin 2008), with a hollow canal in its center. It is called the Haversian canal and contains blood vessels and nerves. The rest of the space is filled with bone fluid. The walls of the Haversian canal are covered by bone cells. Behind this bone cell layer, the walls of the Haversian canal are perforated by a network of small interconnected channels known as canaliculi (Yoon and Cowin 2008). The canaliculi network serves as a connection between the Haversian canal and lacunae. Lacunae are small ellipsoidal cavities that each contain one bone-creating cell,*i.e.* an osteocyte. The lacunar-canalicular network (further referred to by LCN) is saturated by bone fluid that transports nutrients and information about mechanical loading, which interests us the most.

Bone matrix

The bone matrix consists of a tension-resistant network of collagen fibers and crystals of calcium hydroxyapatite, (Lemaire et al. 2008). The incorporation of hydroxyapatite within the collagen fibers contributes to the overall compressive strength of bone. However, due to the presence of collagen, the bone matrix is still deformable. Moreover, it exhibits piezoelectric behavior that was first reported by (Fukada and Yasuda 1957) in a paper concerning dry cortical bone. The authors attribute the origin of this behavior to the collagen fibers that exhibit a polar uniaxial orientation of their molecular dipoles in their structure and so can be considered as a sort of dielectric material. However, this remains only one of the explanations as the exact nature of bone piezoelectricity still remains a subject of scientific research.

Bone fluid

As mentioned previously, small cavities in the bone matrix are saturated by the so-called bone fluid. Sometimes, the term ”bone fluid” is used to describe the serum in the space outside of the blood vessels filling osteonal canals. However, we will use it to refer to the extracellular fluid filling the LCN, (Cowin 1999). The bone fluid serves an important role in the bone structure. It is a coupling medium through which the mechanical forces are translated into mechanobiological, biochemical, mechanochemical, and electromechanical phenomena at the cellular level, see (Milovanovic et al. 2013) and (Hillsley and Frangos 1994).

For the purpose of modeling, we imagine the bone fluid as a salt-water solution. Thus, there are two types of ions with opposite polarization: the cations Na^+ and anions Cl^-, both defined by their respective diffusivity coefficients $D^0_{Na^+}$ and $D^0_{Cl^-}$. The bone fluid is characterized by its dynamic viscosity η_f and is assumed to be an incompressible Newtonian fluid.

5.1.2 Piezoelectricity of the bone

The importance of piezoelectricity in bone was explored since the first description of the phenomena by (Fukada and Yasuda 1957). Piezoelectricity has been shown to play a role in bone adaptation and regeneration. In addition, stress-generated electrical phenomena have been shown to affect the activity of bone cells. However, the exact mechanism remains yet to be fully explained.

The exact origins of piezoelectric properties of the bone tissue are still not fully understood. According to (Mohammadkhah et al. 2019), different piezoelectric responses have been measured for a dry and wet bone which have been attributed to different processes in the bone matrix. The following text briefly describes these processes.

Piezoelectricity of the dry vs. wet bone

The piezoelectric properties of the dry bone are usually attributed to the molecular asymmetry of collagen, which was defined as the main mechanism behind strain-generated potentials in the bone matrix. (Fukada and Yasuda 1957) showed a dependency of generated electric potential on the direction of loading. However, further research performed on the wet bone, (Pienkowski and Pollack 1983), led to diminishing the importance of matrix piezoelectricity as the main contributor to strain-generated potentials.

In comparison to the dry bone, the measurements in a wet bone usually show a lower piezoelectric effect. The research suggests that fluid and ions driven by mechanical loading may have a role in determining the piezoelectric properties of bone tissue. According to findings made by (MacGinitie et al. 1997) and (Pienkowski and Pollack 1983), the streaming potential was proposed as an alternative mechanism to matrix piezoelectricity. Let us remind that streaming potential is generated by a potential difference between two points along the stream of flowing electrolyte solution in the proximity of EDL, see Sec. 2.2.2 for a more detailed explanation.

Properties of Collagen-hydroxyapatite

The experimental measurement in the bone showed that piezoelectricity appears only when the shearing force acts on the oriented collagen fibers so that they slip past one another, (Nalwa 1995). According to (Silva et al. 2001), biopolymers, such as collagen-hydroxyapatite, usually belong to the symmetry group denoted by $D\infty(\infty 2)$, which shows only shear piezoelectricity. For this type of symmetry, the tensors $\boldsymbol{g}$ and $\boldsymbol{d}$ are given by

$$\boldsymbol{g} = \begin{bmatrix} 0 & 0 & 0 & g_{14} & 0 & 0 \\ 0 & 0 & 0 & 0 & g_{25} & 0 \\ 0 & 0 & 0 & 0 & 0 & 0 \end{bmatrix}, \qquad \boldsymbol{d} = \begin{bmatrix} d_{11} & 0 & 0 \\ 0 & d_{22} & 0 \\ 0 & 0 & d_{33} \end{bmatrix}, \tag{5.1.1}$$

where $g_{25} = -g_{14}$ and $d_{22} = d_{11}$. Elastic properties of this type of material are transversal isotropic with the elastic tensor

$$\boldsymbol{A} = \begin{bmatrix} A_{11} & A_{12} & A_{13} & 0 & 0 & 0 \\ A_{12} & A_{11} & A_{13} & 0 & 0 & 0 \\ A_{13} & A_{13} & A_{33} & 0 & 0 & 0 \\ 0 & 0 & 0 & A_{55} & 0 & 0 \\ 0 & 0 & 0 & 0 & A_{55} & 0 \\ 0 & 0 & 0 & 0 & 0 & A_{66} \end{bmatrix}.$$

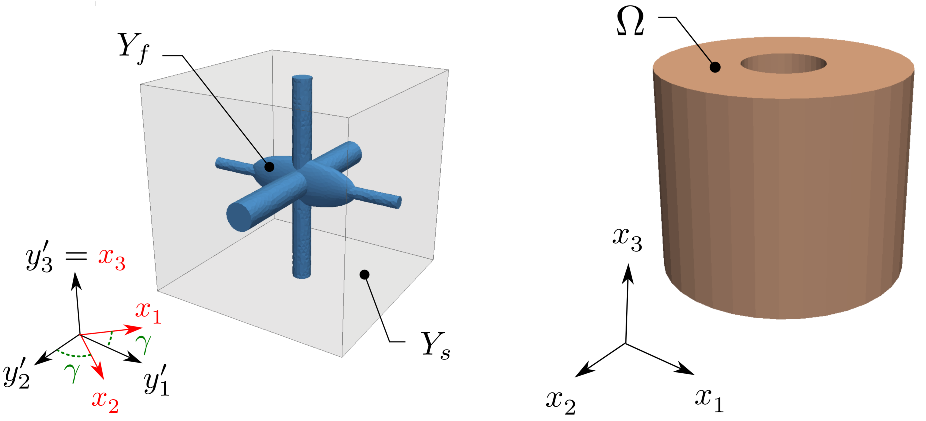

(a) Microstructure geometric representation

(b) Geometric representation of macroscopic (osteonal) level

Figure 5.2: Geometric representation of micro- and macroscopic structure.

The transversal-isotropic elasticity tensor, which may be characterized by Young's moduli E_1, E_3, shear modulus G_{13} and Poisson's ratios ν_{12}, ν_{31}, is than given by

$$\boldsymbol{A} = \begin{bmatrix} \frac{1-\nu_{13}\nu_{31}}{E_1E_3\Theta} & \frac{\nu_{12}+\nu_{13}\nu_{31}}{E_1E_3\Theta} & \frac{\nu_{31}+\nu_{12}\nu_{31}}{E_1E_3\Theta} & 0 & 0 & 0 \\ \frac{\nu_{12}+\nu_{13}\nu_{31}}{E_1E_3\Theta} & \frac{1-\nu_{13}\nu_{31}}{E_1E_3\Theta} & \frac{\nu_{31}+\nu_{12}\nu_{31}}{E_1E_3\Theta} & 0 & 0 & 0 \\ \frac{\nu_{31}+\nu_{12}\nu_{31}}{E_1E_3\Theta} & \frac{1-\nu_{12}^2}{E_1^2\Theta} & \frac{1-\nu_{12}^2}{E_1^2\Theta} & 0 & 0 & 0 \\ 0 & 0 & 0 & 2G_{13} & 0 & 0 \\ 0 & 0 & 0 & 0 & 2G_{13} & 0 \\ 0 & 0 & 0 & 0 & 0 & \frac{E_1}{2(1+\nu_{12})} \end{bmatrix}, \tag{5.1.2}$$

where $\Theta = (1+\nu_{12})(1-\nu_{12}-2\nu_{13}\nu_{31})(E_1^2E_3)^{-1}$ and $\nu_{13} = \nu_{31}E_1E_3^{-1}$.

5.1.3 Modeling of the geometry

The structure of the cortical bone is very complex with multiple porosity levels. We will focus on the osteonal level and refer to it as the macroscopic level. The LCN will represent the porosity of the microscopic level. For the purpose of numerical modeling, we need to simplify the geometry representation on both structural levels. Let us remind that the used homogenization method assumes periodicity of the microstructure and its representation by a cubic RPC Y. Thus, in what follows, we provide a brief description of geometry representation of both the microscopic and the macroscopic levels.

Geometry of microstructure

The microscopic level represents the LCN filled with bone fluid. For the purpose of modeling, we have to simplify the complex geometry of this network into a lattice of RPC Y. This section introduces the main geometric parameters of our model and focuses on a literature survey for estimating their values.

First, we focus on the dimensions of lacunae. The lacunae are usually described as ellipsoidal cavities containing one osteocyte each. We can define the shape of a lacuna as a triaxial ellipsoid with dimensions of semi-axes $a_\mathrm{L}, b_\mathrm{L}, c_\mathrm{L}$. The density of lacunae in the bone tissue can be characterized by the distance l_{L} from one lacuna to another, see (Beno et al. 2006).

The main two parameters describing the geometry of the canaliculi are their radius r_{c} and their number per Lacunae N_{Ca}, which can be obtained following the surface area method from (Beno et al. 2006). This method uses the number of canaliculi per lacunae N_{Ca} and the planar projection to compute the number of canaliculi in each direction. This means that the number of canaliculi in each direction depends on the size of lacunae, *i.e.* semi-axes $a_{\mathrm{L}}, b_{\mathrm{L}}, c_{\mathrm{L}}$.

Modeling a high number of such small channels demands fine meshing, which results in a high number of DOFs and requires a lot of computational time and memory. So, for the sake of simplicity, we choose to approximate the canaliculi in three bigger canals in each direction instead. The three channels have a cross-sectional area corresponding to the sum of all the canaliculi cross-sectional areas in the given direction to preserve the flow rate between lacunae.

Having this in mind, we choose a cubic RPC Y with three cylindrical channels leading in different directions and connected by the ellipsoidal cavity. The geometrical parameters are stated in Tab. 5.1 and the final RPC representing canalicular-lacunar network is depicted in Fig. 5.2a.

Geometry at the osteonal level

The macroscopic level is represented by a single osteon which has an approximately cylindrical shape with a hollow canal in its center. The radius of the cylindrical body is denoted by R_{o} and the radius of the osteonal canal is denoted by r_{o}. The values of both these parameters can be found in Tab. 5.1. Note that these values are highly approximative because of large differences between the dimensions of each osteon. The resulting geometry used for the macroscopic model is depicted in Fig. 5.2b.

Remark 5.1.1 (Microstructure orientation in the osteon) *In the context of the osteonal structure, the microporosity has orthotropic properties aligned with a cylindrical coordinate system introduced for a central canal of the osteon. Therefore, in* (3.3.40)*, we consider all the macroscopic tensors rotated according to such local coordinate system. In Fig. 5.2a, the RVE Y is defined in a local coordinate system $\boldsymbol{y}' = (y'_1, y'_2, y'_3)$ labeled by prime. Thus, within the osteon, the orthotropy axes arising from the homogenization vary, as illustrated in Fig. 5.2a. Thus, to transform effective tensors between orthogonal coordinate systems in 3D, we are using transformation matrix $\boldsymbol{R}$, that should express rotation of the original coordinate system to the new system denoted by $\sqcup'$. the transformation expression for second order tensors reads*

$$\mathcal{Q}'_{ij} = R_{ip} R_{jq} \mathcal{Q}_{pq},$$

and for fourth order tensors it reads

$$\mathcal{Q}'_{ijkl} = R_{ip} R_{jq} R_{kr} R_{ls} \mathcal{Q}_{pqrs}.$$

Symbol	Quantity	Value	Unit	Source
a_{L}	y_1 semi-axis of lacuna in	2.5	μm	(Beno et al. 2006)
b_{L}	y_2 semi-axis of lacuna in	12.5	μm	(Beno et al. 2006)
c_{L}	y_3 semi-axis of lacuna in	5	μm	(Beno et al. 2006)
l_{L}	distance between lacunae	43	μm	(Beno et al. 2006)
r_{c}	radius of canaliculi	0.6	μm	(Beno et al. 2006)
N_{Ca}	canaliculi per lacuna	106	-	(Beno et al. 2006)
R_{o}	radius of osteon	90	μm	(Gauthier et al. 2019)
r_{o}	radius of osteonal canal	30	μm	(Gauthier et al. 2019)

Table 5.1: Geometry parameters of micro- and macrostructure representation

5.2 Identification of material parameters

The aim is to set up a microstructural model of cortical bone tissue with a couple of material parameters related to the microstructure level and to identify these parameters with the help of experimental data and numerical algorithms.

We are interested in the identification of mechanical and piezoelectric properties of the cortical bone. And thus, the vector of optimization parameters $\boldsymbol{a}$ will consist of components of the piezoelectric coupling tensor $\boldsymbol{g}$, the dielectric tensor $\boldsymbol{d}$, and the parameters defining elasticity tensor $\boldsymbol{A}$. We consider the solid matrix consisting of collagen-hydroxyapatite and thus the tensor describing its material properties has the symmetry type and sparsity pattern as given in Sec. 5.1.2. Then, the vector of optimization parameters consists of components of piezoelectricity coupling g_{14}, components of dielectric tensor d_{11}, d_{33} Young's moduli E_1, E_3, shear modulus G_{13} and Poisson's ratios ν_{12}, ν_{31}, so that

$$\boldsymbol{a} = [g_{14}, d_{11}, d_{33}, E_1, E_3, G_{13}, \nu_{12}, \nu_{31}]^T \,. \tag{5.2.1}$$

and $\boldsymbol{a} \in A$, where is a set of all admissible optimization parameters, *i.e.* those that obey admissibility conditions such as constraints, bounds, or other imposed conditions.

In this thesis, we focus on the identification of these parameters in dry bone. Even though the origin of bone piezoelectricity is not attributed solely to the collagen-hydroxyapatite matrix, it should be explored first. Investigation of parameters contributing to piezoelectricity of wet bone should be pursued in follow-up papers.

5.2.1 Identification of parameters in dry bone

This section deals with the identification of the material parameters that characterize mechanical and piezoelectric properties of dry solid skeleton. It presents the identification approach based on optimization and sensitivity analysis.

Firstly, we have to define a state problem. In its general form, a state problem reads: Find $\boldsymbol{x}^0$ such that $\boldsymbol{F}(\boldsymbol{a}, \boldsymbol{x}^0) = 0$, where $\boldsymbol{x}^0$ a vector of state variables that is dependent on the optimization parameters $\boldsymbol{a}$, so that $\boldsymbol{x}^0 = \boldsymbol{x}^0(\boldsymbol{a})$.

State problem

We consider a macroscopic specimen consisting of a drained PEPM. The specimen is fixed on the boundary $\partial_u\Omega$ and subjected to traction force $\boldsymbol{b}$ on the boundary $\partial_\sigma\Omega$.

To describe such a state problem, we start with the steady state of the homogenized problem (3.3.40). Assuming there is no electrolyte present, there is no pressure P^0 nor ionic potentials Φ^0_α to influence the mechanics of solid and the problem (3.3.40) simplifies to the following: Find $\boldsymbol{u}^0$ such that

$$\begin{aligned} -\nabla_x \cdot \boldsymbol{\mathcal{A}} e_x\left(\boldsymbol{u}^0\right) &= 0 \quad \text{in } \Omega, \\ \boldsymbol{\mathcal{A}} e_x\left(\boldsymbol{u}^0\right) \cdot \boldsymbol{n} &= \boldsymbol{b} \text{ on } \partial_\sigma\Omega, \\ \boldsymbol{u}^0 &= \boldsymbol{0} \text{ on } \partial_u\Omega, \end{aligned} \tag{5.2.2}$$

where effective tensor $\boldsymbol{\mathcal{A}}$ is given by $3.3.38_1$. To obtain the weak formulation of this problem, we employ following bilinear forms

$$a_\Omega\left(\boldsymbol{u},\, \boldsymbol{v}\right) = \int_\Omega \boldsymbol{\mathcal{A}} e_x\left(\boldsymbol{u}\right) : e_x\left(\boldsymbol{v}\right), \quad L_\Omega\left(\boldsymbol{v}\right) = \int_{\partial\Omega_b} \boldsymbol{v}\cdot\boldsymbol{b}\,\mathrm{d}S. \tag{5.2.3}$$

Let us define a set U of admissible states, which obey boundary conditions, and set V of state variations by

$$\begin{aligned} U &= \left\{\boldsymbol{u}, \boldsymbol{u} = \boldsymbol{0} \text{ on } \partial_u\Omega\right\}, \\ V &= \left\{\boldsymbol{v}, \boldsymbol{v} = \boldsymbol{0} \text{ on } \partial_u\Omega\right\}. \end{aligned} \tag{5.2.4}$$

Then, the weak form of the state problem (5.2.2) reads: Find $\boldsymbol{u}^0 \in U$ such that

$$a_\Omega\left(\boldsymbol{u}^0,\, \boldsymbol{v}\right) = L_\Omega\left(\boldsymbol{v}\right), \forall \boldsymbol{v} \in V. \tag{5.2.5}$$

This problem will be referred to as the state problem. The only state variable, which occurs in the state problem describing drained bone tissue, is the displacement $\boldsymbol{u}^0 = \boldsymbol{u}^0(\boldsymbol{a})$ and will be referred to as such in the following part of the text.

Optimization problem

Generally, the identification problem is defined as follows: find set of parameters $\hat{\boldsymbol{a}}$ as a solution to the following optimization problem:

$$\begin{gathered} \min_{\hat{\boldsymbol{a}}, \boldsymbol{u}^0(\boldsymbol{a})} F(\boldsymbol{a}, \boldsymbol{u}^0), \boldsymbol{a} \in A, \boldsymbol{u}^0 \in U, \\ \boldsymbol{u}^0 \text{ obeys state problem:} \\ a_\Omega\left(\boldsymbol{u}^0,\, \boldsymbol{v}\right) = L_\Omega\left(\boldsymbol{v}\right), \forall \boldsymbol{v} \in V, \end{gathered} \tag{5.2.6}$$

where F is an objective function. Let us define a projection of displacement field into a direction of the loading by $u^0 = \boldsymbol{u}^0 \cdot \boldsymbol{n}$. The objective function is given by the expression

$$F(\boldsymbol{a}, \boldsymbol{u}^0) = \sum_{i\in\mathcal{I}} \int_{\partial\Omega_\sigma} (u^{\mathrm{exp,i}} - u^{0,i})^2 \tag{5.2.7}$$

with $u^{\mathrm{exp,i}} = \boldsymbol{u}^{\mathrm{exp,i}} \cdot \boldsymbol{n}$ and $u^{0,i} = \boldsymbol{u}^{0,i} \cdot \boldsymbol{n}$, where $\boldsymbol{u}^{\mathrm{exp,i}}$ is the displacement field that was obtained from $i-$th experiment, and $\boldsymbol{u}^{0,\mathrm{i}}$is obtained as solution to the state problem (5.2.5), which simulates i-th experiment. By $i \in \mathcal{I}$, we refers to an index of experimental data, where $\mathcal{I}$ is a set of different setups of the experiments.

The optimization problem (5.2.6) is usually solved by the sequential algorithms with k iterations. Each iteration consists of solving the state problem for a given approximation of optimal parameters $\boldsymbol{a}^k$, obtaining the solution $\boldsymbol{u}^k$ and computing the total differential of objective function $\delta_a^{\mathrm{tot}} F(\boldsymbol{a}^k, \boldsymbol{u}^k)$. Thus, we have to find a way to compute the total differential of the objective function $\delta_a^{\mathrm{tot}} F(\boldsymbol{a}, \boldsymbol{u}^0)$. That can be achieved by sensitivity analysis.

Sensitivity analysis

The sensitivity analysis in the context of material parameter identification is understood as a computation of sensitivity formulas that characterize the dependence of the objective function F on the change of material parameters $\boldsymbol{a}$. This is achieved by computing total derivative of the function $\delta^{\mathrm{tot}} F(\boldsymbol{a}, \boldsymbol{u}^0(\boldsymbol{a}))$ while respecting the admissible states $\boldsymbol{u}^0 = \boldsymbol{u}^0(\boldsymbol{a})$.

In the following text, we introduce the necessary mathematic formulas for the computation of sensitivity and identification of parameters $\boldsymbol{a}$.

One of the effective methods to compute the total derivative $\delta^{\mathrm{tot}} F(\boldsymbol{a}, \boldsymbol{x}(\boldsymbol{a}))$ is the method of adjoint variables. Its advantage is that it results in fewer numerical computations. This can be highly time and memory-saving, especially in the case of a high number of optimization parameters. This method lies in the introduction of adjoint variables $\boldsymbol{\lambda}$ and the so-called adjoint problem.

First, we assign the Lagrange function $\mathcal{L}$ to the optimization problem (5.2.6) in the following form

$$\mathcal{L}(\boldsymbol{a}, \boldsymbol{u}^0, \boldsymbol{\lambda}) = F(\boldsymbol{a}, \boldsymbol{u}^0) + a_\Omega \left(\boldsymbol{u}^0,\, \boldsymbol{\lambda}\right) - L_\Omega\left(\boldsymbol{\lambda}\right), \tag{5.2.8}$$

where $\boldsymbol{\lambda} \in V$ refers to the variable adjoint to the state variable $\boldsymbol{u}^0$.

The adjoint problem is derived from (5.2.8), see for example (Kleiber et al. 1997), and reads

$$a_\Omega \left(\boldsymbol{w},\, \hat{\boldsymbol{\lambda}}\right) = -\delta_u F(\hat{\boldsymbol{a}}, \hat{\boldsymbol{u}}; \boldsymbol{w}) = 2 \int_{\partial\Omega_\sigma} (u^{\mathrm{exp}} - \hat{u}) \cdot \boldsymbol{w}, \quad \forall \boldsymbol{w} \in V, \tag{5.2.9}$$

where the $\hat{\boldsymbol{a}}$ is current approximation of the optimal parameters, $\hat{\boldsymbol{\lambda}}$ is the current solution of the adjoint problem (5.2.9), and $\hat{u} = \hat{\boldsymbol{u}} \cdot \boldsymbol{n}$ is the projection of current solution $\hat{\boldsymbol{u}} = \hat{\boldsymbol{u}}(\hat{\boldsymbol{a}})$ to the state problem (5.2.5) into the direction of loading. The r.h.s. of (5.2.9) was obtained as a partial derivative of theobjective function (5.2.6).

It can be shown that the total derivative of the objective function is equal to the total derivative of the Lagrange function, so that $\delta_a^{\mathrm{tot}} F = \delta_a^{\mathrm{tot}} \mathcal{L}$ and thus we express $\delta_a^{\mathrm{tot}} \mathcal{L}$ in $(\hat{\boldsymbol{a}}, \hat{\boldsymbol{u}}, \hat{\boldsymbol{\lambda}})$ which yields

$$\delta_a^{\mathrm{tot}} \mathcal{L}(\hat{\boldsymbol{a}}, \hat{\boldsymbol{u}}, \hat{\boldsymbol{\lambda}}) = \delta_a F(\hat{\boldsymbol{a}}, \hat{\boldsymbol{u}}) + \delta_a a_\Omega \left(\hat{\boldsymbol{u}},\, \hat{\boldsymbol{\lambda}}\right) - \delta_a L_\Omega \left(\hat{\boldsymbol{\lambda}}\right) + \delta_u F(\hat{\boldsymbol{a}}, \hat{\boldsymbol{u}}; \delta \boldsymbol{u}) + a_\Omega \left(\widehat{\delta \boldsymbol{u}},\, \hat{\boldsymbol{\lambda}}\right). \tag{5.2.10}$$

Because $\hat{\boldsymbol{\lambda}}$ is the adjoint state, the last two terms in (5.2.10) fulfill the adjoint equation (5.2.9) and the total differential of the objective function is given by

$$\delta_a^{\mathrm{tot}} F(\boldsymbol{a}, \boldsymbol{u}) = \delta_a F(\boldsymbol{a}, \boldsymbol{u}) + \delta_a a_\Omega \left(\boldsymbol{u},\, \boldsymbol{\lambda}\right) - \delta_a L_\Omega \left(\boldsymbol{\lambda}\right), \tag{5.2.11}$$

where $\boldsymbol{\lambda} \in V$ is the adjoint state to state $\boldsymbol{u} \in U$. To evaluate total differential of the objective function, we need to express partial derivatives of all the terms of (5.2.11). However, it is evident from the definition of $F(\boldsymbol{a}, \boldsymbol{u})$ and $L_\Omega(\boldsymbol{v})$ that their partial derivatives with respect to the components of vector $\boldsymbol{a}$ are

$$\delta_a F(\boldsymbol{a}, \boldsymbol{u}) = 0, \quad \delta_a L_\Omega(\boldsymbol{v}) = 0. \tag{5.2.12}$$

Thus, what remains to deal with, is the partial derivative $\delta_a a_\Omega(\boldsymbol{u},\, \boldsymbol{v})$.

The change of optimization parameters $\boldsymbol{a}$ will influence the material characteristics given on the microscopic scale and, in turn, computation of the corrector base functions involved in the expressions of effective coefficients. Thus, the computation of the partial derivative $\delta_a a_\Omega(\boldsymbol{u},\, \boldsymbol{v})$ lies in the computation of sensitivity of effective elasticity $\boldsymbol{\mathcal{A}}$ with respect to change of material parameters $\boldsymbol{a}$.

Sensitivity analysis of homogenized elasticity tensor

In this part of the text, we perform sensitivity analysis of the effective elasticity tensor $\boldsymbol{\mathcal{A}}$ defined in (3.3.38). We will follow a similar approach as in (Rohan 2003).

For the sake of brevity, we shall employ the following notation related to the correctors introduced in (3.3.33),

$$\Xi^{ij} = \boldsymbol{w}^{ij} + \Pi^{ij}, \quad \delta_a \Xi^{ij} = \delta_a \boldsymbol{w}^{ij}. \tag{5.2.13}$$

Then, the sensitivity of the elasticity tensor $\mathcal{A}_{ijkl}$ is obtained by differentiating $(3.3.38)_1$, which yields

$$\begin{aligned}\delta_a \mathcal{A}_{ijkl} = {} & \delta_a a_{Y_s}\left(\Xi^{ij},\, \Xi^{kl}\right) + a_{Y_s}\left(\delta_a \boldsymbol{w}^{ij},\, \Xi^{kl}\right) + a_{Y_s}\left(\Xi^{ij},\, \delta_a \boldsymbol{w}^{kl}\right) + \\ & + \delta_a d_{Y_s}\left(\eta^{ij},\, \eta^{kl}\right) + d_{Y_s}\left(\delta_a \eta^{ij},\, \eta^{kl}\right) + d_{Y_s}\left(\eta^{ij},\, \delta_a \eta^{kl}\right).\end{aligned} \tag{5.2.14}$$

Now, to eliminate $\delta_a \boldsymbol{w}^{kl}$, we substitute $\tilde{\boldsymbol{v}} \equiv \delta_a \boldsymbol{w}^{kl}$ into the local problem $(3.3.33)_1$, which yields

$$a_{Y_s}\left(\Xi^{ij},\, \delta_a \boldsymbol{w}^{kl}\right) = g_{Y_s}\left(\delta_a \boldsymbol{w}^{kl},\, \eta^{ij}\right). \tag{5.2.15}$$

The same relation will serve to eliminate $\delta_a \boldsymbol{w}^{ij}$, only for $ij = kl$. Then, we differentiate the local problem $(3.3.33)_2$ for $ij = kl$ and for $\tilde{\psi}_f \equiv \eta^{ij}$, which yield

$$\delta_a g_{Y_s}\left(\Xi^{kl},\, \eta^{ij}\right) = -g_{Y_s}\left(\delta_a \boldsymbol{w}^{kl},\, \eta^{ij}\right) - \delta_a d_{Y_s}\left(\eta^{kl},\, \eta^{ij}\right) - d_{Y_s}\left(\delta_a \eta^{kl},\, \eta^{ij}\right). \tag{5.2.16}$$

Once again, this expression can be rewritten for $ij = kl$. All that remains is to substitute (5.2.15) and (5.2.16) into (5.2.14), which yields

$$\delta_a \mathcal{A}_{ijkl} = \delta_a a_{Y_s}\left(\Xi^{ij},\, \Xi^{kl}\right) - \delta_a d_{Y_s}\left(\eta^{kl},\, \eta^{ij}\right) - \delta_a g_{Y_s}\left(\Xi^{kl},\, \eta^{ij}\right) - \delta_a g_{Y_s}\left(\Xi^{ij},\, \eta^{kl}\right). \tag{5.2.17}$$

For numerical computation of terms present in (5.2.17), we need to express partial derivatives of material tensors on the microscopic scale, *i.e.* $\delta_a \boldsymbol{A}, \delta_a \boldsymbol{g}, \delta_a \boldsymbol{d}$. These can be found in Appendix C.

Following this approach, we compute the sensitivities of elastic tensor $\boldsymbol{\mathcal{A}}$ with respect to optimization parameters $\boldsymbol{a}$. For further reference, the sensitivities obtained by sensitivity formula (5.2.17) will be denoted by $\delta_a \boldsymbol{\mathcal{A}}|_{SA}$.

Sensitivity by finite differences

The finite difference method is sometimes used as a simple way to calculate sensitivities but usually is very demanding on the computational time and memory. However, it can be used to check the sensitivity of effective elasticity $\boldsymbol{\mathcal{A}}$ that we computed by sensitivity formula given by (5.2.17). Note that the sensitivities to the specific material parameter a_i are given in Appendix C.

Remark 5.2.1 (Approximation of sensitivity by finite differences) *The derivative of any function* φ *at point* x *can be approximated by the central finite difference formula which reads*

$$\frac{d\varphi(x)}{dx} \approx \frac{\varphi(x+\Delta x) - \varphi(x-\Delta x)}{2\Delta x},$$

where Δx *denotes a step in the value of* x*. In a similar fashion, the sensitivity to the parameter* $\boldsymbol{a}$ *of the general effective coefficient* $\mathcal{Q}$ *can be approximated by central difference, which yields*

$$\delta_{a}\mathcal{Q}|_{FD} \approx \frac{\mathcal{Q}|_{+\Delta\boldsymbol{a}} - \mathcal{Q}|_{-\Delta\boldsymbol{a}}}{2\Delta\boldsymbol{a}},$$

where $\quad \mathcal{Q}|_{+\Delta\boldsymbol{a}} = \mathcal{Q}(\boldsymbol{a}+\Delta\boldsymbol{a})$ *and* $\mathcal{Q}|_{-\Delta\boldsymbol{a}} = \mathcal{Q}(\boldsymbol{a}-\Delta\boldsymbol{a})$*.*

Following Remark 5.2.1, we find an approximation of sensitivities of the elastic tensor $\boldsymbol{\mathcal{A}}$ to each component of vector of optimization parameters $\boldsymbol{a} = (a_i)$ and refer to it by $\delta_{a_i}\boldsymbol{\mathcal{A}}|_{\mathrm{FD}}$. Then, we use it to verify the sensitivity formula (5.2.17) for $\delta_{a_i}\boldsymbol{\mathcal{A}}|_{SA}$. For this purpose, we define the relative error between components of sensitivities $\delta_{a_i}\boldsymbol{\mathcal{A}}|_{\mathrm{FD}} = \{\delta_{a_i}\mathcal{A}_{klmn}|_{\mathrm{FD}}\}$ and $\delta_{a_i}\boldsymbol{\mathcal{A}}|_{SA} = \{\delta_{a_i}\mathcal{A}_{klmn}|_{\mathrm{SA}}\}$ as

$$\epsilon_{\mathrm{rel}}(\delta_{a_i}\mathcal{A}_{klmn}) = \frac{\mathrm{abs}\left(\delta_{a_i}\mathcal{A}_{klmn}|_{FD} - \delta_{a_i}\mathcal{A}_{klmn}|_{SA}\right)}{\mathrm{abs}(\delta_{a_i}\mathcal{A}_{klmn}|_{FD})}. \tag{5.2.18}$$

Using this expression, the order of relative error between $\delta_{a_i}\boldsymbol{\mathcal{A}}|_{FD}$ and $\delta_{a_i}\boldsymbol{\mathcal{A}}|_{SA}$ is depicted in Fig. 5.3. While using Voigt form, the order of relative error $\epsilon_{\mathrm{rel}}(\delta_{a_i}\boldsymbol{\mathcal{A}})$ is visualized for each component of sensitivity $\delta_{a_i}\boldsymbol{\mathcal{A}} = \{\delta_{a_i}\mathcal{A}_{klmn}\}$.

Similarly, we may compute the total differential of the objective function by finite differences which give us an approximation $\delta^{\mathrm{tot}}_{a_i}F|_{FD}$. Once again, this approximation can serve to verify the total differential of the objective function $\delta^{\mathrm{tot}}_{a_i}F|_{SA}$. The relative error between these values for each component a_i of the optimization vector $\boldsymbol{a}$ is given by

$$\epsilon_{\mathrm{rel}}(\delta^{\mathrm{tot}}_{a_i}F) = \frac{\mathrm{abs}\left(\delta^{\mathrm{tot}}_{a_i}F|_{FD} - \delta^{\mathrm{tot}}_{a_i}F|_{SA}\right)}{\mathrm{abs}(\delta^{\mathrm{tot}}_{a_i}F|_{FD})}. \tag{5.2.19}$$

This expression was used to compute the relative error $\epsilon_{\mathrm{rel}}(\delta^{\mathrm{tot}}_{a_i}F)$ for each identification parameter in the vector $\boldsymbol{a} = (a_i)$ and for decreasing value of step $\Delta a_i \in \{10^{-1}, 10^{-2}, 10^{-3}\}$. These values are shown in Tab. 5.2 from which it is evident, that with decreasing step Δa_i the relative errors are also decreasing. However, at a certain length of the step Δa_i, the relative errors stop decreasing and stabilize around a certain value with only minor fluctuations, as seen in Fig. 5.4.

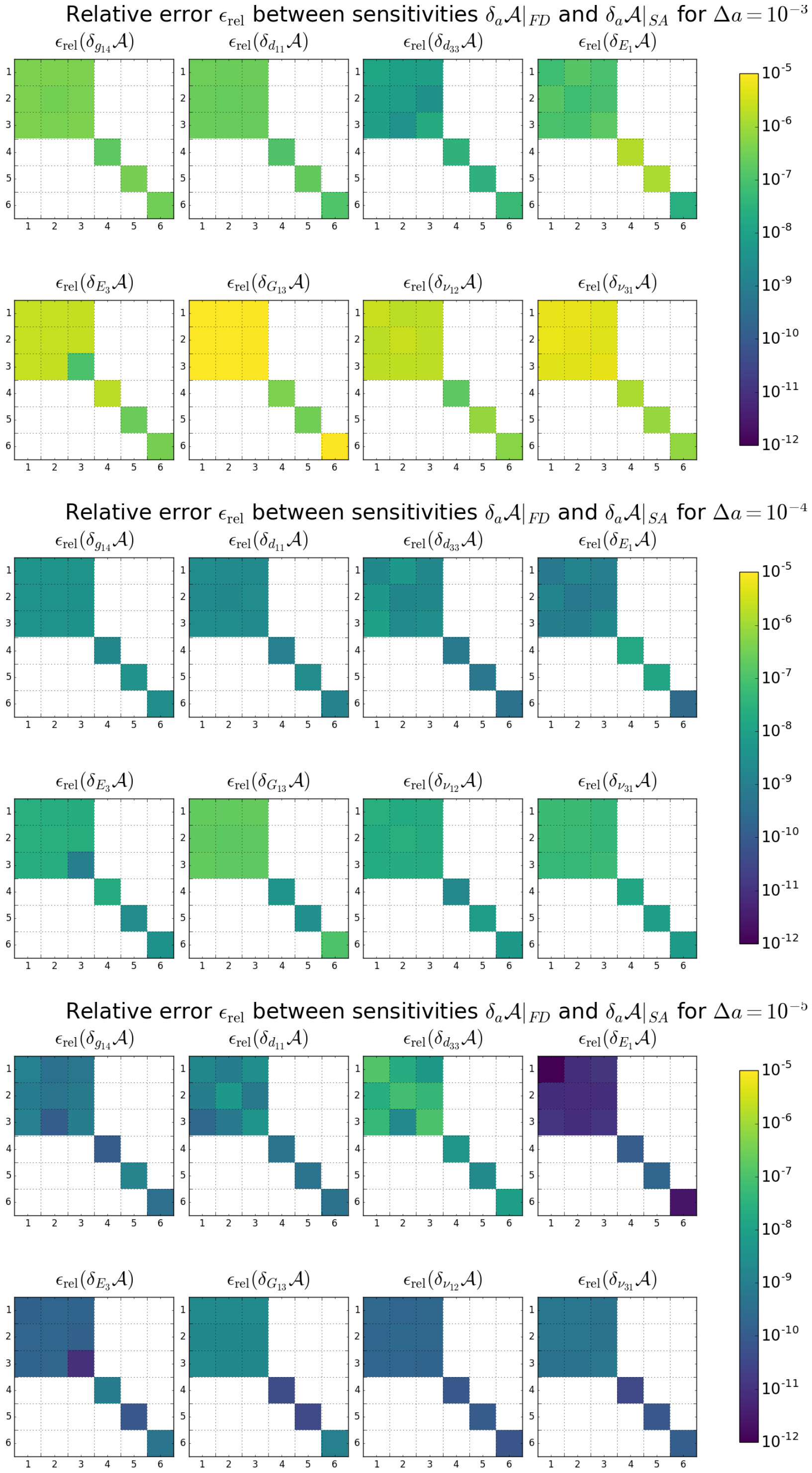

Figure 5.3: The orders of magnitude of relative error $\epsilon_{\rm rel}$ between sensitivities $\delta_a\boldsymbol{\mathcal{A}}$ obtained by sensitivity formulas and by finite difference approximations for $\Delta a \in \{10^{-3}, 10^{-4}, 10^{-5}\}$. The relative error of each component of the tensor $\delta_a\boldsymbol{\mathcal{A}} = \{\delta_a\mathcal{A}_{ijkl}\}$ is shown.The expression of relative error $\epsilon_{\rm rel}$ is given by (5.2.18).

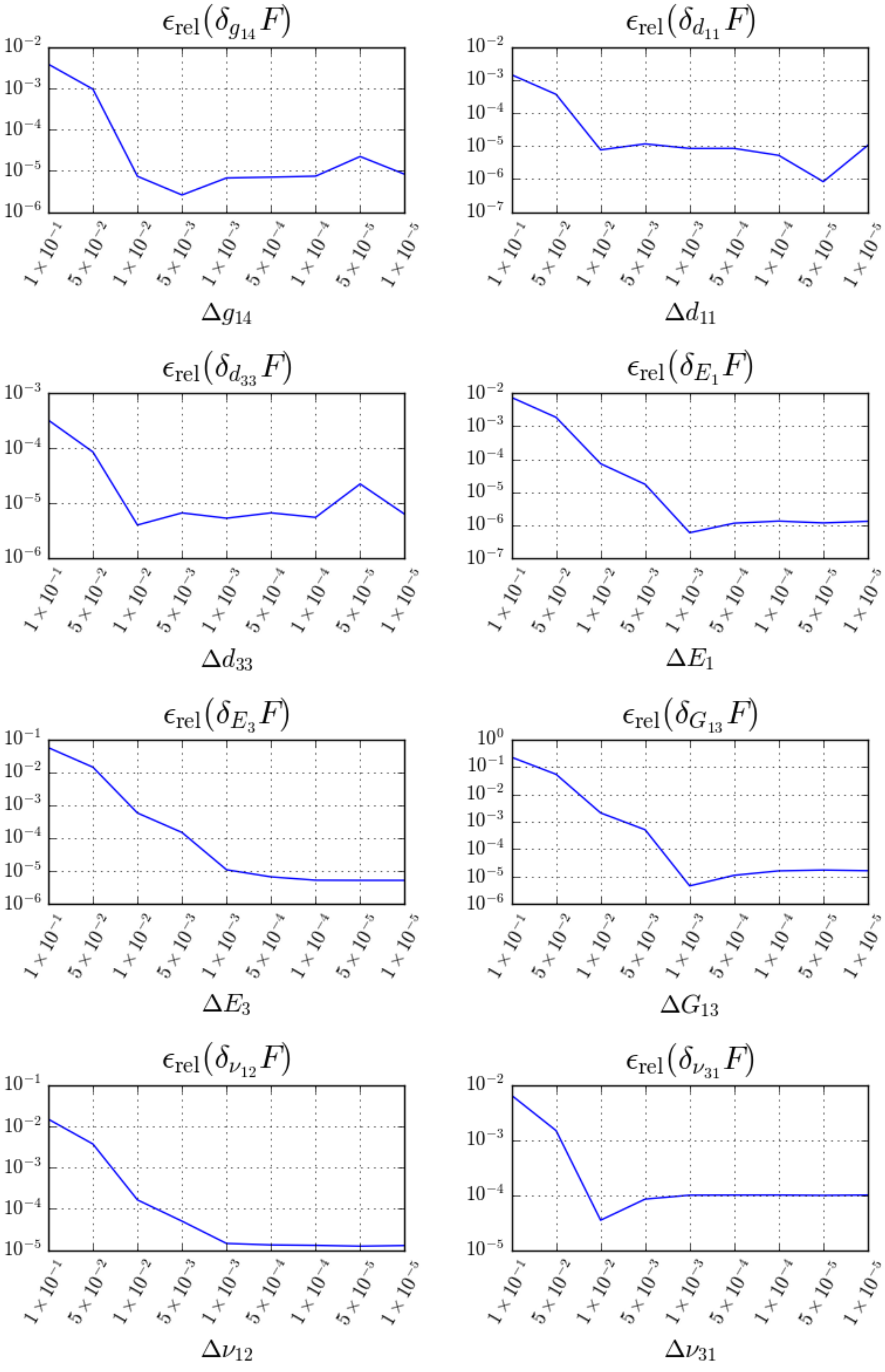

Figure 5.4: The order of magnitude of the relative error ϵ_{rel} between the total differential of the objective function obtained by sensitivity formulae $\delta_{a_i}^{\mathrm{tot}}F|_{SA}$ and its approximation by finite difference $\delta_{a_i}^{\mathrm{tot}}F|_{FD}$ for $\Delta a_i \in \{10^{-1}, ..., 10^{-5}\}$. After certain length of the step Δa_i is achieved, the relative error cease to decrease and stop at certain order of magnitude with minor fluctuations only.

a_i	$\delta_{a_i}^{\mathrm{tot}}F$	$\epsilon_{\mathrm{rel}}(\delta_{a_i}^{\mathrm{tot}}F)$		
		$\Delta a_i = 10^{-1}$	$\Delta a_i = 10^{-2}$	$\Delta a_i = 10^{-3}$
E_1	-7.48×10^{-4}	7.50×10^{-3}	7.31×10^{-5}	5.88×10^{-7}
E_3	-5.67×10^{-5}	5.57×10^{-2}	5.80×10^{-4}	1.10×10^{-5}
G_{13}	-6.81×10^{-3}	2.22×10^{-1}	2.09×10^{-3}	4.60×10^{-6}
ν_{12}	-6.09×10^{-5}	1.50×10^{-2}	1.65×10^{-4}	1.44×10^{-5}
ν_{31}	-3.05×10^{-4}	6.57×10^{-3}	3.49×10^{-5}	9.97×10^{-5}
g_{14}	-3.14×10^{-6}	3.88×10^{-3}	7.40×10^{-6}	6.74×10^{-6}
d_{11}	9.99×10^{-8}	1.47×10^{-3}	7.72×10^{-6}	8.52×10^{-6}
d_{33}	2.69×10^{-8}	3.24×10^{-4}	4.00×10^{-6}	5.31×10^{-6}

Table 5.2: The relative error ϵ_{rel} between the total differential of the objective function $\delta_{a_i}^{\mathrm{tot}}F|_{SA}$ and its approximation by finite difference $\delta_{a_i}^{\mathrm{tot}}F|_{FD}$ for $\Delta a_i \in \{10^{-1}, 10^{-2}, 10^{-3}\}$.

Tab. 5.2 also shows the computed values of the total differential of the objective function with regard to each optimization parameter. The sensitivity of objective function $F(\boldsymbol{a}, \boldsymbol{u})$ on dielectric permitivity parameters d_{11} and d_{33} is very low and they would proof difficult to identify by optimization. However, these parameters can be measured directly through a dielectric measurement, see for example Silva et al. 2001. Thus, we may assume that the dielectric permitivity parameters d_{11} and d_{33} are known and reduce the number of parameters to be identified from eight to six. From now on, we will work with the reduced vector of identification parameters $\boldsymbol{a} = (a_i)$ with the following components

$$\boldsymbol{a} = [g_{14}, E_1, E_3, G_{13}, \nu_{12}, \nu_{31}]^T . \tag{5.2.20}$$

5.2.2 Implementation and numerical results

This part will provide an insight into the implementation of the identification procedure and the chosen optimization method.

Fictitious experiment

A set of experimentally measured data is necessary to successfully identify any material parameters. In our case it would be the set of measured displacement $\boldsymbol{u}^{exp,i}, i \in \mathcal{I}$ as it appears in our definition of objective function (5.2.7). If we want to test the identification process, knowing the correct material parameters $\boldsymbol{a}$ beforehand may be beneficial. We can make use of the so-called fictitious experiment to achieve this. The idea behind the fictitious experiment is to generate a set of $\boldsymbol{u}^i_{exp}$ for known material parameters $\hat{\boldsymbol{a}}$. Then, we forgo "correct" parameters $\hat{\boldsymbol{a}}$ and use the data set $\boldsymbol{u}^i_{exp}$ as an input to our identification framework. If the identification process works correctly, we expect it to identify original parameters $\boldsymbol{a}^{\mathrm{opt}} \approx \hat{\boldsymbol{a}}$.

We propose following setup of a fictitious experiment to generate data $\boldsymbol{u}^i_{exp}$. We imagine a set $\mathcal{I}$ of n cubic macroscopic specimens with different orientations of microstructure, see Fig. 5.5. Similarly to the Remark 5.1.1, the RVE Y is defined in a local coordinate system $\boldsymbol{y}' = (y_1', y_2', y_3')$ labeled by prime. Then, the microstructure orientation within the macroscopic specimen is defined by the angle of rotation $\gamma^i, i \in \mathcal{I}$ of the RVE Y around $y'_2 = x_2$ axis.

As a fictitious experiment setting, we use a static uniaxial tensile test. However, one uniaxial test does not provide enough information to evaluate five independent elastic constants of transversally isotropic material, see for example (Nejati et al. 2019). As a compensation, we will perform a tensile tests on each specimen from set $\hat{\mathcal{I}}$, with loading force $\boldsymbol{b}$ acting in direction x_1, see Fig. 5.5. Thus, we will obtain set $\mathcal{I}$ of n experimental data $\boldsymbol{u}^i_{exp}, i \in \mathcal{I}$, which should provide enough information to identify all of the six independent material parameters, *i.e.* one piezoelectric and five elastic parameters.

For the set of known optimal parameters $\hat{\boldsymbol{a}}$ that describes the material of specimens used in the fictitious experiment, we chose the values stated in Tab. 5.3. These values represent the optimum $\boldsymbol{a}^{\text{opt}} \equiv \hat{\boldsymbol{a}}$ and, assuming that the identification procedure works correctly, we expect to arrive at these values through the identification process.

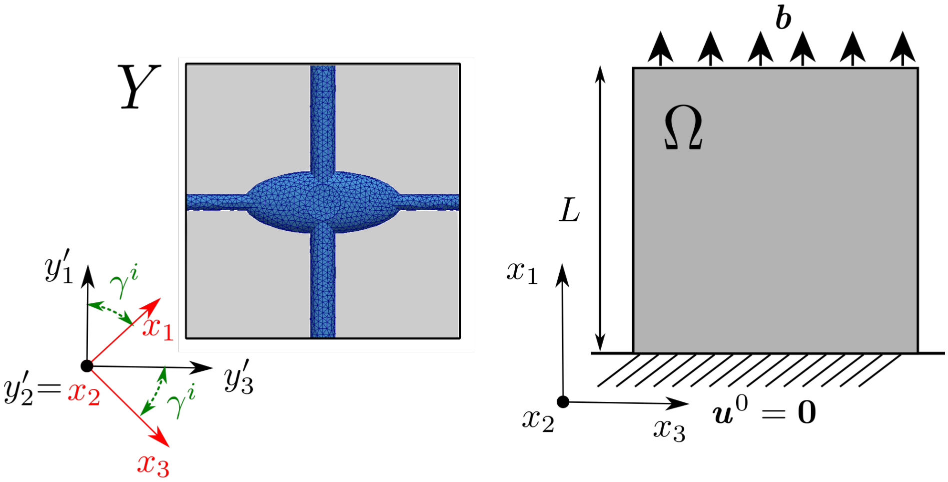

Figure 5.5: Left: Microscopic RVE Y with local coordinate system $\boldsymbol{y}'$; Right: Fictitious experiment setup for identification of material parameters.

Symbol	Quantity	Value	Unit
g_{14}	Piezoelectric coupling	18.4559×10^{-4} †	C/m^2
d_{11}	Dielectric permitivity	88.54×10^{-12}	$\text{C}^2/\text{N}\cdot\text{m}^2$
d_{33}	Dielectric permitivity	106.25×10^{-12}	$\text{C}^2/\text{N}\cdot\text{m}^2$
E_1	Young modulus	13.90×10^9	Pa
E_3	Young modulus	22.21×10^9	Pa
G_{14}	Shear modulus	3.18×10^9	Pa
ν_{12}	Poisson's ratio	0.2537	-
ν_{31}	Poisson's ratio	0.3002	-

Table 5.3: The mechanical and piezoelectric parameters characterizing the collagen-hydroxyapatite matrix of cortical bone tissue. Sources: (Silva et al. 2001),(Fotiadis et al. 1999) and (Predoi-Racila and Crolet 2008)

† Computed from piezoelectric coefficient of strain-charge form.

Component of $\boldsymbol{a}$	$\boldsymbol{a}^0$	$\boldsymbol{a}^L$	$\boldsymbol{a}^U$	Units
g_{14}	1×10^{-3}	0.0	5×10^{-3}	C/m^2
E_1	12×10^9	7×10^9	25×10^9	Pa
E_3	20×10^9	7×10^9	25×10^9	Pa
G_{13}	2×10^9	1×10^9	5×10^9	Pa
ν_{12}	0.24	0.22	0.29	-
ν_{31}	0.28	0.26	0.4	-

Table 5.4: The chosen initial values and lover and upper limits of components of vector of optimization parameters $\boldsymbol{a}$.

Implementation of identification procedure

Implementation of the identification problem consists of four separate parts: computation of homogenized coefficients for given approximation of identification parameters $\boldsymbol{a}_{\text{opt}} \approx \boldsymbol{a}^k$, computation of solution $\boldsymbol{u}^k = \boldsymbol{u}(\boldsymbol{a}^k)$ of state problem (5.2.2), solution $\lambda^k = \lambda(\boldsymbol{a}^k, \boldsymbol{u}^k)$ of adjoint problem (5.2.9), and finally, implementation of the sequential algorithm which calls the previous parts and solves optimization problem (5.2.6)–(5.2.7).

We implemented the homogenization script and the simulation of state problem in the *SfePy* software. The implementation process was described in more detail in Sec. 4.1.1. The identification script is written in Python programing language with the help of *SciPy.optimize* module, which provides a collection of optimization algorithms, see (Virtanen et al. 2020).

To find a minimum of the objective function (5.2.7), we chose the truncated Newton (TNC) algorithm, (Nash 2000). This particular method uses the Conjugate-Gradient method to approximately solve the Newton system in a finite number of iterations, (Dixon and Price 1988). It works well with a large number of independent parameters and enables us to easily apply box constraints, *i.e.* $\boldsymbol{a} \in [\boldsymbol{a}^L, \boldsymbol{a}^U]$. We have chosen the values of bounds after considering the usual range of values of material properties of cortical bone found in literature, *e.g.* (Rho et al. 1998; Yoon and Cowin 2008; Vatsa et al. 2008). The values of bounds are shown in Tab. 5.4 as well as the initial approximation of optimum $\boldsymbol{a}_{\text{opt}} \approx \hat{\boldsymbol{a}}$.

To better understand the structure of implementation, we list the main steps of the identification procedure, see Fig. 5.6:

1. Generate the experimental data $\boldsymbol{u}^i_{exp}, i \in \mathcal{I}$ by the simulation of fictitious experiment for known $\boldsymbol{a}^{\text{opt}} := \hat{\boldsymbol{a}}$.
2. Choose the initial value of material parameters $\boldsymbol{a}^0$, setup the bounds $\boldsymbol{a}^L$ and $\boldsymbol{a}^U$ and the stopping condition $|F(\boldsymbol{a}, \boldsymbol{u})| < \epsilon$.
3. Begin the iteration process for $k := 0$:
    (a) Set current approximation of optimum as $\boldsymbol{a}^{\text{opt}} \approx \boldsymbol{a}^k$.
    (b) Compute the cell problems (3.3.29)–(3.3.35) and evaluate the effective coefficients (3.3.36)–(3.3.38) for current approximation of the material parameters $\boldsymbol{a}^{\text{opt}} \approx \boldsymbol{a}^k$.

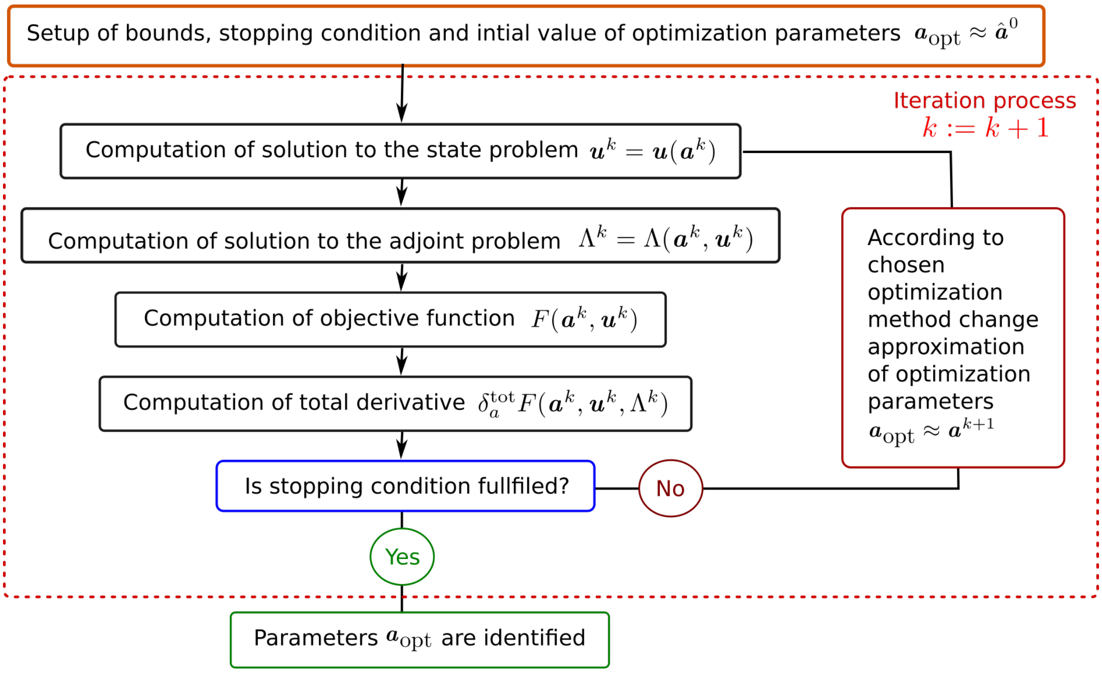

Figure 5.6: Illustration of sequential algorithm used for identification of material parameters $\boldsymbol{a}$.

(c) Solve the state problem (5.2.2) that simulates setup of the fictitious experiment for current approximation of material parameters $\boldsymbol{a}^{\text{opt}} \approx \boldsymbol{a}^k$ and obtain the solution $\boldsymbol{u}^k = \boldsymbol{u}(\boldsymbol{a}^k)$.

(d) Enumerate current value of the objective function $F(\boldsymbol{a}^k, \boldsymbol{u}^k)$ given by (5.2.7).

(e) Find the solution $\lambda^k = \lambda(\boldsymbol{a}^k, \boldsymbol{u}^k)$ of the adjoint problem (5.2.9).

(f) Compute the total differential of the objective function $\delta_{a_i}^{\text{tot}} F(\boldsymbol{a}^k, \boldsymbol{u}^k, \lambda^k)$ for each material parameter a_i using expression (5.2.11).

(g) Check if stopping condition $|F(\boldsymbol{a}, \boldsymbol{u})| < \epsilon$ on objective function is met:

   i. If the stopping condition is not met: According to the chosen optimization scheme use the total differential of the objective function $\delta_{a_i}^{\text{tot}} F(\boldsymbol{a}^k, \boldsymbol{u}^k, \lambda^k)$ to determine new iteration $\boldsymbol{a}^{k+1}$. Then set $k := k + 1$ and repeat from step (a).

   ii. If the stopping condition is met: Stop the iteration process and proceed to step 4 with $\boldsymbol{a}^{\text{opt}} := \boldsymbol{a}^k$.

4. Check, that the identified parameters $\boldsymbol{a}^{\text{opt}} \approxeq \hat{\boldsymbol{a}}$.

Results

In this part, we report on the result of the identification procedure described above. Setting the initial value $\boldsymbol{a}^0$ and bounds $\boldsymbol{a}^L$ and $\boldsymbol{a}^U$ to values shown in Tab. 5.4 and choosing the suitable stopping condition $|F(\boldsymbol{a}, \boldsymbol{u})| < \epsilon$ with $\epsilon = 10^{-8}$.

One of the challenges was finding a suitable line search precision setting for the Conjugate-Gradient method since the more ”coarse” precision showed to be

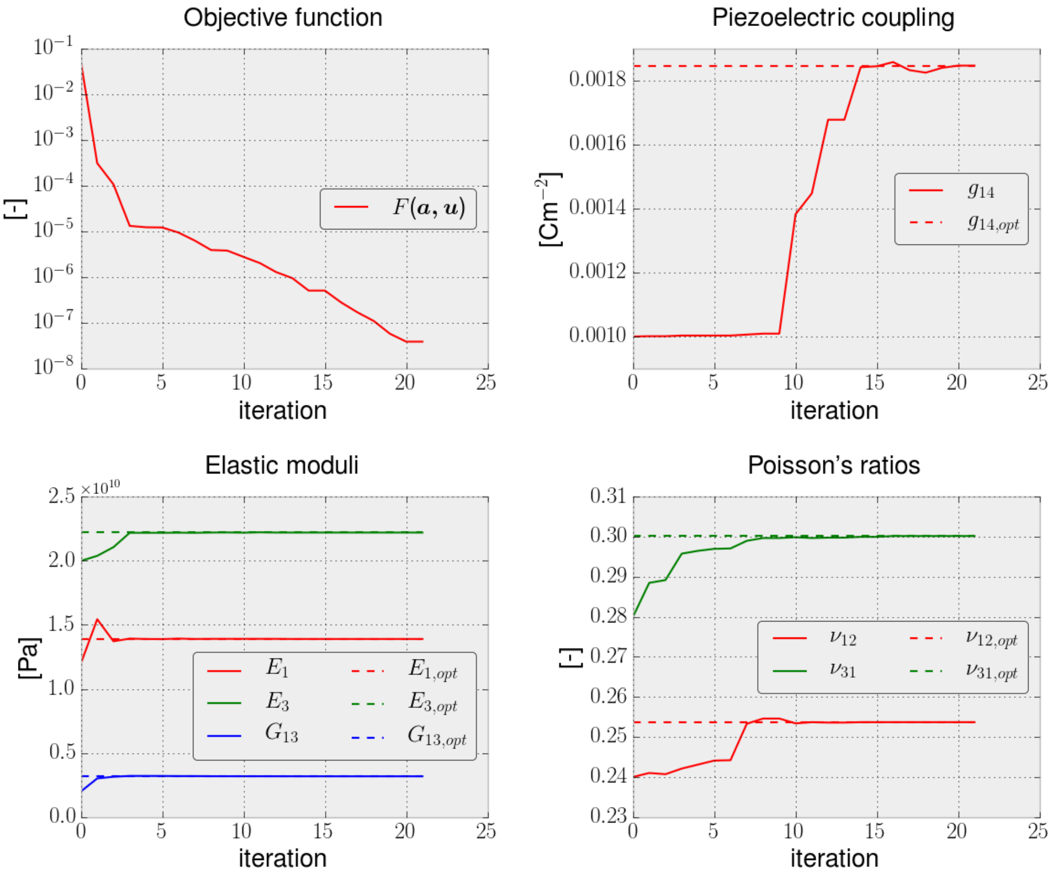

Figure 5.7: The evolution of the objective function $F(\boldsymbol{a}, \boldsymbol{u})$ and of the identification of the material parameters $\boldsymbol{a}$, where the known optima are visualized by a dashed line.

ineffective. After setting the line precision to 10^{-3} and limit of maximum objective function evaluation to 500, we start the identification process. After 21 iterations, it ends with success. The evolution of objective function and all optimization parameters is shown in Fig. 5.7, where a dashed line visualizes the known optimum of each parameter. We also provide the relative error of each identified parameter a_i^{opt} in relation to its known optimum value $\hat{a}_i$, see Tab. 5.5. The order of the error is satisfactory. Thus we may conclude that the proposed identification process and its implementation work within reasonable precision to identify material parameters of dry poropiezoelectric medium.

a_i	g_{14}	E_1	E_3	G_{13}	ν_{12}	ν_{31}
$\frac{\lvert\hat{a}_i - a_i^{\text{opt}}\rvert}{\lvert\hat{a}_i\rvert}$	4.8×10^{-4}	-8.0×10^{-7}	-1.9×10^{-5}	6.6×10^{-7}	3.1×10^{-6}	6.1×10^{-5}

Table 5.5: The relative error of the identified parameters a_i^{opt} in relation to their known optimum value $\hat{a}_i$.

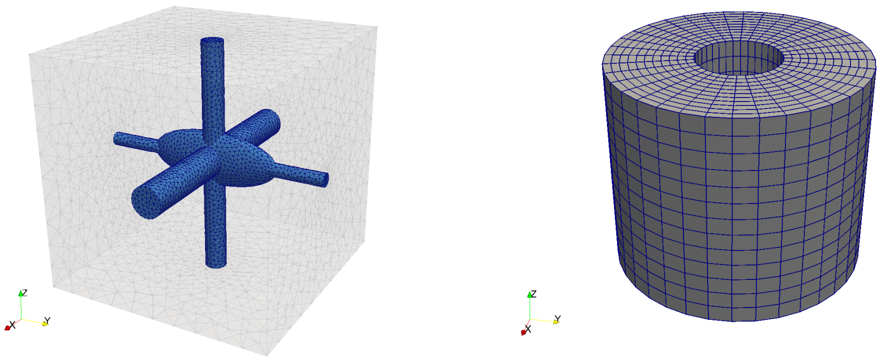

(a) Mesh representation of RVE Y

(b) Mesh representation of single bone osteon

Figure 5.8: Mesh representation of micro- and macroscopic structure made within software *GMSH*.

5.3 Numerical modeling of single bone osteon

In this part of the text, we use all the knowledge about osteonal geometry, microstructure, and material properties to provide a computational model of a single bone osteon.

Following up on the Sec. 5.1.3 and using geometric parameters from Tab. 5.1, we present the FE mesh of both micro- and macroscopic geometry in Fig. 5.8. At the macroscopic scale, the mesh represents a single bone osteon with the Haversian canal. At the microscopic level, the mesh represents cubic periodic RVE Y containing a single lacuna with channels representing the collection of canaliculi leading in the directions of the three coordinate axes. We created both meshes in the open-source software *GMSH*that provides a wide variety of meshing algorithms and is suitable for modeling periodic meshes, (Geuzaine and Remacle 2009). The microstructure size is given by $\varepsilon := \varepsilon_0 = 0.03$ which determines the influence of the piezoelectric coupling $\boldsymbol{g}$ and dielectric tensor $\boldsymbol{d}$.

To describe the material properties at the microscopic structure, we use the values from Tab. 5.3 that characterize collagen-hydroxyapatite matrix as a transversally isotropic material with weak piezoelectric properties. Electrochemical properties of bone fluid were taken from Tab. 4.1.

Once again, to compute the homogenized coefficients and to simulate processes on the macroscopic scale, we used the implementation made in the *SfePy* software. Then, to respect the orientation of LCN in osteon, the computed effective coefficients are circumferentially rotated around the x_3-axis of the central canal, see Remark 5.1.1.

For more informations about implementation and discretization we refer to Chapter 4 and especially its parts Sec. 4.1.1 and Sec. 4.2.2.

Boundary conditions To complete the macroscopic problem (3.3.39) we need to define a set of boundary conditions that will reflect the embedding of osteon in the cortical bone porous matrix. For simplicity, we denote the inner and outer osteonal wall and its top and bottom base by $\Gamma_{\mathrm{I}}, \Gamma_{\mathrm{O}}, \Gamma_{\mathrm{T}}$, and Γ_{B}, respectively. These boundaries are shown in Fig. 5.9.

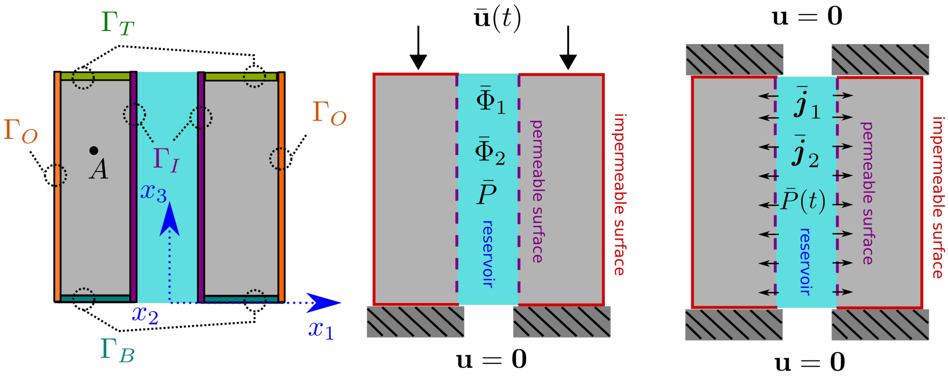

Figure 5.9: Left: Definition of boundaries on the macroscopic specimen; Middle: Boundary conditions defining BVP IV; Right: Boundary conditions defining BVP V.

On the outer wall of osteon Γ_{O} there is the so-called cement surface, through which only a few canaliculi can cross. Thus, as an idealization, it is reasonable to consider the outer wall to be impermeable with no fluid flow and no ionic exchanges, see (Rémond et al. 2008). In addition, we also consider the top and bottom bases of osteon Γ_{T} and Γ_{B} to be impermeable.

Even though we model the osteon as a hollow cylindrical body, the influence of the fluid in the Haversian canal has to be reflected by the boundary conditions. Relatively to the porosity of the LCN network, the Haversian canal is large enough to enable the fluid inside to relax so that the pressure can be assumed to be constant at the osteonal inner wall Γ_{I}. With regards to the ionic potential, we have two possible scenarios:

- **The inner wall Γ_{I} is considered to be permeable for both ionic species.** This results in Neumann's conditions describing ionic flux through the inner wall Γ_{I}.

- **The ionic potentials are considered constant at the inner osteonal wall Γ_{I}.** This leads to a prescribed Dirichlet condition on the boundary Γ_{I}.

In addition, we also consider the inner wall to be stress-free, see (Nguyen et al. 2010).

With this assumptions we define two boundary value problems (BVP) to demonstrate the macroscopic behavior of our effective model. Both BVPs are defined below. The initial values of effective quantities $(P, \Phi_\alpha^{\mathrm{eff}}, \boldsymbol{u}^{\mathrm{eff}}), \alpha = 1, 2$, for both BVPs were taken from their steady state solution for $\boldsymbol{f} = \mathbf{0}, \boldsymbol{E} = \mathbf{0}$. The computational time was taken $t \in]0, T[$, where $T = 1\mathrm{s}$ and time step $\Delta t \approx 0.05\mathrm{s}$.

5.3.1 The boundary value problem IV

The BVP IV describes a situation, where we consider the inner osteonal wall Γ_I to be non-permeable. At the top of the osteon, *i.e.* at Γ_T, the gradual compression is applied which is realized through the boundary condition on $u_3(t)$ given as a ramp-and- hold function

$$\bar{u}(t) = \begin{cases} -\hat{u}t & \text{for } 0 \leq t < t_r, \\ -\hat{u}t_r & \text{for } t_r \leq t < T, \end{cases} \tag{5.3.1}$$

where $t_r = 0.45\mathrm{s}$ and $\hat{u} = 0.1$.

The BVP IV is defined by (3.3.40) and by the boundary conditions of Neumann type (3.3.43) and Dirichlet type (3.3.44). The boundary conditions are applied to the parts of macroscopic specimen boundary, see Fig. 5.9, in the following manner (for all $t \in]0, T[$):

- $u_1 = u_2 = 0, \quad u_3(t) = \bar{u}(t)t, \quad \boldsymbol{n} \cdot \boldsymbol{j}_\alpha = 0, \quad \boldsymbol{n} \cdot \boldsymbol{w} = 0$, on Γ_T
- $\boldsymbol{u}(t) = \boldsymbol{0}, \quad \boldsymbol{n} \cdot \boldsymbol{j}_\alpha = 0, \quad \boldsymbol{n} \cdot \boldsymbol{w} = 0$, on Γ_B
- $\boldsymbol{n} \cdot \boldsymbol{j}_\alpha = 0, \quad \boldsymbol{n} \cdot \boldsymbol{w} = 0, \quad \boldsymbol{n} \cdot \boldsymbol{\sigma}_s^p = 0$, on Γ_O
- $P = \bar{P}, \quad \Phi_1 = \bar{\Phi}_1, \quad \Phi_2 = \bar{\Phi}_2, \quad \boldsymbol{n} \cdot \boldsymbol{\sigma}_s^p = 0$, on Γ_I

where $\boldsymbol{\sigma}, \boldsymbol{w}$ and $\boldsymbol{j}_\alpha, \alpha = 1, 2$, are given by (3.3.41) and $\bar{u}(t)$ is given by (5.3.1). The prescribed values of boundary conditions are $\bar{P} = 1.0, \bar{\Phi}_1 = -0.01, \bar{\Phi}_2 = 0.01$.

Initial conditions are taken from the steady-state solution (*i.e.* for $t = 0$) of the macroscopic problem (3.3.40) with a set of boundary conditions given above.

We solve the macroscopic problem in its dimensionless form. However, using the dimensional choices made in Sec. 3.2.1, we present all the following results in dimensionalized form denoted by $\sqcup^{\mathrm{eff}}$; see also Remark 3.3.1.

Fig. 5.10 depicts the time dependency of the macroscopic solution in one point inside of the macroscopic specimen (point A in Fig. 5.9). The gradually increasing displacement is illustrated in Fig. 5.10a together with the slow increase in global pressure P^{eff}. In Fig. 5.10b, ionic potentials decrease with the increasing displacement.

All the presented results are axially symmetric, which is the direct consequence of the circumferential orientation of the microstructure in the macroscopic specimen. Thus, Fig. 5.11 shows the distribution of macroscopic solution $(p^{\mathrm{eff}}, \boldsymbol{u}^{\mathrm{eff}}, \Phi_\alpha^{\mathrm{eff}})$, $\alpha = 1, 2$, of BVP IV at $t = T$ along the radial axis that passes through point A, see Fig. 5.9.

To better illustrate the evolution of the spatial distribution of solution of $(p^{\mathrm{eff}}, \boldsymbol{u}^{\mathrm{eff}}, \Phi_\alpha^{\mathrm{eff}})$, $\alpha = 1, 2$, in the macroscopic specimen, we provide additional figures at the end of this chapter. These figures are Figs. 5.14–5.16 and depict the solution of BVP IV at the selected time steps $t \in \{t_0, t_1, t_2, t_r, T\} = \{0, 0.15, 0.30, 0.45, 1\}\mathrm{s}$. We observe a visible deformation of the macroscopic specimen, which is mainly due to the increasing displacement on the boundary Γ_T, but is partly caused by the swelling of the specimen. In this case, the distribution of displacement $\boldsymbol{u}$ directly influences all the other macroscopic quantities, showing a direct connection between specimen deformation and ion distribution, (represented by ionic potentials $\Phi_\alpha, \alpha = 1, 2$ here).

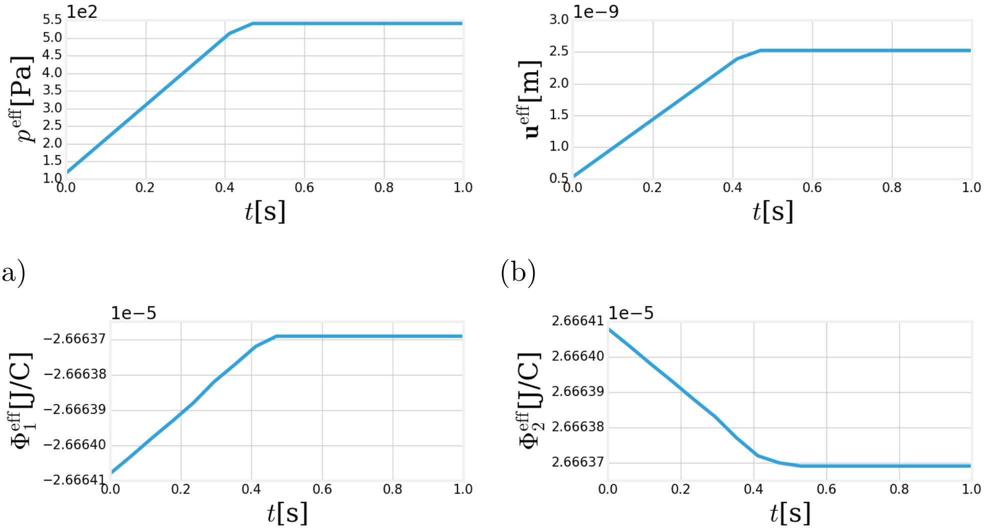

(a) (b)

(c) (d)

Figure 5.10: BVP IV:Evolution of macroscopic fields $(p^{\mathrm{eff}}, \boldsymbol{u}^{\mathrm{eff}}, \Phi_\alpha^{\mathrm{eff}}), \alpha = 1, 2$, in point A, $t \in [0, 1]$s with the relaxation time $t_r = 0.45$s.

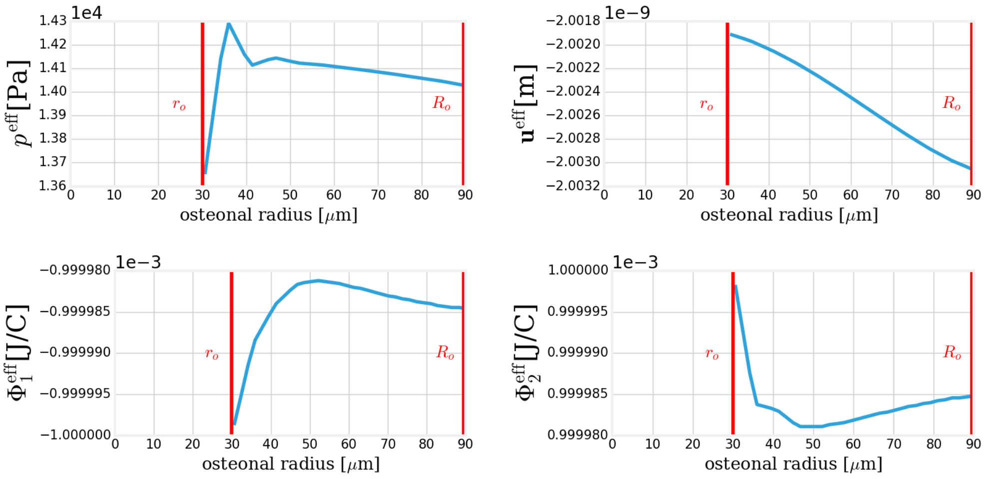

Figure 5.11: BVP IV: Distribution of macroscopic fields $(p^{\mathrm{eff}}, \boldsymbol{u}^{\mathrm{eff}}, \Phi_\alpha^{\mathrm{eff}}), \alpha = 1, 2$, at $t = T$ along the radial axis. The values of radius of Haversian canal r_o and radius of osteon R_0 are denoted by red vertical lines.

Reconstruction of macroscopic solution

Once the macroscopic BVP IV has been solved, the macroscopic functions p^{eff}, $\boldsymbol{u}^{\mathrm{eff}}$ and $\Phi_\alpha^{\mathrm{eff}}, \alpha = 1, 2$, can be used to reconstruct the local responses at the microscopic level, while using formulae (3.3.47)–(3.3.49). For a given $\varepsilon_0 = 0.03$, the macroscopic functions are reconstructed in the recovery region that lies in the proximity of point A, see Fig. 5.9. This region encompasses the block of six periodically repeated copies of the RVE $Y^{\varepsilon_0} = \varepsilon_0 Y$ on the microscopic level. Reconstructions $(\Phi_1^{\mathrm{rec}}, \Phi_2^{\mathrm{rec}})$ and $(P^{\mathrm{rec}}, \boldsymbol{u}^{\mathrm{rec}})$ of macroscopic fields $P^{\mathrm{eff}}, \boldsymbol{u}^{\mathrm{eff}}$ and $\Phi_\alpha^{\mathrm{eff}}, \alpha = 1, 2$, are shown in Figs. 5.17 and 5.19, respectively. To illustrate the time evolution of the reconstructed quantities, their state in chosen time steps

$t \in \{t_0, t_r, T\} = \{0, 0.45, 1\}$s is shown. Because there is already a number of the figures and we do not want to split the text any further, we place the visualizations of reconstructions at the and of this chapter for better readability of the text.

The microscopic reconstructions follow a similar pattern as the macroscopic solutions from whose they are computed. We observe a slow increase in both p^{rec}, $\boldsymbol{u}^{\text{rec}}$, and Φ_2^{rec} and the decrease in Φ_1^{rec}.

5.3.2 Boundary value problem V

The BVP V describes a situation where we consider the inner osteonal wall Γ_{I} to be semi-permeable for both ionic species. This time, we will also gradually increase pressure inside the Haversian canal. This is realized by the evolving boundary condition on P at Γ_{I}.

The BVP V is defined by (3.3.40) and by the boundary conditions of Neumann's type (3.3.43) and Dirichlet's type (3.3.44). The boundary conditions are applied to the parts of macroscopic specimen boundary, see 5.9, in the following manner (for all $t \in]0, T[$ and $\alpha = 1, 2$):

- $\boldsymbol{u} = \boldsymbol{0}, \quad \boldsymbol{n} \cdot \boldsymbol{j}_\alpha = 0, \quad \boldsymbol{n} \cdot \boldsymbol{w} = 0$, on Γ_{T}
- $\boldsymbol{u} = \boldsymbol{0}, \quad \boldsymbol{n} \cdot \boldsymbol{j}_\alpha = 0, \quad \boldsymbol{n} \cdot \boldsymbol{w} = 0$, on Γ_{B}
- $\boldsymbol{n} \cdot \boldsymbol{j}_\alpha = 0, \quad \boldsymbol{n} \cdot \boldsymbol{w} = 0, \quad \boldsymbol{n} \cdot \boldsymbol{\sigma}_s^p = 0$, on Γ_{O}
- $P(t) = \bar{P}t, \quad \boldsymbol{n} \cdot \boldsymbol{j}_1 = \bar{j}_1, \quad \boldsymbol{n} \cdot \boldsymbol{j}_2 = \bar{j}_2, \quad \boldsymbol{n} \cdot \boldsymbol{\sigma}_s^p = 0$, on Γ_{I}

where $\boldsymbol{\sigma}$, $\boldsymbol{w}$ and $\boldsymbol{j}_\alpha, \alpha = 1, 2$, are given by (3.3.41). The prescribe values of boundary conditions are $\bar{P} = 1.0, \bar{j}_1 = 0.01, \bar{j}_2 = 0.01$. Initial conditions are taken from the steady-state solution of the macroscopic problem (3.3.40) with a set of boundary conditions given above.

Once again, we compute the macroscopic problem in its dimensionless form and dimensionalize the results by following Remark 3.3.1.

Fig. 5.12 depicts the time dependency of the macroscopic solution in a single point inside of the macroscopic specimen (point A in Fig. 5.9). It shows a linear increase in pressure p^{eff}, which is reflected in the linear dependency of the evolution of potentials Φ_1^{eff} and Φ_1^{eff}. Curiously, the evolution of displacement magnitude $|\boldsymbol{u}^{\text{eff}}|$ shows a nonlinear decrease, suggesting the nonlinear coupling between pressure and displacement.

Finally, Fig. 5.13 depicts the distribution of dimensionalized macroscopic solution $(p^{\text{eff}}, \boldsymbol{u}^{\text{eff}}, \Phi_\alpha^{\text{eff}})$, $\alpha = 1, 2$, of BVP V at $t = T$ along the radial axis that passes through point A (for the placement of point A see Fig. 5.9).

In the case of BVP V, we provide the visualizations of the spatial distribution of solution $(p^{\text{eff}}, \boldsymbol{u}^{\text{eff}}, \Phi_\alpha^{\text{eff}})$, $\alpha = 1, 2$, only at two time steps, at steady state $t = 0$ and at $t = T = 1$s. These are Figs. 5.20 and 5.21. We observe a visible deformation of the macroscopic specimen, which is mainly due to the increasing pressure on the boundary Γ_{I}. In this case, the distribution of displacement $\boldsymbol{u}^{\text{eff}}$ and pressure p^{eff} directly influences all the other macroscopic quantities, showing a direct connection between specimen deformation and ion distribution, (represented by ionic potentials $\Phi_\alpha, \alpha = 1, 2$ here).

The reconstructions of the macroscopic solution at the microscopic scale can be obtained for the BVP V by the same process that was described for the BVP IV. However, we do not provide their visualizations, as this process was already demonstrated on the previous BVP IV.

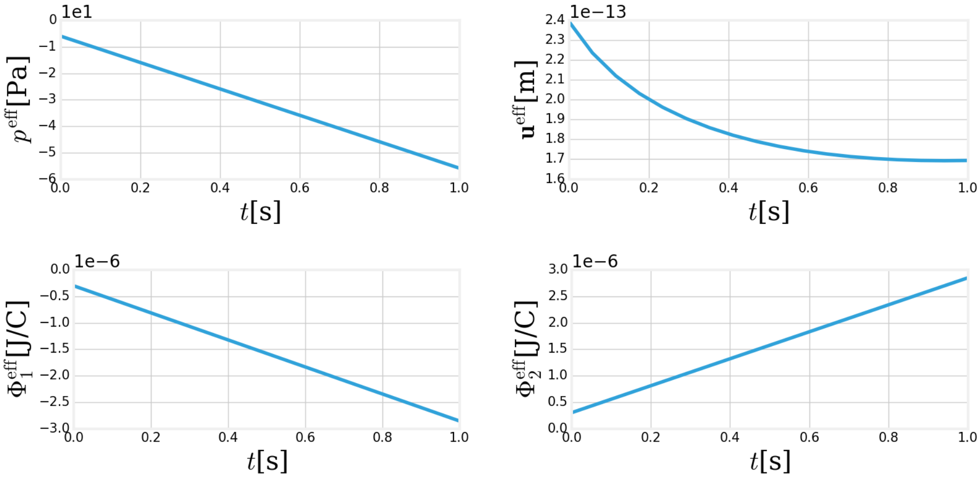

Figure 5.12: BVP V: Evolution of macroscopic solution $(p^{\mathrm{eff}}, \boldsymbol{u}^{\mathrm{eff}}, \Phi_\alpha^{\mathrm{eff}}), \alpha = 1, 2,$ in point A, $t \in [0, 1]$s.

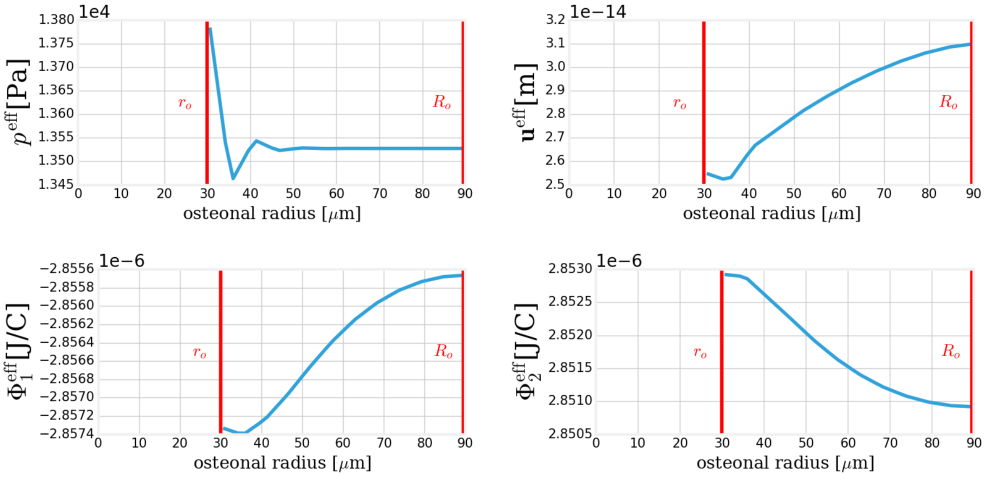

Figure 5.13: BVP V: Distribution of macroscopic fields $(p^{\mathrm{eff}}, \boldsymbol{u}^{\mathrm{eff}}, \Phi_\alpha^{\mathrm{eff}}), \alpha = 1, 2,$ at $t = T = 1$s along the radial axis. The values of radius of Haversian canal r_{o} and radius of osteon R_{o} are denoted by red vertical lines.

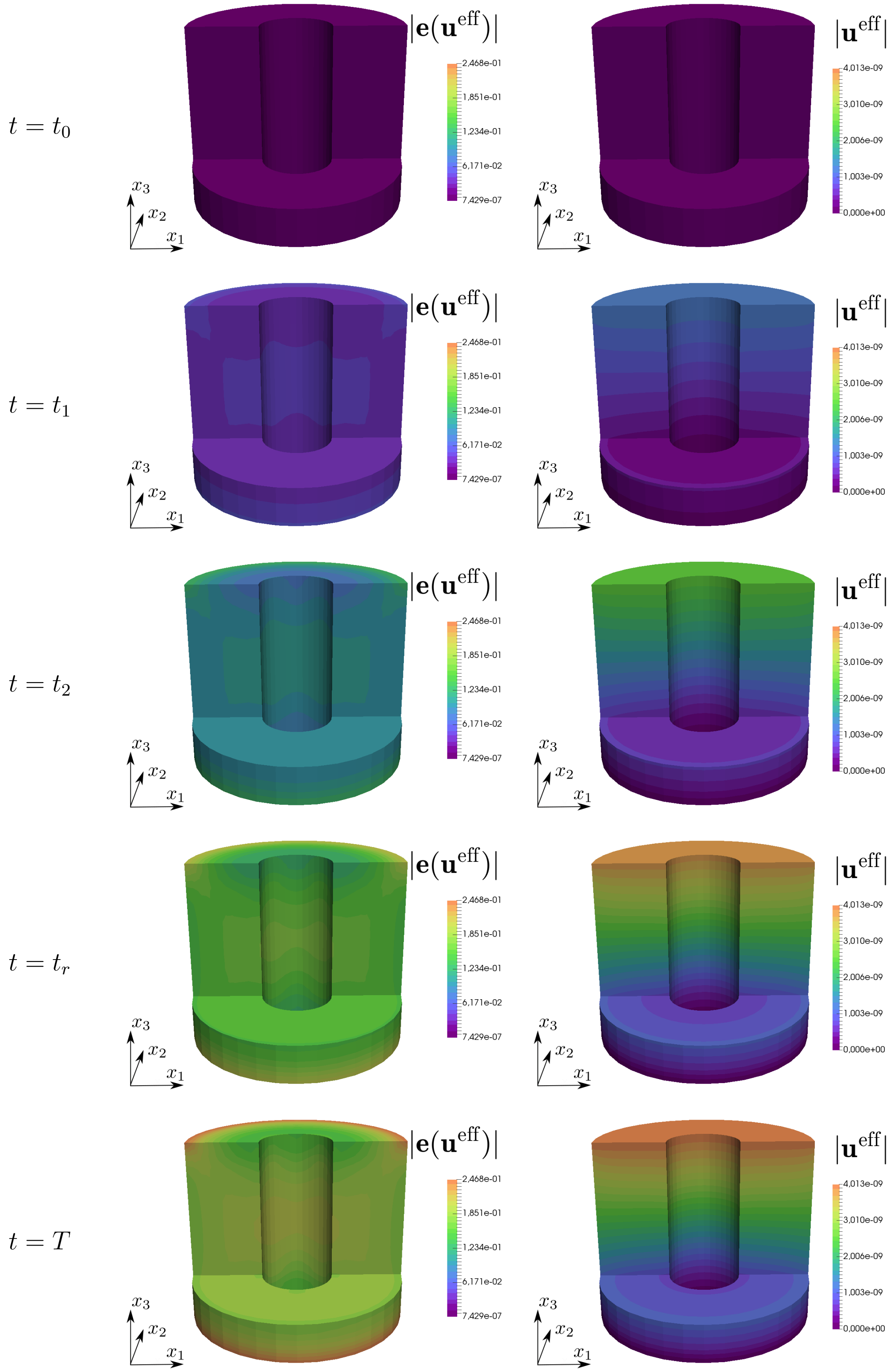

Figure 5.14: BVP IV: Evolution of magnitude of macroscopic field $\boldsymbol{u}^{\text{eff}}$ and of the strain $\boldsymbol{e}\left(\boldsymbol{u}^{\text{eff}}\right)$ in the macroscopic specimen. The distribution of the macroscopic fields is shown at time steps $t \in \{t_0, t_1, t_2, t_r, T\} = \{0, 0.15, 0.3, 0.45, 1\}$s, where t_r is time included in the definition of the ramp-and-hold function (5.3.1).

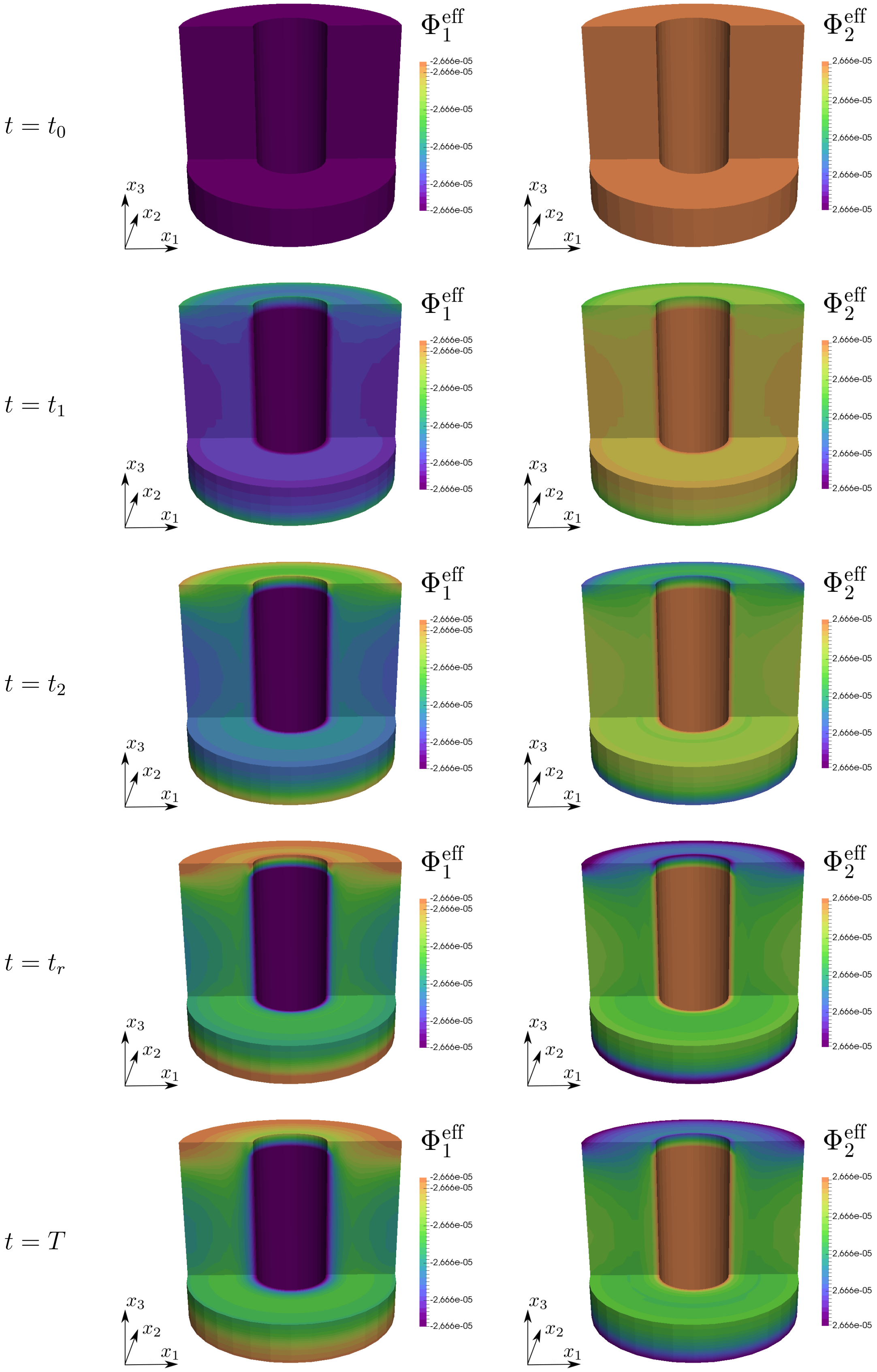

Figure 5.15: BVP IV: Evolution of macroscopic fields $(\Phi_1^{\text{eff}}, \Phi_2^{\text{eff}})$ in the macroscopic specimen. The distribution of the macroscopic fields is shown at time steps $t \in \{t_0, t_1, t_2, t_r, T\} = \{0, 0.15, 0.3, 0.45, 1\}$s, where t_r is time included in the definition of the ramp-and-hold function (5.3.1).

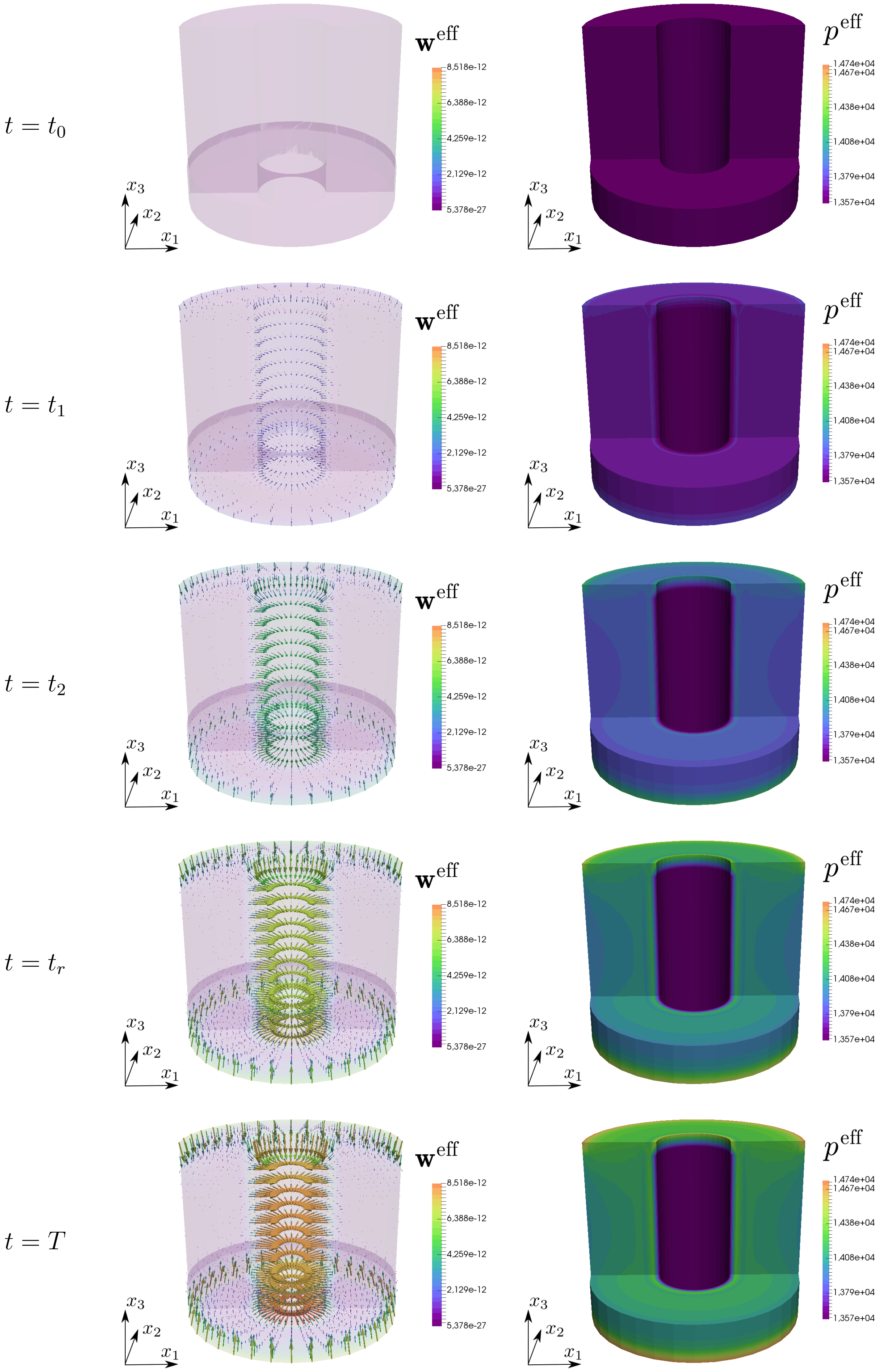

Figure 5.16: BVP IV: Evolution of macroscopic fields $\boldsymbol{w}^{\text{eff}}$ and p^{eff}. The distribution of the macroscopic fields is shown at time steps $t \in \{t_0, t_1, t_2, t_r, T\} = \{0, 0.15, 0.3, 0.45, 1\}$s, where t_r is time included in the definition of the ramp-and-hold function (5.3.1).

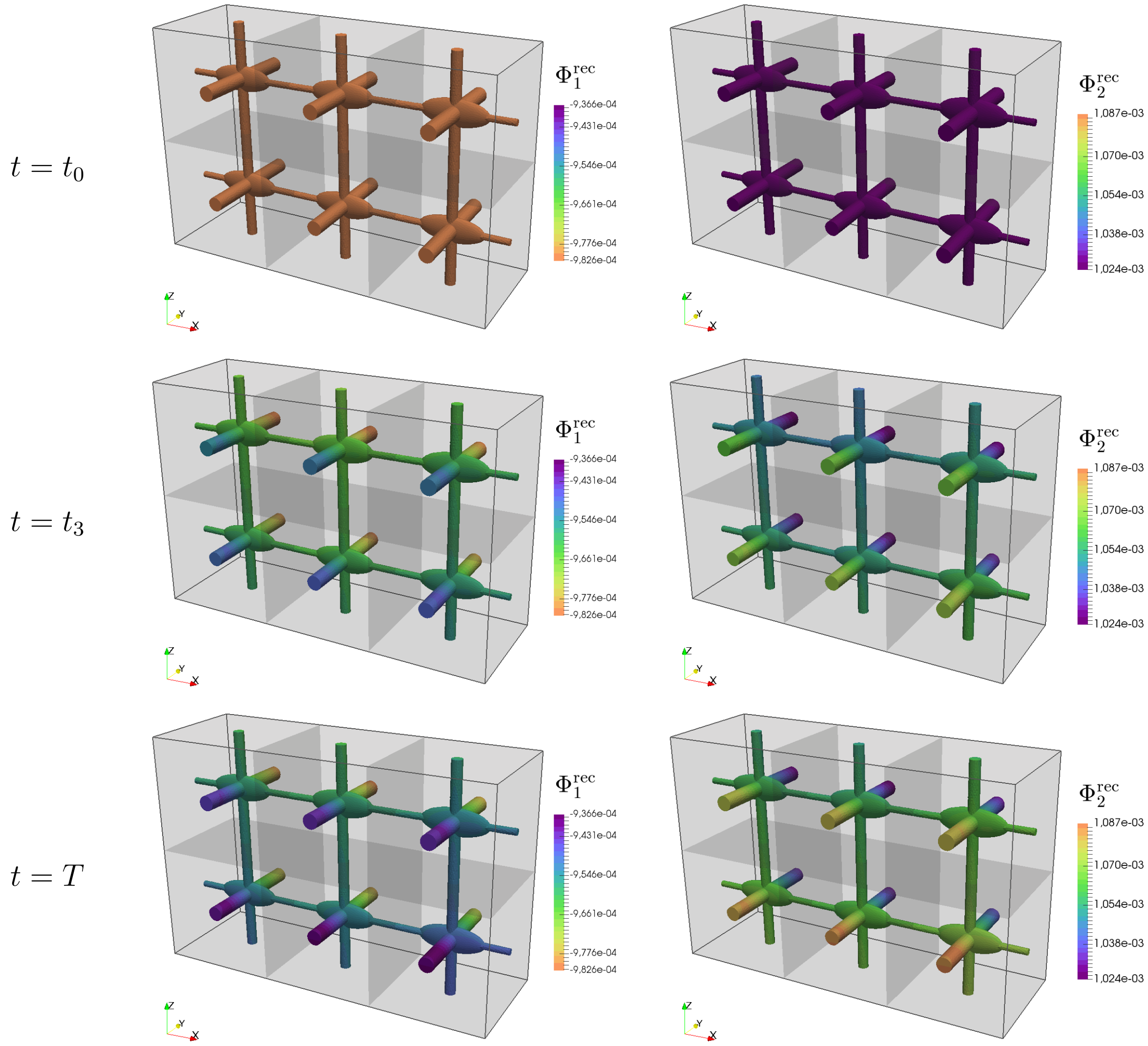

Figure 5.17: Evolution of total reconstructions of macroscopic potential fields obtained as solution of the BVP IV, $t \in \{t_0, t_r, T\} = \{0, 0.45, 1\}$. Left: total reconstruction Φ_1^{rec}; Right: total reconstruction Φ_2^{rec}

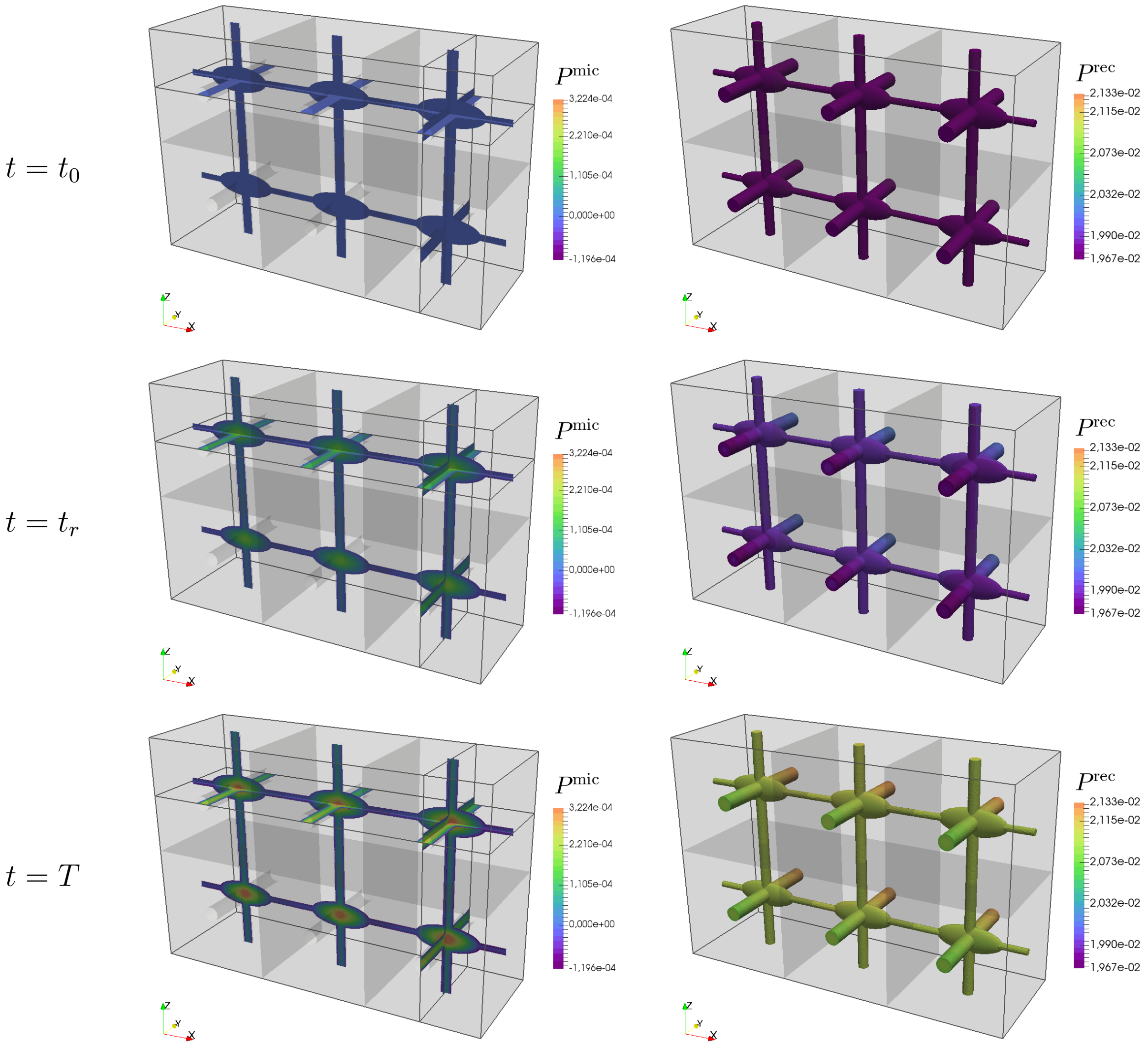

Figure 5.18: Evolution of reconstruction of pressure field obtained as solution of the BVP IV, $t \in \{t_0, t_r, T\} = \{0, 0.45, 1\}$. Left: fluctuation part P^{mic}; Right: total reconstruction P^{rec}.

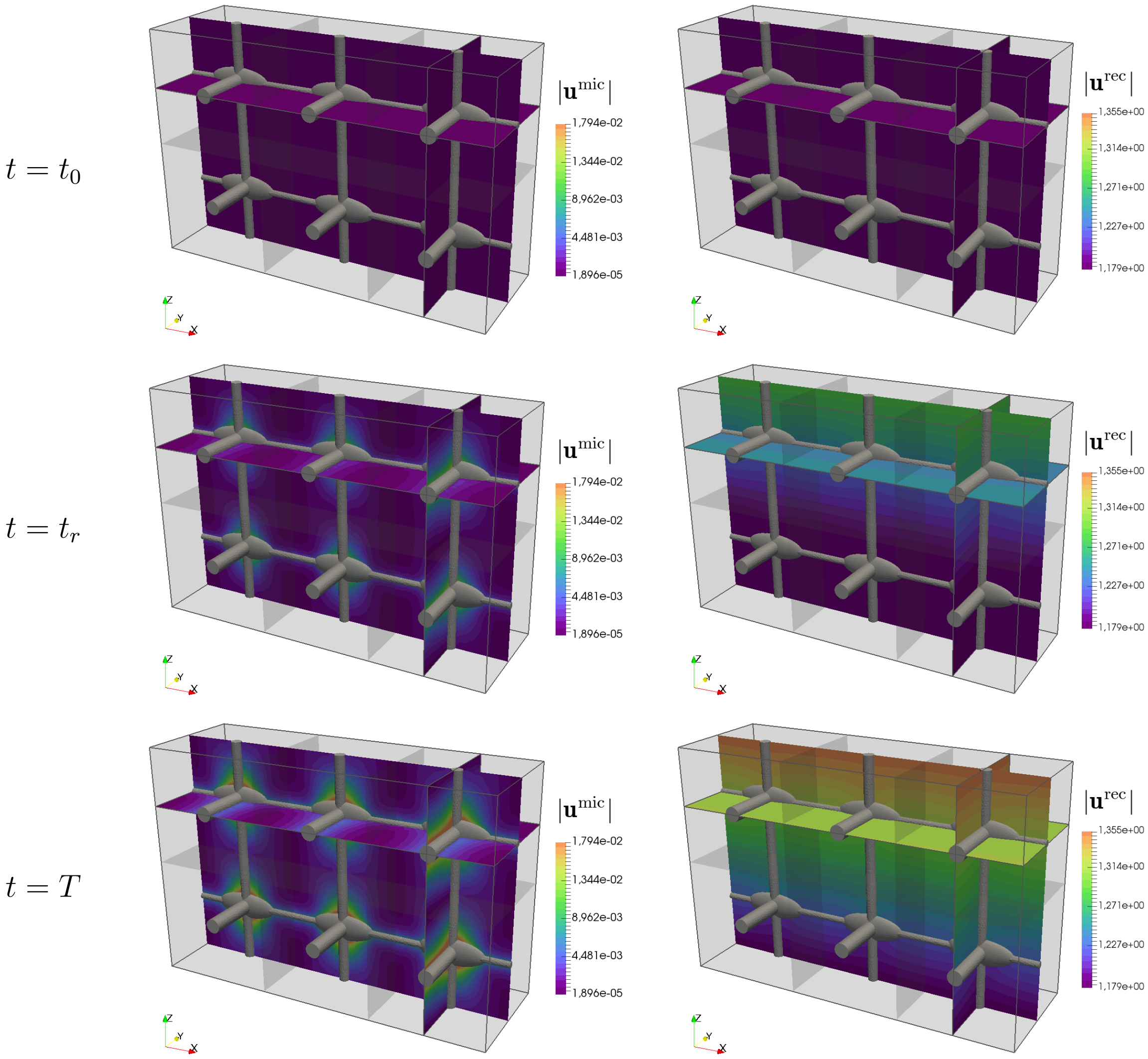

Figure 5.19: Evolution of reconstruction of displacement field obtained as solution of the BVP IV, $t \in \{t_0, t_r, T\} = \{0, 0.45, 1\}$. Left: fluctuation part $\boldsymbol{u}^{\mathrm{mic}}$; Right: total reconstruction $\boldsymbol{u}^{\mathrm{rec}}$.

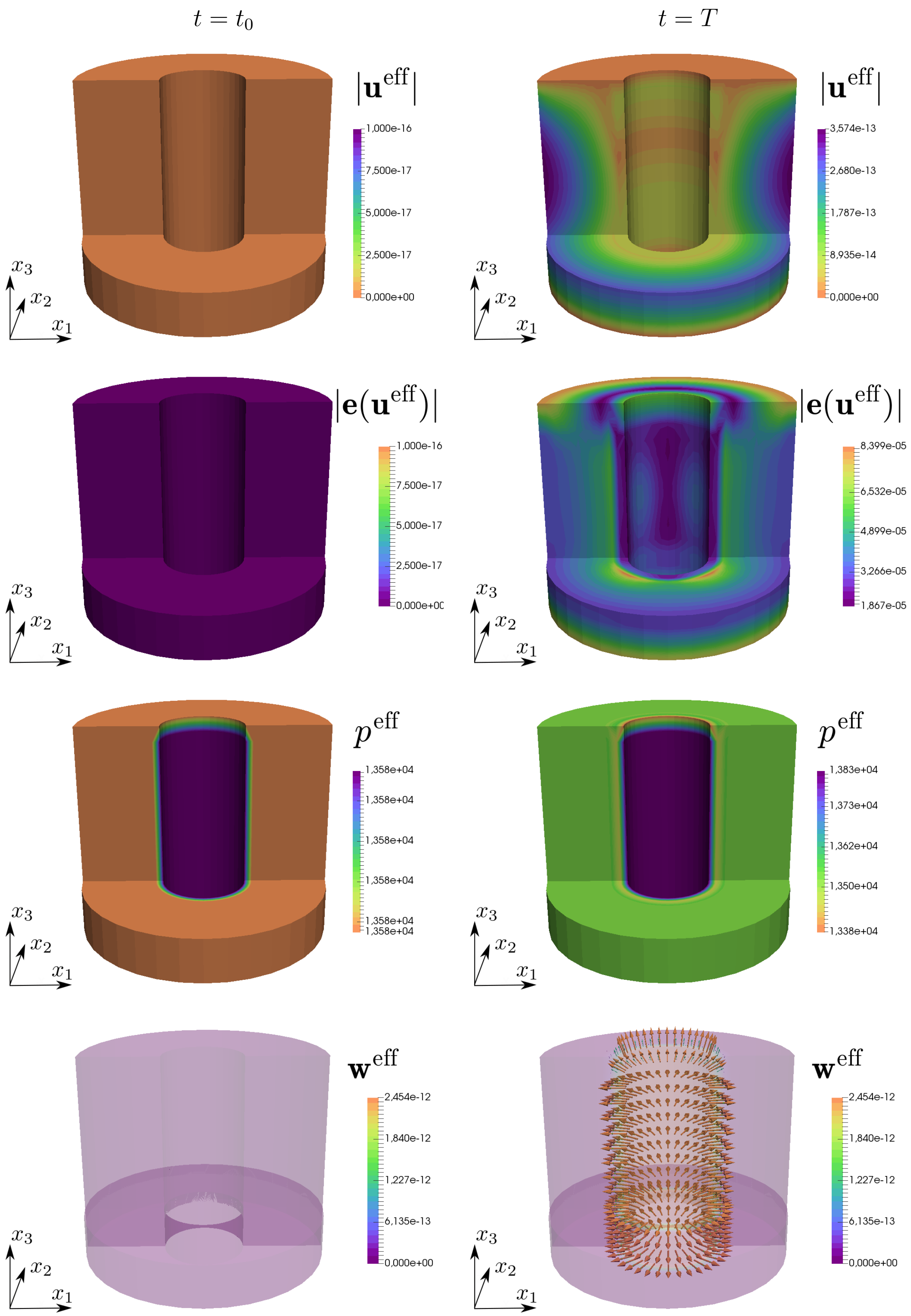

Figure 5.20: BVP V: Distribution of macroscopic fields $(\boldsymbol{u}^{\text{eff}}, \boldsymbol{w}^{\text{eff}}, p^{\text{eff}})$ in macroscopic specimen. Left: Distribution of macroscopic solution at $t = 0$ (steady state); Distribution of macroscopic solution at $t = T = 1\text{s}$.

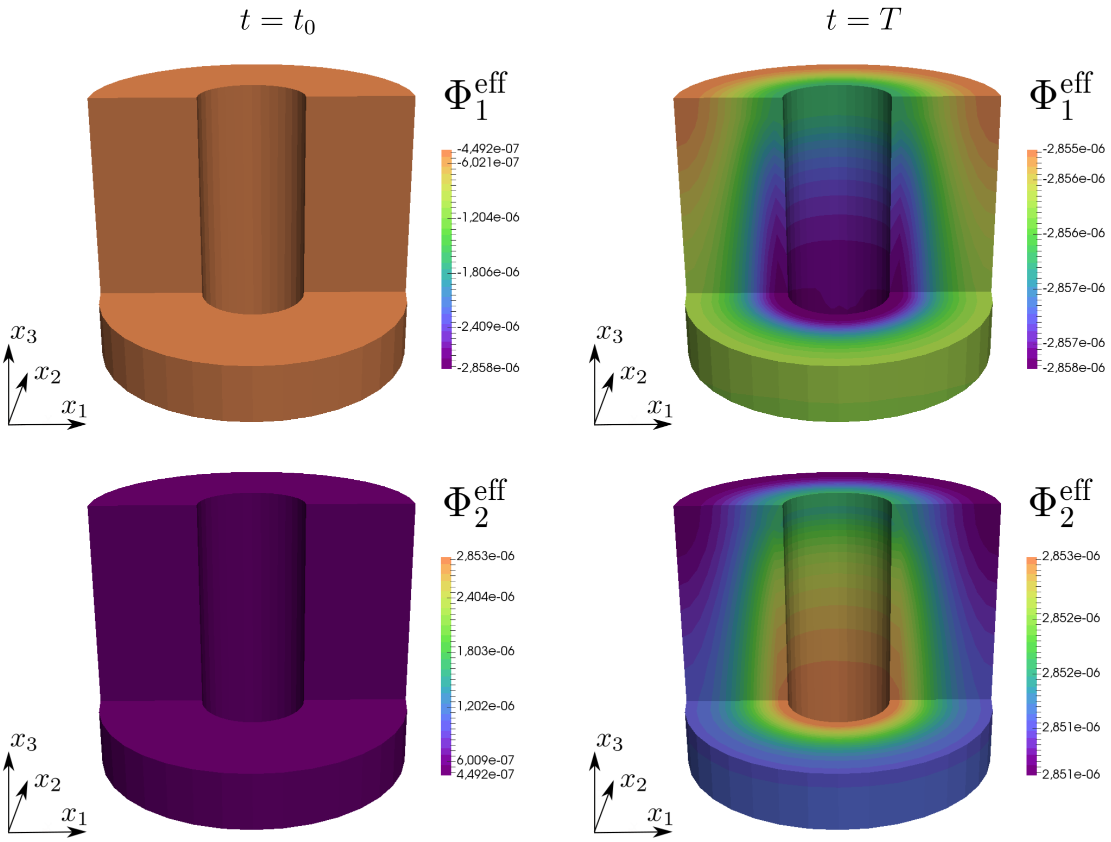

Figure 5.21: BVP V: Distribution of macroscopic fields $(\Phi_1^{\text{eff}}, \Phi_2^{\text{eff}})$ in macroscopic specimen. Left: Distribution of macroscopic solution at $t = 0$ (steady state); Distribution of macroscopic solution at $t = T = 1$s.

Chapter 6

Conclusion

6.1 Conclusion and discussion

The submitted doctoral thesis deals with the two-scale modeling of ionic transport in porous media. It was motivated by modeling the processes that occur in the cortical bone tissue, but its findings can be applied to other applications.

We summarize the contributions of the presented thesis in the following points that correspond to the aims of the thesis:

- The thesis briefly summarizes the origins of electrochemomechanical phenomena that occur in the porous medium saturated by an incompressible symmetric electrolyte and which influence the ionic movement and distribution.

- It proposes the suitable mathematical model, which considers linear elastic porous medium and can be easily expanded to describe the weakly piezoelectric porous medium, and extends it to describe the quasi-static behavior. Further, it introduces suitable boundary and interface conditions to explain the interactions on the solid-fluid interface.

- To simplify the complexity of both mathematical models, the thesis gives their dimensional analysis and proposes the linearization procedure to deal with their nonlinearity.

- The thesis deals with the upscaling procedure and derivation of expressions of two scale models for both types of porous media by the suitable homogenization method based on the so-called unfolding. The upscaling procedure results in the derivation of two effective macroscopic models. The first model describes the steady state of the electrolyte flow in the solid skeleton made of an elastic electric conductor. The second model is the extension of the first one and describes quasi-static electrolyte flow in the solid skeleton consisting of weakly piezoelectric material.

- The thesis formulates the expressions to reconstruct responses at the microscopic level from macroscopic fields by virtue of the ”downscaling” procedure.

- A software for the numerical simulations on both microscopic and macroscopic levels was developed in the *Python*-based framework *SfePy* that uses

FEM discretization. It is used to simulate the steady state and quasi-steady state of problems in both of the proposed types of porous media. One of the features of this software is the ability to reconstruct the solution at microscopic scales.

- This thesis gives a series of numerical simulations mimicking an experiment to provide information about the macroscopic behavior of both studied models. These simulations use a simple geometrical representation of microstructure so that homogenization results can be interpreted easily. A parametric study was performed to illustrate the microstructure influence on the resulting effective coefficients. Both the proposed homogenized models, *i.e.* model describing the flow of the electrolyte through linear elastic porous medium and model describing the flow of the electrolyte through the weakly piezoelectric porous medium, were compared on a macroscopic problem.
- The thesis discusses the possible range of applications of these models in the final part of this thesis. The main attention is given to the application to the modeling of cortical bone tissue. A geometry representation of the microscopic structure of the lacunar-canalicular network and the macroscopic specimen that represents a single bone osteon is proposed while using the data from the available literature. The literature research of possible material parameters describing solid phase on microscopic level shows that they are not easily and definitively measurable. Thus, this thesis proposes a material identification procedure to obtain parameters of dry bone. The identification procedure was implemented in *Python* (with the use of publicly available Python-based libraries). It uses two-scale computational software for the numerical simulations mimicking a fictitious experiment.
- The thesis presents a numerical simulation that illustrates the behavior of the two-scale model of a single bone osteon under the loading. It provides both the solution of the quasi-steady homogenized problem and its reconstruction at the microscopic level.

The presented two-scale models undergo a series of significant simplifications. For example, the linearization process limits the problem to the small perturbations from equilibrium only. This also limits the problem to a quasi-steady state, as all of the dynamic terms are neglected. Due to these simplifications, the models lose some of the complexity and interconnectedness. Thus, the resulting equations of the homogenized model are only weakly coupled and some degree of fidelity to the real issue is lost. However, these simplifications prove to be useful to lower the computational requirements of simulations. Alternatively, the fully coupled macroscopic model could be proposed in the forthcoming work.

We believe that the main contribution of this work lies in the development of the 3D computational model for numerical simulation on both microscopic and macroscopic levels. This software can also be used to reconstruct macroscopic solutions at the chosen region of the macroscopic specimen and thus provide more detailed information about their distribution at the microscale. This can contribute to a better understanding of the processes that occurs at the microscopic level.

Another advantage to the two-scale computational modeling is its use in identifying material parameters of the solid skeleton at the microstructure. Up to now, the origins of bone piezoelectricity have not been fully clarified. The identification process in conjunction with the experimentally obtained measurements can provide the non-directly measurable material parameters that contribute to the piezoelectric behavior of the cortical bone tissue. Even though this thesis uses only the results of the fictitious experiment, the proposed algorithm and software should be able to identify these parameters from real experimental data as well.

This doctoral thesis contributes to the computational modeling of heterogeneous materials with complex microstructure, such as cortical bone tissue. The software for numerical modeling of both microscopic and macroscopic problems, which have been developed during the work on this thesis, can be employed to model other engineering applications as well (e. g. swelling clays, energy cells, etc.).

6.2 Topics of future work

The topic of multi-scale modeling of ionic transport in piezoelectric porous media is not a new one. However, it still presents numerous challenges and possibilities, especially in its application to the modeling of biological materials with complex structures. The following text proposes a few of these issues which would be worthy of exploring further.

The presented two-scale models undergo a series of significant simplifications that limit the problem to linear and quasi-static only. The modeling of a nonlinear problem would bring a whole set of new challenges, both mathematical and numerical, and will significantly increase the computational requirements. In the case of non-steady flow, the fluid-structure interaction will be more involved, thus leading to a strong coupling between the fluid flow, ionic concentrations, and deformation. The scale decoupling procedure will become more complicated and will lead to fading memory effects of the macroscopic responses, as the homogenized coefficients will serve for time convolution kernels, (Auriault and Boutin 1993; Rohan et al. 2012). However, such a model would better reflect the time evolution of the phenomena happening in the tissue and could be used for modeling of wave propagation.

As was briefly discussed in Sec. 5.1.2, there are significant differences between findings of mechanical and piezoelectric properties obtained by measurements of the dry and wet bone. This work describes the identification of material parameters based on the fictitious experiment performed on the specimen of dry bone. One of the possible extensions of this work would be to propose a similar identification process for the experiment performed on the wet bone, *i.e.* using the proposed model of ionic transport in the poropiezoelectric medium. The comparison between the identified parameters of wet and dry bone could serve to determine the real origin of bone piezoelectricity, as was discussed in (Mohammadkhah et al. 2019).

The bones are known to be an ever-changing material that is constantly remodeling its inner structure to respond to loading optimally. This can be explored further through the topology optimization of the microstructure; see for example

(Rohan and Miara 2006). Additionally, the process of remodeling is governed by the osteocytes nested in the lacunae, which send signals of bone forming or resorption to osteoblasts and osteoclasts. In this work, however, we completely ignored the presence of these cells in the lacunar-canalicular network. The possible extension of this work would be to include the osteocyte cell in the model and study its response to the mechanical loading. Some insight into this problem can already provide the work (Joukar et al. 2016).

To summarize, let us list some tasks that should be worked on in the near future:

- derivation of the dynamic effective homogenized model,
- modeling of wave propagation,
- identification of piezoelectric material parameters of the wet bone and comparison to identification in the dry bone,
- optimal structure design,
- inclusion of the osteocyte cell into the model.

There are multiple other possibilities to expand on this subject, *i.e.* modeling of an evolving microstructure, modeling of young versus old bone tissue, application to the different problematics, etc. However, we feel that the topics stated above are crucial to the further understanding of the phenomena and are necessary steps to take before progressing further.

Appendix A

Dimensional analysis

This appendix clarifies, how the scale parameter ε (see Section 3.2.1) is introduced into the system of equations (2.3.2)-(2.3.8) through the dimensional analysis. Simultaneosly, it presents the derivation of their dimensionless form (3.2.8)-(3.2.10).

Having in mind the scaling of the domain, we recall the dimensionless operators ∇' and ∂_t'

$$\nabla' = L_c \nabla, \qquad \nabla = (\partial_x), \qquad \partial_t' = t_c \partial_t, \tag{A.1}$$

however, we drop the superscript for the sake of brevity, see also Remark 3.2.1.

The dimensionless variables are expressed as follows

$$p^\varepsilon = \frac{p}{p_c}\;, \quad \boldsymbol{v}^\varepsilon = \frac{\boldsymbol{v}}{v_c}\;, \quad \boldsymbol{w}^\varepsilon = \frac{\boldsymbol{w}}{v_c}\;, \quad \Psi_f^\varepsilon = \frac{\Psi_f}{\zeta}\;, \quad c_\alpha^\varepsilon = \frac{c_\alpha}{c_c}\;, \quad \boldsymbol{u}^\varepsilon = \frac{\boldsymbol{u}}{u_c}\;, \tag{A.2}$$

where p_c is characteristic pressure, $\boldsymbol{v}_c$ characteristic velocity, c_c characteristic concentration, u_c characteristic displacement and ζ stands for the $\zeta-$potential mentioned in Sec. 2.2.2.

Modified Stokes problem The characteristic pressure p_c is expressed using the ideal gas law,

$$p_c = c_c k_B T. \tag{A.3}$$

Then, by inserting the dimensionless quantities (A.2) and the dimensionless operator (A.1) into (2.3.7), we get

$$\nabla p^\varepsilon - \frac{v_c \eta_f}{L_c p_c} \Delta \boldsymbol{w}^\varepsilon = \frac{L_c}{p_c} \boldsymbol{f} - \frac{e c_c \Psi_c}{p_c} \sum_{\beta=1}^{2} z_\beta c_\beta^\varepsilon \nabla \Psi_f^\varepsilon\;, \tag{A.4}$$

hence (3.2.7) introduces the dimensionless force $\boldsymbol{f} = \frac{L_c}{p_c}\boldsymbol{f}$. Upon substituting expressions $\Psi_c = k_B T/e$ and (A.3) into (A.4), we get $\frac{e c_c \Psi_c}{p_c} = 1$. According to (Lemaire et al. 2011), the ration between the velocity and pressure magnitudes $\lambda_c := \frac{v_c \eta_f}{L_c p_c}$ is obtained by the dimensional analysis of the Darcy law which can also represent the viscous flow in pores. This yields

$$v_c = \frac{k p_c}{\eta_f L_c},$$

where k denotes the intrinsic permeability (units $[\mathrm{m}^2]$) depending only on the size of the micropores, $k \sim l^2$, hence holds and

$$\lambda_c = \frac{v_c \eta_f}{L_c p_c} = \frac{k}{L_c^2} \sim \frac{l^2}{L_c^2} = \varepsilon^2. \tag{A.5}$$

Consequently from (A.3)-(A.5), the dimensionless form (2.3.7) reads,

$$\nabla p^{\varepsilon} - \varepsilon^2 \Delta \boldsymbol{w}^{\varepsilon} = \boldsymbol{f}' - \sum_{\beta=1}^{2} z_\beta c_\beta^{\varepsilon} \nabla \Psi_f^{\varepsilon}. \tag{A.6}$$

Electrostatics Upon substituting (A.2) and (A.1) in the Gauss-Poisson equation (2.3.5), it yields

$$\frac{\mathcal{E}\Psi_c}{L_c^2} \Delta \Psi_f^{\varepsilon} = -e c_c \sum_{\beta=1}^{2} z_\beta c_\beta^{\varepsilon}. \tag{A.7}$$

Using the Debye length definition (3.2.4) and parameter $\gamma = l^2(\lambda_D \sum_{\beta=1}^{2} z_\beta^2)^{-1}$, we may express the characteristic concentration c_c as

$$c_c = \frac{\mathcal{E} k_b T}{(e\lambda_D)^2 \sum_{\beta=1}^{2} z_\beta^2} = \gamma \frac{\mathcal{E} k_b T}{(el)^2}. \tag{A.8}$$

By substituting c_c and Ψ_c into (A.7), we get

$$\frac{\mathcal{E} k_b T}{e L_c^2} \Delta \Psi_f^{\varepsilon} = -\frac{e\gamma \mathcal{E} k_b T}{(el)^2} \sum_{\beta=1}^{2} z_\beta c_\beta^{\varepsilon}, \tag{A.9}$$

so that $c_c L_c = \varepsilon^2$, hence (A.7) reads

$$\varepsilon^2 \Delta \Psi_f^{\varepsilon} = -\gamma \sum_{\beta=1}^{2} z_\beta c_\beta^{\varepsilon}. \tag{A.10}$$

Similarly, by inserting (3.2.1), (A.2) and (3.2.7) into (2.3.6), we get

$$\frac{\mathcal{E}\Psi_c}{L_c} \nabla \Psi_f^{\varepsilon} \cdot \boldsymbol{n} = -\Sigma_c \Sigma'. \tag{A.11}$$

After a few easy adjustments we get its dimensionless form as follows

$$\varepsilon \nabla \Psi_f^{\varepsilon} \cdot \boldsymbol{n} = -\frac{el\Sigma_c}{\mathcal{E} k_B T} \Sigma' = -N_\sigma \Sigma' \quad \text{on } \Gamma^{\varepsilon}, \tag{A.12}$$

where $N_\sigma = \frac{el\Sigma_c}{\mathcal{E} k_B T}$ is the ratio between electrical and thermal energy and it is usually of order $\mathcal{O}(1)$ in ε, (Moyne and Murad 2002).

Mass balance Upon substituting (A.2), (A.1) in the (2.3.3) one gets

$$\boldsymbol{j}_\alpha^{\varepsilon} j_c = -\frac{c_\alpha^{\varepsilon} c_c D_\alpha^0}{k_B T L_c} \nabla \left(k_B T \ln c_\alpha^{\varepsilon} c_c + e z_\alpha \zeta \Psi_f^{\varepsilon} \right). \tag{A.13}$$

By adding expression $\zeta = \frac{k_B T}{e}$ and using logarithm of a product formula we get

$$\boldsymbol{j}_\alpha^{\varepsilon} j_c = -\frac{c_\alpha^{\varepsilon} c_c D_\alpha^0}{L_c} \nabla \left(\ln c_\alpha^{\varepsilon} \exp(z_\alpha \Psi_f^{\varepsilon}) \right). \tag{A.14}$$

By comparing left and right side of this expression, we may found $j_c = \frac{c_c D_\alpha^0}{L_c}$ and thus

$$\boldsymbol{j}_\alpha^{\varepsilon} = -c_\alpha^{\varepsilon} \nabla \left(\ln c_\alpha^{\varepsilon} \exp(z_\alpha \Psi_f^{\varepsilon}) \right). \tag{A.15}$$

This expression is then added (together with (A.2) and (3.2.1)) into the mass balance equation (2.3.2), and by employing $\boldsymbol{w} = \boldsymbol{v} - \partial_t \boldsymbol{u}$, it becomes

$$\partial_t c^\varepsilon_\alpha + \frac{v_c L_c}{D^0_\alpha} \nabla \cdot (\boldsymbol{v}^\varepsilon c^\varepsilon_\alpha) + \nabla \cdot \boldsymbol{j}^\varepsilon_\alpha + \frac{u_c L_c}{D^0_\alpha t_c} \nabla \cdot (\partial_t \boldsymbol{u}^\varepsilon c^\varepsilon_\alpha) = 0, \tag{A.16}$$

where time scale is diffusion time $t_c = L_c^2 / D^0_\alpha$ and we may define so-called Peclet number $\mathrm{Pe}_\alpha = \frac{v_c L_c}{D^0_\alpha}$ that is also defined as a product of the Reynolds number $\mathrm{Re} = \frac{v_c L_c}{\eta_f}$ and Schmidt number $\mathrm{Sc}_\alpha = \frac{\eta_f}{D^0_\alpha}$. Finally, adding (A.2) and (A.1) into ionic exchanges condition (2.3.4) and after few adjustments we get

$$\boldsymbol{j}^\varepsilon_\alpha \frac{c_c D^0_\alpha}{L_c} \cdot \boldsymbol{n} = \frac{\alpha_c c_c D^0_\alpha}{L_c^2}{}_\alpha \frac{\partial c_\alpha}{\partial t} \qquad \text{on } \Gamma, i = 1, 2, \tag{A.17}$$

where there is so-called Damkohler number $\mathrm{D}^i_\alpha = \alpha_c L_c / t_c D^0_\alpha$. It can be shown, that because $k_\alpha \equiv l$ and thus the condition (A.17) becomes

$$\boldsymbol{j}^\varepsilon_\alpha \cdot \boldsymbol{n} = \varepsilon k_\alpha \frac{\partial c_\alpha}{\partial t} \qquad \text{on } \Gamma, i = 1, 2. \tag{A.18}$$

Elasticity

By substituting (A.2) and (A.1) into the elasticity equation (2.4.3) we obtain

$$-\frac{1}{L_c} \nabla \cdot (\frac{u_c}{L_c} \boldsymbol{A} \boldsymbol{e}(\boldsymbol{u}^\varepsilon)) = \boldsymbol{f} / \cdot \frac{L_c}{p_c}, \tag{A.19}$$

$$\nabla \cdot (\frac{u_c}{p_c L_c} \boldsymbol{A} \boldsymbol{e}(\boldsymbol{u}^\varepsilon)) = \boldsymbol{f}'. \tag{A.20}$$

Further, let E_c be the characteristic size of elastic moduli. The condition (2.4.6) then implies relation

$$E_c = \frac{p_c L_c}{u_c}, \tag{A.21}$$

and (A.20) becomes

$$\nabla \cdot (\frac{1}{E_c} \boldsymbol{A} \boldsymbol{e}(\boldsymbol{u}^\varepsilon)) = \boldsymbol{f}'. \tag{A.22}$$

We may introduce the dimensionless elasticity tensor $\boldsymbol{A}' = \boldsymbol{A} E_c^{-1}$. The rest of the procedure is similar, thus we only present its results.

The dimensionless form of elasticity equation and its boundary condition reads:

$$\nabla \cdot (\boldsymbol{A}' \boldsymbol{e}(\boldsymbol{u}^\varepsilon)) = \boldsymbol{f}' \quad \text{in } \Omega^\varepsilon_s, \tag{A.23}$$

$$\boldsymbol{A}' \boldsymbol{e}(\boldsymbol{u}^\varepsilon) \cdot \boldsymbol{n} = \left(-p^\varepsilon \boldsymbol{I} + 2\varepsilon^2 \boldsymbol{e}(\boldsymbol{v}^\varepsilon) + \frac{\varepsilon^2}{\beta} \left(\boldsymbol{E}^\varepsilon \otimes \boldsymbol{E}^\varepsilon - \frac{1}{2} |\boldsymbol{E}^\varepsilon|^2 \boldsymbol{I} \right) \right) \cdot \boldsymbol{n} \quad \text{on } \Gamma^\varepsilon, \tag{A.24}$$

and $\boldsymbol{u}^\varepsilon$ is Y-periodic, and continuity of velocity on interface becomes

$$\frac{\eta}{t_c E_c \varepsilon^2} \partial_t \boldsymbol{u}^\varepsilon = \boldsymbol{v}^\varepsilon, \quad \text{on } \Gamma. \tag{A.25}$$

Appendix B

Solution of Poisson-Boltzmann equation in equilibrium

The outcome of this appendix relies heavily on the asymptotic analysis of the dimensionless Poisson-Boltzmann equation given by (3.2.13) performed in (Allaire et al. 2013a) and (Allaire et al. 2013b), so we recommend referring to it for more detailed treatment. We recall its results for the sake of completeness. It can be shown, that in equilibrium ($\boldsymbol{f} = 0, \Psi^{\text{ext}} = 0$ and the fluxes are zero), the concentration is $c_\alpha^{\text{eq},\varepsilon}(x) = c_\alpha^b \exp(-z_\alpha \Psi^{\text{eq},\varepsilon})$ and Poisson-Boltzmann equation (3.2.13) can be rewritten as

$$\varepsilon^2 \Delta \Psi^{\text{eq},\varepsilon} = \gamma \sum_{\beta=1}^{N} z_\beta c_\beta^b \exp(-z_\beta \Psi^{\text{eq},\varepsilon}) \quad \text{in } \Omega_f^\varepsilon, \tag{B.1}$$

$$\varepsilon \nabla \Psi^{\text{eq},\varepsilon} \cdot \boldsymbol{n} = -\Sigma \quad \text{on } \Gamma^\varepsilon, \tag{B.2}$$

where c_β^b is concentration in infinite dilution. To guarantee, that for $\Sigma = 0$ there exists a unique solution $\Psi^{\text{eq},\varepsilon}$, we impose the so-called electroneutrality condition in bulk

$$\sum_{\beta=1}^{N} z_\beta c_\beta^b = 0. \tag{B.3}$$

We adhere to this condition, hence the existence of a unique solution $\Psi_f^{\text{eq},\varepsilon} \in H_\#^1(\Omega_f^\varepsilon)$ is guaranteed, see (Allaire et al. 2010). From the physical point of view, it ensures that $\Psi_f^{\text{eq},\varepsilon}$ vanishes for the zero surface charge.

Although we assume Σ to be a constant defined on the interface Γ^ε, even for a periodic distribution of charges $\mathcal{T}_\varepsilon(\Sigma) = \tilde{\Sigma}(y)$, $y \in \Gamma_Y$, the problem (**??**) yields εY-periodic solutions $\Psi^{\text{eq},\varepsilon}$ in Ω_f^ε, recalling the "macroscopic" L-periodicity on $\partial_{\text{ext}} \Omega_f^\varepsilon$. This property allows us to consider only the local problem in the zoomed RVE represented by cell Y_f.

By the periodicity of domain Ω^ε, we have also

$$\Psi_f^{\text{eq},\varepsilon}(x) = \Psi_f^{\text{eq}}(y), \quad c_\alpha^{\text{eq},\varepsilon}(x) = c_\alpha^{\text{eq}}(y), \tag{B.4}$$

where concentrations $c_\alpha^{\text{eq}}(y), \alpha = 1, 2$ obey the form of the Boltzmann distribution

$$c_\alpha^{\text{eq}}(y) = c_\alpha^b \exp(-z_\alpha \Psi_f^{\text{eq}}(y)). \tag{B.5}$$

The potential $\Psi_f^{\mathrm{eq}}(y) \in H^1_{\#}(Y_f)$ is a solution to the Poisson-Boltzmann equation (3.2.13) imposed in Y_f, in particular

$$\begin{aligned} \nabla_y^2 \Psi_f^{\mathrm{eq}} =& \gamma \sum_{\beta=1}^{2} z_\beta c_\beta^b \exp(-z_\beta \Psi_f^{\mathrm{eq}}) \quad \text{in } Y_f, \\ \nabla_y \Psi_f^{\mathrm{eq}} \cdot \boldsymbol{n} =& - N_\sigma \Sigma \quad \text{on } \Gamma_Y. \end{aligned} \tag{B.6}$$

The solution of this problems depends on the assymptotic analysis for parameter $\gamma \to 0$. Recall that

$$\gamma = \left(\frac{l}{\lambda_D} \right)^2. \tag{B.7}$$

The parameter γ is the fundamental physical characteristic that drives the transport properties of an electrolyte solution in porous media. For large γ, the electrical potential is concentrated in a diffuse layer next to the solid-fluid interface. According to (Allaire et al. 2013a),the Poisson-Boltzmann (B.1) exhibits the different regimes, depending on the values of parameter γ:

- If the parameter γ is large, it suggests that the size of a pore l is much large than Debye length λ_D. In this case, the electrical potential is concentrated in a diffuse layer next to the solid-fluid interface. Co-ions that exhibit the same charge as that of a solid phase are able to move freely inside a pore. In such cases, the effects of EDL on ionic transport are too small to consider.

- If the parameter γ is small, it suggests that the size of a pore is smaller than Debye length. In such a case, the EDL has a significant influence on the ionic movement and its effects have to be taken into account. In the case of two small γ, the effect of the EDL is too strong and co-ions do not have access to the small pores (Donnan effect).

In our case, we focus on the case of small γ.

As the literature suggests, the asymptotic analysis for small parameter γ, in other words for small pore size, is not trivial and for $\gamma \to 0$ even reveals the so-called Donnan effect. It is not our aim to reproduce this analysis, thus we only state its result. For the more rigorous analysis, we refer to (Allaire et al. 2013a).

Let as assume that $\int_{\Gamma_Y} \Sigma = 0$. Then potential in equilibrium Ψ^{eq} is quantified by

$$\Psi^0(y) = \Psi_{N0}(y) + O(\gamma), \tag{B.8}$$

where $\Psi_{N0}(y)$ is solution of

$$\Delta \Psi_{N0} = 0, \quad \text{in } Y_f, \tag{B.9}$$

$$\nabla \Psi_{N0} \cdot \boldsymbol{n} = -\Sigma \quad \text{on } \Gamma_Y, \tag{B.10}$$

and $\Psi_{N0}(y)$ is Y-periodic.

Appendix C

Partial derivatives for sensitivity analysis

In this section, we will give partial derivatives of material tensors describing microscopic scale with respect to the vector of optimization parameters $\boldsymbol{a}$. We consider, that tensor of piezoelectric coupling $\boldsymbol{g}$, dielectricity tensor $\boldsymbol{d}$ and elasticity tensor $\boldsymbol{A}$ have symmetry types and sparsity pasterns as given in Sec. 5.1.2, but we will recapitulate it for better readability: The transversal-isotropic elasticity tensor is characterized by Young's moduli E_1, E_3, shear modulus G_{13} and Poisson's ratios ν_{12}, ν_{31} and it is given by

$$\boldsymbol{A} = \begin{bmatrix} \frac{1-\nu_{13}\nu_{31}}{E_1 E_3 \Theta} & \frac{\nu_{12}+\nu_{13}\nu_{31}}{E_1 E_3 \Theta} & \frac{\nu_{31}+\nu_{12}\nu_{31}}{E_1 E_3 \Theta} & 0 & 0 & 0 \\ \frac{\nu_{12}+\nu_{13}\nu_{31}}{E_1 E_3 \Theta} & \frac{1-\nu_{13}\nu_{31}}{E_1 E_3 \Theta} & \frac{\nu_{31}+\nu_{12}\nu_{31}}{E_1 E_2 \Theta} & 0 & 0 & 0 \\ \frac{\nu_{31}+\nu_{12}\nu_{31}}{E_1 E_3 \Theta} & \frac{1-\nu_{12}^2}{E_1^2 \Theta} & \frac{1-\nu_{12}^2}{E_1^2 \Theta} & 0 & 0 & 0 \\ 0 & 0 & 0 & 2G_{13} & 0 & 0 \\ 0 & 0 & 0 & 0 & 2G_{13} & 0 \\ 0 & 0 & 0 & 0 & 0 & \frac{E_1}{2(1+\nu_{12})} \end{bmatrix}, \tag{C.1}$$

where $\Theta = (1+\nu_{12})(1-\nu_{12}-2\nu_{13}\nu_{31})(E_1^2 E_3)^{-1}$ and $\nu_{13} = \nu_{31} E_1 E_3^{-1}$.

The vector of optimization parameters $\boldsymbol{a}$ was given in Sec. 5.2 as

$$\boldsymbol{a} = \left[g_{14}, d_{11}, d_{33}, E_1, E_3, G_{13}, \nu_{12}, \nu_{31}\right]^T .$$

Then, we introduce following partial derivations:

$$\delta_{g_{14}} \boldsymbol{g} = \begin{bmatrix} 0 & 0 & 0 & 1 & 0 & 0 \\ 0 & 0 & 0 & 0 & -1 & 0 \\ 0 & 0 & 0 & 0 & 0 & 0 \end{bmatrix}, \tag{C.2}$$

$$\delta_{d_{11}} \boldsymbol{d} = \begin{bmatrix} 1 & 0 & 0 \\ 0 & 1 & 0 \\ 0 & 0 & 0 \end{bmatrix}, \quad \delta_{d_{33}} \boldsymbol{d} = \begin{bmatrix} 0 & 0 & 0 \\ 0 & 0 & 0 \\ 0 & 0 & 1 \end{bmatrix}. \tag{C.3}$$

For the sake of brevity, we will take advantage of symmetry of elasticity tensor $\boldsymbol{A}$ and write only partial derivation of its components. Let us also introduce function Θ and its partial derivatives:

$$\begin{aligned} &\Theta = \Theta_1\Theta_2, \quad \Theta_1 = (1+\nu_{12}), \quad \Theta_2 = (1-\nu_{12}-2\nu_{31}^2 E_1 E_3^{-1}),\\ \delta_{E_1}\Theta &= (1+\nu_{12})(-2\nu_{31}^2 E_3^{-1}),\\ \delta_{E_3}\Theta &= (1+\nu_{12})(2\nu_{31}^2 E_1 E_3^{-2}),\\ \delta_{\nu_{12}}\Theta &= (1-\nu_{12}-2\nu_{31}^2 E_1 E_3^{-1}) - (1+\nu_{12})\\ \delta_{\nu_{31}}\Theta &= (1+\nu_{12})(-4\nu_{31} E_1 E_3^{-1}). \end{aligned} \tag{C.4}$$

Using these expressions, we introduce the list of the non-zero partial derivatives of components of elasticity tensor $\boldsymbol{A}$ with symmetry (C.1):

- Partial derivatives of A_{ij} with respect to E_1

$$\begin{aligned} \delta_{E_1}A_{11} &= \left[(1-2\nu_{31}^2 E_1 E_3^{-1})\Theta - (E_1 - \nu_{31}^2 E_1^2 E_3^{-1})\delta_{E1}\Theta\right]\Theta^{-2},\\ \delta_{E_1}A_{12} &= \left[(\nu_{12}+2\nu_{31}^2 E_1 E_3^{-1})\Theta - (\nu_{12}E1 + \nu_{31}^2 E_1^2 E_3^{-1})\delta_{E_1}\Theta\right]\Theta^{-2},\\ \delta_{E_1}A_{33} &= \delta_{E_1}\Theta(\nu_{12}^2 E_3 - E_3)\Theta^{-2},\\ \delta_{E_1}A_{13} &= \left[(\nu_{31}+\nu_{12}\nu_{31})\Theta - (\nu_{31}E_1 + \nu_{12}\nu_{31}E_1)\delta_{E_1}\Theta\right]\Theta^{-2},\\ \delta_{E_1}A_{66} &= (2+2\nu_{12})^{-1}, \end{aligned} \tag{C.5}$$

- Partial derivatives of A_{ij} with respect to E_3

$$\begin{aligned} \delta_{E_3}A_{11} &= \left[(\nu_{31}^2 E_1^2 E_3^{-2})\Theta - (E_1 - \nu_{31}^2 E_1^2 E_3^{-1})\delta_{E_3}\Theta\right]\Theta^{-2},\\ \delta_{E_3}A_{12} &= \left[(-\nu_{31}^2 E_1^2 E_3^{-2})\Theta - (\nu_{12}E_1 + \nu_{31}^2 E_1^2 E_3^{-1})\delta_{E_3}\Theta\right]\Theta^{-2},\\ \delta_{E_3}A_{13} &= \delta_{E_3}\Theta(-\nu_{31}\nu_{12}E_1 - \nu_{31}E_1)\Theta^{-2},\\ \delta_{E_3}A_{33} &= \left[(1-\nu_{12}^2)\Theta - (E_3 - \nu_{12}^2 E_3)\delta_{E3}\Theta\right]\Theta^{-2}, \end{aligned} \tag{C.6}$$

- Partial derivatives of A_{ij} with respect to G_{13}

$$\delta_{G_{13}}A_{44} = 2, \tag{C.7}$$

- Partial derivatives of A_{ij} with respect to ν_{12}

$$\begin{aligned} \delta_{\nu_{12}}A_{11} &= (-E_1 + \nu_{31}^2 E_1^2 E_3^{-1})\left[\Theta_1^{-2}\Theta_2^{-1} - \Theta_1^{-1}\Theta_2^{-2}\right],\\ \delta_{\nu_{12}}A_{12} &= \left[E_1\Theta - (\nu_{12}E_1 + \nu_{31}^2 E_1^2 E_3^{-1})\delta_{\nu_{12}}\Theta\right]\Theta^{-2},\\ \delta_{\nu_{12}}A_{13} &= \left[E_1\nu_{31}\Theta - (\nu_{31}E_1 + \nu_{12}\nu_{31}E_1)\delta_{\nu_{12}}\Theta\right]\Theta^{-2},\\ \delta_{\nu_{12}}A_{33} &= \left[-2\nu_{12}E_3\Theta - (E_3 - \nu_{12}^2 E_3)\delta_{\nu_{12}}\Theta\right]\Theta^{-2},\\ \delta_{\nu_{12}}A_{66} &= -2E_1(1+\nu_{12})^{-2}, \end{aligned} \tag{C.8}$$

- Partial derivatives of A_{ij} with respect to ν_{31}

$$\begin{aligned} \delta_{\nu_{31}}A_{11} &= \left[(-2\nu_{31}E_1^2 E_3^{-1})\Theta - (E_1 - \nu_{31}^2 E_1^2 E_3^{-1})\delta_{E_3}\Theta\right]\Theta^{-2},\\ \delta_{\nu_{31}}A_{12} &= \left[(2\nu_{31}E_1^2 E_3^{-1})\Theta - (\nu_{12}E_1 + \nu_{31}^2 E_1^2 E_3^{-1})\delta_{\nu_{31}}\Theta\right]\Theta^{-2},\\ \delta_{\nu_{31}}A_{13} &= \left[(E_1 + E_1\nu_{12})\Theta - (\nu_{31}E_1 + \nu_{12}\nu_{31}E_1)\delta_{\nu_{31}}\Theta\right]\Theta^{-2},\\ \delta_{\nu_{31}}A_{33} &= (\nu_{12}^2 E_3 - E_3)\delta_{\nu_{31}}\Theta\Theta^{-2}. \end{aligned} \tag{C.9}$$

These partial derivatives serve to calculate total derivative of objective function $\delta^{\text{tot}}F(\boldsymbol{u},\boldsymbol{a})$.

Bibliography

Allaire, G., Bernard, O., Dufrêche, J.-F. and Mikelić, A. (2015). 'Ion transport through deformable porous media: derivation of the macroscopic equations using upscaling'. In: *Computational and Applied Mathematics*, pp. 1–32.

Allaire, G., Dufrêche, J.-F., Mikelić, A. and Piatnitski, A. (2013a). 'Asymptotic analysis of the Poisson–Boltzmann equation describing electrokinetics in porous media'. In: *Nonlinearity* 26.3, p. 881.

Allaire, G., Mikelić, A. and Piatnitski, A. (2010). 'Homogenization of the linearized ionic transport equations in rigid periodic porous media'. In: *Journal of Mathematical Physics* 51.12, p. 123103.

Allaire, G. et al. (2013b). 'Ion transport in porous media: derivation of the macroscopic equations using upscaling and properties of the effective coefficients'. In: *Computational Geosciences* 17.3, pp. 479–495.

Amirat, Y. and Shelukhin, V. (2008). 'Electroosmosis law via homogenization of electrolyte flow equations in porous media'. In: *Journal of Mathematical Analysis and Applications* 342.2, pp. 1227–1245.

Andreasen, C. S. and Sigmund, O. (2013). 'Topology optimization of fluid–structure-interaction problems in poroelasticity'. In: *Computer Methods in Applied Mechanics and Engineering* 258, pp. 55–62.

Auriault, J. and Boutin, C. (1993). 'Deformable porous media with double porosity. Quasi-statics. II: Memory effects'. In: *Transport in porous media* 10.2, pp. 153–169.

Beno, T., Yoon, Y.-J., Cowin, S. C. and Fritton, S. P. (2006). 'Estimation of bone permeability using accurate microstructural measurements'. In: *Journal of biomechanics* 39.13, pp. 2378–2387.

Benveniste, Y. (1987). 'A new approach to the application of Mori-Tanaka's theory in composite materials'. In: *Mechanics of materials* 6.2, pp. 147–157.

Chapman, D. L. (1913). 'LI. A contribution to the theory of electrocapillarity'. In: *The London, Edinburgh, and Dublin philosophical magazine and journal of science* 25.148, pp. 475–481.

Cimrman, R. (2014). 'SfePy-write your own FE application'. In: *arXiv preprint arXiv:1404.6391*.

Cioranescu, D., Damlamian, A. and Griso, G. (2002). 'Periodic unfolding and homogenization'. In: *Comptes Rendus Mathematique* 335.1, pp. 99–104.

— (2008). 'The periodic unfolding method in homogenization'. In: *SIAM Journal on Mathematical Analysis* 40.4, pp. 1585–1620.

Cowin, S. C. (1999). 'Bone poroelasticity'. In: *Journal of biomechanics* 32.3, pp. 217–238.

Dixon, L. C. W. and Price, R. C. (1988). ‘Numerical experience with the truncated Newton method for unconstrained optimization’. In: *Journal of optimization theory and applications* 56.2, pp. 245–255.

Emereuwa, C. A. (2020). ‘Mathematical homogenization and stochastic modeling of energy storage systems’. In: *Current Opinion in Electrochemistry* 21, pp. 117–124.

Eshelby, J. D. (1957). ‘The determination of the elastic field of an ellipsoidal inclusion, and related problems’. In: *Proceedings of the royal society of London. Series A. Mathematical and physical sciences* 241.1226, pp. 376–396.

Fotiadis, D. I., Foutsitzi, G. and Massalas, C. V. (1999). ‘Wave propagation modeling in human long bones’. In: *Acta mechanica* 137.1, pp. 65–81.

Frank, F., Ray, N. and Knabner, P. (2011). ‘Numerical investigation of homogenized Stokes–Nernst–Planck–Poisson systems’. In: *Computing and visualization in science* 14.8, pp. 385–400.

Fukada, E. and Yasuda, I. (1957). ‘On the piezoelectric effect of bone’. In: *Journal of the physical society of Japan* 12.10, pp. 1158–1162.

Gauthier, R. et al. (2019). ‘3D analysis of the osteonal and interstitial tissue in human radii cortical bone’. In: *Bone* 127, pp. 526–536. ISSN: 8756-3282.

Geuzaine, C. and Remacle, J.-F. (2009). ‘Gmsh: A 3-D finite element mesh generator with built-in pre-and post-processing facilities’. In: *International journal for numerical methods in engineering* 79.11, pp. 1309–1331.

Gouy, M. (1910). ‘Sur la constitution de la charge électrique à la surface d’un électrolyte’. In: *J. Phys. Theor. Appl.* 9.1, pp. 457–468.

Helmholtz, H. V. (1879). ‘Studien über electrische Grenzschichten’. In: *Annalen der Physik* 243.7, pp. 337–382.

Hillsley, M. and Frangos, J. (1994). ‘Bone tissue engineering: the role of interstitial fluid flow’. In: *Biotechnology and bioengineering* 43.7, pp. 573–581.

Hunter, R. J. (2001). *Foundations of colloid science.* Oxford University Press.

Joukar, A., Niroomand-Oscuii, H. and Ghalichi, F. (2016). ‘Numerical simulation of osteocyte cell in response to directional mechanical loadings and mechanotransduction analysis: Considering lacunar–canalicular interstitial fluid flow’. In: *Computer methods and programs in biomedicine* 133, pp. 133–141.

Karniadakis, G., Beskok, A. and Aluru, N. (2005). ‘Microflows and nanoflows: fundamentals and simulation’. In: p. 123.

Kleiber, M., Hien, T. D., Antúnez, H. and Kowalczyk, P. (1997). *Parameter sensitivity in nonlinear mechanics: Theory and finite element computations.* John Wiley & Son Limited.

Langtangen, H. P. and Pedersen, G. K. (2016). *Scaling of differential equations.* Springer Nature.

Lemaire, T., Kaiser, J., Naili, S. and Sansalone, V. (2010a). ‘Modelling of the transport in electrically charged porous media including ionic exchanges’. In: *Mechanics Research Communications* 37.5, pp. 495–499.

Lemaire, T., Naili, S. and Rémond, A. (2006). ‘Multiscale analysis of the coupled effects governing the movement of interstitial fluid in cortical bone’. In: *Biomechanics and modeling in mechanobiology* 5.1, pp. 39–52.

— (2008). ‘Study of the influence of fibrous pericellular matrix in the cortical interstitial fluid movement with hydroelectrochemical effects’. In: *Journal of Biomechanical Engineering* 130.1.

Lemaire, T., Naili, S. and Sansalone, V. (2010b). ‘Multiphysical modelling of fluid transport through osteo-articular media’. In: *Anais da Academia Brasileira de Ciências* 82.1, pp. 127–144.

Lemaire, T. et al. (2011). ‘A multiscale theoretical investigation of electric measurements in living bone’. In: *Bulletin of mathematical biology* 73.11, pp. 2649–2677.

Looker, J. R. and Carnie, S. L. (2006). ‘Homogenization of the ionic transport equations in periodic porous media’. In: *Transport in porous media* 65.1, pp. 107–131.

MacGinitie, L., Stanley, G., Bieber, W. and Wu, D. (1997). ‘Bone streaming potentials and currents depend on anatomical structure and loading orientation’. In: *Journal of biomechanics* 30.11-12, pp. 1133–1139.

Miara, B., Rohan, E., Zidi, M. and Labat, B. (2005). ‘Piezomaterials for bone regeneration design—homogenization approach’. In: *Journal of the Mechanics and Physics of Solids* 53.11, pp. 2529–2556.

Mikelić, A. and Wheeler, M. F. (2012). ‘On the interface law between a deformable porous medium containing a viscous fluid and an elastic body’. In: *Mathematical Models and Methods in Applied Sciences* 22.11, p. 1250031.

Milovanovic, P. et al. (2013). ‘Osteocytic canalicular networks: morphological implications for altered mechanosensitivity’. In: *ACS nano* 7.9, pp. 7542–7551.

Mohammadkhah, M., Marinkovic, D., Zehn, M. and Checa, S. (2019). ‘A review on computer modeling of bone piezoelectricity and its application to bone adaptation and regeneration’. In: *Bone* 127, pp. 544–555.

Moyne, C. and Murad, M. A. (2002). ‘Electro-chemo-mechanical couplings in swelling clays derived from a micro/macro-homogenization procedure’. In: *International Journal of Solids and Structures* 39.25, pp. 6159–6190.

— (2003). ‘Macroscopic behavior of swelling porous media derived from micromechanical analysis’. In: *Transport in porous media* 50.1-2, pp. 127–151.

— (2006). ‘A two-scale model for coupled electro-chemo-mechanical phenomena and onsager’s reciprocity relations in expansive clays: I homogenization analysis’. In: *Transport in Porous Media* 62.3, pp. 333–380.

Murad, M. A. and Moyne, C. (2008). ‘A dual-porosity model for ionic solute transport in expansive clays’. In: *Computational Geosciences* 12.1, p. 47.

Nalwa, H. S. (1995). *Ferroelectric polymers: chemistry: physics, and applications.* CRC Press.

Nash, S. G. (2000). ‘A survey of truncated-Newton methods’. In: *Journal of Computational and Applied Mathematics* 124.1. Numerical Analysis 2000. Vol. IV: Optimization and Nonlinear Equations, pp. 45–59. ISSN: 0377-0427.

Nejati, M., Dambly, M. L. T. and Saar, M. O. (2019). ‘A methodology to determine the elastic properties of anisotropic rocks from a single uniaxial compression test’. In: *Journal of Rock Mechanics and Geotechnical Engineering* 11.6, pp. 1166–1183.

Nguyen, V.-H., Lemaire, T. and Naili, S. (2009). ‘Numerical study of deformation-induced fluid flows in periodic osteonal matrix under harmonic axial loading’. In: *Comptes Rendus Mecanique* 337.5, pp. 268–276.

— (2010). ‘Poroelastic behaviour of cortical bone under harmonic axial loading: A finite element study at the osteonal scale’. In: *Medical engineering & physics* 32.4, pp. 384–390.

Oatley-Radcliffe, D., Aljohani, N., Williams, P. and Hilal, N. (2017). 'Electrokinetic phenomena for membrane charge'. In: *Membrane Characterization.* Elsevier, pp. 405–422.

O'Brien, R. W. and White, L. R. (1978). 'Electrophoretic mobility of a spherical colloidal particle'. In: *Journal of the Chemical Society, Faraday Transactions 2: Molecular and Chemical Physics* 74, pp. 1607–1626.

Oldham, K. B. (2008). 'A Gouy–Chapman–Stern model of the double layer at a (metal)/(ionic liquid) interface'. In: *Journal of Electroanalytical Chemistry* 613.2, pp. 131–138.

Pienkowski, D. and Pollack, S. (1983). 'The origin of stress-generated potentials in fluid-saturated bone'. In: *Journal of Orthopaedic Research* 1.1, pp. 30–41.

Predoi-Racila, M. and Crolet, J. M. (2008). 'Human cortical bone: the SiNuPrOs model: Part I—description and elastic macroscopic results'. In: *Computer methods in biomechanics and biomedical engineering* 11.2, pp. 169–187.

Ray, N., Muntean, A. and Knabner, P. (2012a). 'Rigorous homogenization of a Stokes–Nernst–Planck–Poisson system'. In: *Journal of Mathematical Analysis and Applications* 390.1, pp. 374–393.

Ray, N., Noorden, T. van, Frank, F. and Knabner, P. (2012b). 'Multiscale modeling of colloid and fluid dynamics in porous media including an evolving microstructure'. In: *Transport in porous media* 95.3, pp. 669–696.

Rémond, A., Naıli, S. and Lemaire, T. (2008). 'Interstitial fluid flow in the osteon with spatial gradients of mechanical properties: a finite element study'. In: *Biomechanics and modeling in Mechanobiology* 7.6, pp. 487–495.

Rho, J.-Y., Kuhn-Spearing, L. and Zioupos, P. (1998). 'Mechanical properties and the hierarchical structure of bone'. In: *Medical engineering & physics* 20.2, pp. 92–102.

Rohan, E. and Lukeš, V. (2015). 'Modeling nonlinear phenomena in deforming fluid-saturated porous media using homogenization and sensitivity analysis concepts'. In: *Applied Mathematics and Computation* 267, pp. 583–595.

Rohan, E. (2003). 'Sensitivity strategies in modelling heterogeneous media undergoing finite deformation'. In: *Mathematics and Computers in Simulation* 61.3-6, pp. 261–270.

Rohan, E. et al. (2010). *Homogenization of electro-osmosis in porous solid saturated by ionized fluid.*

Rohan, E. and Lukeš, V. (2018). 'Homogenization of the fluid-saturated piezoelectric porous media'. In: *International Journal of Solids and Structures* 147, pp. 110–125.

Rohan, E. and Miara, B. (2006). 'Homogenization and shape sensitivity of microstructures for design of piezoelectric bio-materials'. In: *Mechanics of Advanced Materials and Structures* 13.6, pp. 473–485.

Rohan, E., Naili, S., Cimrman, R. and Lemaire, T. (2012). 'Multiscale modeling of a fluid saturated medium with double porosity: Relevance to the compact bone'. In: *Journal of the Mechanics and Physics of Solids* 60.5, pp. 857–881.

Rohan, E., Naili, S. and Lemaire, T. (2016a). 'Double porosity in fluid-saturated elastic media: deriving effective parameters by hierarchical homogenization of static problem'. In: *Continuum Mechanics and Thermodynamics* 28.5, pp. 1263–1293.

Rohan, E., Turjanicová, J. and Lukeš, V. (2016b). ‘A Darcy-Brinkman model of flow in double porous media - two-level homogenization and computational modeling’.

— (2019). ‘The Biot–Darcy–Brinkman model of flow in deformable double porous media; homogenization and numerical modelling’. In: *Computers & Mathematics with Applications* 78.9, pp. 3044–3066.

— (2021). ‘Multiscale modelling and simulations of tissue perfusion using the Biot-Darcy-Brinkman model’. In: *Computers & Structures* 251, p. 106404.

Sandström, C., Larsson, F. and Runesson, K. (2016). ‘Homogenization of coupled flow and deformation in a porous material’. In: *Computer Methods in Applied Mechanics and Engineering* 308, pp. 535–551.

Schmuck, M. and Bazant, M. Z. (2015). ‘Homogenization of the Poisson–Nernst–Planck equations for ion transport in charged porous media’. In: *SIAM Journal on Applied Mathematics* 75.3, pp. 1369–1401.

Siddique, J. I., Ahmed, A., Aziz, A. and Khalique, C. M. (2017). ‘A review of mixture theory for deformable porous media and applications’. In: *Applied Sciences* 7.9, p. 917.

Silva, C. et al. (2001). ‘Collagen–hydroxyapatite films: piezoelectric properties’. In: *Materials Science and Engineering: B* 86.3, pp. 210–218.

Stern, O. (1924). ‘Zur theorie der elektrolytischen doppelschicht’. In: *Zeitschrift für Elektrochemie und angewandte physikalische Chemie* 30.21-22, pp. 508–516.

Turjanicová, J., Rohan, E. and Lukeš, V. (2019). ‘Homogenization based two-scale modelling of ionic transport in fluid saturated deformable porous media’. In: *Computers & Mathematics with Applications* 78.9, pp. 3211–3235.

Vatsa, A. et al. (2008). ‘Osteocyte morphology in fibula and calvaria—is there a role for mechanosensing?’ In: *Bone* 43.3, pp. 452–458.

Virtanen, P. et al. (2020). ‘SciPy 1.0: Fundamental Algorithms for Scientific Computing in Python’. In: *Nature Methods*.

Yoon, Y. J. and Cowin, S. C. (2008). ‘The estimated elastic constants for a single bone osteonal lamella’. In: *Biomechanics and modeling in mechanobiology* 7.1, pp. 1–11.

Zou, W.-N., Tang, C.-X. and Pan, E. (2013). ‘Symmetry types of the piezoelectric tensor and their identification’. In: *Proceedings of the Royal Society A: Mathematical, Physical and Engineering Sciences* 469.2155, p. 20120755.

Authors own publications

Journal papers

Turjanicová, J., Rohan, E. and Naili, S. (2014). 'Three-scale model of single bone osteon modelled as double-porous fluid saturated body: Study of influence of micro/meso-structure'. In: *Applied and Computational Mechanics* 8.2, pp. 199–214. ISSN: 1802-680X.

Rohan, E., Lukeš, V. and Turjanicová, J. (2017a). 'A Darcy-Brinkman model of flow in double porous media - two-level homogenization and computational modelling'. In: Submitted in: Computers and Structures.

Rohan, E., Turjanicová, J. and Lukeš, V. (2020). 'Homogenization based modelling of the perfused liver tissue'. In: *6th European Conference on Computational Mechanics – Conference proceedings*, pp. 870–881.

Rohan, E., Turjanicová, J. and Lukeš, V. (2018). 'A Darcy-Brinkman model of flow in double porous media–Two-level homogenization and computational modelling'. In: *Computers & Structures* 207, pp. 95–110.

— (2019c). 'The Biot–Darcy–Brinkman model of flow in deformable double porous media; homogenization and numerical modelling'. In: *Computers & Mathematics with Applications* 78.9, pp. 3044–3066.

— (2021b). 'Multiscale modelling and simulations of tissue perfusion using the Biot-Darcy-Brinkman model'. In: *Computers & Structures* 251, pp. 1–20.

Turjanicová, J., Rohan, E. and Lukeš, V. (2019a). 'Homogenization based two-scale modelling of ionic transport in fluid saturated deformable porous media'. In: *Computers & Mathematics with Applications* 78.9, pp. 3211–3235.

Conference proceedings

Rohan, E., Lukeš, V. and Turjanicová, J. (2016a). 'Computational homogenization for hierarchically arranged porous media'. In: *Book of abstracts ESCO 2016, 5th European Seminar on Computing*, p. 220. ISBN: 978-80-01-06039-1.

— (2016b). 'Computational modeling of liver perfusion respecting the lobular structure of the tissue'. In: *16th Conference on Human Biomechanics 2016 – Conference proceedings.* Kladno: České vysoké učení technické v Praze, pp. 26–27. ISBN: 978-80-01-06039-1.

Rohan, E., Lukes, V., Turjanicová, J. and Cimrman, R. (2017b). 'Two level homogenization of flows in deforming double porosity media: Biot-Darcy-Brinkman model'. In: *COMPLAS XIV: proceedings of the XIV International Conference on Computational Plasticity: fundamentals and applications.* CIMNE, pp. 184–195.

Rohan, E., Lukeš, V., Turjanicová, J. and Jiřık, M. (2017c). ‘Towards image-based analysis of the liver perfusion using a hierarchical flow model’. In: *European Congress on Computational Methods in Applied Sciences and Engineering*. Springer, pp. 593–598.

Rohan, E., Naili, S., Turjanicová, J. and Lemaire, T. (2013). ‘Models of poroelastic double porous structures based on hierarchical homogenization - application to compact bone’. In: *Poromechanics V : proceedings of the 5th Biot Conference on Poromechanics*. American Society of Civil Engineers, pp. 1152–1159. ISBN: 978-0-7844-1299-2.

Rohan, E., Turjanicová, J. and Lukeš, V. (2015). ‘Modelling Flows in Multi-Porous Media using Homogenization with application to Liver Lobe Perfusion’. In: *Proceedings of the Fifteenth International Conference on Civil, Structural and Environmental Engineering Computing*. Civil-Comp Press, pp. 1–15. ISBN: 978-1-905088-63-8.

— (2019a). ‘Multicompartment Biot-Darcy-Brinkman models of flow in deformable double porous media: application to the liver tissue perfusion’. In: *The Sixteenth International Conference on Civil, Structural & Environmental Engineering Computing*, pp. 1–3.

Rohan, E., Turjanicová, J. and Lukes, V. (2019b). ‘Multiscale modelling of liver perfusion’. In: *COMPLAS XV: proceedings of the XV International Conference on Computational Plasticity: fundamentals and applications*. CIMNE, pp. 343–353.

Turjanicová, J., Lukeš, V. and Rohan, E. (2016). ‘Multiscale modeling of ionic transport in deformable porous media’. In: *32 th conference with international participation Computational Mechanics 2016*. Pilsen: University of West Bohemia, pp. 133–134. ISBN: 978-80-261-0647-0.

Turjanicová, J. and Rohan, E. (2013). ‘Anisotropic behaviour of an osteon multiscale model’. In: *29th conference with international participation Computational Mechanics 2013*. Pilsen: University of West Bohemia, pp. 135–136. ISBN: 978-80-261-0282-3.

— (2014a). ‘Electro-osmosis in a cortical bone porous structure: Parametric study’. In: *Studentská vědecká konference 2014 : magisterské a doktorské studijní programy : sborník rozšířených abstraktů*. Pilsen: University of West Bohemia, pp. 33–34. ISBN: 978-80-261-0365-3.

— (2014b). ‘Homogenization of electro-osmosis phenomena in the cortical bone porous structure’. In: *Engineering mechanics*. Brno: Brno University of Technology, Institute of Solid Mechanics, Mechatronics and Biomechanics, pp. 668–671. ISBN: 978-80-214-4871-1.

— (2014c). ‘Macroscopic modeling of electro-osmosis in the porous structure of a cortical bone tissue’. In: *30th conference with international participation Computational Mechanics 2014*. Pilsen: University of West Bohemia, pp. 177–178. ISBN: 978-80-261-0429-2.

— (2015b). ‘Modelling of ionic transport in cortical bone porous structure’. In: *31 th conference with international participation Computational Mechanics 2015*. Pilsen: University of West Bohemia, pp. 119–120. ISBN: 978-80-261-0568-8.

Turjanicová, J., Rohan, E., Lemaire, T. and Naili, S. (2018a). ‘Modelling of Quazistationary Ionic Transport in Fluid Saturated Deformable Porous Media’. In:

ESCO 2018 - 6th European Seminar on Computing. Pilsen: University of West Bohemia, p. 173.

Turjanicová, J., Rohan, E. and Lukeš, V. (2017). 'Quasi-static model of ionic transport through deformable porous media.' In: *32 th conference with international participation Computational Mechanics 2017.* Pilsen: University of West Bohemia, pp. 143–144. ISBN: 978-80-261-0748-4.

— (2018b). 'Numerical simulation of ionic transport through deformable porous media: Application to cortical bone tissue modeling'. In: *The 9th International Conference on Multiscale Materials Modeling 2018 (MMM2018).*

— (2018c). 'Numerical simulation of quasi-static model of ionic transport through deformable porous media.' In: *Applied Mechanics 2018 : proceedings of extended abstracts.* Pilsen: University of West Bohemia, pp. 163–169. ISBN: 978-80-261-0766-8.

— (2019b). 'Two-scale modelling of electromechanical behavior of cortical bone tissue: from micro- to mezo-scale'. In: *Book of Abstracts of the 25th Congress of the European Society of Biomechanics (ESB 2019).* Wien: TU Verlag, p. 62. ISBN: 978-3-903024-96-0.

Turjanicová, J., Rohan, E., Naili, S. and Cimrman, R. (2013a). 'Cortical bone tissue modelled as double-porous medium: Parameter study'. In: *SVK FAV 2013 - magisterské a doktorské studijní programy, sborník rozšířených abstraktů.* Pilsen: University of West Bohemia, pp. 29–30. ISBN: 978-80-261-0238-0.

— (2013b). 'Modelling of cortical bone tissue as a fluid saturated double-porous material - parametric study'. In: *Sborník vědeckých prací Vysoké školy báňské-Technické univerzity Ostrava.* Ostrava: VŠB - Technical University, pp. 131–136.

— (2013c). 'Parametric study of cortical bone tissue modelled as a fluid saturated double-porous material'. In: *Applied Mechanics 2013 : proceedings of extended abstracts.* Ostrava: VŠB - Technical University, pp. 1–2. ISBN: 978-80-248-2978-4.

Unpublished Papers

Rohan, E., Camprová Turjanicová, J. and Liška, V. (2021a). 'Geometrical model of lobular structure and its importance for the liver perfusion analysis'. PLOS One.